Dissertation
submitted to the
Joint Faculties for Natural Sciences and Mathematics
of the Ruperto Carola University of
Heidelberg, Germany,
for the degree of
Doctor of Natural Sciences

Put forward by

Dipl.-Phys. Stefan Jaumann
Born in Ellwangen (Jagst)

Oral examination:
10. January 2018

Estimation of Soil Water Dynamics
Based on Hydrogeophysical Measurements

Referees
Prof. Dr. Kurt Roth
Prof. Dr. Norbert Frank

The original version of this dissertation has been deposited in the library of Heidelberg University. This electronically available version contains minor editorial changes that have come up during the review process of Jaumann and Roth (2018).

Stefan Jaumann Nanjing, May 2018

Estimation of Soil Water Dynamics Based on Hydrogeophysical Measurements

Quantitative understanding of soil water movement is essential to develop methods that allow for a more sustainable use of limited freshwater resources. In this study, methods are developed that allow to estimate the spatial distribution of these materials, their effective soil hydraulic material properties, and the effect of unrepresented model errors on these properties. To acquire the necessary data, a 2D subsurface architecture (ASSESS) was forced with a fluctuating groundwater table. The resulting hydraulic dynamics were essentially monitored with time domain reflectometry (TDR) and ground-penetrating radar (GPR). Based on the TDR data, the effect of unrepresented model errors on estimated soil hydraulic material properties is analyzed with a structural error analysis. This method compares inversions of increasingly complex models, since the required model complexity for a consistent description of the measurement data is application-dependent and unknown a priori. It is demonstrated that the method can indicate unrepresented model errors and quantify their effects on the resulting material properties. Based on the GPR data, a new heuristic event detection and association algorithm was developed that allows to identify and to extract relevant information from GPR data. It is demonstrated for synthetic and measured data that this approach provides reasonably accurate estimates for the spatial distribution of materials and their soil hydraulic material properties.

Schätzung der Bodenwasserdynamik anhand hydrogeophysikalischer Messungen

Ein quantitatives Verständnis von Bodenwasserbewegungen ist wesentlich für die Entwicklung von Methoden, die eine nachhaltigere Nutzung begrenzter Süßwasserressourcen ermöglichen. In dieser Studie werden Methoden entwickelt, die es erlauben, die räumliche Verteilung dieser Materialien, ihre effektiven bodenhydraulischen Materialeigenschaften und die Auswirkung von nicht dargestellten Modellfehlern auf diese Eigenschaften abzuschätzen. Um die notwendigen Daten zu erhalten, wurde der Grundwasserspiegel in einer 2D-Untergrundarchitektur (ASSESS) variiert. Die resultierende hydraulische Dynamik wurde im Wesentlichen mit Zeitbereichsreflektometrie (TDR) und Bodenradar (GPR) überwacht. Basierend auf den TDR-Daten wird der Einfluss von nicht dargestellten Modellfehlern auf geschätzte bodenhydraulische Materialeigenschaften mit einer Strukturfehleranalyse analysiert. Diese Methode vergleicht Inversionen zunehmend komplexer Modelle, da die erforderliche Modellkomplexität für eine konsistente Beschreibung der Messdaten anwendungsabhängig und a priori unbekannt ist. Es wird gezeigt, dass das Verfahren nicht dargestellte Modellfehler anzeigen und deren Auswirkungen auf die resultierenden Materialeigenschaften quantifizieren kann. Basierend auf den GPR-Daten wurde ein neuer heuristischer Ereignisdetektions- und Assoziierungsalgorithmus entwickelt, der es erlaubt, relevante Informationen aus GPR-Daten zu identifizieren und zu extrahieren. Für synthetische und gemessene Daten wird gezeigt, dass dieser Ansatz hinreichend genaue Schätzungen für die räumliche Verteilung von Materialien und ihre bodenhydraulischen Materialeigenschaften liefern.

Contents

List of Figures

List of Tables

Acronyms and symbols

Acronyms

3DFM	3D Fast Marching	27
ATLC	arbitrary transmission line calculator	39
BATEA	Bayesian total error analysis	66
CMP	common mid point	41
CO	common offset	41
CRIM	complex refractive index model	35
EnKF	ensemble Kalman filter	52
ERT	electrical resistance tomography	65
FDTD	finite-difference time-domain	27
FFT	fast Fourier transform	94
FMM	fast marching method	27
GMCS	global multilevel coordinate search	91
GPR	ground-penetrating radar	2
MCMC	Markov chain Monte Carlo	65
MEEP	MIT electromagnetic equation propagation	28
NMS	Nelder–Mead simplex	91
PML	perfectly matched layer	29
REV	representative elementary volume	10
SCE-UA	shuffled complex evolution developed at the University of Arizona	52
SHIP	soil hydraulics and hydrogeophysics inversion package	52
TDR	time domain reflectometry	2
WARR	wide angle reflection and refraction	41

Symbols

The symbols are chosen to be consistent with the conventional use in the discussed topics. Double assignment was avoided through the use of indices if this was possible without making the notation excessively complicated. For the other cases, the definition of the variable should be clear from the context. The association of parameters with materials is indicated with superscripts.

Mathematical notation

$\odot$	elementwise multiplication
a, A	scalar
$\boldsymbol{a}$, $\boldsymbol{A}$	vector
$\boldsymbol{A}$	tensor
$\boldsymbol{e}_\diamond$	unit vector in direction $\diamond$
i	complex unit
$\mathcal{U}(\diamond, \triangleleft)$	uniform distribution sampled from $[\diamond, \triangleleft]$

Latin lower case symbols

a	GPR antenna separation [m]	3.69
c	velocity of electromagnetic fields in media [m]	3.41
c_0	velocity of electromagnetic fields in vacuum ($3.0 \cdot 10^8$ m s^{-1})	3.41
d	subsurface architecture parameter [m]	6.4
e_{MA}	mean absolute error	5.1
e_{RMS}	root mean square error	5.1
f	model function	3.70
f_{w}	frequency of an electromagnetic wave [Hz]	6.5
g	gravitational constant (9.81 m s^{-2})	3.11
$\boldsymbol{g}$	Earth's gravitation vector [m s^{-2}]	3.4
g	model function	3.78
h	height [m]	3.11
h_0	Brooks–Corey parameter [m]	3.20
h_{m}	matric head [m]	3.16
h_{w}	water head [m]	3.16
i_{iter}	iterator for iterations of an algorithm	3.91
i_{meas}	iterator for measurements	3.88

i_{param}	iterator for parameters	3.89
$\boldsymbol{j}$	flux [$\mathrm{m\,s^{-1}}$]	3.2
$\boldsymbol{j}_{\text{w}}$	water flux [$\mathrm{m\,s^{-1}}$]	3.17
j_x	flux in x direction [$\mathrm{m\,s^{-1}}$]	3.10
$\boldsymbol{k}$	wave vector	3.39
k	wave number	3.41
k_{SA}	simulated annealing parameter [−]	3.95
m	mass [g]	3.4
$\boldsymbol{m}$	measurement vector	3.72
m	measurement	3.88
m_{SA}	simulated annealing parameter [−]	3.93
n	refraction index [−]	3.56
n_{vG}	van Genuchten parameter [−]	3.23
p	pressure [Pa]	3.4
$\boldsymbol{p}$	parameter vector	3.70
p	parameter	3.89
p_{a}	pressure in air [Pa]	3.15
p_l	pressure in liquid phase [Pa]	3.11
p_v	pressure in vapor phase [Pa]	3.11
p_{w}	pressure in water [Pa]	3.15
r	radial (total) distance in cylindrical (spherical) coordinates [m]	3.9
$\boldsymbol{r}$	standardized residual vector [−]	3.88
r	standardized residual [−]	3.88
r_{C}	capillary radius [m]	3.9
$\boldsymbol{s}$	Poynting vector [$\mathrm{J\,m^{-2}\,s^{-1}}$]	3.63
t	time [s]	3.6
u_{d}	random number drawn from uniform distribution: $\sim \mathcal{U}(0,1)$	3.94
u_{p}	random number drawn from uniform distribution: $\sim \mathcal{U}(-1,1)$	3.93
$\boldsymbol{v}$	velocity [$\mathrm{m\,s^{-1}}$]	3.1
$\boldsymbol{x}$	position in three dimensional space [m]	3.14
x	position in x dimension [m]	3.10
y	position in y dimension [m]	3.59
z	position in z dimension [m]	3.9
z_0	reference position in z dimension [m]	3.15

Latin upper case symbols

$\boldsymbol{A}$	surface area with unit normal vector pointing outwards [m^2]	3.1
A	normalized amplitude [−]	6.0
$\boldsymbol{B}$	magnetic flux density [T]	3.23
$\boldsymbol{C}$	covariance matrix	3.81
$\boldsymbol{D}$	electric displacement field [$C\,m^{-2}$]	3.23
$\boldsymbol{D}$	damping matrix	3.90
$\boldsymbol{E}$	electric field [$V\,m^{-1}$]	3.23
E_x	x dimension of the electric field [$V\,m^{-1}$]	3.60
$\boldsymbol{F}_g$	gravitational force [N]	3.4
$\boldsymbol{F}_p$	pressure force [N]	3.4
$\boldsymbol{F}_v$	frictional force [N]	3.4
$\boldsymbol{H}$	magnetic field [$A\,m^{-1}$]	3.23
$\boldsymbol{H}$	Hesse matrix	3.89
$\boldsymbol{H}_{\mathrm{obs}}$	observation operator	3.72
$\boldsymbol{J}$	current density [$A\,m^{-2}$]	3.26
$\boldsymbol{J}$	Jacobian matrix	3.89
$\boldsymbol{J}_{\mathrm{s}}$	source current density [$A\,m^{-2}$]	3.27
K	hydraulic conductivity function [$m\,s^{-1}$]	3.19
K_{p}	cell constant of a TDR probe [m^{-1}]	3.68
K_{s}	Mualem parameter [$m\,s^{-1}$]	3.22
L_{A}	characteristic length of an antenna [m]	3.60
L_{TDR}	length of TDR rods [m]	3.66
N_{epp}	number of cost function evaluations per parameter	3.97
N_{eval}	number of cost function evaluations	3.97
N_{i}	number of iterations	3.92
N_{m}	number of measurements	3.88
N_{param}	number of parameters	3.89
$\boldsymbol{P}$	electrical polarization density [$C\,m^{-2}$]	3.33
P	probability density function	3.79
R_{c}	cable resistivity [$\Omega\,m^{-1}$]	3.67
R_∞	reflection coefficient at infinite time [−]	3.65
R_{s}	soil resistivity [$\Omega\,m^{-1}$]	3.67
R_{tot}	total resistivity [$\Omega\,m^{-1}$]	3.66
R_{w}	reflection coefficient for a plane wave [−]	3.58
$\boldsymbol{S}$	sensitivity matrix	3.91
S	cost function [−]	3.84

S_C	Courant number [–]	3.60
T	temperature [°C]	3.34
T_s	soil temperature [°C]	3.64
T_{SA}	simulated annealing parameter [–]	3.93
T_w	transmission coefficient for a plane wave [–]	3.58
V	volume [m^3]	3.1
V_w	water volume [m^3]	3.13
Z_c	cable impedance [Ω]	3.67

Greek lower case symbols

α_{CRIM}	CRIM parameter [–]	3.64
α_H	Heimovaara parameter [–]	3.68
α_{SA}	simulated annealing parameter [–]	3.94
α_{vG}	van Genuchten parameter [m^{-1}]	3.23
α_w	angle of reflection and incidence of a plane wave	3.57
ε	permittivity [$F\,m^{-1}$]	3.29
ε_0	permittivity of vacuum ($8.85 \cdot 10^{-12}$ $F\,m^{-1}$)	3.34
ε_r	relative permittivity [–]	3.35
$\varepsilon_{r,0}$	instantaneous relative permittivity [–]	3.48
$\varepsilon_{r,a}$	relative permittivity of air [–]	3.64
$\varepsilon_{r,b}$	relative permittivity of soil bulk [–]	5.0
$\varepsilon_{r,\infty}$	relaxation relative permittivity [–]	3.48
$\varepsilon_{r,s}$	relative permittivity of soil matrix [–]	3.64
$\varepsilon_{r,w}$	relative permittivity of water [–]	3.53
$\boldsymbol{\eta}_{obs}$	observation error	3.73
$\boldsymbol{\eta}_{mod}$	model error	3.71
$\boldsymbol{\eta}_{total}$	combined model and observation error	3.78
θ_a	volumetric air content [–]	3.13
θ_w	volumetric water content [–]	3.13
$\theta_{w,r}$	residual water content [–]	3.14
$\theta_{w,s}$	water content at saturation [–]	3.14
λ	Brooks–Corey parameter [–]	3.20
λ_{LM}	Levenberg–Marquardt parameter [–]	3.90
λ_w	wave length [m]	3.60
μ	permeability [$H\,m^{-1}$]	3.29
μ_0	permeability of vacuum ($4\pi \cdot 10^{-7}$ $H\,m^{-1}$)	3.37

μ_f	momentum flux [$\mathrm{N\,m^{-2}}$]	3.4
μ_r	relative permeability [−]	3.37
ξ	Miller scaling factor [−]	3.22
ρ	density [$\mathrm{g\,m^{-3}}$]	3.1
ρ_e	internal volume charge density [$\mathrm{C\,m^{-3}}$]	3.24
ρ_l	density liquid [$\mathrm{g\,m^{-3}}$]	3.11
ρ_v	density vapor [$\mathrm{g\,m^{-3}}$]	3.11
ρ_w	water density ($\approx 10^6$ $\mathrm{g\,m^{-3}}$)	3.15
σ	electrical conductivity [$\mathrm{S\,m^{-1}}$]	3.29
σ_dc	direct current electrical conductivity [$\mathrm{S\,m^{-1}}$]	3.36
σ_{lv}	interfacial energy density of liquid and vapor [$\mathrm{J\,m^{-2}\,s^{-1}}$]	3.11
τ	Mualem parameter [−]	3.22
τ_D	Debye model parameter [s]	3.49
ϕ	porosity [−]	3.10
χ^2	cost function [−]	3.88
χ_e	electric susceptibility [−]	3.33
χ_m	magnetic susceptibility [−]	3.37
ψ_g	gravity potential [Pa]	3.15
ψ_m	matric potential [Pa]	3.15
ψ_w	water potential [Pa]	3.15
ω	angular frequency [$\mathrm{s^{-1}}$]	3.34

Greek upper case symbols

Θ	water saturation [−]	3.14
$\boldsymbol{\Psi}$	state variable	3.70

1 Introduction

Fresh water is scarce in many regions of the world. This causes a wide range of ecological and human crises comprising destruction of aquatic ecosystems, extinction of species, threats to human health, and increased potential for regional and international conflicts (Gleick, 1998).

Although 70% of Earth's surface is covered with water, only 3% of the total water volume are freshwater including 2% that are locked in ice and glaciers. Hence, far less than 1% of the total water volume is accessible for humanity (Henderson et al., 2009). However, in order to assess the total amount of available freshwater resources, an analysis of the accessible water flux is more adequate, as water cycles naturally in the hydrological cycle. Hence, the available renewable freshwater resources comprises the annual discharge of 45500 $km^3\,a^{-1}$, which essentially flows through the rivers from continents to the sea (Oki and Kanae, 2006).

Postel et al. (1996) estimated that humanity uses 26% of the total evapotranspiration and 54% of the runoff that is geographically and temporally accessible. However, in particular the global runoff is geographically not evenly distributed. While Asia has 61% of the global population, it only receives 36% of the global runoff (Postel et al., 1996). In order to provide the required water resources, groundwater reservoirs are tapped and often overdrafted. Thus, with the increasing global population also the global water demand as well as the global groundwater abstraction and depletion increased from 1960 to 2000 (Wada et al., 2010).

In order to investigate the sustainability of the global groundwater consumption, Gleeson et al. (2012) define the *groundwater footprint* as the area required to sustain groundwater use and groundwater-dependent ecosystem services. They showed that humans are overexploiting groundwater in many large aquifers that are critical to agriculture, especially in Asia and North America. According to the authors, the size of the global groundwater footprint is currently about 3.5 times the actual area of the aquifers and that about 1.7 billion people live in areas where groundwater resources and/or groundwater-dependent ecosystems are under threat.

Irrigation accounts for 70% of the global freshwater withdrawals and 90% of consumptive water uses (Siebert et al., 2010). Hence, one step towards a more sustainable usage of the freshwater resources comprises the development of methods for more efficient use of irrigation water. Generally, this requires a quantitative understanding of soil water movement.

Quantitative understanding of soil water movement can be defined as the ability to describe and predict the soil water content in space and time accurately with a physics-based model. Typically, soil water movement is modeled with the Richards equation

(Eq. 3.20). Besides boundary conditions and an initial water content distribution, the solution of this partial differential equation requires knowledge of the subsurface material distribution (subsurface architecture) and the corresponding soil hydraulic material properties. These material properties are highly nonlinear, vary over many orders of magnitude, and are unknown a priori (Eqs. 3.21–3.22). Also, the soil hydraulic material properties have to be determined directly at the scale of interest due to the multi-scale heterogeneity of soils (e.g., Vogel and Roth, 2003). Hence, methods are required that (i) allow for efficient and noninvasive identification of the subsurface architecture as well as the subsurface material distribution on the field-scale and (ii) account for uncertainties in the model and in the measurement data.

Hydrogeophysical measurement methods (Rubin and Hubbard, 2005; Robinson et al., 2008a) are suitable to provide the data required to analyze the subsurface quantitatively. Many of these methods yield spatiotemporal distributions of electromagnetic material properties, in particular electrical conductivity and permittivity. Subsequently, these material properties can be transferred to soil water content distributions with the help of petrophysical relationships.

During the last decades, much effort has been made for the application and evaluation of hydrogeophysical measurement methods on the plot-scale ($\mathcal{O}(10\text{ m})$). However, many applications in hydrology require data that cover larger scales (Binley et al., 2015). Currently, various methods are available to determine the soil water content at different scales (Robinson et al., 2008b). A standard method to measure soil water content at the point-scale $\mathcal{O}(10^{-1}\text{ m})$ is time domain reflectometry (TDR, e.g., Robinson et al., 2003). This method uses the propagation of an electromagnetic pulse which is guided along a metal rod. The travel time of this pulse depends in particular on the permittivity of the surrounding medium. Due to the large difference between the relative permittivity of air and water, this method provides accurate measurements of the soil water content. Working on a global scale, remote sensing satellites (e.g., Kerr et al., 2001; Entekhabi et al., 2010) provide estimates for the soil water content with a spatial measurement resolution of $\mathcal{O}(10^{4}\text{ m})$. Ground-penetrating radar (GPR, e.g., Daniels, 2004) is a promising method to acquire accurate data for the intermediate scale. Similar to TDR, it is based on the propagation of electromagnetic pulses. In contrast to TDR, GPR uses pulses that propagate freely within the subsurface medium. These pulses are reflected at changes of the electromagnetic properties. Hence, the method can be used to estimate the subsurface architecture as well as the soil hydraulic material properties.

Since the application of GPR for the estimation of soil hydraulic material properties is a relatively new method, there is still a need for efficient quantitative evaluation methods of GPR data. In order to develop and improve such methods, the test site ASSESS (Sect. 2) was constructed. This site is essentially a sand tank which is filled with three different kinds of sands that are arranged in an effectively 2D structure. ASSESS was in particular used (i) to estimate the subsurface architecture and the effective water content distribution (Buchner et al., 2012), (ii) to identify the appropriate parameterization model for the soil hydraulic material properties (Dagenbach et al., 2013), and (iii) to develop GPR measurement methods that yield high precision data (Klenk et al., 2015a).

For this study, ASSESS was forced with a fluctuating groundwater table and the resulting hydraulic dynamics was monitored with both TDR and GPR. Based on the methods outlined in Sect. 3, the acquired data (Sect. 4) are analyzed with different foci. The TDR data are used to investigate the effect of model errors on estimated soil hydraulic material properties (Sect. 5). The GPR data are used to develop a new heuristic GPR data evaluation method that is applied subsequently to identify the subsurface architecture and effective soil hydraulic material properties of ASSESS (Sect. 6). The results of this study are summarized in Sect. 7.

Note that the main results of this PhD-project have been published in Jaumann and Roth (2017) and Jaumann and Roth (2018). As stated in the *author contributions* of both publications, "S. Jaumann designed and conducted the experiment, developed the main ideas, implemented the algorithms, and analyzed the measurement data. K. Roth contributed with guiding discussions. S. Jaumann prepared the manuscript with contributions of both authors". Hence, large parts of these publications have been copied to this thesis.

2 ASSESS

For the development of methods which improve the quantitative understanding of soil water movement, an approximately 4 m × 20 m × 2 m large test site *ASSESS* (Fig. 2.1) was built near Heidelberg, Germany, in 2010. This test site consists of three different kinds of sand (materials A, B, and C) which are arranged in an effective 2D subsurface architecture (Fig. 2.2). The grain size distributions of these materials are presented in Table 2.1. A geotextile separates the sand from an approximately 0.1 m thick gravel layer below, which (i) ensures a rapid water pressure distribution and (ii) connects a groundwater well with the rest of the test site. Below this gravel layer, a basement layer confines the site. As the test site is built into a former fodder-silo, a reinforced concrete L-element serves as additional wall. The test site is equipped with a weatherstation which in particular controls 32 soil temperature and TDR sensors. Each TDR sensor has three cylindrical rods (length: 0.20 m, diameter: 0.004 m) which are separated by 0.03 m. They are operated by a Campbell Scientific TDR100. In 2011, a tensiometer (UMS T4-191) was added.

So far, ASSESS was in particular used to improve and develop GPR measurement and evaluation methods, comprising the measurement of the mean water content (Buchner et al., 2011), the estimation of the position of material interfaces as well as the effective relative permittivity distribution (Buchner et al., 2012), the identification of necessary properties of the parameterization model which is applied to describe the soil hydraulic material properties for a given material (Dagenbach et al., 2013), high precision monitoring of fluctuating groundwater table and infiltration experiments (Klenk et al., 2014, 2015a,b), the estimation of soil hydraulic material properties based on TDR data (Jaumann and Roth, 2017), and the estimation of soil hydraulic material properties and the subsurface architecture based on GPR data (Jaumann and Roth, 2018).

Figure 2.1 View over ASSESS with tensiometer access tube, weatherstation, and groundwater well along the left boundary. The jump in color reveals different sands that crop out at the surface. [from Jaumann and Roth (2017)]

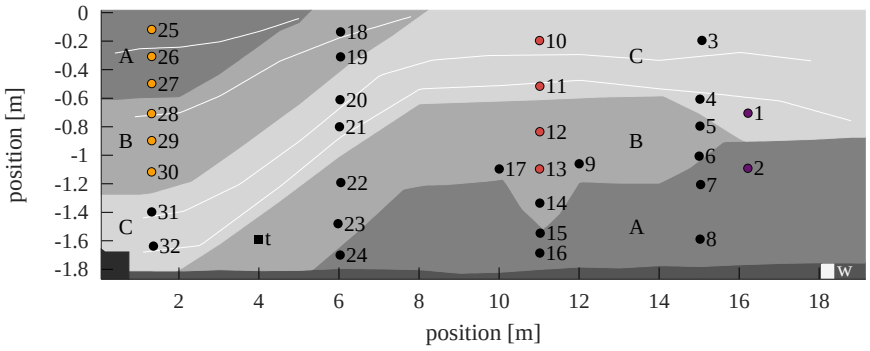

Figure 2.2 ASSESS features an effective 2D architecture with three different kinds of sand (A, B, and C). The hydraulic state can be manipulated with a groundwater well (white square, at 18.2 m) and is automatically monitored with 32 TDR sensors (dots) and one tensiometer (black square, at 4.0 m). The color of the dots associates some of the TDR sensors with different cases of the 1D study discussed in Sect. 5.5.1. The gravel layer at the bottom of the site ensures a rapid water pressure distribution over the site. An L-element (black polygon, at 0.4 m, vertical part serves as wall and is not shown) and compaction interfaces (white lines) were introduced during the construction. Additionally to those visualized, GPR evidence indicates additional compaction interfaces (e.g., Fig. 6.12 or Figs. 1b and 6 in Klenk et al. (2015a)). Note the different scales on the horizontal and the vertical axis.

Within the framework of this PhD-project, several changes have been made to ASSESS. These are discussed in more detail in Sect. A.1.

Table 2.1 The grain size distribution in percent by weight displays the different granularity of the materials A, B, and C of ASSESS (G. Schukraft, personal communication, Institute of Geography, Heidelberg University, 2010). Whereas the composition of the materials B and C is similar, material A features a higher percentage of fine sand. Since the mechanical wet analysis is time-consuming and laborious, only material B was sampled twice. Thus, 80 g out of approximately 400 Mg were sampled. Due to rounding, the sum of the values is not always 100.

		grain size range		A	B_1	B_2	C
gravel	total	$2 - 63$ mm	[%]	2	5	4	5
sand	total	$63 - 2000$ µm	[%]	97	96	95	95
	coarse	$630 - 2000$ µm	[%]	10	24	20	17
	medium	$200 - 630$ µm	[%]	65	64	68	72
	fine	$63 - 200$ µm	[%]	22	8	7	6
silt	total	$2 - 63$ µm	[%]	0	0	0	0
clay	total	< 2 µm	[%]	0	0	0	0

3 Background

In this chapter, aspects of soil water movement (Sect. 3.1), the propagation of electromagnetic waves (Sect. 3.2), the applied hydrogeophysical measurement methods (Sect. 3.4), and optimization mathods (Sect. 3.5) are shortly sketched. A concise presentation of the developed software and implemented optimization algorithms in Sect. 3.6 concludes the chapter.

3.1 Hydraulics

The development of a more sustainable use of the available freshwater requires the understanding of Earth's system dynamics (e.g., Schellnhuber et al., 2005) including the hydraulic cycle, as it provides renewable freshwater resources (Fig. 3.1). Evapotranspiration is an important process in the terrestrial hydrological cycle, because it transports more than 60% of the land precipitation back to the atmosphere (Oki and Kanae, 2006).

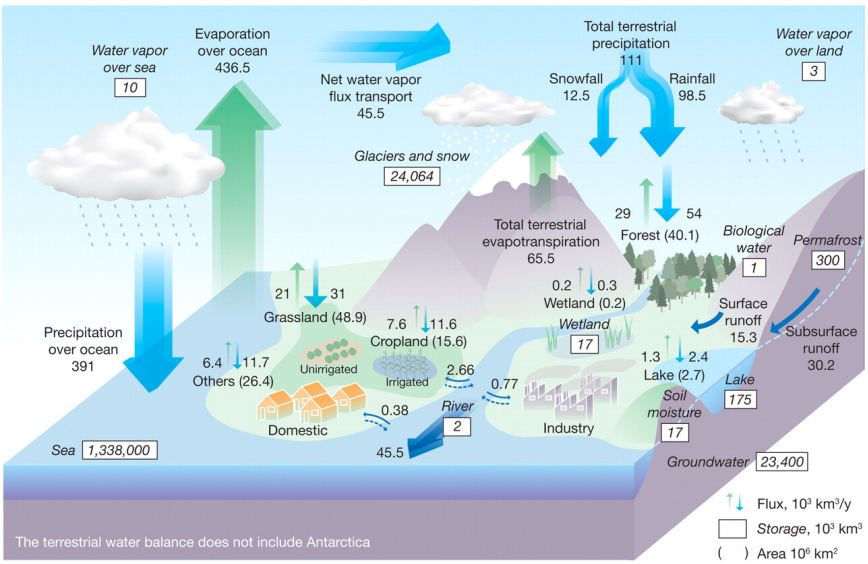

Figure 3.1 Powered by solar radiation, evaporation over the ocean and terrestrial evapotranspiration lead to many hydrological cycles. Essentially, the generated runoff and river discharge are considered as renewable fresh water resources. However, these are spatially and temporally unevenly distributed, leading to water scarcity in particular in Asia and Northern America. [from Oki and Kanae (2006)]

Also the energy flux is considerably large, as the terrestrial evapotranspiration uses more than half of the total solar energy that is absorbed by land surfaces (Trenberth et al., 2009).

Soils separate the precipitation water flow in runoff, groundwater recharge, and evapotranspiration. Hence, soil water is a crucial variable for modeling hydrological systems (Brutsaert, 2005; Robinson et al., 2008b; Vereecken et al., 2008). In particular through filtering pollution, soils ensure high freshwater quality (e.g., Keesstra et al., 2012). Soil moisture is the amount of water stored in the unsaturated soil zone. Although its proportion in the hydrological cycle is small (Fig. 3.1), soil moisture significantly interacts with the climate system in particular through limiting evapotranspiration (e.g., Seneviratne et al., 2010). Also, the quantitative knowledge of the spatiotemporal soil moisture distribution allows to improve precipitation forecasts (Beljaars et al., 1996; Koster et al., 2004).

Evapotranspiration is connected with biochemical cycles, for example the assimilation of CO_2 in plants and water loss through transpiration (e.g., Sellers et al., 1997). Nemani et al. (2003) reported that water availability limits vegetation growth on over 40% of Earth's vegetated surface. Since vegetation as well as soil moisture change the albedo of the surface, they also influence the net amount of radiant energy absorbed by the surface (Sellers et al., 1997).

Permafrost regions are sensitive to temperature variations, due to melting or freezing of the active layer. Unfrozen soil water in the freezing and frozen active layer and near-surface permafrost significantly changes its thermal properties and protects the permafrost below from rapid temperature changes (e.g., Romanovsky and Osterkamp, 2000). Soil water influences in particular the energy transport between the atmosphere and the permafrost and thus also the thawing process which is connected with the release of greenhouse gases and vegetation changes (e.g., Christensen et al., 2004).

The above findings illustrate the role of soils in the Earth system dynamics acting as the interface between atmosphere and groundwater. Subsequently, theoretical aspects of soil water movement are sketched along the lines of Roth (2012), who gives a more elaborate introduction to the subject.

3.1.1 General fluid dynamics

Conservation of mass In an Eulerian framework, where the volume element is fixed in space, the conservation of mass can be described with an influx through the boundary area

$$\partial_t \int_V \rho \mathrm{d}V = -\int_{\partial V} [\rho \boldsymbol{v}] \cdot \mathrm{d}\boldsymbol{A} = -\int_V \nabla \cdot [\rho \boldsymbol{v}] \, \mathrm{d}V, \tag{3.1}$$

assuming a constant density ρ. Note that (i) the Gaussian theorem was applied and (ii) the normal vector of the surface $\boldsymbol{A}$ is defined to point outwards. As the volume V is arbitrary, this yields the *continuity equation*

$$\partial_t \rho + \nabla \cdot \boldsymbol{j} = 0 \tag{3.2}$$

with the flux given as

$$\boldsymbol{j} = \rho \boldsymbol{v}. \tag{3.3}$$

Conservation of momentum The Lagrangian framework, where the volume element is moving with the fluid element, is suitable to formulate the conservation of momentum. Dominating forces for soils are originating from gravity, pressure gradients, and friction. Hence, the balance of forces is given by

$$m \mathrm{d}_t \boldsymbol{v} = \boldsymbol{F}_g + \boldsymbol{F}_p + \boldsymbol{F}_v. \tag{3.4}$$

Assuming an incompressible ($\mathrm{d}_t \rho = 0$) Newtonian fluid, the active forces are given by $\boldsymbol{F}_g = \int_V \rho \boldsymbol{g} \, \mathrm{d}V$, $\boldsymbol{F}_p = -\int_V \nabla p \, \mathrm{d}V$, and $\boldsymbol{F}_v = \int_V \mu_\mathrm{f} \nabla^2 \boldsymbol{v} \, \mathrm{d}V$. Insertion in Eq. 3.4 yields

$$\left[\int_V \rho \, \mathrm{d}V \right] \mathrm{d}_t \boldsymbol{v} = \int_V \left[\rho \boldsymbol{g} - \nabla p + \nabla^2 \boldsymbol{v} \right] \, \mathrm{d}V. \tag{3.5}$$

Equation 3.5 has to hold for volume elements with arbitrary but temporally constant size. This leads to

$$\rho \mathrm{d}_t \boldsymbol{v} = \rho \boldsymbol{g} - \nabla p + \mu_\mathrm{f} \nabla^2 \boldsymbol{v}. \tag{3.6}$$

Navier–Stokes equation In the Eulerian framework, where the coordinate system is fixed in space, the time differential operator in Eq. 3.6 may be rewritten as $\mathrm{d}_t = \partial_t + \boldsymbol{v} \cdot \nabla$. For a fluid exposed to the mechanical forces originating from gravity, pressure gradients, and friction, Eq. 3.2 and Eq. 3.6 yield

$$\nabla \cdot \boldsymbol{v} = 0, \tag{3.7}$$

$$\rho \partial_t \boldsymbol{v} + \rho [\boldsymbol{v} \cdot \nabla] \boldsymbol{v} = \rho \boldsymbol{g} - \nabla p + \mu_\mathrm{f} \nabla^2 \boldsymbol{v}, \tag{3.8}$$

where Eq. 3.8 is the Navier–Stokes equation. For slow flow, where the macroscopic forcing is slow for microscopic timescales and the viscosity dominates inertia, $\mathrm{d}_t \boldsymbol{v} = 0$ may be assumed, yielding

$$\mu_\mathrm{f} \nabla^2 \boldsymbol{v} = \nabla p - \rho \boldsymbol{g}. \tag{3.9}$$

Equation 3.9 can be solved for a long cylinder with radius r_C in cylindrical coordinates $\{r, \varphi, z\}$ leading to the Hagen–Poiseuille flux

$$j_x = -\frac{1}{8} \frac{{r_\mathrm{C}}^2}{\mu_\mathrm{f}} \partial_x p. \tag{3.10}$$

Note that the flux j_x is proportional to the square of a characteristic length scale r_C.

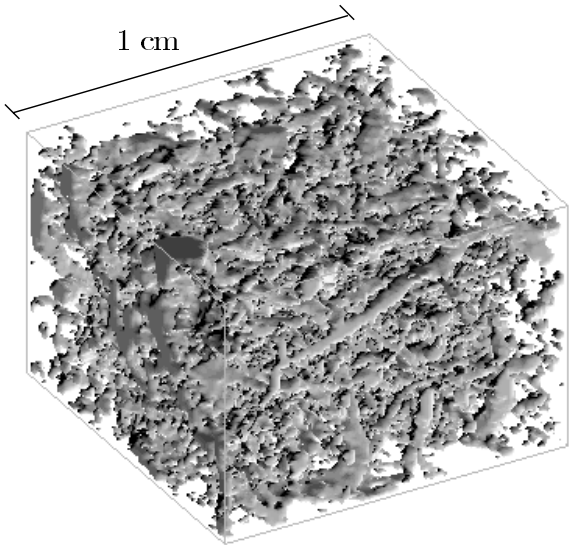

Figure 3.2 This three dimensional reconstruction of a macropore system sampled from a loamy-clay soil near Beauce, France (Cousin et al., 1996) features a horizontal (vertical) resolution of 0.12 mm (0.10 mm).
[from Roth (2012, p. 37), data courtesy of I. Cousin, image courtesy of H.-J. Vogel]

3.1.2 Soil as porous medium

In general, the pore space of soils corresponds to a three dimensional network of corrugated pores with a characteristic length scale that varies in space and generally also in time (Fig. 3.2).

In this work, soil is approximated as *porous medium* which requires (i) that down to a characteristic length scale, a volume element consists of a solid phase and a pore phase and (ii) that all pores are connected. Furthermore, it is assumed that the solid phase is rigid and completely wettable, such that the water flow in the porous medium is bounded to the pore space. This approximation may describe a heap of sand grains or glass beads. The porosity ϕ of a porous medium is typically defined as the volume fraction of its pore space.

It is instructive to simplify the pore space even further and to consider the pore space as a bundle of capillaries with a distribution of radii r_C (Fig. 3.3). Roth (2012) gives the Young–Laplace law for a spherical interface between liquid and vapor

$$\Delta p_{lv} \coloneqq p_l - p_v = \frac{2\sigma_{lv}}{r_\mathrm{C}}, \tag{3.11}$$

with the pressure in the liquid p_l and vapor p_v phase, the interfacial energy density σ_{lv}, and the interface radius r_C. Applying Eq. 3.11, the capillary rise for a single capillary can be calculated from the force from interfacial tension $2\pi\sigma_{lv}r_\mathrm{C}$ which equals the weight of the hanging liquid column $\pi {r_\mathrm{C}}^2 h\rho_{lv}g$ with $\rho_{lv} \coloneqq \rho_l - \rho_v$. Neglecting the small meniscus, this yields

$$h = \frac{2\sigma_{lv}}{\rho_{lv}g r_\mathrm{C}}. \tag{3.12}$$

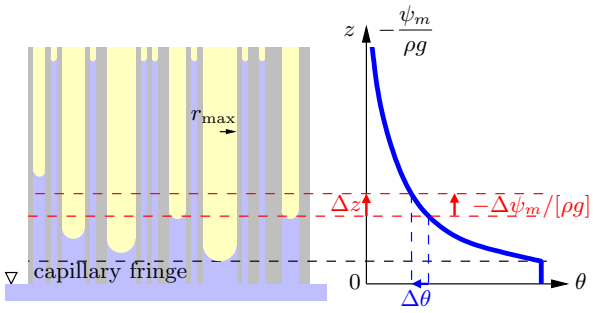

Figure 3.3 The capillary bundle is an instructive model for a porous medium. The rise of the water phase in a capillary is inversely proportional to its radius. Typically, the pore size distribution of the capillary bundle has a lower bound. Hence, a *capillary fringe* develops above the groundwater table (▽), where all the pores are water saturated. [from Roth (2012, p. 58)]

Note that the capillary rise h is inversely proportional to the characteristic length scale r_C. Together with the Hagen–Poiseuille law (Eq. 3.10), this illustrates the importance of the capillary radius to describe soil water flow.

3.1.3 State variables

Based on the description of the pore space with a three dimensional network of corrugated capillaries, it may be presumed that soil hydraulic material properties can be deduced with a physics-based model from the pore scale once the geometry of the network is known. However, the determination of the network geometry typically requires taking a soil sample and thus is a destructive method that is time-consuming and impossible for larger scales. Typically, the spatial scale of interest in soil hydrology starts at $\mathcal{O}(1\text{ m})$ and ranges up to $\mathcal{O}(10^6\text{ m})$.

Due to the multi-scale heterogeneity of soils, upscaling from the pore scale to the scale of interest is not possible. Therefore, in analogy to thermodynamics, the process description and the state variables have to be defined directly at the scale of interest. Hence, a suitable method is required to determine the characteristic length scale for the description at the continuum scale (Fig. 3.4). This is investigated with the representative elementary volume (REV). As defined in Sect. 3.1.2, the porous medium consists of a soil matrix and a pore space. To determine the characteristic length scale of the REV, the size of the average volume is increased until the state variable is constant for a macroscopically homogeneous medium. Hence, the resulting value of the state variable does not depend on the shape or extent of the averaging volume. In order to ensure the validity of the transition from the micro-scale to the macro-scale, the microscopic processes are required to be fast compared to the time scale of the macroscopic processes. Thus, the temporal evolution of the macroscopic states has to follow a sequence of equilibrium microscopic states.

Volume content The volumetric soil water content

$$\theta_w = \frac{V_w}{V} \tag{3.13}$$

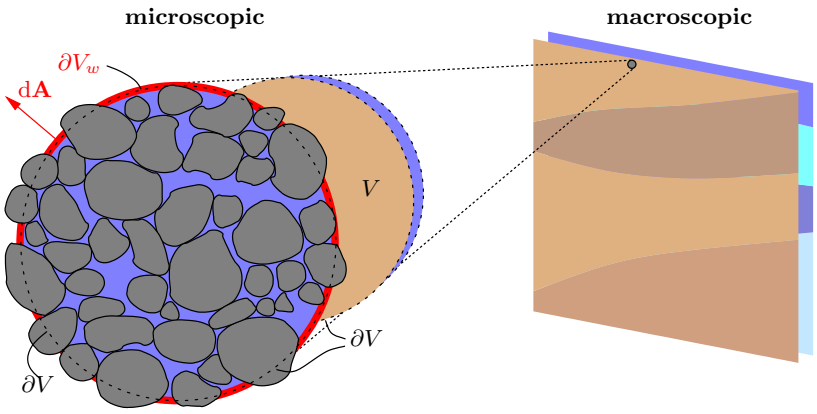

Figure 3.4 As upscaling of soil material properties is not possible due to the multi-scale heterogeneity of soils, a definition of state variables on the continuum scale is required. The characteristic length scale for these state variables is determined with an REV.
[from Roth (2012, p. 47)]

is given by the fraction of water volume V_w relative to the total volume V. Note that the volumetric content of other materials, e.g, the volumetric soil air content θ_a, is defined analogously. Generally, there also exists a gravimetric definition which is based on the mass fraction instead of the volume fraction. Since the gravimetric definition is not used in this work, the volumetric soil water content is referred to as water content subsequently.

The water saturation is defined as

$$\Theta := \frac{\theta_\mathrm{w} - \theta_\mathrm{w,r}}{\theta_\mathrm{w,s} - \theta_\mathrm{w,r}}. \tag{3.14}$$

It specifies the water content relative to the residual water content $\theta_\mathrm{w,r}$ and the water content of the saturated material $\theta_\mathrm{w,s}$. The latter is closely connected with the porosity ϕ. If no air is entrapped in the pore space while the soil is saturated, i.e. $\theta_\mathrm{a} \equiv 0$, then $\theta_\mathrm{w,s} \equiv \phi$.

Potential energy The active forces in a porous medium comprise (i) the capillary force which originates from the minimization of the interfacial surface tension (Eq. 3.11) and (ii) the gravitational force. Hence, with the z dimension pointing upwards, it follows for the hydraulic potential of the water phase at position $\boldsymbol{x}$

$$\psi_\mathrm{w}(\boldsymbol{x}) = \psi_\mathrm{m} + \psi_\mathrm{g} = \underbrace{p_\mathrm{w}(\boldsymbol{x}) - p_\mathrm{a}}_{\psi_\mathrm{m}} + \underbrace{\int_{z_0}^{z} \rho_\mathrm{w}(z') g \, \mathrm{d}z'}_{\psi_\mathrm{g}}. \tag{3.15}$$

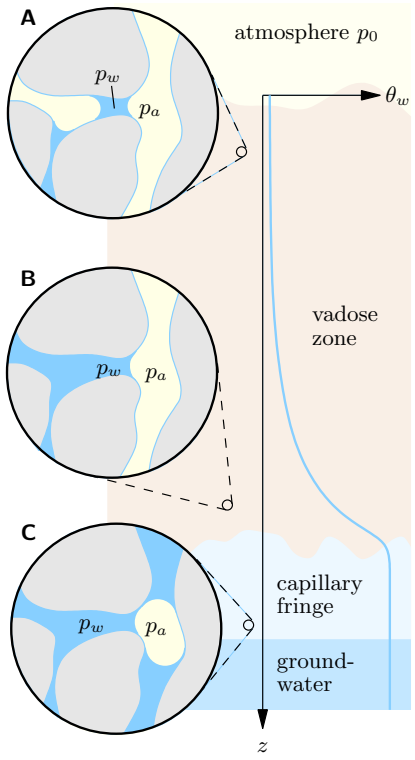

Figure 3.5 The vadose zone describes the unsaturated water content distribution between the groundwater table and the soil surface. Above the groundwater table the material is still water saturated due to capillary rise. This leads to the capillary fringe. In a macroscopically homogeneous material, the water content in the vadose zone decreases continuously with the distance from the groundwater table. The vadose zone can be partitioned into three different regimes. In the *degenerate multiphase regime* (A), the air phase is two orders of magnitude more mobile than the water phase. Hence, the water phase decouples from the air phase. Thus, the dynamics of the water phase may be described with a single phase flow model, such as the Buckingham–Darcy law (Eq. 3.19). In the *continuous multiphase regime* (B), the pressure gradients in the air and water phases are comparable in size, hence the phases are coupled. Thus, the description of this regime requires a multiphase flow model. Note that the Buckingham–Darcy law is not applicable in this regime. In the *discontinuous multiphase regime* (C), the air phase is not continuous anymore, because it is entrapped in bubbles. Hence, the air flow is limited to diffusion of air in water. In this regime, typical flux laws are not applicable anymore.
[from Roth (2012, p. 134)]

Note that the hydraulic potential is negative for bound water corresponding to a hanging water column. It is convenient to divide the hydraulic potential by $\rho_\mathrm{w} g$ leading to the hydraulic head

$$h_\mathrm{w}(\boldsymbol{x}) = h_\mathrm{m}(\boldsymbol{x}) + [z - z_0], \tag{3.16}$$

with the matric head $h_\mathrm{m} = \frac{\psi_\mathrm{m}}{\rho_\mathrm{w} g}$.

3.1.4 Dynamics

Assuming a rigid soil matrix (Fig. 3.4), the water flux is given according to Eq. 3.3 as

$$\boldsymbol{j}_\mathrm{w} = \theta_\mathrm{w} \boldsymbol{v} \tag{3.17}$$

and the continuity equation (Eq. 3.3) may be written as

$$\partial_t [\theta_\mathrm{w} \rho_\mathrm{w}] + \nabla \cdot [\rho_\mathrm{w} \boldsymbol{j}_\mathrm{w}] = 0. \tag{3.18}$$

As explained with Fig. 3.5, the vadose zone can be separated into three regimes, namely the degenerate multiphase regime, the continuous multiphase regime, and the discontinuous multiphase regime. In the degenerate multiphase regime far from the groundwater

table, the air phase can be assumed as arbitrarily mobile. This is a prerequisite to quantitatively describe soil water flow with a single phase model.

Assuming that the external forcing is required to be slow, i.e. that the time scale of macroscopic processes is slow on the time scale of microscopic processes, the heuristic Darcy flux law can be (i) motivated on the micro-scale, (ii) upscaled to the macro-scale assuming an incompressible fluid (Roth, 2012, p. 53ff), and (iii) extended to a flux law with more than one fluids by applying Buckingham's conjecture which states that the Darcy flux law remains valid, if the hydraulic conductivity is assumed to depend on the volumetric content of the fluid (Roth, 2012, p. 71). This leads to the Buckingham–Darcy flux law

$$\boldsymbol{j}_{\mathrm{w}} = -K(\theta_{\mathrm{w}})\nabla\psi_{\mathrm{w}}. \tag{3.19}$$

Note that in general the conductivity is a tensor. However, it is typically assumed to be isotropic and a scalar.

Assuming ρ_{w} to be spatially and temporally constant, the insertion of Eq. 3.19 in Eq. 3.18 finally yields the Richards equation (Richards, 1931)

$$\partial_t\theta_{\mathrm{w}} - \nabla\cdot[K(\theta_{\mathrm{w}})[\nabla h_{\mathrm{m}}(\theta_{\mathrm{w}}) + \boldsymbol{e}_z]] = 0, \tag{3.20}$$

with the matric head h_{m}, the upward pointing unit vector in z dimension $\boldsymbol{e}_z$, the *soil water characteristic* $\theta_{\mathrm{w}}(h_{\mathrm{m}})$, and *hydraulic conductivity function* $K(\theta_{\mathrm{w}})$. The Richards equation is the standard model to describe the soil water dynamics. In order to solve this partial differential equation, the material properties $\theta_{\mathrm{w}}(h_{\mathrm{m}})$ and $K(\theta_{\mathrm{w}})$ have to be specified. Generally, these material properties are nonlinear and vary over many orders of magnitude.

3.1.5 Material properties

In order to forecast the spatial water content distribution in a medium, the corresponding soil hydraulic material properties are required. Thus, the soil hydraulic material properties are essential to understand soil water movement quantitatively. However, since the soil hydraulic material properties depend on the details of the pore structure, they are unknown a priori.

Topp and Miller (1966) measured the soil water characteristic and the hydraulic conductivity function of glass beads with a mean diameter of 180 µm and found that the soil water characteristic shows a hysteretic behavior (Fig. 3.6). This is in contrast to the hydraulic conductivity (Fig. 3.7). Since so far no model is available to describe this hysteresis adequately, it is typically neglected and the soil hydraulic material properties are approximated as heuristic scalar parameterization functions.

A large number of different parameterization models for the soil water characteristic $\theta_{\mathrm{w}}(h_{\mathrm{m}})$ have been published. The most popular parameterization model has been proposed by van Genuchten (1980). However, in this study the Brooks–Corey parameterization (Brooks and Corey, 1966) is chosen, since it describes the materials in ASSESS

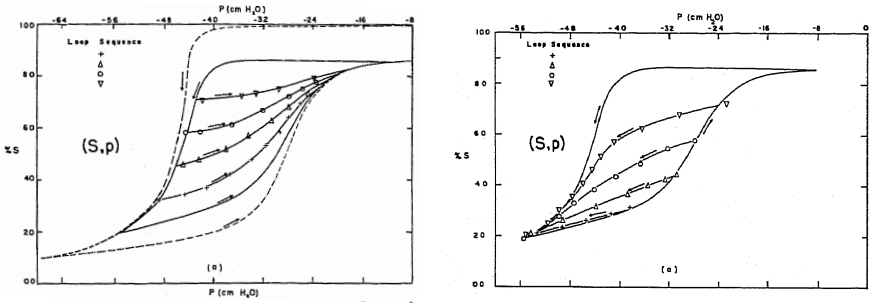

Figure 3.6 Topp and Miller (1966) measured the soil water characteristic of glass beads with a mean diameter of 180 µm. The material shows hysteretic behavior (left: wetting loops, right: drying loops). The arrows indicate the direction of movement. Note that (i) the curves are rotated to the left compared to the previous illustrations and (ii) % S denotes the saturation Θ (Eq. 3.14) and is given on the vertical axis.
[from Roth (2012, p. 60)]

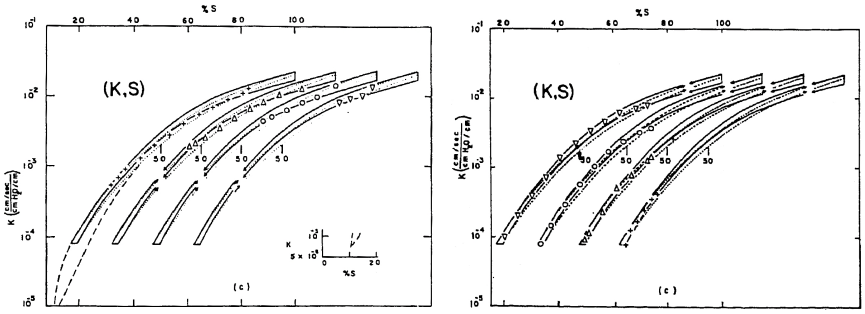

Figure 3.7 Topp and Miller (1966) measured the hydraulic conductivity function $K(\theta_\mathrm{w})$ of glass beads with a mean diameter of 180 µm. In contrast to the soil water characteristic (Fig. 3.6), no significant hysteretic behavior was detected (left: wetting loops, right: drying loops). Note that % S denotes the saturation Θ (Eq. 3.14) and is given on the horizontal axis.
[from Roth (2012, p. 65)]

well (Dagenbach et al., 2013). The Brooks–Corey parameterization has four parameters: (i) a scaling parameter h_0 [m] related to the air entry pressure ($h_0 < 0$ m) which corresponds to the negative height of the capillary fringe, (ii) the water content of the saturated material $\theta_{\mathrm{w,s}}$ [−], (iii) the residual water content $\theta_{\mathrm{w,r}}$ [−], and (iv) a shape parameter λ [−] related to the pore size distribution ($\lambda > 0$). Neglecting hysteresis, the parameterization may be inverted for $\theta_{\mathrm{w,r}} \leq \theta_\mathrm{w} \leq \theta_{\mathrm{w,s}}$. This leads to

$$h_\mathrm{m}(\theta_\mathrm{w}) = h_0 \left(\frac{\theta_\mathrm{w} - \theta_{\mathrm{w,r}}}{\theta_{\mathrm{w,s}} - \theta_{\mathrm{w,r}}} \right)^{-1/\lambda} . \tag{3.21}$$

Inserting the Brooks–Corey parameterization into the hydraulic conductivity model of Mualem (1976) yields

$$K(\theta) = K_\mathrm{s} \left(\frac{\theta_\mathrm{w} - \theta_\mathrm{w,r}}{\theta_\mathrm{w,s} - \theta_\mathrm{w,r}} \right)^{\tau+2+2/\lambda} \tag{3.22}$$

for the hydraulic conductivity function where K [$\mathrm{m\,s^{-1}}$] is the saturated hydraulic conductivity and τ [$-$] a heuristic tortuosity factor. The dependency of the shape of the parameterization functions Eq. 3.21 and Eq. 3.22 on their respective parameters is investigated in Sect. A.2.

The parameterization models for the soil water characteristic and the hydraulic conductivity function describe macroscopically homogeneous materials. Small-scale heterogeneities, i.e. the texture of the porous medium, can be represented with *Miller scaling* if the pore spaces at any two points are assumed geometrically similar (Miller and Miller, 1956). Scaling the macroscopic reference material ${h_\mathrm{m}}^*(\theta_\mathrm{w})$, $K^*(\theta_\mathrm{w})$ with a local ratio of characteristic lengths ξ [$-$] leads to locally scaled material functions (Roth, 1995):

$$h_\mathrm{m}(\theta_\mathrm{w}) = {h_\mathrm{m}}^*(\theta_\mathrm{w}) \cdot \xi, \quad K(\theta_\mathrm{w}) = K^*(\theta_\mathrm{w})/\xi^2. \tag{3.23}$$

3.1.6 Richards solver

In this thesis, the Richards equation (Eq. 3.20) is solved numerically with muPhi ($\mu\varphi$, Ippisch et al., 2006) on a rectangular structured grid using a cell-centered finite-volume scheme with full upwinding in space and an implicit Euler scheme in time. The nonlinear equations are linearized with an inexact Newton method with line search and the linear equations are solved with an algebraic multigrid solver.

3.1.7 Characteristic phenomena

The characteristic hydraulic phenomena which originate from the nonlinear material properties are illustrated subsequently with exemplary simulations. Two synthetic experiments, one forced with a fluctuating groundwater table and the other with an infiltration pulse, showcase the distinct characteristic hydraulic behavior of sand and silt. The corresponding material parameters are taken from Table 3.1 and lead to the material functions are given in Fig. 3.8. All simulations use a vertical one dimensional structured grid with a spatial resolution of 0.01 m. The simulations are started from static hydraulic equilibrium based on a groundwater table at the bottom boundary. The simulated time for each experiment is 48 h. To facilitate the comparison of the behavior of the materials, identical boundary conditions are used for sand and silt.

Fluctuating water table experiment The fluctuating groundwater table is modeled with a Dirichlet boundary condition changing the water potential at the bottom boundary. For the remaining boundaries, a Neumann flux boundary condition of 0.0 $\mathrm{m\,s^{-1}}$

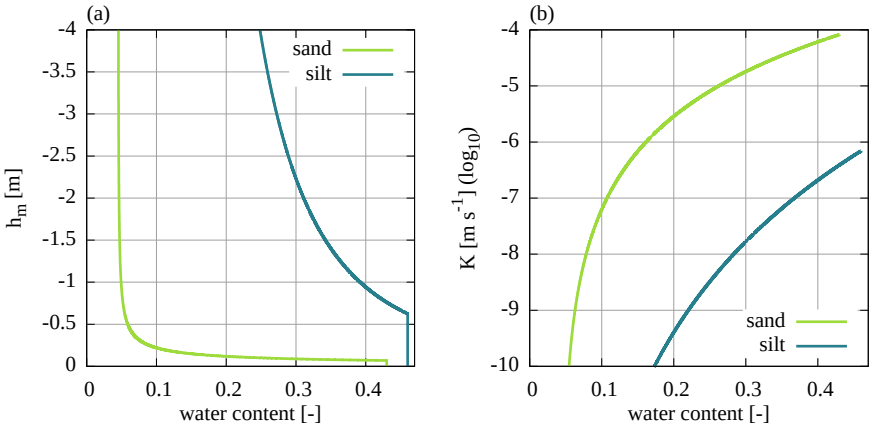

Figure 3.8 The soil water characteristic (a) and the hydraulic conductivity function (b) determined by the reference parameters for sand and silt (Table 3.1) show characteristic deviations for the two materials. These deviations can partly be motivated with their disparity of the grain size and of the grain size distribution. According to the capillary bundle model, this effects the size of the capillary fringe (Eq. 3.12) as well as the hydraulic conductivity of the water saturated material (Eq. 3.10). Note that the respective dependency on the characteristic length scale given in Eq. 3.23 is also supported by the measurements of Carsel and Parrish (1988): ${h_0}^{\text{silt}}/{h_0}^{\text{sand}} \approx 10$ and ${K_\text{s}}^{\text{silt}}/{K_\text{s}}^{\text{sand}} \approx 10^{-2}$. Additionally, since the pore size distribution of silt is wider than that of sand, the water content changes more gradually for silt than that for sand.

was chosen (no-flow). Initially at 0.0 m, the groundwater table rises linearly to 2.0 m in 8 h and equilibrates for 16 h. Subsequently, the groundwater table is linearly lowered to 0.0 m over 8 h. Finally, the hydraulic dynamics equilibrates during the remainder of the experiment. The resulting simulations are shown in Fig. 3.9.

Subfigure 3.9a shows the simulation for sand. Initially, the water content distribution features a kink close to saturation (1). With the rising groundwater table, the position of this kink at high water contents changes (2) and an additional kink develops in the soil water distribution at low water contents (3). This is due to the nonlinear dependency of the hydraulic conductivity function on the soil water content. This leads to a much

Table 3.1 The reference parameters for sand and silt determined by Carsel and Parrish (1988) where transferred from the Mualem–van Genuchten parameterization model to the Mualem–Brooks–Corey parameterization model using $h_0 = 1/\alpha_\text{vG}$, $\lambda = n_\text{vG} - 1$ (Roth, 2012, Eq. 3.46, p. 63). The parameters K_s and τ are assumed to be the same for both parameterizations. The corresponding material functions are given in Fig. 3.8.

	h_0 [m]	λ [−]	K_s [m s^{-1}]	τ [−]	$\theta_\text{w,s}$ [−]	$\theta_\text{w,r}$ [−]
sand	−0.069	1.68	$8.25 \cdot 10^{-5}$	0.5	0.43	0.045
silt	−0.625	0.37	$6.94 \cdot 10^{-7}$	0.5	0.46	0.034

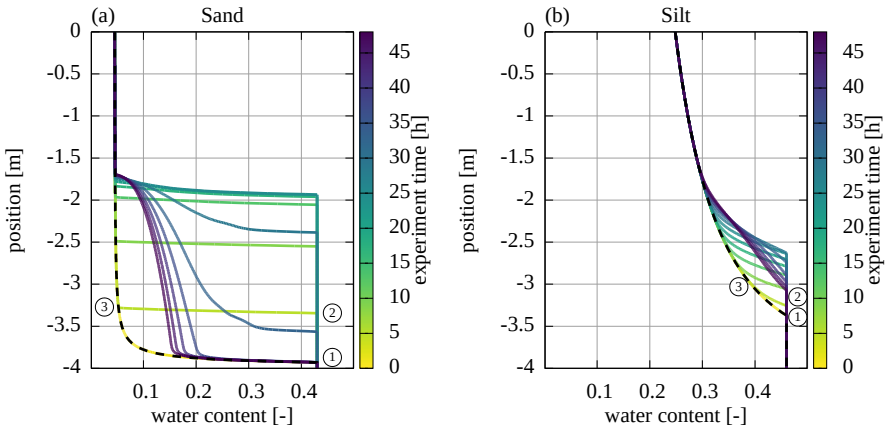

Figure 3.9 The spatiotemporal water content distribution is simulated for a fluctuating groundwater table experiment in sand (a) and silt (b) using reference material properties (Table 3.1). The experiment time is given in color code and the initial state is marked with a black dashed line. The main characteristic phenomenon is the additional kink (3) in the water content distribution during imbibition. The markers are explained in the text and used consistently in this section.

smaller hydraulic conductivity for low water contents (Fig. 3.8). The additional kink smoothes during the equilibration phase in which the water content distribution would ultimately assume its initial shape only shifted by 2.0 m. However, since the hydraulic conductivity is small for low water contents, a complete equilibration would require a long time. Hence, the groundwater table is set back again before a completely equilibrated state is reached. During this drainage phase, the regions with high water contents drain first due to their high hydraulic conductivity.

Subfigure 3.9b shows the simulation for silt. Due to its smaller grain size and the wider grain size distribution, silt has (i) a smaller saturated hydraulic conductivity than the sand and (ii) a higher water content than sand in equilibrium for the given domain (Fig. 3.8). Compared to sand, the fluctuating groundwater table experiment shows a similar characteristic in silt as (i) an additional kink (3) develops and (ii) the drainage is faster for regions with high water content. However, since the gradient of the water content distribution is not as steep as for the sand, these effects are not as pronounced for the silt.

Infiltration experiment Although a Neumann boundary condition would be more intuitive, the infiltration experiment is forced with a Dirichlet boundary condition at the top boundary. This way, using the same boundary condition for both materials leads to a comparable hydraulic dynamics despite the large difference in hydraulic conductivity. Initially, the Dirichlet boundary condition at the top boundary is set to -0.1 m for 24 h. Afterwards, the boundary condition is changed to a Neumann no-flow condition. During

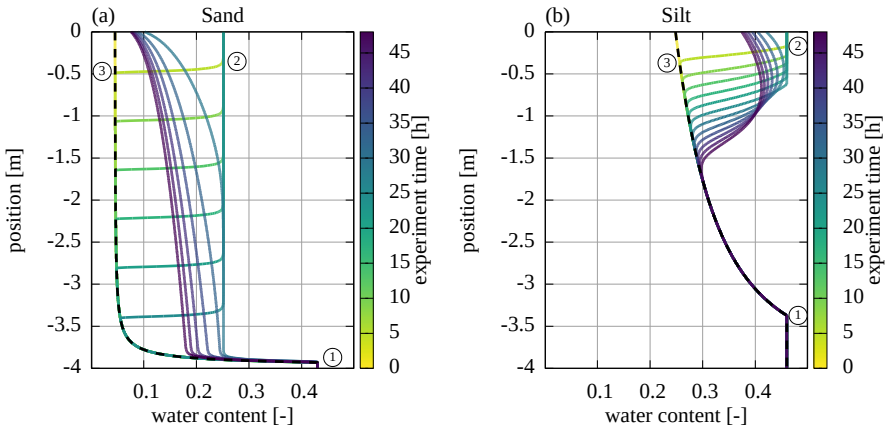

Figure 3.10 The spatiotemporal water content distribution is simulated for an infiltration pulse in sand (a) and silt (b) using reference material properties (Table 3.1). The experiment time is given in color code and the initial state is marked with a black dashed line. The main characteristic phenomenon is the development of a self-sharpening front during infiltration which is in particular visible for the sand. The markers are explained in the text and used consistently in this section.

the whole experiment, the Dirichlet boundary condition at the bottom boundary is set to 0.0 m. The resulting simulations are shown in Fig. 3.10.

Subfigure 3.10a shows the simulation for sand. There, the infiltration causes a self-sharpening front as the hydraulic conductivity is smaller for low water contents. This corresponds to the phenomenon discussed for the fluctuating groundwater table experiment, except for (i) the initial water content which is lower due to the forcing at the top boundary and (ii) the opposite direction of the forcing relative to gravity. Thus, similar to the fluctuating groundwater table experiment, an additional kink develops in the water content distribution (3). Depending on the infiltration flux, the water content in the infiltration front changes. Note that this corresponds to the kink in high water contents (2). Ultimately, the infiltration front reaches the groundwater table during the forcing phase. During the subsequent equilibration phase, the material is still draining, however, with decreasing water content also the hydraulic conductivity decreases. This increases the time required for complete drainage.

Subfigure 3.10b shows the simulation for silt. Here, the hydraulic conductivity is smaller than for the sand. Hence, the duration of the infiltration does not suffice for a similar characteristic front to develop. Still, the forcing and equilibration processes are clearly visible. Once the equilibration phase starts, the water content distribution equilibrates and the integral water content stays constant as no water is leaking into the groundwater. As for the fluctuating groundwater table experiment, the silt shows a similar characteristic behavior compared to the sand. However, this behavior is less pronounced due to the lower hydraulic conductivity and the smaller gradients in the water content distribution.

Note that in order to showcase the different hydraulic behavior of sand and silt, these simulations show extreme experiments up to and beyond the validity range of the Richards equation. In particular close to saturation, either caused by a fluctuating groundwater table or the infiltration, the pressure in the air phase or even the entrapment of air bubbles is generally not negligible in reality (Fig. 3.5).

3.2 Electromagnetics

In this study, the hydraulic state (Sect. 3.1) is monitored with hydrogeophysical measurement methods (Sect. 3.4) that rely on the propagation of electromagnetic fields. Hence, the theoretical background concerning the propagation of electromagnetic fields in media is shortly sketched in this section. Naturally, this also comprises the discussion of electromagnetic material properties and their dependencies on the frequency and the temperature. A thorough introduction to the subject is given by Zangwill (2012) which complements the classic Jackson (1999).

3.2.1 Maxwell's equations

The simulation of GPR data based on a hydraulic state involves the solution of the time-dependent Maxwell equations. These equations quantify the propagation of the electric field $\boldsymbol{E}$, the magnetic field $\boldsymbol{B}$, and the respective fields in media $\boldsymbol{D}$ and $\boldsymbol{H}$ (Jackson, 1999)

$$\nabla \cdot \boldsymbol{D} = \rho_e, \tag{3.24}$$

$$\nabla \cdot \boldsymbol{B} = 0, \tag{3.25}$$

$$\nabla \times \boldsymbol{H} - \frac{\partial \boldsymbol{D}}{\partial_t} = \boldsymbol{J}, \tag{3.26}$$

$$\nabla \times \boldsymbol{E} + \frac{\partial \boldsymbol{B}}{\partial_t} = 0. \tag{3.27}$$

An external forcing can be realized via the charge density ρ_e and the source current density $\boldsymbol{J}_\mathrm{s}$ which enters the current density $\boldsymbol{J}$ together with the internal current density $\boldsymbol{J}_\mathrm{in}$ via

$$\boldsymbol{J} = \boldsymbol{J}_\mathrm{in} + \boldsymbol{J}_\mathrm{s}. \tag{3.28}$$

Note that Maxwell's equations implicitly comply with the continuity equation of the charge density ρ_e

$$\partial_t \rho_e + \nabla \cdot \boldsymbol{J} = 0. \tag{3.29}$$

3.2.2 Material properties

In order to solve Maxwell's equations, material properties are required to relate $\boldsymbol{D}$ to $\boldsymbol{E}$ and $\boldsymbol{B}$ to $\boldsymbol{H}$. Typically, linear material constants are assumed which are independent of $\boldsymbol{E}$ and $\boldsymbol{B}$. These material properties are (i) the permittivity ε, (ii) the electrical conductivity σ, and (iii) the permeability μ. Together, the equations for these material properties yield

$$\boldsymbol{D} \coloneqq \varepsilon \boldsymbol{E}, \tag{3.30}$$

$$\boldsymbol{J}_{\text{in}} \coloneqq \sigma \boldsymbol{E}, \tag{3.31}$$

$$\boldsymbol{H} \coloneqq \frac{\boldsymbol{B}}{\mu}, \tag{3.32}$$

$$\tag{3.33}$$

including Ohm's law (Eq. 3.31). Generally, each of these material properties are complex and vary in space and time. Subsequently, these material properties are used to decouple and solve Maxwell's equations.

Permittivity This paragraph follows Smyth (1955) who gives a detailed analysis of dielectric media. Generally, a dielectric material is an electric insulator that can be polarized in the presence of an externally applied electric field. This polarization leads to an electric field within the material that is opposed to the externally applied electric field. The resulting polarization density $\boldsymbol{P}$ of the material is defined with the electric susceptibility χ_e

$$\boldsymbol{P} \coloneqq \varepsilon_0 \chi_e \boldsymbol{E} \tag{3.34}$$

The value of the permittivity ε (Eq. 3.30) is generally assumed to be complex and depending on the angular frequency ω of the electric field as well as on the temperature T of the medium:

$$\varepsilon \coloneqq \varepsilon_0(1+\chi_e) = \varepsilon_0 \varepsilon_{\text{r}} = \varepsilon_0 \varepsilon_{\text{r}}(\omega, T) =: \varepsilon_0 \left({\varepsilon_{\text{r}}}'(\omega, T) - \mathrm{i} {\varepsilon_{\text{r}}}''(\omega, T) \right). \tag{3.35}$$

The polarization of a dielectric medium by an externally applied field leads to a low-frequency dielectric constant. Depending on the frequency of the externally applied field, the equilibration of the resulting polarization may exhibit an observable lag. This lag is also referred to as relaxation. The external field always causes a rapidly forming polarization but may also involve slowly forming polarization. The former is realized through displacement of electrons in the atoms relative to the nucleus at a time scale of 10^{-15} s. Additionally, the displacement of the atoms in the molecule relative to another happens at a time scale of $\approx 10^{-13}$ s. The time required for a dipolar molecule to relax depends on the frictional resistance of the medium to the change of molecular orientation. For molecules in liquids this may take between 10^{-6} s and 10^{-11} s.

Conductivity According to Ohm's law (Eq. 3.31), the electrical conductivity describes the possibility of charges to move in a medium due to an externally applied electric field. The solution of Maxwell's equations for dispersive and lossy media (Sect. 3.2.3.1) shows that the permittivity and the electrical conductivity are intertwined and the formal separation is actually of artificial nature. Typically, the electrical conductivity is associated with the imaginary part of the permittivity. Hence, also the electrical conductivity is in general depending on the angular frequency ω of the applied field and the temperature T of the medium

$$\sigma = \sigma(\omega, T). \tag{3.36}$$

With decreasing frequency, the conductivity approaches the direct current conductivity $\lim_{\omega \to 0} \sigma(\omega, T) = \sigma_{\mathrm{dc}}(T)$.

Permeability The permeability is typically defined as

$$\mu \coloneqq \mu_0 \mu_{\mathrm{r}} = \mu_0(\chi_m + 1), \tag{3.37}$$

with the magnetic susceptibility χ_m. Depending on the relative permeability μ_{r}, typical materials are essentially either diamagnetic, paramagnetic, or ferromagnetic. In contrast to paramagnetic materials, the induced magnetic field in diamagnetic materials has an opposite orientation with respect to the externally applied magnetic field ($\mu_{\mathrm{r}} < 1$ or $\chi_m < 0$). Note that for diamagnetic materials the induced magnetic field (i) vanishes with the externally applied field and (ii) is low for typical materials but strong in superconductors.

Thompson and Oldfield (1986, p. 18) provide the magnetic mass susceptibility ${\chi_m}^{\mathrm{mass}} = \frac{\chi_m}{\rho}$ for quartz ($-0.6 \cdot 10^{-8}$ $\mathrm{m^3\,kg^{-1}}$), feldspar ($-0.5 \cdot 10^{-8}$ $\mathrm{m^3\,kg^{-1}}$), calcite ($-0.5 \cdot 10^{-8}$ $\mathrm{m^3\,kg^{-1}}$), and water ($-0.9 \cdot 10^{-8}$ $\mathrm{m^3\,kg^{-1}}$). Hence, these materials exhibit diamagnetic behavior. Approximating the density of these materials with $\mathcal{O}(10^3$ $\mathrm{kg\,m^{-3}})$, the magnetic susceptibility of a sandy soil matrix is $\mathcal{O}(10^{-5})$. Therefore, $\mu_{\mathrm{r}} = 1$ is typically a good approximation in soil hydrology.

3.2.3 Solution of Maxwell's equations

There exists a multitude of methods to solve Maxwell's equations (i) analytically for special cases and (ii) numerically for more complicated applications. In this section, analytical solutions for two special cases are provided initially in order to discuss the resulting material properties (Sect. 3.2.3.1). Finally, numerical solutions are discussed for some typical examples used in soil hydrology (Sect. 3.2.3.2).

3.2.3.1 Analytic solutions

With the assumptions for the electromagnetic material properties made in Sect. 3.2.2, Maxwell's equations become linear. Hence, they can be decoupled and the *superposition*

principle holds, i.e. the sum of two solutions is again a solution. Thus, it often suffices to solve Maxwell's equations for a plane wave. The Fourier transformation is an elegant way to solve Maxwell's equations in the frequency space, however, the inverse transformation typically leads to complex integrals which can only be solved analytically for low orders and simple material architectures. Naturally, analytical solutions are more general compared to numerical solutions.

Vacuum A classical way to solve Maxwell's equations in vacuum with the assumptions $\rho_e = 0$ and $\boldsymbol{J} = 0$ involves four steps: (i) take the rotation of Eq. 3.27, (ii) insert the material properties Eq. 3.32 and Eq. 3.30 in Eq. 3.26 and Eq. 3.27, respectively, (iii) insert the result for Eq. 3.26 in Eq. 3.27, (iv) apply the equality $\nabla \times (\nabla \times \boldsymbol{E}) = \underbrace{\nabla(\nabla \boldsymbol{E})}_{=0} - \nabla^2 \boldsymbol{E}$.

This algorithm yields the wave equation for the electric field

$$\nabla^2 \boldsymbol{E} = \mu\varepsilon \frac{\partial^2 \boldsymbol{E}}{\partial_t^2} \tag{3.38}$$

and can be applied analogously for the magnetic field. The wave equation (Eq. 3.38) can be solved with a plane wave approach

$$\boldsymbol{E}(\boldsymbol{x}, t) = \boldsymbol{E}_0 \mathrm{e}^{\mathrm{i}(\boldsymbol{k}\boldsymbol{x} - \omega t)}, \tag{3.39}$$

$$\boldsymbol{B}(\boldsymbol{x}, t) = \boldsymbol{B}_0 \mathrm{e}^{\mathrm{i}(\boldsymbol{k}\boldsymbol{x} - \omega t)}, \tag{3.40}$$

with the wave vector $\boldsymbol{k}$ and the angular frequency ω. Inserting the plane wave for the electric field (Eq. 3.39) in Eq. 3.38 yields relation for the wave number

$$\|\boldsymbol{k}\|^2 = k^2 = \mu\varepsilon\omega^2 = \frac{\omega^2}{c^2} = \frac{\omega^2}{{c_0}^2} \mu_\mathrm{r} \varepsilon_\mathrm{r} \tag{3.41}$$

with velocity of the wave

$$c = \frac{1}{\sqrt{\mu\varepsilon}} \tag{3.42}$$

which in vacuum equals to $c_0 = \frac{1}{\sqrt{\mu_0 \varepsilon_0}}$.

The plane wave approach has to be a solution of Maxwell's equations. Inserting it in Eq. 3.24 and in Eq. 3.25 yields that both the electric field $\boldsymbol{E}$ and the magnetic field $\boldsymbol{B}$ are perpendicular to the direction of propagation $\boldsymbol{k}$. Inserting the approach in Eq. 3.26 and in Eq. 3.27 yields that the electric field $\boldsymbol{E}$ and the magnetic field $\boldsymbol{B}$ are perpendicular to each other.

Homogeneous dispersive and lossy materials Generally, $\sigma \neq 0$ holds for dispersive and lossy media. Applying the same algorithm as in the previous paragraph and inserting Ohm's law yields the telegrapher equation for the electric field

$$\nabla^2 \boldsymbol{E} = \mu\varepsilon \frac{\partial^2 \boldsymbol{E}}{\partial_t^2} + \mu\sigma \partial_t \boldsymbol{E}. \tag{3.43}$$

Note that (i) the derivation for the magnetic field $\boldsymbol{H}$ works analogously and (ii) $\boldsymbol{J}_\mathrm{s} = 0$ is assumed. Inserting the plane wave approach (Eq. 3.39) in Eq. 3.43 and assuming $\mu_\mathrm{r} = 1$ yields

$$\|\boldsymbol{k}\|^2 = \mu\omega^2 \underbrace{\left(\varepsilon + \mathrm{i}\frac{\sigma}{\omega}\right)}_{\varepsilon^*(\omega)} = \varepsilon_0\mu_0\mu_\mathrm{r}\omega^2 \left(\varepsilon_\mathrm{r} + \mathrm{i}\frac{\sigma}{\omega\varepsilon_0}\right) = \frac{\omega^2}{{c_0}^2}\left({\varepsilon_\mathrm{r}}' + \mathrm{i}\left(\frac{\sigma}{\omega\varepsilon_0} - {\varepsilon_\mathrm{r}}''\right)\right) \tag{3.44}$$

where $\varepsilon^*(\omega)$ describes a generalized frequency dependent permittivity that indicates a close relation between the permittivity and the electrical conductivity. Although the electrical conductivity is generally complex, it is assumed to be real valued in this case. Additionally inserting the definition for the complex permittivity (Eq. 3.35), yields a connection between the electrical conductivity σ and the imaginary part of the permittivity ${\varepsilon_\mathrm{r}}''$ in Eq. 3.44.

To simplify the subsequent calculations, the real and imaginary parts of the wave number

$$k = \frac{\omega}{c_0}\sqrt{{\varepsilon_\mathrm{r}}' + \mathrm{i}\left(\frac{\sigma}{\omega\varepsilon_0} - {\varepsilon_\mathrm{r}}''\right)} =: a + \mathrm{i}b \tag{3.45}$$

are substituted with a and b, respectively. The complex wave number k has further implications which already become evident in one dimension as

$$\boldsymbol{E}(x,t) = \boldsymbol{E}_0\mathrm{e}^{\mathrm{i}(kx-\omega t)} = \boldsymbol{E}_0\mathrm{e}^{\mathrm{i}((a+\mathrm{i}b)x-\omega t)} = \boldsymbol{E}_0\mathrm{e}^{\mathrm{i}(ax-\omega t)}\mathrm{e}^{-bx}. \tag{3.46}$$

Hence, the wave propagates with wave number a and is damped with damping factor b. In order to investigate the dependency of a and b on the permittivity and electrical conductivity, the real and imaginary parts of Eq. 3.45 and their corresponding substitution are compared. Some calculation leads to

$$a^2 = \frac{1}{2}\frac{\omega^2}{{c_0}^2}\left({\varepsilon_\mathrm{r}}' + \sqrt{{\varepsilon_\mathrm{r}}'^2 - \left(\frac{\sigma}{\omega\varepsilon_0} - {\varepsilon_\mathrm{r}}''\right)^2}\right) \quad \text{and} \tag{3.47}$$

$$b^2 = \frac{1}{2}\frac{\omega^2}{{c_0}^2}\left({\varepsilon_\mathrm{r}}' - \sqrt{{\varepsilon_\mathrm{r}}'^2 - \left(\frac{\sigma}{\omega\varepsilon_0} - {\varepsilon_\mathrm{r}}''\right)^2}\right). \tag{3.48}$$

Hence, for ${\varepsilon_\mathrm{r}}'' = 0$ and $\sigma = 0$, the damping factor b is zero and a corresponds to k in Eq. 3.41. This also holds for ${\varepsilon_\mathrm{r}}'' = \frac{\sigma}{\omega\varepsilon_0}$. Assuming $\omega = 2\pi \cdot 400$ MHz and ${\varepsilon_\mathrm{r}}'' = 0$, the dependency of a and b on ${\varepsilon_\mathrm{r}}'$ and σ is shown in Fig. 3.11. For the given assumptions a is mainly influenced by ${\varepsilon_\mathrm{r}}'$, whereas b is mainly influenced by σ.

The dependency of the permittivity on the frequency can be described with the Debye model which is shortly sketched subsequently following Smyth (1955, p. 52ff). In order to describe the polarization of dielectric materials, Debye (1929) introduced an instantaneous high-frequency permittivity limit $\varepsilon_{\mathrm{r},\infty}$ as well as an absorptive limit $\varepsilon_{\mathrm{r},0}$ for low frequencies. Given a time-harmonic field $\boldsymbol{E}(t) = \boldsymbol{E}_0\mathrm{e}^{\mathrm{i}\omega t}$, the permittivity may

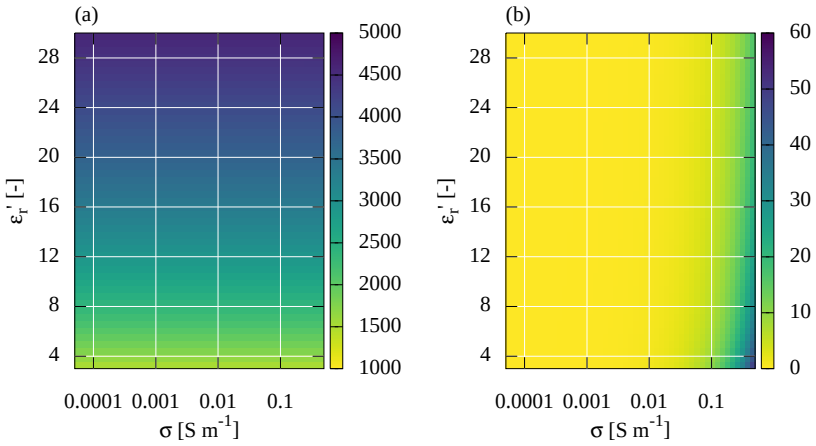

Figure 3.11 In dispersive and lossy materials, the wave number becomes complex and may be separated into the corresponding real and imaginary parts a and b. The real part a can be associated with the wave velocity whereas b can be associated with the damping of the wave amplitude. Both parts depend on the relative permittivity ${\varepsilon_\mathrm{r}}'$ and the electrical conductivity σ. This dependency was plotted for (a) a and (b) b assuming $\omega = 2\pi \cdot 400$ MHz and ${\varepsilon_\mathrm{r}}'' = 0$ using Eqs. 3.47–3.48. Although both ${\varepsilon_\mathrm{r}}'$ and σ enter Eqs. 3.47–3.48, ${\varepsilon_\mathrm{r}}'$ has a stronger influence on a, whereas the electrical conductivity σ has a stronger influence on b.

be separated into one part describing the instantaneous polarization and another part describing the absorptive polarization

$$\boldsymbol{D}(t) = \underbrace{\varepsilon_{\mathrm{r},\infty}\boldsymbol{E}(t)}_{\text{instantaneous}} + \underbrace{\int_{-\infty}^{t} \boldsymbol{E}(t')f(t-t')\mathrm{d}t'}_{\text{absorptive}}. \tag{3.49}$$

The temporal evolution of the polarization in a dielectric medium after the externally applied field is removed may be described with an exponential decay using a characteristic time τ_D corresponding to

$$f(t) \propto \mathrm{e}^{-t/\tau_\mathrm{D}}. \tag{3.50}$$

The detailed solution of the integral in Eq. 3.49 is given in Smyth (1955, p. 55f). The resulting complex and frequency-dependent relative permittivity is given by

$$\varepsilon_\mathrm{r} = \varepsilon_{\mathrm{r},\infty} + \frac{\varepsilon_{\mathrm{r},0} - \varepsilon_{\mathrm{r},\infty}}{1 + \mathrm{i}\omega\tau_\mathrm{D}}, \tag{3.51}$$

with corresponding real and imaginary parts

$${\varepsilon_\mathrm{r}}' = \varepsilon_{\mathrm{r},\infty} + \frac{\varepsilon_{\mathrm{r},0} - \varepsilon_{\mathrm{r},\infty}}{1 + \omega^2{\tau_\mathrm{D}}^2} \quad \text{and} \quad {\varepsilon_\mathrm{r}}'' = \frac{(\varepsilon_{\mathrm{r},0} - \varepsilon_{\mathrm{r},\infty})\omega\tau_\mathrm{D}}{1 + \omega^2{\tau_\mathrm{D}}^2}. \tag{3.52}$$

Temperature-induced oscillations generally decrease the polarization density $\boldsymbol{P}$ and thus the permittivity. Kaatze (1989) measured ${\varepsilon_\mathrm{r}}'(\omega, T)$ as well as ${\varepsilon_\mathrm{r}}''(\omega, T)$ and estimated the parameters for the Debye model (Fig. 3.12). The proposed ad hoc model

$$\lim_{\omega\to 0} \varepsilon_\mathrm{r}(\omega, T) = \varepsilon_{\mathrm{r},0}(T) = 10^{1.94404 - 1.991\cdot 10^{-3}(T - 273.15)} \tag{3.53}$$

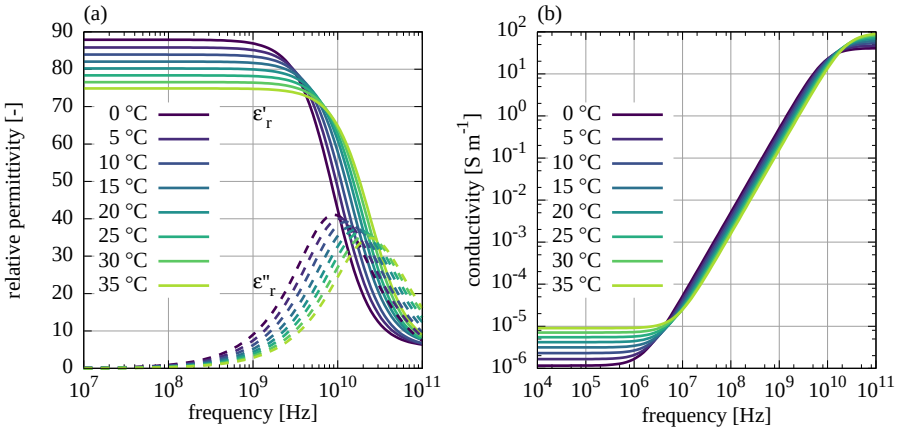

Figure 3.12 The Debye model describes the frequency dependency of the relative permittivity with the parameters $\varepsilon_{r,0}$, $\varepsilon_{r,\infty}$, and τ_D. The temperature dependency of these parameters was determined from measurement data by Kaatze (1989). The resulting frequency and temperature dependency of the relative permittivity is shown in (a). The electrical conductivity may be associated with the relative permittivity according to Eq. 3.55. The combination of the temperature dependency of the Debye model parameters with the temperature dependency of σ_{dc} measured by Light et al. (2005) yields the model for the frequency and temperature dependency of the electrical conductivity that is shown in (b).

assuming temperature data T measured in °C is used in the evaluation of measured TDR data to correct for the temperature-dependence of $\varepsilon_{r,w}$ (Sect. 3.4.1).

Since the permittivity and the electrical conductivity are closely related (Eq. 3.44), the Debye model may also be used to describe the frequency and temperature dependence of the electrical conductivity. Corresponding to Eq. 3.44, von Hippel (1988) identifies the electrical conductivity with the imaginary part of the relative permittivity according to $\sigma = \varepsilon_r''\omega\varepsilon_0$. Insertion of this equation in Eq. 3.52 leads to

$$\sigma(\omega) =: \sigma_D(\omega) = \varepsilon_r''\omega\varepsilon_0 = \frac{(\varepsilon_{r,0} - \varepsilon_{r,\infty})\omega^2\tau_D\varepsilon_0}{1 + \omega^2{\tau_D}^2} = \frac{\sigma_{D,max}\omega^2{\tau_D}^2}{1 + \omega^2{\tau_D}^2}, \tag{3.54}$$

with the high-frequency limit $\sigma_{D,max} = \frac{(\varepsilon_{r,0}-\varepsilon_{r,\infty})\varepsilon_0}{\tau_D}$. The limit of this model for low frequencies is $\lim_{\omega\to 0}\sigma_D(\omega) = 0$. Hence, this model is not valid for $\omega \to 0$, because experiments (e.g., Light et al., 2005) yield $\lim_{\omega\to 0}\sigma_D(\omega) = \sigma_{dc}$. One possible way to include this information in Eq. 3.54 is

$$\sigma(\omega) =: \sigma_D(\omega) + \sigma_{dc}. \tag{3.55}$$

The temperature dependence can be incorporated in this model by using (i) the measurement data of Light et al. (2005) for $\sigma_{dc}(T)$ and (ii) the temperature dependence of the parameters for the Debye model measured by Kaatze (1989). For pure water, the resulting model for $\sigma(\omega, T)$ is shown in Fig. 3.12.

Boundaries The behavior of electromagnetic waves at boundaries is sketched subsequently according to Jackson (1999, p. 302ff). The kinematic behavior of the electromagnetic wave depends on the refraction index

$$n = \sqrt{\mu_\mathrm{r}\varepsilon_\mathrm{r}}. \tag{3.56}$$

At the boundary of two materials A and B with refection indices n^A and n^B, the nature of the wave requires (i) the angle of reflection to be equal to the angle of incidence and (ii) the angle of refraction to comply to

$$\frac{\sin\left({\alpha_\mathrm{w}}^\mathrm{A}\right)}{\sin\left({\alpha_\mathrm{w}}^\mathrm{B}\right)} = \frac{n^\mathrm{B}}{n^\mathrm{A}}, \tag{3.57}$$

which was proposed by Snellius.

The amplitudes of reflected and refracted waves, their polarization and phase changes depend on the boundary conditions at material interfaces which require the normal components of $\boldsymbol{D}$ and $\boldsymbol{B}$ as well as the tangential components of $\boldsymbol{E}$ and $\boldsymbol{H}$ to be continuous. Ultimately, this leads to the Fresnel equations (Jackson, 1999, p. 305f) which describe the ratio of the reflected and refracted amplitudes for the polarization perpendicular and parallel to the plane of incidence. These equations can be simplified for normal incidence ($\alpha_\mathrm{w} = 0$) to

$$T_\mathrm{w} = \frac{2n^\mathrm{B}}{n^\mathrm{A} + n^\mathrm{B}} \quad \text{and} \quad R_\mathrm{w} = \frac{n^\mathrm{A} - n^\mathrm{B}}{n^\mathrm{A} + n^\mathrm{B}} \tag{3.58}$$

with the transmission coefficient T_w and the reflection coefficient R_w which give the ratio of amplitude that is refracted and reflected, respectively. Note, that according to the sign convention for polarization parallel to the plane of incidence, $n^\mathrm{A} < n^\mathrm{B}$ leads to a phase reversal for the reflected wave.

Wavelets A thorough introduction to the subject of wavelet analysis is given, e.g., by Burrus et al. (1997). Waves are oscillating in time and space (Eq. 3.39). The Fourier analysis expands a given wave signal in terms of sinusoids. Naturally, this yields the frequency components of the signal but no time information. Hence, the wave analysis is suitable to study periodic, time-invariant, and stationary phenomena. A wavelet (*small wave*) is a wave package which still exhibits a wave-like oscillation but where the energy is emitted over a limited period of time. This allows for a simultaneous time and frequency analysis. In this study, the Ricker wavelet is used as a source wavelet for all electromagnetic simulations (Fig. 3.13).

3.2.3.2 Numerical solutions

Naturally, numerical methods provide approximate solutions of Maxwell's equations for a limited spatial and temporal extent. Yet, they allow for general forcing and distribution of material properties, which however, have to be given specifically for each grid cell.

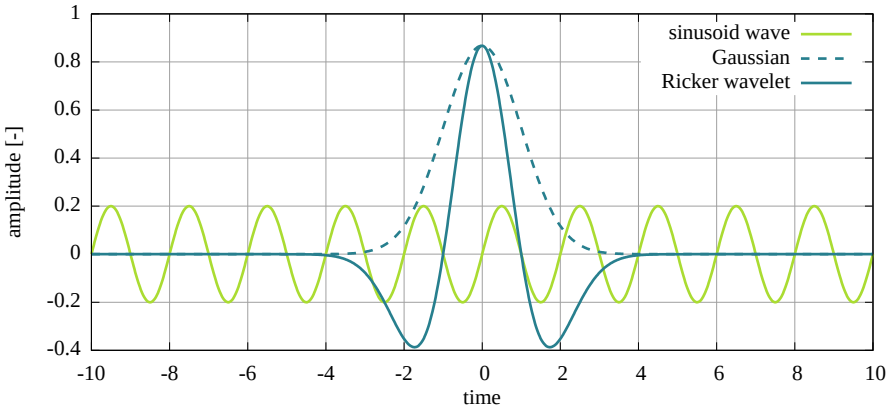

Figure 3.13 Waves fill all space and can be represented with sinusoids. Wavelets still exhibit wave-like oscillations, but their extent is limited to a certain period of time. Hence, a frequency and time analysis of the wavelet is possible and allows for the investigation of time-varying processes. In this work, the Ricker wavelet or Mexican-hat wavelet is used which is the negative normalized second derivative of a Gaussian.

This yields specific solutions and thus the solver has to be rerun for a different forcing or different material properties.

There exist different discretization methods to solve Maxwell's equations in the time-domain, e.g., the finite-volume method (Piperno et al., 2002), the finite-element method (Jin, 2015), the discontinuous Galerkin method (Fezoui et al., 2005), and the finite-difference time-domain (FDTD) method (Taflove and Hagness, 2000). Since it is an explicit method, the FDTD does not require any matrix inversion and hence is comparably fast. The comparably low computational cost makes the FDTD a popular method to simulate GPR measurements (Lampe et al., 2003; Giannopoulos, 2005; Buchner et al., 2012).

If merely the travel time t associated with a homogeneous layer reflection at distance s is required, the application of the velocity model

$$v = \frac{c_0}{\sqrt{\varepsilon_\mathrm{r}\mu_\mathrm{r}}} = \frac{s}{t} \tag{3.59}$$

based on the relative permittivity of the material ε_r is typically more efficient than a full solution of Maxwell's equations. For more complicated permittivity distributions, ray tracing methods such as the fast marching method (FMM), e.g., implemented by de Kool et al. (2006) in the 3D Fast Marching (3DFM) software package, provide an efficient solution.

Finite-Differences Time-Domain The FDTD method is discussed in detail by Taflove and Hagness (2000). This method solves Maxwell's equations very efficiently when assuming a structured grid with the same grid size in each spatial dimension ($\Delta x = \Delta y =$

Δz). Accordingly, Eq. 3.26 and Eq. 3.27 are discretized in space and time (Δt) using constant values for the material properties and fields within the grid cells. The spatial and temporal derivatives are approximated with a first order Taylor expansion. The work of Yee (1966) improved the stability of the solution by shifting the discretization of $\boldsymbol{E}$ and $\boldsymbol{B}$ by $0.5\Delta x$ in space and by $0.5\Delta t$ in time. Note that the FDTD method is fully explicit and requires no matrix inversion. The method is still computationally demanding for real applications, thus Maxwell's equations are typically rather solved in 2D than in 3D. Hence, if the simulated signal is compared with measured data in this study, frequency and amplitude of the simulated signal are corrected with the method proposed by Bleistein (1986). This method is discussed in more detail in Sect. 6.2.1.1.

The spatial and the temporal discretization are connected via the time $t = \Delta x/c$ that is necessary for the signal to travel over one grid cell. If the temporal step width Δt is larger than this time, the wave may propagate more than one grid cell per time step. Since the discretization of differential operators merely use the neighboring grid cells, this will result in exponential growth of the field. Hence, in order to ensure numerical stability, the Courant number for a two-dimensional Yee grid with $\Delta x = \Delta y$ is defined according to Taflove and Hagness (2000, p. 136f) as

$$\Delta t > \frac{1}{c\sqrt{\frac{1}{(\Delta x)^2} + \frac{1}{(\Delta y)^2}}} = \frac{1}{c\sqrt{\frac{2}{(\Delta x)^2}}} = \frac{1}{\sqrt{2}}\frac{\Delta x}{c} := S_\mathrm{C}\frac{\Delta x}{c}. \tag{3.60}$$

Hence, $S_\mathrm{C} \leq \frac{1}{\sqrt{2}} = 0.71$ is required for numerical stability. For the simulations in this thesis, $S_\mathrm{C} = 0.5$ was applied.

Numerical dispersion is also influenced by the absolute size of the spatial grid resolution. According to Fig. 3.14, at least a grid resolution of $\Delta x \leq 0.08\lambda_{\mathrm{w}0}$ is required to keep the error of the phase velocity below 1%.

MEEP and MEEPGPR Oskooi et al. (2010) introduced the MIT electromagnetic equation propagation (MEEP) as FDTD solver for Maxwell's equations. It uses central differences for the finite-differences calculations and thus is second order accurate in space. The output preserves this accuracy through bilinear interpolation. Hence, the resulting electromagnetic fields may be extracted at arbitrary positions within the domain. In order to maintain this accuracy for discontinuous material properties, the sub-grid smoothing procedure proposed by Farjadpour et al. (2006) was implemented in MEEP. Note that the convergence properties of MEEP are given in Oskooi et al. (2009, 2010).

In order to use MEEP for the simulation of GPR radargrams, Buchner et al. (2012) added the interface MEEPGPR. For this study, I extended MEEPGPR by implementing various GPR measurement setups as well as their time-lapse realization (Sect. 3.4.2). Those can be set up with a key-value file, which simplifies the application of MEEPGPR considerably. Additionally, MEEPGPR and muPhi (Sect. 3.1.6) were coupled and synchronized (Sect. 3.6), such that simulated permittivity distributions can be directly used by MEEPGPR. Optionally, also walls at the sides and a basement at the bottom of the domain can be modeled by specifying their extent and permittivity.

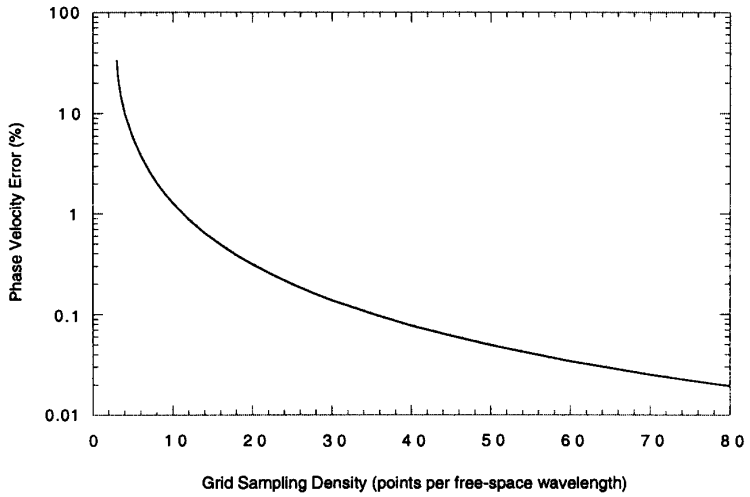

Figure 3.14 The error of the phase velocity $c = \omega/k$ decreases with the grid sampling density. For the Courant number $S_C = 0.5$, 12 grid cells are required per free-space wavelength λ_{w0} to keep the error of the phase velocity below 1%.
[from Taflove and Hagness (2000, p. 50)]

All simulations in this study use a structured squared grid and perfectly matched layer (PML) boundary conditions of 0.15 m thickness. The transmitter antenna is represented with an infinite dipole pointing in the x dimension. The applied source current density $\boldsymbol{J}_s$ leads to a Ricker wavelet with a center frequency of 400 MHz. The receiver antenna is not represented explicitly. Instead, E_x is read directly at the position of the receiver antenna. Thus, any effects originating from the real bow-tie antenna geometry, cross-coupling or antenna shielding are neglected. For the simulations, the antenna separation of the used GPR system (0.14 m) is applied unless stated otherwise. Initially, all fields and currents are set to zero in the simulation.

Characteristics of the solution In order to analyze the characteristic results for a numerical solution of Maxwell's equations from a soil hydraulic perspective, a layered subsurface architecture was set up. The three layers comprise an air layer and the two subsurface layers A and B with the relative permittivities 1, 5, and 10, respectively. Figure 3.15 shows the subsurface architecture as well as the electric field after 21 ns. The electric field comprises a circular wave in air (1) as well as a circular wave in layer A (2). Close to the surface, being the interface between air and layer A, wave (1) is referred to as the direct air wave and wave (2) as ground wave. The head wave (3), e.g., described by Ott (1942), is nearly visible. According to the Huygens principle, this wave originates from the air wave which excites circular waves in the layer A close to the surface. These circular waves interfere constructively in layer A, leading to the characteristic shape of this reflection. However, since these circular waves traveled in layer A for some time, they destructively interfere with the air wave. Wave (2) is reflected at the material

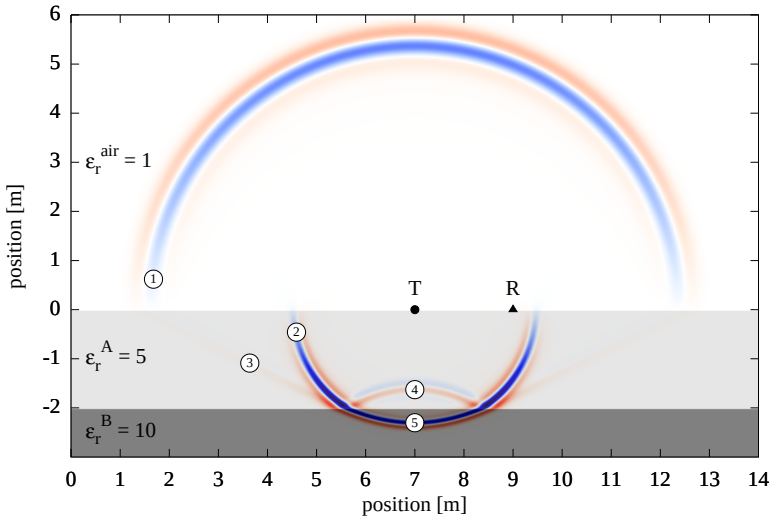

Figure 3.15 Maxwell's equations were solved numerically for a layered architecture consisting of an air layer and two subsurface layers A and B using MEEPGPR. Initially, a Ricker wavelet is excited by the transmitter (T). The resulting electrical field is recorded by the receiver (R). After 21 ns, the electric field features circular waves in the air (1) and the layer A (2). The head wave (3) has its origin in the air wave and is merely visible. The wave (2) is reflected at the material interface between layer A and B. The reflected wave (4) features a phase reversal as ${\varepsilon_r}^B > {\varepsilon_r}^A$, whereas the refracted wave (5) shows the original phase. The electrical conductivity σ is set to zero.

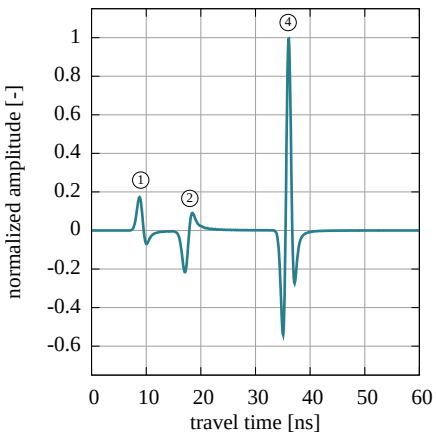

Figure 3.16 The trace recorded with the receiver of the simulation presented with Fig. 3.15 shows the air wave (1), the ground wave (2), as well as the reflected wave (4). The signal of the refracted wave (5) is not recorded by the receiver as it is attenuated by the PML boundary condition. Note that compared to Fig. 3.13, the sign of the Ricker wavelet is flipped, such that it corresponds to the wavelet of the used antennas.

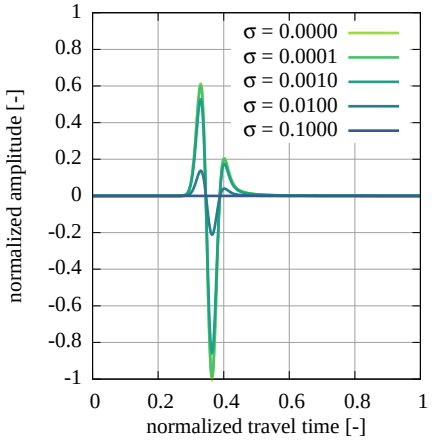

Figure 3.17 The attenuation due to the electrical conductivity (given in $\mathrm{S\,m^{-1}}$) is investigated with different simulations of an electromagnetic wave in a homogeneous material with a constant separation of the transmitter and the receiver. Corresponding to Fig. 3.11, the amplitude of the wave decreases with increasing electrical conductivity and the travel time stays approximately constant.

interface. The reflected wave (4) shows a phase reversal, as ${\varepsilon_\mathrm{r}}^\mathrm{B} > {\varepsilon_\mathrm{r}}^\mathrm{A}$, whereas the refracted wave (5) still exhibits its original phase.

Generally, GPR measurements do not acquire the electric field in the whole domain but at one position instead. Thus, the electric field is read at the position of the receiver (R). This data (trace), is shown in Fig. 3.16. Note that the shape of the air wave (1) and the ground wave (2) is different from the reflected wave (4). This is due to interface effects and analyzed in more detail, e.g., by Sommerfeld (1909) and Annan (1973).

In order to investigate the influence of the electrical conductivity σ on the signal amplitude, an additional simulation was set up with one homogeneous material and a separation of 1.0 m between the transmitter and receiver. Starting with $\sigma = 0$, the electrical conductivity was increased steadily. The resulting traces are shown in Fig. 3.17. Corresponding to Fig. 3.11, the amplitude decreases with increasing electrical conductivity but the influence on the travel time remains small.

3.2.4 Antennas

An antenna basically consists of a conducting material which is excited with a time-dependent source current density $\boldsymbol{J}_\mathrm{s}$. According to Eq. 3.26 and Eq. 3.27, this causes time-dependent electromagnetic fields. Hence, the antenna design naturally influences the radiation pattern which is also referred to as *antenna characteristic*. Balanis (1997) gives a list of different types of antennas which includes wire, aperture, microstrip, array, reflector, and lens antennas. According to Millard et al. (2002), most commercially available antennas are either horn or dipole antennas. Dipole antennas may be grouped in linear dipoles and bow-tie dipoles (Fig. 3.18). The length and diameter of short linear dipole antennas are very small compared to the wavelength λ_w. In contrast to the short linear dipole and the linear dipole antennas which consist of a wire with length $\lambda_\mathrm{w}/2$, the characteristic shape of the bow-tie allows to emit broadband radiation.

Analytically calculating the electromagnetic fields from the source current density is only possible for special cases. Jackson (1999, p. 410ff) exercises this for a dipole in a homogeneous material with permeability μ and permittivity ε. This dipole is centered at the origin and forced with a time-harmonic charge current density with frequency ω. Based on a first order approximation, the resulting electromagnetic fields yield

$$\boldsymbol{B}(\boldsymbol{x}) = \mu \frac{ck^2}{4\pi} (\boldsymbol{e}_x \times \boldsymbol{P})\, \mathrm{e}^{\mathrm{i}kr} \left(\frac{1}{r} + \frac{\mathrm{i}}{kr^2} \right), \tag{3.61}$$

and

$$\boldsymbol{E}(\boldsymbol{x}) = \frac{1}{4\pi\varepsilon_0} \left(k^2 (\boldsymbol{e}_x \times \boldsymbol{P}) \times \frac{\mathrm{e}^{\mathrm{i}kr}}{r} \boldsymbol{e}_x + [3\boldsymbol{e}_x (\boldsymbol{e}_x \cdot \boldsymbol{P}) - \boldsymbol{P}] \left(\frac{1}{r^3} - \frac{\mathrm{i}k}{r^2} \right) \mathrm{e}^{\mathrm{i}kr} \right) \tag{3.62}$$

with $r = \|\boldsymbol{x}\|$ and $\boldsymbol{e}_x = \boldsymbol{x}/\|\boldsymbol{x}\|$. The complete mathematical description of these fields is quite complicated. Hence, it is instructive to investigate their limits following Balanis (1997, p. 32ff) and Jackson (1999, p. 410ff).

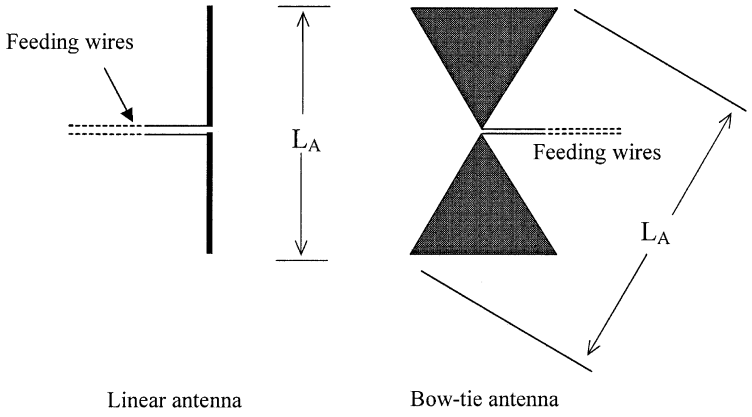

Figure 3.18 The wavelength and the bandwidth of the excited electromagnetic waves depend in particular on the characteristic length L_A of the dipole antennas. In contrast to the linear dipole antenna, the shape of the bow-tie antenna allows for a broader bandwidth. [from Millard et al. (2002)]

The space around the antenna can be separated into three zones, namely the reactive near-field, the radiative near-field, and the far-field (Fig. 3.19).
The *reactive near-field* is that portion of the near-field that directly surrounds the antenna and thus influences its characteristics ($kr \ll 1$). Here, the terms $\boldsymbol{B} \propto 1/r^2$ and $\boldsymbol{E} \propto 1/r^3$ are dominant in Eq. 3.61 and Eq. 3.62, respectively. The upper limit for the extent of the reactive near-field is specified by Balanis (1997) with $R_1 = 0.62\sqrt{L_A/\lambda_w}$ for a long linear dipole antenna and with $R_1 = \lambda_w/(2\pi)$ for a short linear dipole antenna.
The *radiating near-field*, which is also known as the Fresnel zone, is located between the reactive near-field and the far-field ($kr > 1$). Hence, the terms $\boldsymbol{B} \propto 1/r$ and $\boldsymbol{E} \propto 1/r^2$ are dominant in Eq. 3.61 and Eq. 3.62, respectively. Balanis (1997) specifies the limits for this Fresnel zone with $R_2 = 2{L_A}^2/\lambda_w$. Note that this complies with $R_1 \leq r < R_2$.
In the *far-field*, which is also known as the Fraunhofer zone, the angular field distribution is independent of the distance from the antenna. In this zone, the radiative terms predominate, leading to $\boldsymbol{B} \propto 1/r$ and $\boldsymbol{E} \propto 1/r$. Using these dependencies to calculate the Poynting vector

$$\boldsymbol{s} = \frac{1}{\mu}(\boldsymbol{E} \times \boldsymbol{B}) \tag{3.63}$$

yields that the power decreases with $\propto r^{-2}$. This is consistent with the conservation of energy, because the spherical surface increases with $\propto r^2$.

The three dimensional electric field of a short linear dipole antenna is sketched in Fig. 3.20. Aiming for a simpler visualization of the fields, typically the intersections of the fields with the H plane and the E plane are given (Fig. 3.21). Millard et al. (2002) compared the theoretical fields for a short linear dipole antenna and a long linear dipole antenna with the measured field of a bowtie dipole antenna in a homogeneous medium (Fig. 3.21). They found that the bow-tie dipole antenna generates a more directed radiation pattern compared to linear dipole antennas.

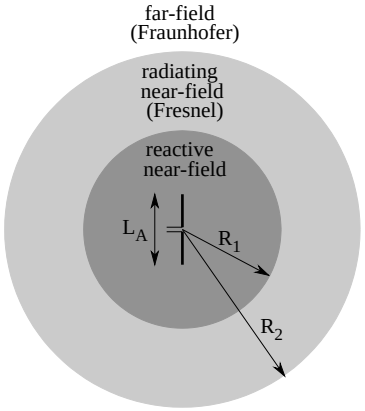

Figure 3.19 The electromagnetic fields of a radiating linear dipole antenna (Eqs. 3.61–3.62) can be approximated differently depending on the distance from the antenna. In the *reactive near-field*, where $kr \ll 1$, the terms $\boldsymbol{B} \propto 1/r^2$ and $\boldsymbol{E} \propto 1/r^3$ are dominant for distances smaller than $R_1 = 0.62\sqrt{L_\mathrm{A}/\lambda_\mathrm{w}}$. Then, in the *radiating near-field*, where $kr > 1$, the terms $\boldsymbol{B} \propto 1/r$ and $\boldsymbol{E} \propto 1/r^2$ are dominant for distances smaller than $R_2 = 2{L_\mathrm{A}}^2/\lambda_\mathrm{w}$. Finally, in the *far-field* the electromagnetic fields decline with $\boldsymbol{B} \propto 1/r$ and $\boldsymbol{E} \propto 1/r$.
[after Balanis (1997, p. 32)]

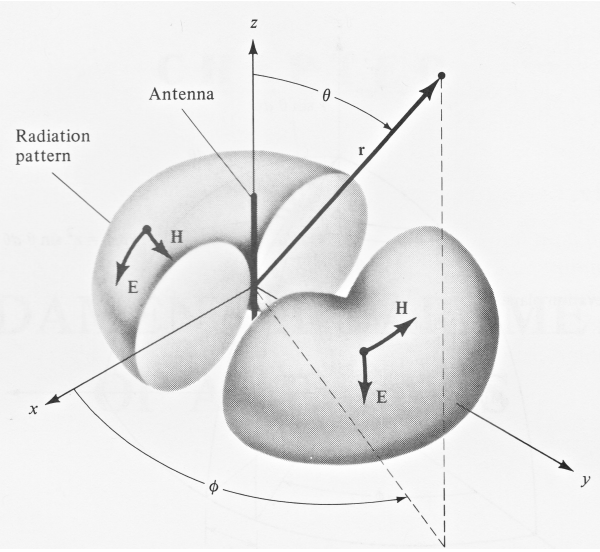

Figure 3.20 As the omnidirectional radiation pattern of a dipole antenna is rather complicated to visualize, typically only the intersection of the electromagnetic fields with E plane and the H plane are given (Fig. 3.21). These planes are defined corresponding to the direction of the electric field $\boldsymbol{E}$ and the magnetic field $\boldsymbol{H}$. Hence, the E plane is spanned by the x and the z dimension and parallel to the length and containing the dipole. The H plane is spanned by the x and the y dimension, perpendicular to the length, and bisecting the dipole.
[from Balanis (1997, p. 30)]

Depending on the application, GPR antennas are often applied directly on dielectric media. According to Millard et al. (2002), the coupling to a dielectric medium effects the center frequency, the effective radiation pattern, and hence the effective beamwidth. The effect of interfaces on the radiation pattern of dipoles has been investigated for decades, e.g., by Ott (1942); Annan (1973); Annan et al. (1975); Engheta et al. (1982); Rutledge and Muha (1982); Dai and Young (1997); Radzevicius et al. (2003); Diamanti and Annan (2013). The characteristic effects of an interface on the radiation pattern of a linear dipole antenna are shown in Fig. 3.22. The two most important effects are (i) that the antenna radiates more energy into the material with a higher relative permittivity and (ii) that the directivity of the radiation increases with the relative permittivity of the material.

Note that these remarks concerning antennas are merely of instructive nature, because the radiation pattern of real bow-tie GPR antennas is more complicated due their com-

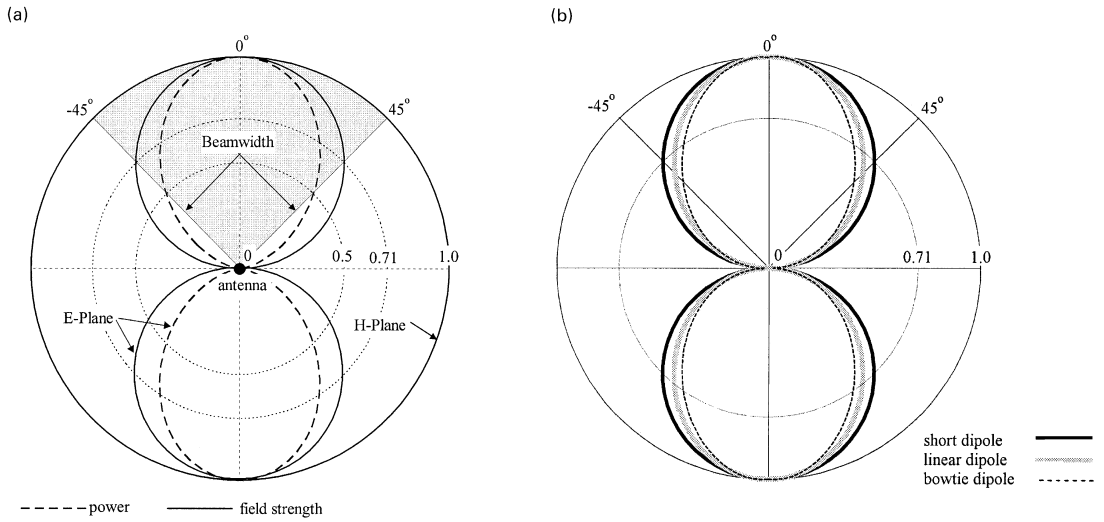

Figure 3.21 (a) The theoretical patterns of the relative field and the power of a short antenna are given for the E- and the H plane (Fig. 3.20). In order to determine the beamwidth of the antenna, typically either 71% of the maximum of the field pattern or 50% of the maximum point of the power pattern are used.
(b) The theoretical field patterns of the electric field in air for the short linear dipole antenna and the long linear dipole antennas are compared with the measured field pattern of a bow-tie antenna. Note that the bow-tie antenna is slightly more directed than the linear dipole antennas.
[from Millard et al. (2002)]

Figure 3.22 The field pattern of a short linear dipole antenna on a dielectric interface is shown for the H plane. With increasing relative permittivity of the subsurface, the radiation pattern becomes more directed towards the ground.
[from Millard et al. (2002)]

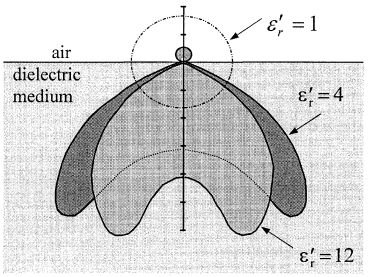

position. Typically, this comprises an embedding with a particular relative permittivity as well as a shielding of the bow-tie dipoles, e.g., with conducting half-cylinders (Millard et al., 2002). This design of the shielding (i) directs and focusses the radiation and (ii) protects the antennas from external influences and vice versa. The radiation pattern of more realistic antennas is investigated, e.g., by Warren and Giannopoulos (2012) or Diamanti and Annan (2013).

3.3 Petrophysical relationships

In order to (i) solve Maxwell's equations based on a simulated water content distribution and (ii) transfer the measured permittivity in water content, petrophysical relationships are required that allow to relate water content with electromagnetic properties in particular relative permittivity and electrical conductivity. Similar to the soil hydraulic material properties, these petrophysical relationships are described heuristically with empirical models.

Popular parameterizations for $\varepsilon_{\mathrm{r}}(\theta_{\mathrm{w}})$ are reviewed, e.g., by Steelman and Endres (2011). These models comprise low-order polynomial models with fitted parameters (Topp et al., 1980), volumetric mixing models (Birchak et al., 1974), and effective medium approximations (Sen, 1984). In this study, the complex refractive index model (CRIM) is used which is a volumetric mixing model introduced by Birchak et al. (1974). According to this model, the relative permittivity of the subsurface ε_{r} can be calculated from the water content distribution θ_{w} via

$$\varepsilon_{\mathrm{r}}(\theta_{\mathrm{w}}, T_{\mathrm{s}}, \phi)^{\alpha_{\mathrm{CRIM}}} = \theta_{\mathrm{w}} \cdot \varepsilon_{\mathrm{r,w}}(T_{\mathrm{s}})^{\alpha_{\mathrm{CRIM}}} + (\phi - \theta_{\mathrm{w}}) \cdot {\varepsilon_{\mathrm{r,a}}}^{\alpha_{\mathrm{CRIM}}} + (1 - \phi) \cdot {\varepsilon_{\mathrm{r,s}}}^{\alpha_{\mathrm{CRIM}}}, \quad (3.64)$$

with the geometry parameter $\alpha_{\mathrm{CRIM}} = 0.5$. In order to apply the CRIM, the porosity ϕ, the relative permittivity of water $\varepsilon_{\mathrm{r,w}}$, the relative permittivity of air $\varepsilon_{\mathrm{r,a}}$, and the relative permittivity of the soil matrix $\varepsilon_{\mathrm{r,s}}$ have to be known. The relative permittivity of air $\varepsilon_{\mathrm{r,a}}$ is typically set to 1. Assuming that the sand matrix consists mainly of quartz (SiO_2) grains, the relative permittivity of the soil matrix $\varepsilon_{\mathrm{r,s}}$ was set to 5 (Carmichael, 1989). In the simulation, the porosity ϕ is typically equal to the saturated water content $\theta_{\mathrm{w,s}}$. A detailed error propagation of the CRIM is given by Roth et al. (1990). Following Kaatze (1989), Eq. 3.53 is used to parameterize the dependency of the relative permittivity of water $\varepsilon_{\mathrm{r,w}}$ on the soil temperature T_{s} [°C]. The effect of the soil temperature T_{s} on the GPR travel time is investigated with Fig. 3.23.

The parameterization models for $\sigma(\theta_{\mathrm{w}})$ are reviewed, e.g., by Friedman (2005). Finding an accurate parameterization model for $\sigma(\theta_{\mathrm{w}})$ is more complicated compared to $\varepsilon_{\mathrm{r}}(\theta_{\mathrm{w}})$, because other processes of comparable size add to the dependence of the bulk electrical conductivity on soil water content. Rhoades et al. (1976) assumed two parallel conductors, a bulk liquid-phase conductivity associated with the free salt in the liquid-filled pores σ_{w} and a bulk surface conductivity σ_{s} associated with the exchangeable ions at the solid-liquid interface and proposed

$$\sigma(\theta_{\mathrm{w}}) = T(\theta_{\mathrm{w}})\theta_{\mathrm{w}}\sigma_{\mathrm{w}} + \sigma_{\mathrm{s}}, \qquad \text{with} \qquad T(\theta_{\mathrm{w}}) = a\theta_{\mathrm{w}} + b. \quad (3.65)$$

The empirical parameters a and b of the transmission coefficient T vary among soils. Difficulties for describing $\sigma(\theta_{\mathrm{w}})$ arise in particular during evaporation, where salt can be deposited within the pore space (e.g., Gran et al., 2011) and dissolved in the soil water subsequently, e.g., after precipitation. Hence, the electrical conductivity of the soil water σ_{w} is not necessarily constant within a single material.

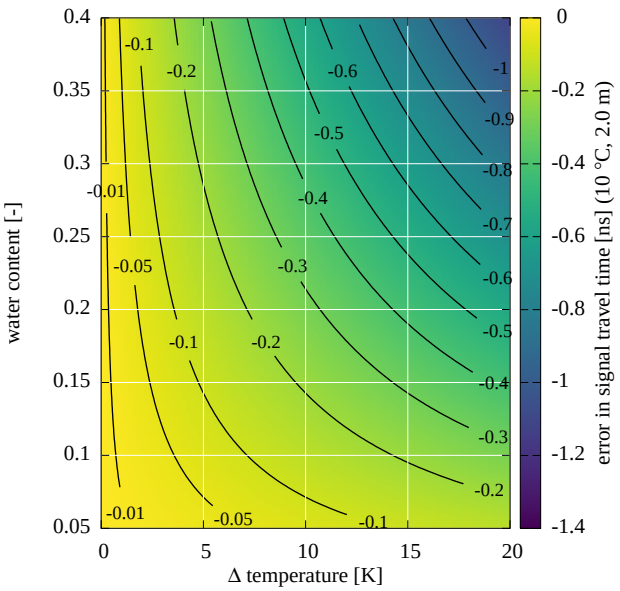

Figure 3.23 The temperature dependence of the relative permittivity of water $\varepsilon_{r,w}$ measured by Kaatze (1989) effects the travel time, e.g., of GPR antennas. In this example, the soil temperature T_s was assumed as 10 °C and a reflector was assumed at 1.0 m depth leading to a vertical travel path length of 2.0 m. The standard deviation of the normalized travel time is estimated as $6 \cdot 10^{-4}$ (Sect. 6.3.1.2). Together with a total measurement time of 60 ns, 1 standard deviation corresponds to 0.04 ns. This value is surpassed, e.g., with a mean water content of $\theta_w = 0.1$ and a temperature deviation of $\Delta T_s = 3$ K or close to saturation with a mean water content of $\theta_w = 0.3$ and a temperature deviation of $\Delta T_s = 1$ K.

In this study, σ_w and σ_s as well as the parameters a and b are unknown. Hence, in a first step, the σ is assumed to be independent of the water content θ_w and constant within the whole domain.

Note (i) that all the parameters for the petrophysical relationships generally vary in space and time and (ii) that both the relative permittivity as well as the electrical conductivity are assumed to be real valued.

3.4 Measurement methods

Since the hydrogeophysical measurement methods which are applied in this study, i.e. TDR and GPR, acquire the travel time of electromagnetic waves, they exploit the large difference of the relative permittivity of air and water. The measurement principle for both methods is identical, yet they differ in particular concerning the type of wave propagation and concerning their measurement volume. The main differences between the methods are listed in Table 3.2. Naturally, these measurement methods are limited to soils with low electrical conductivity, as otherwise the signal is attenuated (Fig. 3.17). This also limits the applicable frequency range (Fig. 3.12) and thereby the measurement resolution.

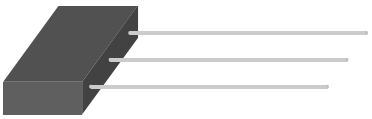

Figure 3.24 The TDR sensors used in this work consist of the probe head and three cylindrical rods. The signal propagates in the center rod and the outer rods are grounded emulating the electric field of a coaxial line. The length of the rods typically varies between 0.1 m and 0.3 m.

3.4.1 TDR

A comprehensive review of the TDR measurement method is given by Robinson et al. (2003). The typical design of the TDR sensor emulates the electric field of a coaxial line with three rods where the electromagnetic wave is guided via the center rod and the outer rods are grounded to protect the signal from external electric fields (Fig. 3.24). Thus, the electromagnetic wave is reflected at the end of the center rod and the signal travels back to the measurement device. The TDR data used in this thesis are acquired with a Campbell Scientific TDR100.

The TDR signal is typically evaluated along two different lines: (i) the two-way travel time t is used for the evaluation of the bulk permittivity and (ii) the reflection coefficient at infinite time of the trace R_∞ is used for the evaluation of the electrical conductivity. Note that to optimally exploit the available measurement resolution, typically two different traces are acquired for the evaluation of the bulk permittivity and the direct electrical conductivity.

The essential steps for the evaluation of the bulk permittivity from a TDR trace are shown in Fig. 3.25. Inflection points of the measured signal can be chosen to mark the reflections at the probe head and at the end of the rods. Hence, the evaluation of the two-way travel time is based on detecting the maxima of the first temporal derivative of the recorded trace. To increase the precision of the evaluation, parabolas are fitted to the detected maxima. Finally, the maxima of the parabolas are employed to evaluate

Table 3.2 Although the measurement methods TDR and GPR apply the same measurement principle, they differ in several points.

	TDR	GPR
wave propagation	guided	free
measurement volume	$\mathcal{O}(10^{-3}$ m$^3)$	$\mathcal{O}(1$ m$^3)$
typical application	temporal	spatial
transferability	stationary	mobile

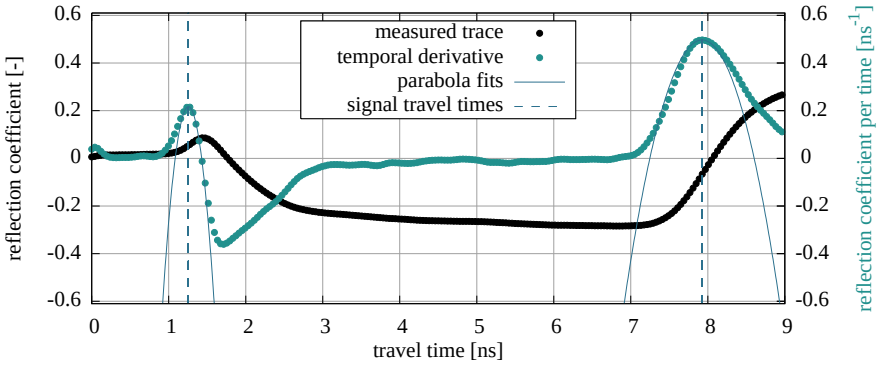

Figure 3.25 The evaluation of a TDR trace is based on the detection of the inflection points caused by reflections at the probe head and at the end of the rod. This evaluation is done automatically after calculating the first temporal derivative of the trace. Parabolas are fitted to the maxima of the temporal derivative to increase the precision of the evaluated travel time t which is transferred to the bulk relative permittivity with calibration data (Eq. 3.66). The measured data approach a constant reflection coefficient R_∞ with time (not shown). This value is used for the evaluation of the direct current electrical conductivity σ_{dc} (Eqs. 3.67–3.68).

the two-way travel time. Using the linear relationship between the two-way travel time t and the square root of the relative permittivity

$$v = \frac{c_0}{\sqrt{\varepsilon_\mathrm{r}\mu_\mathrm{r}}} = \frac{2L_\mathrm{TDR}}{t} \rightarrow \sqrt{\varepsilon_\mathrm{r}} \propto t, \tag{3.66}$$

with the length of the TDR rods L_TDR, the travel time is transferred to relative permittivity with the help of individual calibration data for each sensor comprising measurements in air and desalinated water. The resulting relative permittivity can be transferred to water content, e.g., with the CRIM (Sect. 3.3).

The evaluation of the electrical conductivity follows Heimovaara et al. (1995), who specify the total resistance of the transmission line R_tot via

$$R_\mathrm{tot}(R_\infty) = R_\mathrm{c} + R_\mathrm{s} = Z_\mathrm{c}\frac{1+R_\infty}{1-R_\infty}, \tag{3.67}$$

with the resistance of the cable R_c and the soil R_s, and the cable tester impedance $Z_\mathrm{c} = 50\ \Omega$. Typically, the reflection coefficient at infinite time R_∞ is determined using the mean of a number of samples close to the end of the TDR trace. Heimovaara et al. (1995) further correct the evaluation method for the temperature dependence of the electrical conductivity via

$$\sigma_\mathrm{dc}(R_\infty, T_\mathrm{s}) = \frac{K_\mathrm{p}}{R_\mathrm{tot} - R_\mathrm{c}} \frac{1}{\alpha_\mathrm{H}(T_\mathrm{s} - 25)} \tag{3.68}$$

with $\alpha_\mathrm{H} = 0.0191$. The remaining constants, i.e. R_c and the cell constant of the triple wire probe K_p, are determined for each probe separately with the help of calibration data.

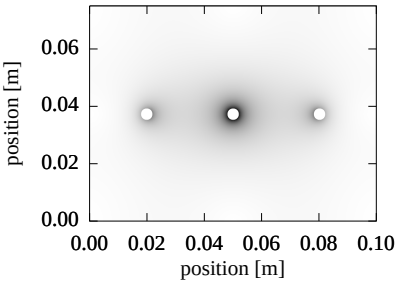

Figure 3.26 In order to investigate the measurement volume of a TDR sensor, the cross-section of the TDR geometry (Fig. 3.24) was used to simulate the normalized energy distribution with the arbitrary transmission line calculator (ATLC). The highest energy density is found around the central rod and between the central rod and the outer rods. Yet, most of the energy is close to the central rod. The insertion of the rods in a natural soil decreases its pore volume. This makes the hydraulic characterization of natural soils with TDR sensors challenging.

Naturally, the evaluation methods provide average values for the relative permittivity and electrical conductivity with respect to the measurement volume. In order to illustrate this measurement volume, the design of the triple wire probe (Fig. 3.24) was used to simulate the spatial energy distribution (Fig. 3.26). Since the highest energy density is found close to the center rod and between the center rod and the outer rods, the measurement volume is rather small ($\mathcal{O}(10^{-3}\ \mathrm{m}^3)$).

TDR is an invasive measurement method, because the rods have to be inserted into the soil. Thus, a large fraction of pore volume around the rods is disturbed and compressed, as the pore volume has to decrease by the volume of the rods. Typically, TDR sensors are applied horizontally in a soil profile which requires digging a trench (e.g., Wollschläger et al., 2009). Hence, after the insertion of the sensors, the soil has to equilibrate for several months. Note that the sensors may also be applied vertically from the surface.

3.4.2 GPR

In this study, bow-tie GPR antennas are used where the transmitter and the receiver are installed in one antenna box (Fig. 3.27). Some introductory and illustrative remarks on antennas have been given in Sect. 3.2.4. Naturally, electromagnetic measurement methods that are based on the propagation of waves are limited to soils with low electrical conductivity, because the signal is highly attenuated otherwise. Compared to the TDR method, this is even more important for the GPR method, as it covers a larger measurement volume leading to a longer travel path. Hence, the frequency range of these hydrogeophysical measurement devices is chosen such that attenuation through the electrical conductivity is avoided. The according trends can be derived from Fig. 3.12: the higher the frequency, the higher the electrical conductivity of water, and the smaller the signal amplitude and thus the penetration depth of the signal. Typically, the imaginary part of the permittivity as well as dispersive effects are neglected ($\varepsilon_\mathrm{r} \in \mathbb{R}$, $\partial\varepsilon_\mathrm{r}/\partial\omega \equiv 0$). However, using a higher center frequency, it is possible to construct smaller wavelets which increases the resolution of the GPR antenna signal. Hence, the choice of the center frequency of the GPR antenna balances (i) the signal attenuation, (ii) the signal resolution, and (iii) the dispersive effects of the material properties. According to

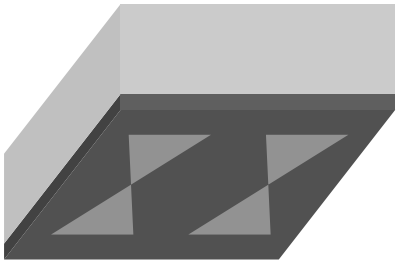

Figure 3.27 The GPR antennas used in this study are shielded, single frequency, and bi-static bow-tie antennas. Hence, they include one transmitter and receiver bow-tie pair per antenna box. Often the shielding is realized with half-cylindrical conductors (not shown here). The antennas that provided the data for this thesis have a center frequency of 400 MHz. The size of the corresponding antenna boxes is approximately 0.3 m × 0.4 m × 0.2 m.

Fig. 3.12 and Fig. 3.17, the tenable frequency spectrum for the application of GPR antennas in soil hydrology ranges from ≈ 0.1 GHz to ≈ 2 GHz.

The measured GPR data are digital, thus discretized in time and in amplitude. The transmitter is iteratively emitting the wavelets and the receiver is recording and stacking the acquired data. The trace is discretely sampled over the measurement time typically using between 1024 and 4096 samples. The mean values of the stacked data are written to a file as soon as a trigger is actuated. The GPR system applied in this study allows to trigger the measurement either equidistantly in space (measurement wheel) or in time and resolves each sample with 16 bit.

For an initial visual evaluation, a radargram is created from the recorded traces by concatenating the data to a matrix. This matrix is then typically shown in color code, e.g., as in Fig. 3.29. The radargram can be evaluated in various ways which are discussed in detail, e.g., by Daniels (2004). These evaluation methods either extract the two-way travel time and possibly also amplitude by tracking either the minimum, the maximum, or the zero-crossing of the signal (picking). Alternatively, the complete shape of the wavelet or even the whole radargram may be evaluated quantitatively.

For a ray-based evaluation, the travel time of a reflection originating from a material interface at depth d is given by

$$t = \frac{s}{v} = \frac{\sqrt{(4d^2 + a^2)}}{\frac{c}{\sqrt{\varepsilon_r \mu_r}}} \tag{3.69}$$

with the distance a between the transmitter and the receiver. The travel path length

$$s = 2 \cdot \sqrt{d^2 + (a/2)^2} \tag{3.70}$$

is determined via geometrical considerations and increases hyperbolically with the antenna separation a. The velocity of the wave is given by Eq. 3.42.

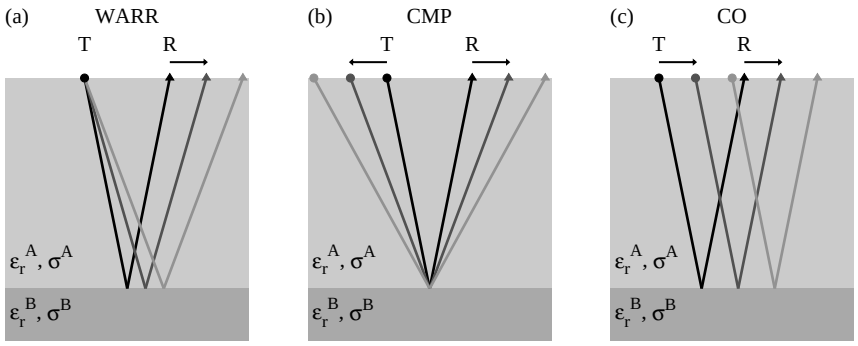

Figure 3.28 The typical GPR measurement setups comprise the WARR, the CMP, and the CO setup. In the WARR setup, one of either the transmitter or the receiver is stationary, whereas the respective other is moved. This allows for a fast and easy to apply measurement which continuously changes the antenna separation. However, this comes at the price of a moving reflection point. This drawback is circumvented with the CMP setup, where both antennas are moved in opposite directions to keep the reflection point stationary. Compared to the WARR measurement setup, the CMP measurement setup is more laborious. The typical shape of WARR and CMP radargrams is discussed in Fig. 3.29. The CO setup is suitable to analyze the subsurface structure for larger scales. In this measurement setup, the antennas have a constant antenna separation. An exemplary CO radargram of ASSESS is shown in Fig. 3.30.

Different measurement setups for spatial surveys comprise the wide angle reflection and refraction (WARR), common mid point (CMP), and common offset (CO) setup (Fig. 3.28). These setups are explained subsequently in more detail.

WARR In the WARR measurement setup, either the transmitter or the receiver is stationary, while the respective other is moved in one direction. This allows for a fast acquisition of a wide range of antenna separations. However, this ease of application comes at the cost of a horizontally moving reflection point at the material interface. An exemplary simulation of a WARR radargram is given in Fig. 3.29. The travel time of the signal that directly travels from the transmitter to the receiver naturally increases linearly with the antenna separation ($t = a/v$). This holds for the air wave (1) and the ground wave (2) which are also described in Fig. 3.15. However, the travel path for the reflected signal (3) and hence also the travel time increases hyperbolically with the antenna separation (Eq. 3.70).

CMP The CMP measurement setup is similar to the WARR measurement setup. However, here both transmitter and receiver are moved for the same distance per trace but in opposite directions. This procedure is more laborious compared to the WARR measurement setup, but ensures a stationary reflection point. This is valuable in particular for undulating reflectors. However, the travel path still may contain changing material pro-

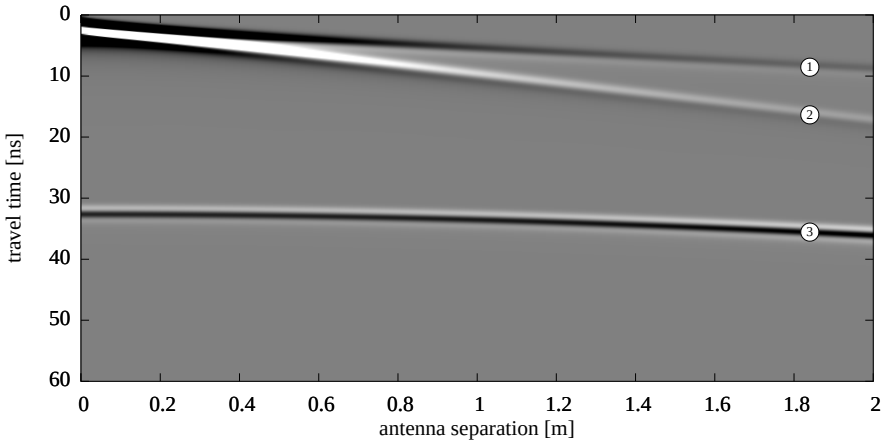

Figure 3.29 This simulation of a WARR measurement shows that the travel time of the air wave (1) and the ground wave (2) increases linearly with the antenna separation. The travel time of the reflected signal (3) increases hyperbolically with the signal travel path (Eq. 3.70). For a homogeneous material and a horizontal reflector, the simulation of a WARR measurement is identical to the corresponding simulation of a CMP measurement. Since the subsurface is typically not homogeneous in reality, differences between measured WARR and CMP radargrams are expected. Note that if the position of the transmitter is stationary, only one electromagnetic field has to be simulated for the WARR radargram.

perties in heterogeneous media. For a homogeneous medium and a horizontal reflector, the CMP radargram corresponds to a WARR radargram which is shown in Fig. 3.29.

CO The CO measurement setup is typically used for site characterizations. Here, the separation is kept constant but the position of the antennas is changed in space, e.g., by dragging the antenna over the surface. This yields a visualization of the subsurface, as changes in the electromagnetic material properties are typically recognizable in the radargram (Fig. 3.30). Evaluating the travel time information for a specific reflector in the radargram with at least two different antenna separations (Eq. 3.69) provides a fast and easy to apply method to determine the reflector depth and the mean relative permittivity along the travel path for larger scales (Gerhards et al., 2008).

Time-lapse Time-lapse measurement setups are complementing spatial measurement setups and are typically used to acquire temporal changes in the subsurface. A simple time-lapse measurement setup consists of a GPR antenna measuring at a stationary position in equidistant temporal intervals. Hence, this setup is similar to the TDR measurement method which also yields temporally highly resolved time-series data measured at a stationary position. This measurement setup is not limited to a stationary antenna. It also allows for more complicate setups such as time-lapse WARR, time-lapse CMP, or time-lapse CO. Except for the time-lapse measurement using a stationary antenna, these kind of measurements are typically laborious in the field but acquire large amounts

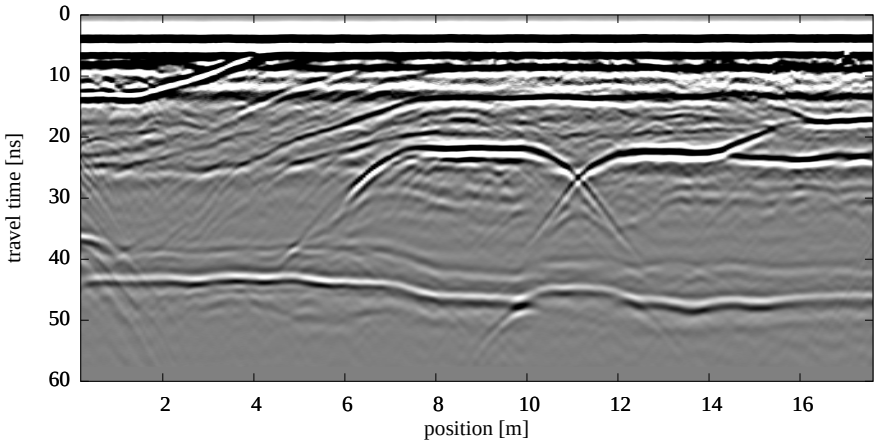

Figure 3.30 This CO measurement of the ASSESS site (Fig. 2.2) shows in particular reflections of material interfaces, compaction interfaces, the groundwater table, and the confining walls. Typically, the assignment of these reflection types on the basis of a single radargram is challenging. For this task, the analysis of GPR measurement data acquired for different hydraulic states is extremely helpful. This particular radargram is analyzed in more detail in Sect. 6.3.2.2, including the assignment of the reflection types.

of data including most valuable information about the hydraulic dynamics. Hence, the time-lapse measurement setup is the main measurement setup used in this thesis.

In order to illustrate the characteristic signal of a time-lapse measurement setup with a stationary antenna, simulated radargrams based on synthetic hydraulic water content distributions of a fluctuating groundwater table experiment and an infiltration experiment in homogeneous sand and silt are discussed subsequently. The hydraulic phenomena of these experiments are analyzed in Sect. 3.1.7. In this section, the focus is on the resulting reflections in the GPR radargrams. For the solution of Maxwell's equations with MEEPGPR, the electrical conductivity σ is set to 0.0 $\mathrm{S\,m^{-1}}$, the relative permittivity above (below) the domain is set to 1 (23), and the soil temperature T_s is set to 8.5 °C. The grid resolution is specified with 0.005 m.

The radargrams for the fluctuating groundwater table and the infiltration experiment are shown in Fig. 3.31 and Fig. 3.32, respectively. Both figures include markers for the characteristic reflections originating from (i) the bottom of the domain (0), (ii) the initial capillary fringe (1), (iii) the kink at saturation (2), and (iv) the additional kink at low water contents (3). These markers are chosen to be consistent with those in Fig. 3.9 and Fig. 3.10.

The radargrams for the fluctuating groundwater table experiment are shown in Fig. 3.31. The fluctuating groundwater table is implemented at the bottom boundary with a Dirichlet boundary condition. The hydraulic potential at this boundary was increased from 0.0 m to 2.0 m over 8 h (imbibition phase), and decreased from 2.0 m to 0.0 m over 8 h (drainage phase). In between, the Dirichlet boundary condition is kept at 2.0 m

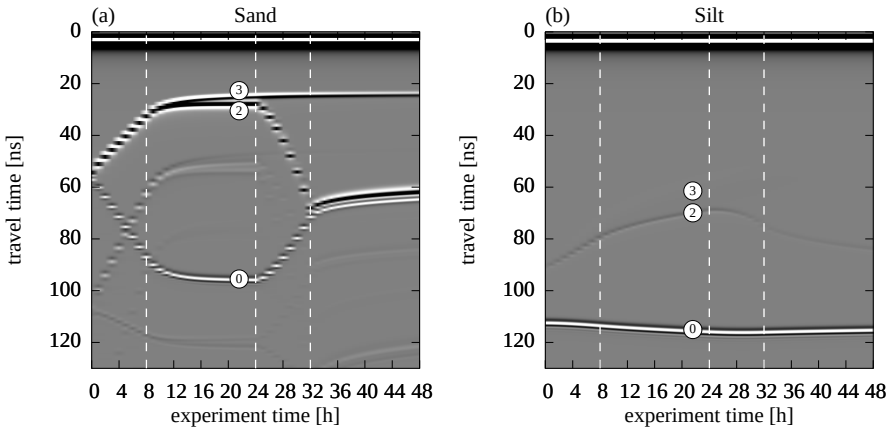

Figure 3.31 The simulation for this time-lapse CO radargram is based on the water content distributions of sand (a) and silt (b) of the fluctuating groundwater table experiment given in Fig. 3.9. The vertical dashed lines indicate the different phases of the experiment comprising the forcing phase, the equilibration phase, the drainage phase, and the final equilibration phase. The markers are explained in the text and are used consistently in this section. In order to facilitate the comparison with the radargrams given in Fig. 3.32, the normalization and the plot range for all radargrams is the same.

(equilibration phase) and after the drainage phase, it is set to 0.0 m. Hence, due to the changing total water content in the domain, the travel time of reflection (0) increases during the imbibition phase and decreases during drainage phase. Due to the constant Dirichlet boundary condition at the end of the experiment, the total water content and hence the travel time of reflections (0) and (3) decrease after the drainage phase, as water still drains at the bottom boundary. Note that the reflection (0) relates to the total water content in the domain.

In the sand, the reflections (2) and (3) are not separable during the imbibition. As the additional kink smoothes and moves to lower water contents during the equilibrations phase, the reflections become separable and the amplitude of reflection (3) decreases over time. As the Dirichlet boundary condition at the bottom is set to 0.0 m again, reflections (2) and (3) approach each other and their distance finally indicates the height of the capillary fringe.

In the silt, the amplitude of the reflections (2) and (3) is very low, because the gradients in the water content distribution are smaller compared to the sand (Fig. 3.9). Note that the reflection (3) exists but is merely visible. Hence, this characteristic reflection is less evaluable in this case. Due to the lower hydraulic conductivity compared to the sand (i) the travel time of reflection (2) still increases during the equilibration phase and decreases after the drainage phase and (ii) the change of the total water content indicated by reflection (0) is much smaller for the silt compared to the sand.

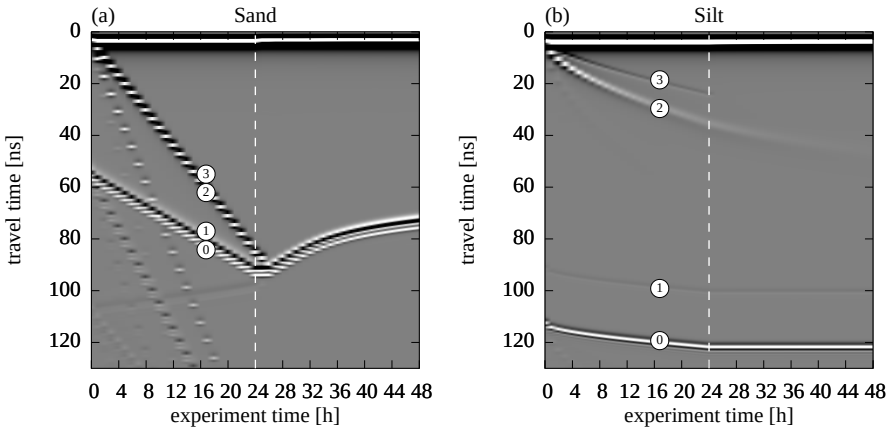

Figure 3.32 The simulation for this time-lapse CO radargram is based on the water content distributions of sand (a) and silt (b) of the infiltration experiment given in Fig. 3.10. The vertical dashed lines indicate the different phases of the experiment comprising the forcing phase and the equilibration phase. The markers are explained in the text and are used consistently in this section. In order to facilitate the comparison with the radargrams given in Fig. 3.31, the normalization and the plot range for all radargrams is the same.

The radargrams for the infiltration experiment are shown in Fig. 3.32. The applied infiltration pulse is modeled with a Dirichlet boundary condition using a hydraulic head of -0.1 m at the top boundary during the forcing phase between 0 h and 24 h. During the whole experiment, a Dirichlet boundary condition of 0.0 m was chosen at the bottom boundary. With the advancing infiltration front, the total water content in the domain and the travel time of the reflections (0) and (1) increase for both materials. Due to the infiltration front, the relative permittivity close to the surface increases. This changes the direct signal.

In the sand, a steep infiltration front develops (Fig. 3.10). Hence, the refections (2) and (3) have a high amplitude and are not separable. This is also true for the capillary fringe reflection (1) and the reflection (0). Once the infiltration stops, the total water content and hence the travel time of all reflection decrease, as water is draining through the bottom boundary out of the domain. The steepness of the infiltration front and the high contrast in relative permittivity lead to multiple reflections.

In the silt, the gradient of the water content distribution is smaller compared to the sand (Fig. 3.10) leading to reflections with lower amplitude. Since also the hydraulic conductivity is smaller, the infiltration front moves slower and is not as steep as for the sand. Hence, the reflections (2) and (3) are easily separable. After the forcing phase, the material close to the infiltration front is desaturated and the water content distribution smoothes. Hence, in particular the reflection (3) is barely visible. Without the forcing at the top boundary, also the water content distribution of the reflection (2) smoothes. This leads to a broadening of the reflection and a decreasing amplitude. Since the infiltration front does not reach the groundwater table at the bottom boundary, the

total water content and the travel time of the reflection (0) remains constant after the forcing phase.

3.5 Optimization

The basis for the quantitative understanding of a system is its representation. According to Bauser et al. (2016), the representation is defined as a set consisting of (i) the *dynamics* which mathematically describes the propagation of the state variable in space and time at the scale of interest, (ii) the *forcing* which couples the system to the super-scale physics in space (initial state) and time (boundary condition), (iii) the *subscale physics* which is not explicitly described by the dynamics but with a parameterization using parameters which are generally varying in space and time, and (iv) the *state* which corresponds to the spatial distribution of the variable that is propagated by the dynamics. This representation is an overdetermined system, meaning if three components are perfectly known, the fourth can be calculated. This opens several possibilities to deal with possible lack of knowledge.

If the future state of the system is unknown, the *forward problem* is solved to forecast the state. This forecast is based on the assumption that the other components of the representation are perfectly known.

Differences between the forecasted state and eventually existing measurements hint at incomplete quantitative understanding of at least one of the other parts of the representation, e.g., the material properties. Historically, this motivated to approximate the state with available measurements and to solve the representation for the material properties. This procedure is known as *inverse problem*.

However, for the forecast to be accurate, even a perfect model requires a perfect initial state. This is particularly relevant for forecasting chaotic systems, i.e. the atmosphere or the ocean. These systems have rather well defined and accurately known material properties, i.e. density or viscosity of air and water, but their state is only sparsely covered with measurements and unknown to a large degree. Hence, the available measurements are incorporated into a modeled state. This procedure is known as *data assimilation*. In contrast to the inverse problem, data assimilation traditionally includes the estimation of the states but not the material properties. As the material properties typically are also uncertain, data assimilation methods have been extended to additionally allow for the estimation of material properties, e.g., using a generalized state that augments the original state with the material parameters (*augmented state*).

However, generally all components of the representation are only incompletely known and connected with uncertainties. The derivation of a consistent representation which aggregates all available information is the goal of *knowledge fusion*. This concept is explained in more detail by Bauser et al. (2016). The properties of the different methods are sketched in Table 3.3.

For a mathematical description of these ideas, assume a model function f that predicts the state $\boldsymbol{\Psi}_{\text{mod}}$ depending on a priori knowledge of the state $\boldsymbol{\Psi}_{\text{prior}}$ and on the material parameters $\boldsymbol{p}$

$$\boldsymbol{\Psi}_{\text{mod}} =: f\left(\boldsymbol{\Psi}_{\text{prior}}, \boldsymbol{p}\right). \tag{3.71}$$

In general, the model, the initial state, and the material parameters are imperfect. Assuming the existence of a true state $\boldsymbol{\Psi}_{\text{true}}$, the error $\boldsymbol{\eta}_{\text{mod}}$ of the modeled state $\boldsymbol{\Psi}_{\text{mod}}$ is given by

$$\boldsymbol{\Psi}_{\text{true}} - \boldsymbol{\Psi}_{\text{mod}} =: \boldsymbol{\eta}_{\text{mod}}. \tag{3.72}$$

Further assume that there exists a generally nonlinear observation operator $\boldsymbol{H}_{\text{obs}}$ that maps from the state space to the observation space. Hence, the true state $\boldsymbol{\Psi}_{\text{true}}$ is mapped to the true measurement data $\boldsymbol{m}_{\text{true}}$ via

$$\boldsymbol{m}_{\text{true}} =: \boldsymbol{H}_{\text{obs}}\left(\boldsymbol{\Psi}_{\text{true}}\right). \tag{3.73}$$

The true measurement data $\boldsymbol{m}_{\text{true}}$ are not observable in reality. Instead, the observed data $\boldsymbol{m}_{\text{obs}}$ are disturbed with the observation error $\boldsymbol{\eta}_{\text{obs}}$ according to

$$\boldsymbol{m}_{\text{true}} - \boldsymbol{m}_{\text{obs}} =: \boldsymbol{\eta}_{\text{obs}}. \tag{3.74}$$

In order to compare the observed measurements $\boldsymbol{m}_{\text{obs}}$ with the modeled measurements, the latter are approximated with $\widetilde{\boldsymbol{m}}_{\text{obs}}$ (approximations are denoted with $\widetilde{\ }$) using the

Table 3.3 The representation of a system is defined by Bauser et al. (2016) as a set consisting of the dynamics, the forcing, the subscale physics, and the state. This set is overdetermined. Hence, if three components are perfectly known (✓) and the fourth one is perfectly unknown (✗), the forth component can be calculated. The solution of the forward problem of a system, e.g., a thread pendulum, describes the forecast the states of the system, e.g., the position of the pendulum over time. The state can also be approximated with measurement data. This allows to calculate the material properties, e.g., the thread length or the mass, by solving the *inverse problem*. *Data assimilation* methods are traditionally applied for chaotic systems where the correct knowledge of the states is typically more important than the material properties. Instead of assuming that the states and the material properties are completely known or completely unknown, data assimilation methods work with uncertain prior knowledge (?). In general, the prior knowledge for all the components of the representation is uncertain. Thus, the concept of *knowledge fusion* is aiming at a consistent representation of the system (Bauser et al., 2016)

	forward problem	inverse problem	data assimilation	knowledge fusion
dynamics	✓	✓	✓	?
forcing	✓	✓	✓	?
subscale physics	✓	✗	✓/?	?
state	✗	✓	?	?

observation operator $\boldsymbol{H}_{\text{obs}}$, the model f, the a priori knowledge $\boldsymbol{\Psi}_{\text{prior}}$, the material parameters $\boldsymbol{p}$, as well as the expected errors $\widetilde{\boldsymbol{\eta}}_{\text{mod}}$ and $\widetilde{\boldsymbol{\eta}}_{\text{obs}}$:

$$\begin{aligned}
\widetilde{\boldsymbol{m}}_{\text{obs}} &= \widetilde{\boldsymbol{m}}_{\text{true}} - \widetilde{\boldsymbol{\eta}}_{\text{obs}} && (3.75)\\
&= \boldsymbol{H}_{\text{obs}}\left(\widetilde{\boldsymbol{\Psi}}_{\text{true}}\right) - \widetilde{\boldsymbol{\eta}}_{\text{obs}} && (3.76)\\
&= \boldsymbol{H}_{\text{obs}}\left(f\left(\boldsymbol{\Psi}_{\text{prior}}, \boldsymbol{p}\right) + \widetilde{\boldsymbol{\eta}}_{\text{mod}}\right) - \widetilde{\boldsymbol{\eta}}_{\text{obs}} && (3.77)\\
&=: g\left(\boldsymbol{\Psi}_{\text{prior}}, \boldsymbol{p}\right) + \boldsymbol{\eta}_{\text{total}}. && (3.78)
\end{aligned}$$

In order to simplify the notation, the function g and the total error $\boldsymbol{\eta}_{\text{total}}$ are introduced. Generally, the goal of optimization methods is to estimate the optimal $\boldsymbol{\Psi}_{\text{prior}}$ and $\boldsymbol{p}$ that minimize the difference between the modeled $g\left(\boldsymbol{\Psi}_{\text{prior}}, \boldsymbol{p}\right)$ and the observed data $\boldsymbol{m}_{\text{obs}}$.

Subsequently, it is assumed that the model function g exclusively depends on the parameters $\boldsymbol{p}$. Additionally, the observed data $\boldsymbol{m}_{\text{obs}}$ are referred to as measured data or measurement data $\boldsymbol{m}$ in the remainder of the thesis. For simplicity, it is also assumed that the state $\boldsymbol{\Psi}$ describes the spatial as well as the temporal distribution of the state variable. Consequently, it is also assumed that the measured data $\boldsymbol{m}$ include their temporal distribution.

3.5.1 Bayes' theorem

The search for optimal the material parameters $\boldsymbol{p}$ is typically based on Bayes' theorem (Tarantola, 2005, p. 15ff)

$$P(\boldsymbol{p}, \boldsymbol{m}) = P(\boldsymbol{p}|\boldsymbol{m})\ P(\boldsymbol{m}) = P(\boldsymbol{m}|\boldsymbol{p})\ P(\boldsymbol{p}), \tag{3.79}$$

with the posterior probability distribution $P(\boldsymbol{p}|\boldsymbol{m})$ assessing the probability of the parameters $\boldsymbol{p}$ given the measurements $\boldsymbol{m}$, the probability distribution of the measurements $P(\boldsymbol{m})$, the observation probability distribution $P(\boldsymbol{m}|\boldsymbol{p})$ assessing the probability of the measurements $\boldsymbol{m}$ given the parameters $\boldsymbol{p}$, and the model prior probability distribution $P(\boldsymbol{p})$ assessing the probability of the parameters $\boldsymbol{p}$. Rearranging Eq. 3.79 for the posterior probability distribution yields

$$P(\boldsymbol{p}|\boldsymbol{m}) = \frac{P(\boldsymbol{m}|\boldsymbol{p})\ P(\boldsymbol{p})}{P(\boldsymbol{m})}. \tag{3.80}$$

Typically, $P(\boldsymbol{m})$ is unknown but constant $P(\boldsymbol{m}) = \int \mathrm{d}\boldsymbol{p}\ P(\boldsymbol{m}, \boldsymbol{p}) = \int \mathrm{d}\boldsymbol{p}\ P(\boldsymbol{m}|\boldsymbol{p})\ P(\boldsymbol{p})$. Hence, the most likely parameters $\boldsymbol{p}$ are those that maximize $P(\boldsymbol{p}|\boldsymbol{m})$. To solve this maximization problem, the *likelihood* $P(\boldsymbol{m}|\boldsymbol{p})$ and the *prior* $P(\boldsymbol{p})$ have to be specified. This is analyzed subsequently for two examples following Tarantola (2005, p. 35f).

Gaussian model and measurement error together with a uniform prior Assuming a Gaussian distribution for the combined model and measurement error yields

$$P(\boldsymbol{m}|\boldsymbol{p}) \propto \exp\left(-\frac{1}{2}(\boldsymbol{m}-g(\boldsymbol{p}))^\top \boldsymbol{C}_{\text{total}}^{-1}(\boldsymbol{m}-g(\boldsymbol{p}))\right), \tag{3.81}$$

with the covariance matrix $\boldsymbol{C}_{\text{total}}$, representing the combined error $\boldsymbol{\eta}_{\text{total}}$. A uniform distribution for the model prior

$$P(\boldsymbol{p}) = \begin{cases} \text{const} & \text{if } \boldsymbol{p} \in [\boldsymbol{p}_{\min}, \boldsymbol{p}_{\max}] \\ 0 & \text{otherwise,} \end{cases} \tag{3.82}$$

bounds the parameter space and adds a constant to the Bayes' theorem (Eq. 3.80). Hence, this yields the *sum of squares*

$$P(\boldsymbol{p}|\boldsymbol{m}) \propto \exp\left(-\frac{1}{2}(\boldsymbol{m}-g(\boldsymbol{p}))^\top \boldsymbol{C}_{\text{total}}^{-1}(\boldsymbol{m}-g(\boldsymbol{p}))\right). \tag{3.83}$$

Maximizing the likelihood is equal to minimizing the *cost function*

$$S(\boldsymbol{p}) \coloneqq \frac{1}{2}(\boldsymbol{m}-g(\boldsymbol{p}))^\top \boldsymbol{C}_{\text{total}}^{-1}(\boldsymbol{m}-g(\boldsymbol{p})). \tag{3.84}$$

Gaussian model and measurement error together with a Gaussian prior Assuming a Gaussian distribution for the combined model and measurement error, yields Eq. 3.81. Together with a Gaussian model prior distribution centered at the parameters representing the prior knowledge $\boldsymbol{p}_{\text{prior}}$

$$P(\boldsymbol{p}) \propto \exp\left(-\frac{1}{2}(\boldsymbol{p}-\boldsymbol{p}_{\text{prior}})^\top \boldsymbol{C}_{\text{prior}}^{-1}(\boldsymbol{p}-\boldsymbol{p}_{\text{prior}})\right), \tag{3.85}$$

with the covariance matrix $\boldsymbol{C}_{\text{prior}}$ representing the error of the prior parameters, insertion in Bayes' theorem (Eq. 3.80) yields

$$P(\boldsymbol{p}|\boldsymbol{m}) \propto \exp\left(-\frac{1}{2}\left((\boldsymbol{m}-g(\boldsymbol{p}))^\top \boldsymbol{C}_{\text{total}}^{-1}(\boldsymbol{m}-g(\boldsymbol{p})) + (\boldsymbol{p}-\boldsymbol{p}_{\text{prior}})^\top \boldsymbol{C}_{\text{prior}}^{-1}(\boldsymbol{p}-\boldsymbol{p}_{\text{prior}})\right)\right). \tag{3.86}$$

This corresponds to the cost function

$$S(\boldsymbol{p}) \coloneqq \frac{1}{2}\left((\boldsymbol{m}-g(\boldsymbol{p}))^\top \boldsymbol{C}_{\text{total}}^{-1}(\boldsymbol{m}-g(\boldsymbol{p})) + (\boldsymbol{p}-\boldsymbol{p}_{\text{prior}})^\top \boldsymbol{C}_{\text{prior}}^{-1}(\boldsymbol{p}-\boldsymbol{p}_{\text{prior}})\right) \tag{3.87}$$

3.5.2 Inversion

In this study, optimization methods are used to estimate optimal parameters by minimizing the cost function (Eq. 3.84). The combined model and observation error is described with $\boldsymbol{\eta}_{\text{total}}$. It is assumed that this error can be retrieved from a normal distribution

with zero mean and standard deviation $\boldsymbol{\sigma}$. Thus, the entries of $\boldsymbol{\eta}_{\text{total}}$ are assumed to be uncorrelated. This corresponds to the assumption of a diagonal $\boldsymbol{C}_{\text{total}}$ matrix with the entries $\boldsymbol{\sigma}$ on the diagonal. According to this assumption, the cost function (Eq. 3.84) yields

$$S(\boldsymbol{p}) = \frac{1}{2} \sum_{i_{\text{meas}}=1}^{N_{\text{m}}} \left(\frac{m_{i_{\text{meas}}} - g(\boldsymbol{p})}{\sigma_{i_{\text{meas}}}} \right)^2 = \frac{1}{2} \sum_{i_{\text{meas}}=1}^{N_{\text{m}}} r_{i_{\text{meas}}}^2(\boldsymbol{p}) \tag{3.88}$$

with the model value $g(\boldsymbol{p})$ and the residuals $\boldsymbol{r}$.

The χ^2 distribution describes the sum of N squares of normally distributed quantities that are normalized to their unit variance (Press, 2007, p. 778). Hence, the χ^2 approaches the normal distribution for $N \to \infty$ according to the central limit theorem. Hence, $S(\boldsymbol{p}) = \frac{1}{2}\chi^2(\boldsymbol{p})$ holds for the given assumptions if the number of measurements is large. For models that are linear in $\boldsymbol{p}$, χ^2 may be used as a measure of the *goodness-of-fit* (Press, 2007, p. 776ff).

3.5.2.1 Levenberg–Marquardt

In this work, the Levenberg–Marquardt algorithm is the main tool for parameter estimation. It was implemented following Moré (1978), Press (2007, p. 799ff), and Transtrum and Sethna (2012) together with some further modifications.

The residuals in Eq. 3.88 can be expanded

$$r_{i_{\text{meas}}}(\boldsymbol{p} + \delta\boldsymbol{p}) \approx r_{i_{\text{meas}}}(\boldsymbol{p}) + \sum_{i_{\text{param}}=1}^{N_{\text{param}}} J_{i_{\text{meas}} i_{\text{param}}} \delta p_{i_{\text{param}}} \tag{3.89}$$

with the Jacobian matrix $J_{i_{\text{meas}} i_{\text{param}}} = \partial r_{i_{\text{meas}}} / \partial p_{i_{\text{param}}}$. The Jacobian matrix is assembled numerically with the finite-differences method.

Following Press (2007, p. 800f), the Hessian is approximated as $\boldsymbol{H} \approx \boldsymbol{J}^\top \boldsymbol{J}$, assuming that the second term in the derivative cancels out as $g(\boldsymbol{p}) \to m_{i_{\text{meas}}}$ with increasing number of iterations. For the Gauss–Newton algorithm then follows

$$\delta\boldsymbol{p} = -(\boldsymbol{J}^\top \boldsymbol{J})^{-1} \cdot \nabla S(\boldsymbol{p}). \tag{3.90}$$

Since $\boldsymbol{J}^\top \boldsymbol{J}$ does not always have full rank, the inversion may be ill-conditioned leading to uncontrolled large steps. One possibility to cope with this issue, is to regularize $\boldsymbol{J}^\top \boldsymbol{J}$ by adding a diagonal damping matrix $\boldsymbol{D}^\top \boldsymbol{D}$. This implementation follows Transtrum and Sethna (2012) by choosing the damping matrix, such that the diagonal entry for $p_{i_{\text{param}}}$ contains the corresponding maximal diagonal entry of $\boldsymbol{J}^\top \boldsymbol{J}$ from all previous iterations if this value is larger than a predefined minimal value (1.0) which is used otherwise. The resulting damping matrix is scaled with a parameter λ_{LM} which tunes both the amount of regularization and the step size of the parameter update. Hence, the parameter update $\delta\boldsymbol{p}$ is calculated via

$$\delta\boldsymbol{p} = -(\boldsymbol{J}^\top \boldsymbol{J} + \lambda_{\text{LM}} \cdot \boldsymbol{D}^\top \boldsymbol{D})^{-1} \cdot \nabla S(\boldsymbol{p}), \tag{3.91}$$

where the linear problem is solved with a singular value decomposition (SVD). If the condition number of the sensitivity matrix $\boldsymbol{S} = \boldsymbol{J}^\top \boldsymbol{J} + \lambda_{\mathrm{LM}} \cdot \boldsymbol{D}^\top \boldsymbol{D}$ is larger than a threshold (10^{12}), the linear problem is solved approximately with the conjugate-gradient algorithm by choosing the maximal number of iterations smaller than the number of parameters N_{param}. The proposed parameters at iteration i_{iter} are given as

$$\boldsymbol{p}^{i_{\mathrm{iter}}+1} = \boldsymbol{p}^{i_{\mathrm{iter}}} + \delta \boldsymbol{p}^{i_{\mathrm{iter}}}. \tag{3.92}$$

The convergence path of the Levenberg–Marquardt algorithm is influenced by both the initial size of the scaling parameter λ_{LM} and the choice how to adapt λ_{LM} after each iteration. Unless stated differently, the initial value for λ_{LM} is chosen as 5.0 and the *delayed gratification* strategy proposed by Transtrum and Sethna (2012) is applied. According to this strategy, λ_{LM} is decreased by a previously chosen factor (2.0) if the parameter update is successful and increased by a larger factor (3.0) if the update is not successful.

3.5.2.2 Simulated annealing

The simulated annealing algorithm (Press, 2007) yields relatively cheap improvements of the cost function (Eq. 3.88), because this algorithm is gradient-free and updates the parameters randomly. Hence, the algorithm is in particular suitable to be used in combination with the Levenberg–Marquardt algorithm which is more efficient close to the minimum.

If the parameter update is drawn from the whole parameter space, the algorithm is globally convergent. However, this approach is typically inefficient. Therefore, in this work, merely the neighborhood of the current parameters is searched for better parameters. Additionally, in order to investigate the existence of local minima, the algorithm can be applied for an ensemble of Latin hypercube sampled initial parameters $p_{i_{\mathrm{param}},0}$.

For each iteration i_{iter} $(1, \ldots, N_{\mathrm{i}})$, new parameters are proposed randomly via

$$p_{i_{\mathrm{param}},i_{\mathrm{iter}}+1} = p_{i_{\mathrm{param}},i_{\mathrm{iter}}} + m_{\mathrm{SA}} \cdot (p_{i_{\mathrm{param}},\mathrm{max}} - p_{i_{\mathrm{param}},\mathrm{min}}) \cdot u_{\mathrm{p}}, \tag{3.93}$$

with a mobility parameter $m_{\mathrm{SA}} = 0.1$, uniformly distributed random number $u_{\mathrm{p}} \sim \mathcal{U}(-1, 1)$, and the parameter limits $p_{i_{\mathrm{param}},\mathrm{max}}$ and $p_{i_{\mathrm{param}},\mathrm{min}}$. In order provide the control parameter T_{SA}, which is an analog of temperature, an exponential cooling schedule is chosen

$$T_{\mathrm{SA}i_{\mathrm{iter}}+1} = T_{\mathrm{SA}0} \cdot {\alpha_{\mathrm{SA}}}^{i_{\mathrm{iter}}+1}, \tag{3.94}$$

with $\alpha_{\mathrm{SA}} = 0.85$ and initial temperature $T_{\mathrm{SA}0} = 10^3$ which is of the order of the initial cost function value. According to Metropolis et al. (1953), a uniformly distributed random number $u_{\mathrm{d}} \sim \mathcal{U}(0, 1)$ is drawn to calculate the acceptance probability

$$P_{i_{\mathrm{iter}}+1} = \exp\left(-\frac{S(\boldsymbol{p}_{i_{\mathrm{iter}}+1}) - S(\boldsymbol{p}_{i_{\mathrm{iter}}})}{k_{\mathrm{SA}} \cdot T_{\mathrm{SA}i_{\mathrm{iter}}+1}} \right), \tag{3.95}$$

choosing parameter $k_{\mathrm{SA}} = 1$. The proposed parameter set is accepted if $P_{i_{\mathrm{iter}}+1} > u_{\mathrm{d}}$, else a new parameter set is drawn.

3.6 Implementation

For the estimation of soil hydraulic material properties based on hydrogeophysical measurements, the soil hydraulics and hydrogeophysics inversion package (SHIP) was developed within the framework of this PhD-project. Since the results in this thesis are based on this software package, the SHIP is shortly presented in this section.

3.6.1 Motivation

The motivation to develop this software package was the idea to be able to use different optimization algorithms, such as the fast Levenberg–Marquardt algorithm (Sect. 3.5.2.1), the globally convergent shuffled complex evolution developed at the University of Arizona (SCE-UA) proposed by Duan et al. (1992), the popular simulated annealing (Sect. 3.5.2.2) algorithm, and even data assimilation algorithms, such as the ensemble Kalman filter (EnKF) for soil-hydraulic and hydrogeophysical systems. Therefore, it should be easy to change the forward model and to couple it with the different optimization algorithms. On top of that, the application of the software should be simple to alleviate the entrance into the research field as well as the application by students in lectures and practical courses.

3.6.2 Structure

The SHIP consists of a number of software packages, including muPhi (Sect. 3.1.6) and MEEPGPR (Sect. 3.2.3.2). In order to link muPhi and MEEPGPR and to use them in optimization algorithms, these software packages where forked and adapted. The data handling and the optimization algorithms are implemented within a *Optimization* package. This package is written in an object-oriented way using C++ and comprises three parts, namely (i) model, (ii) measurements, and (iii) optimization. The model part is responsible for preparing and running the forward model as well as for the post-processing of the simulated data. The measurements part mainly stores the measurements and provides an interface to the model and the optimization. The optimization part uses model and measurements objects to estimate the parameters. Each part has its own namespace and is constructed in a hierarchical manner using inheritance. The optimization part takes advantage of function overloading and templates in order to deal with different types of models and measurements.

The Optimization package can be used in three different parallel modes, where (i) the Jacobian matrix of the Levenberg–Marquardt algorithm is assembled in parallel, (ii) MEEPGPR is run in parallel, or (iii) an ensemble of sequential instantiations of the program is run in parallel. These parallel implementations were realized with OpenMPI.

For the analysis of GPR data as described in Sect. 6.2.1, the package ProcessGPR was developed. Since this package is based on the *Constructive Inversion* software provided by Buchner et al. (2012), it uses Matlab and Gnu Octave.

3.6.3 Data assimilation

Although SHIP focusses on inversion, an intermediate version also included an implementation of the EnKF. This implementation was developed further, made operational, and successfully applied by Bauser et al. (2016). With the development of another software, that particularly focusses on data assimilation methods and that is mainly developed in our workgroup by Daniel Berg, this software was interfaced to the SHIP and vice versa. Afterwards, the EnKF version implemented in the SHIP was dropped.

3.6.4 Application

The SHIP is tested on macOS 10.13, ubuntu 16.04, and on the bwforcluster. It is used for (i) a number of publications (Klenk et al., 2015a; Bauser et al., 2016; Jaumann and Roth, 2017; Pan et al., 2017; Jaumann and Roth, 2018), (ii) other PhD projects in our workgroup (Hannes Bauser, Daniel Berg, Lisa Hantschel, and Sven Peyinghaus), and (iii) for master and bachelor projects in our workgroup. Additionally, it was used for teaching in the Modeling Terrestrial Systems lecture and for the F53 practical course.

3.6.5 Simple model

Adding a simple two dimensional model to the SHIP allows to visualize the iterations of the optimization algorithms leading to an intuitive understanding of the implemented optimization algorithms. Thus, the algorithms can be tested and improved easily, as their task is to find the minimum of a surface. This requires the surface to be easily changeable. Thus, the surface was parameterized according to

$$\begin{aligned} f(x,y) = p_0 &+ p_1(p_2+x)^2 + p_3(p_4+y)^2 \\ &+ p_5(\sin(p_6\pi x)) + p_7(\cos(p_8\pi x)) \\ &+ p_9(\sin(p_{10}\pi y)) + p_{11}(\cos(p_{12}\pi y)), \end{aligned} \tag{3.96}$$

using 13 parameters. Thus, this function has essentially a parabolic shape with smooth oscillations in both dimensions creating (i) a large number of local minima and (ii)

continuously changing gradients due to the sinusoid functions. Hence, gradient-based algorithms typically converge to different minima when the initial position is changed. The application of the different algorithms implemented in SHIP is shortly presented subsequently. The parameters for the surface used in this section are given in Table 3.4.

3.6.5.1 Levenberg–Marquardt

Since the Levenberg–Marquardt algorithm is a combination of the Gauss–Newton algorithm and the steepest-descent algorithm (Sect. 3.5.2.1), it is a relatively fast gradient-based algorithm if the cost function is convex and has only one minimum. Hence, this is a quite popular algorithm. However, if the cost function has different local minima, the algorithm is very likely to converge to a local minimum.

As the simple model has a very low dimensionality and computation time, the implications adjusting, e.g., λ_{LM} or $\boldsymbol{D}$, can be studied easily. Most importantly, the larger λ_{LM}, the smaller the step size and the more of the steepest-descent algorithm is used which is according to Eq. 3.91. Hence, the choice of the parameter λ_{LM} is suitable to balance performance and stability of the algorithm. In this case, λ_{LM} is initially set to 2 and decreased (increased) by a factor of 1.5, if the iteration was successful (unsuccessful).

Starting at the initial position $x_0 = 4.0$, $y_0 = -4.0$, the algorithm approximately finds the global minimum after 19 iterations (Fig. 3.33). As the residuum does not improve afterwards, the algorithm increases λ_{LM} to take ever smaller steps. The breaking conditions comprise in particular an absolute and a relative limit for the improvement of the residuum. These conditions are set close to double precision in this case. Note that due to the sinusoid functions in Eq. 3.96, even a small change in the initial position may result in converging to a different minimum.

3.6.5.2 Residuum scanner

The residuum scanner simply evaluates the cost function equidistantly in each dimension. This algorithm was mainly implemented as an educational tool to showcase the *curse of dimensions* which is illustrated subsequently.

Table 3.4 These parameters are inserted in Eq. 3.96 in order to generate a surface which is employed in this section to discuss the convergence properties of the optimization algorithms implemented in SHIP.

parameter	p_0	p_1	p_2	p_3	p_4	p_5	p_6	p_7	p_8	p_9	p_{10}	p_{11}	p_{12}
value	5.0	2.0	1.0	2.0	−2.0	1.0	1.0	−2.0	1.0	1.0	1.0	−2.0	1.0

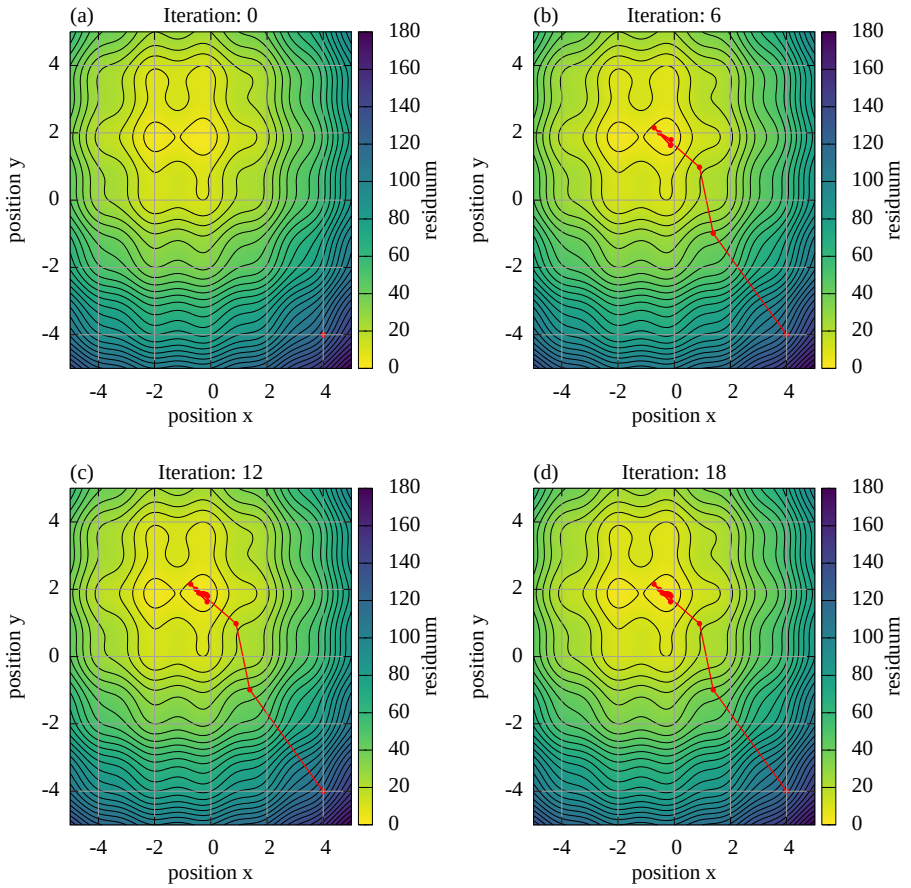

Figure 3.33 For the given initial parameter set, the Levenberg–Marquardt algorithm rapidly converges close to the global minimum. Note (i) that the step size of a single iteration depends in particular on λ_{LM} and (ii) that the algorithm requires many steps to converge although it is already close to the global minimum.

The total number of evaluations of the cost function required by this algorithm is given by

$$N_{\mathrm{eval}} = (N_{\mathrm{epp}})^{N_{\mathrm{param}}}\,, \tag{3.97}$$

with N_{epp} evaluations per parameter and N_{param} parameters. In the given case, for $N_{\mathrm{epp}} = 40$ and $N_{\mathrm{param}} = 2$, the algorithm requires 1600 evaluations of the cost function (Fig. 3.97).

In order to illustrate this further, assume an optimization problem with 18 parameters, i.e. the estimation of 6 soil hydraulic material parameters for 3 materials that is to be solved with $N_{\mathrm{epp}} = 10$ evaluations per parameter. Further assume that each evaluation of the cost function takes 10 s. In total, this corresponds to 10^{19} s computation time on a single processor.

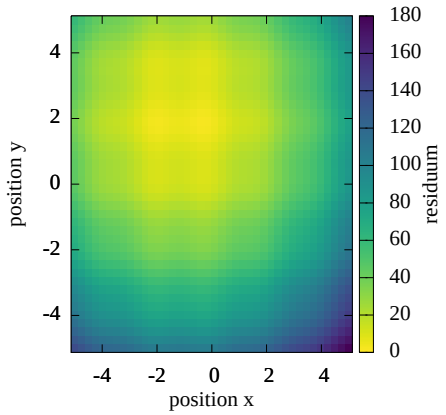

Figure 3.34 The residuum scanner simply iterates over a two dimensional subspace of the parameter space, evaluates the cost function at each iteration and stores the results. This algorithm was mainly implemented to showcase the *curse of dimensions*.

In the literature (e.g., Lambot et al., 2006; Jadoon et al., 2008; Huisman et al., 2010; Jonard et al., 2015), sometimes 2D maps of the cost function are presented for more than two parameters. To this end, the other parameters have to be fixed to some value. Thus, the resulting surface is a projection and does not represent the full dimensionality of the problem at hand, except for synthetic studies where the remaining parameters are set to the true values.

Note that the steepest-descent algorithm (brute force gradient search) and residuum scanner (brute force sampling) are two extremes in the spectrum of optimization algorithms. There exists a multitude of optimization algorithms which use a combination of *clever* parameter sampling and gradient information.

3.6.5.3 Simulated annealing

The simulated annealing algorithm as presented in Sect. 3.5.2.2 does not require any gradient information, since it updates the parameters using a random walk in the neighborhood of the current parameter set. It accepts every parameter set with a smaller residuum. Additionally, there is a low probability that the algorithm also accepts parameter sets with a higher residuum. The implemented neighborhood search increases the performance but also the probability for local convergence.

Assuming a convex parabolic surface with a global minimum at the origin, it can be shown geometrically that the probability for improvement is > 0.28 using a search radius r_1 at a point with the distance r_2 from the global minimum if $r_1 = r_2$. Decreasing the search radius r_1 increases the probability for the improvement to < 0.50 for $r_1 \ll r_2$. Hence, the closer the parameter set is to the minimum, the smaller the search radius

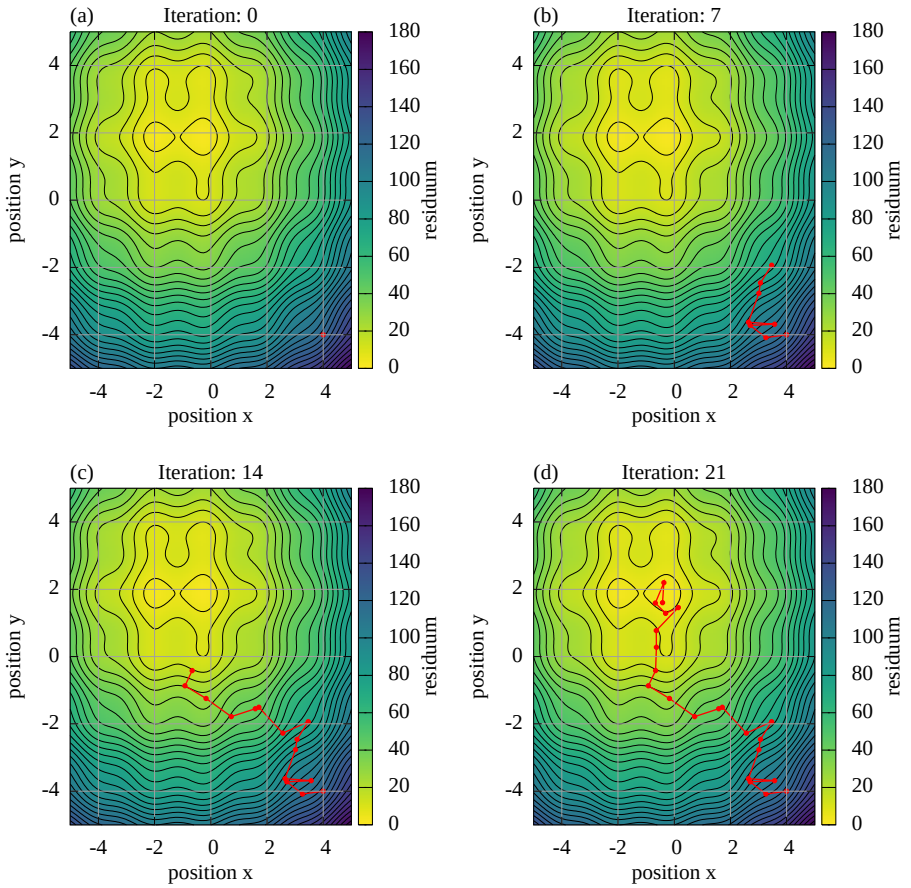

Figure 3.35 The simulated annealing algorithm is a gradient-free optimization algorithm. It updates the parameters using a random walk in the neighborhood. Together with all parameter sets that improve the residuum, the algorithm may also accept parameter sets with a higher residuum.

should be for a parabolic surface. However, this also increases the probability of local convergence.

For the investigated case (Table 3.4), the algorithm is initialized at $x_0 = 4.0$, $y_0 = -4.0$. The resulting path is given in (Fig. 3.35) for 21 successful iterations. The algorithm breaks after 200 evaluations of the cost function. The final improvement was detected at iteration 175. For the sake of decreasing the probability of local convergence, the search radius is not decreased with the number of iterations. Thus, the algorithm is rather inefficient near the optimal parameter set.

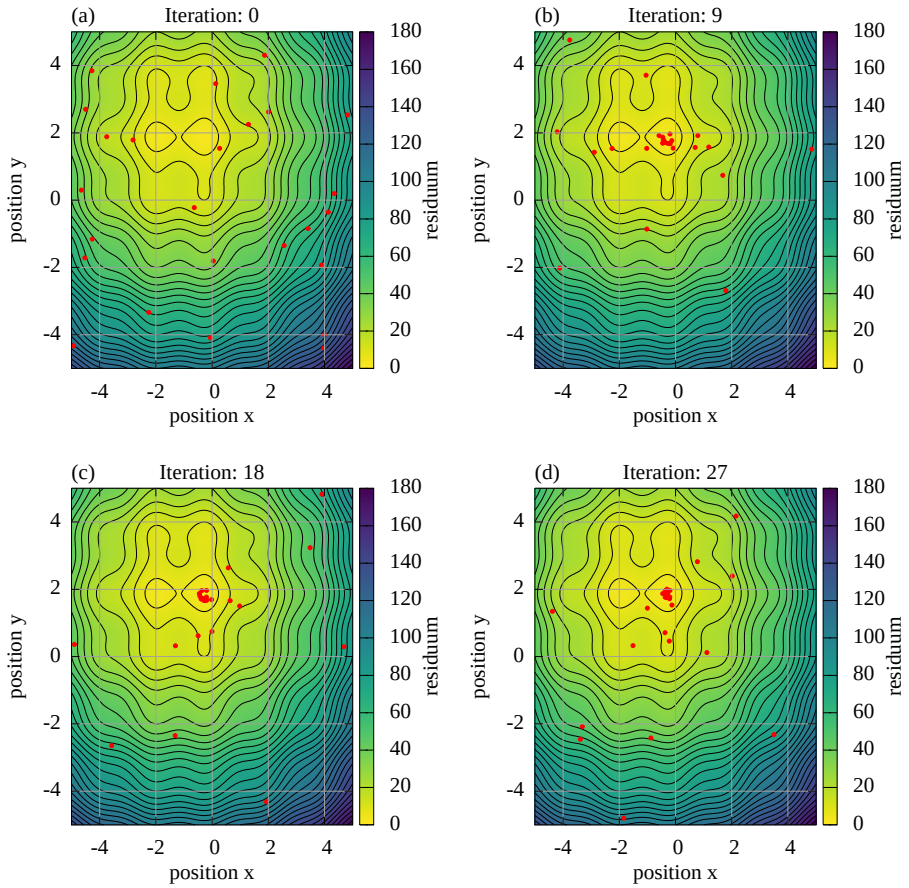

Figure 3.36 The SCE-UA algorithm is based on an ensemble that is divided into different complexes that contain ensemble members with high and low residuals. The algorithm focusses on the improvement of the worst ensemble member in each complex. Note that (i) the ensemble members group closely to the global optimum with increasing number of iteration and (ii) for each iteration there are ensemble members that are sampling the rest of the parameter space.

3.6.5.4 Shuffled complex evolution

Since the SCE-UA algorithm is not used in the application part of this thesis (Sects. 5–6), it is not introduced in Sect. 3.5.2 but sketched subsequently. The SCE-UA algorithm was proposed by Duan et al. (1992) and is an optimization method that is likely to converge globally but also uses gradient information concerning the residuum of ensemble members.

The algorithm comprises six steps: (i) generate an ensemble of random parameter sets (ensemble members), (ii) divide the ensemble in a number of different complexes (groups of ensemble members), (iii) improve the worst member in each complex using the reflection point or the contraction point with respect to the centroid of all the members in the complex (if this does not improve the member, draw a random parameter that does),

(iv) sort all the members of the ensemble according to their residuum, (v) shuffle the complexes (fill the complexes such that ensemble members with high and low residuals are included), (vi) complete the iteration by going to (iii).

Since the algorithm focuses on improving the worst ensemble member instead of the best, it is rather conservative. This increases the probability of global convergence, especially, if the number of local minima is low. For problems with a low number of local minima and a large number of parameters, this algorithm is not very efficient, especially in cases where step (iii) fails and random parameters are drawn from the whole parameter space to improve the worst member of the complex.

For the investigated case (Table 3.4), the ensemble was initialized with random positions, except for the initial position $x_0 = 4.0$, $y_0 = -4.0$. The algorithm uses 5 complexes, 25 ensemble members, and step (iii) is done twice per iteration. The ensemble is shown in Fig. 3.36 for four specific iterations. The number of ensemble members near the global minimum increases with the number of iterations. The drawing random parameters evaluates the remaining parameter space searching for better minima. Note that this algorithm can provide an estimation for the maximum likelihood distribution close to the global minimum.

Table 3.5 Different optimization algorithms are implemented in the SHIP (Levenberg–Marquardt algorithm (LM), residuum-scanner (RS), simulated annealing (SA), and shuffled complex evolution (SCE-UA)). These algorithms are used to analyze a surface created by the simple model (Eq. 3.96) with the parameters given in Table 3.4. Except for the residuum-scanner, these algorithms are applied to search for the minimum of the surface with a single run starting at the initial position $x_0 = 4.0$, $y_0 = -4.0$. Note that the breaking conditions (i) influence the number of required evaluation and (ii) are different for each algorithm. Hence, the suitability of the given number of evaluations to draw conclusions about the performance of these algorithms is limited. It is additionally emphasized that (i) the results of single runs of the Levenberg–Marquardt algorithm and the simulated annealing algorithm naturally depend on the initial position and (ii) the results of single runs of the simulated annealing algorithm and the SCE-UA depend on the particular random numbers drawn.
The comparison of the results shows that for the given initial position and breaking conditions, the resulting position of all algorithms is close to the global minimum (truth). The parameter set found with the SCE-UA algorithm is slightly better than the one found with the Levenberg–Marquardt algorithm.

	LM	RS	SA	SCE-UA	truth
x	−0.282	−0.385	−0.289	−0.275	−0.282
y	1.866	1.923	2.029	1.880	1.875
S	1.793	1.944	2.093	1.793	1.792
evaluations	95	1600	200	6091	

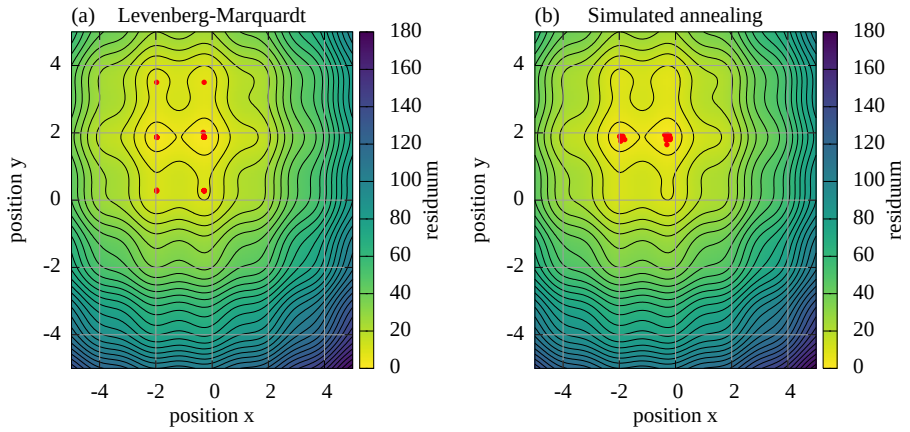

Figure 3.37 In order to increase the comparability of the algorithms, an ensemble of initial parameters was drawn with the Latin hypercube algorithm for the Levenberg–Marquardt algorithm and the simulated annealing algorithm, such that the number of total evaluations is comparable to the SCE-UA. The resulting parameters are shown for the Levenberg–Marquardt algorithm (a) and the simulated annealing algorithm (b). The Levenberg–Marquardt algorithm detects all major minima with a small variance of the resulting parameters due to the gradient search. As the parameter update of the simulated annealing algorithm or the SCE-UA include random improvement of the parameters, the variance of the resulting parameter is larger (Table 3.6).

3.6.5.5 Comparison

The results of a single run of each algorithm that was presented in the previous sections (Sects. 3.6.5.1–3.6.5.4) are compared in Table 3.5. The SCE-UA algorithm yields parameters which are slightly better than those resulting from the Levenberg–Marquardt algorithm. However, the mere comparison of the resulting parameters and the required number of evaluations is misleading, because it does not account for the balance between performance and stability. The Levenberg–Marquardt algorithm is locally convergent, hence it is focussing more on performance than on stability, whereas the SCE-UA is globally convergent and trades performance with stability.

In order to increase the comparability of the algorithms, the application of the Levenberg–Marquardt algorithm and the simulated annealing algorithm is extended in a next step by sampling an ensemble of initial parameters using the Latin hypercube algorithm, such that the total number of evaluations is similar to the number of evaluations required by the SCE-UA. The sampling algorithm was implemented with the help of the pyDOE package (`https://github.com/tisimst/pyDOE`). Due to the fast convergence of the Levenberg–Marquardt algorithm, this allows for 100 ensemble members, whereas one typical run of the simulated annealing algorithm is equaled to 200 evaluations. Thus, this allows for 30 ensemble members. The resulting parameters are given in Fig. 3.6 and in Table 3.6. Since the Levenberg–Marquardt algorithm is based on a gradient search, it (i) identifies all major local minima and (ii) localizes them precisely. Due to

the random neighborhood search, the simulated annealing algorithm does not converge to the minor local minima. However, the resulting parameters show a larger standard deviation. Note that for an increasing number of parameters, gradient search methods become more efficient than sampling methods due to the curse of dimensions.

In conclusion, the Levenberg–Marquardt algorithm provides an efficient and gradient-based solution with high risk of local convergence. This risk can be decreased by using an ensemble of initial parameters. Compared to the Levenberg–Marquardt algorithm, the simulated annealing algorithm has a smaller probability to converge to a local minimum and is in particular suitable, if the calculation of the gradient of the cost function is too expensive or even impossible. Its probability for global convergence can be controlled with the search width parameter m_{SA} (Eq. 3.93) and the number of evaluations. Starting these locally convergent algorithms from Latin hypercube sampled initial parameters allowed to determine the global minimum reasonably well. Note that the Latin hypercube sampled ensemble members do not share any information about the shape of the cost function during the optimization. In contrast, this information is used by the SCE-UA. Yet, its conservative parameter update strategy including randomly sampling the full parameter space is very stable but also comparably slow.

Table 3.6 Similar to the results presented in Table 3.5, the different optimization algorithms Levenberg–Marquardt algorithm (LM), simulated annealing (SA), and shuffled complex evolution (SCE-UA), are used to analyze a surface created by the simple model (Eq. 3.96) with the parameters given in Table 3.4. In this case, the Levenberg–Marquardt algorithm and the simulated annealing algorithm are initialized with an ensemble of initial parameter sets, such that the total number of evaluations is comparable to those required by the SCE-UA. The resulting parameters are shown in Fig. 3.37. Here, the mean and the standard deviation of the position are given together with the mean of the according cost for successful members with $S \leq 2$.

	LM	SA	SCE-UA	truth
x	-0.284 ± 0.003	-0.28 ± 0.05	-0.30 ± 0.07	-0.282
y	1.867 ± 0.004	1.87 ± 0.05	1.91 ± 0.06	1.875
S	1.793	1.86	1.91	1.792
successful members	40/100	20/30	4/25	
evaluations	6457	6000	6091	

4 Experiment

Over the course of the PhD-project, a number of fluctuating groundwater table and infiltration experiments have been realized at ASSESS (Sect. 2) in collaboration with Patrick Klenk. One of these experiments is analyzed in this thesis. For the analysis of further experiments, the reader is kindly referred to Klenk et al. (2014, 2015a,b). The experiment that serves as basis for this study is described subsequently.

The hydraulic state of ASSESS was forced with a fluctuating groundwater table by pumping water in and out of a groundwater well. The experiment was arranged in three different phases: (i) initial drainage phase, (ii) multistep imbibition phase, and (iii) multistep drainage phase. The detailed forcing is presented in Table 4.1. Throughout the forcing, equilibration steps were included in-between, such that the relaxation of the capillary fringe happened within the measurement volume of the TDR sensors where possible. The natural forcing at the top boundary, e.g., through evaporation, is neglected in the following, because the experiment took place at the end of November and the weather was cloudy with 2–7 °C air temperature. The last precipitation was measured approximately 10 days before the experiment.

The hydraulic potential was assessed via the position of the fluctuating groundwater table. This position was measured (i) manually in the groundwater well and (ii) automatically with the tensiometer (Fig. 4.1). The gradient between the hydraulic potential

Table 4.1 During the experiment, ASSESS was forced with a fluctuating groundwater table. Therefore, 17.8 m^3 of water were pumped in and 14.7 m^3 were pumped out of the groundwater well. For the calculation of the flux and equivalent height of the water column Δh_{eq}, the surface area of ASSESS was approximated with 80 m^2. All times are given in UTC.

phase	time start	time end	duration [min]	water volume [m^3]	flux [10^{-6} m s^{-1}]	Δh_{eq} [m]
initial drainage	12:55:00	13:20:00	25	−0.76	−6.4	−0.01
multistep imbibition	14:20:00	18:50:00	270	8.39	6.4	0.10
	20:35:00	23:10:00	155	4.78	6.4	0.06
	07:25:00	09:55:00	150	4.64	6.4	0.06
multistep drainage	12:35:00	14:00:00	85	−4.00	−9.8	−0.05
	15:00:00	16:10:00	70	−3.17	−9.4	−0.04
	16:40:00	19:15:00	155	−6.73	−9.0	−0.08

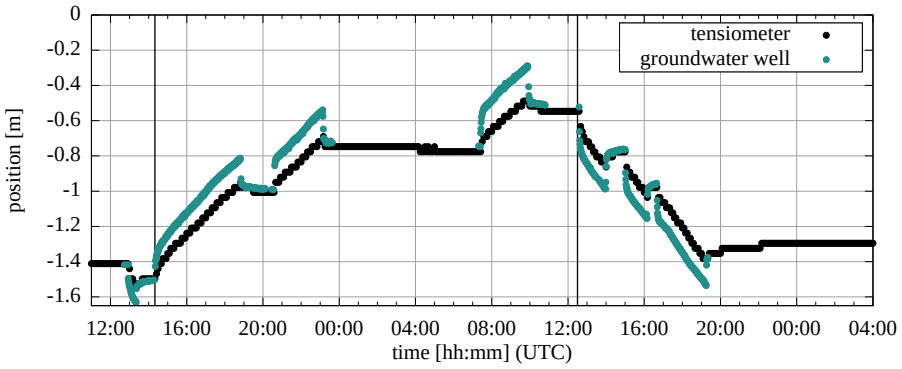

Figure 4.1 The position of the groundwater table was measured manually in the groundwater well and automatically with the tensiometer during three different phases (initial drainage, multistep imbibition, and multistep drainage – separated by the vertical black lines in the figure) of the experiment. Note that the discrete measurement steps reflect the resolution of the tensiometer.

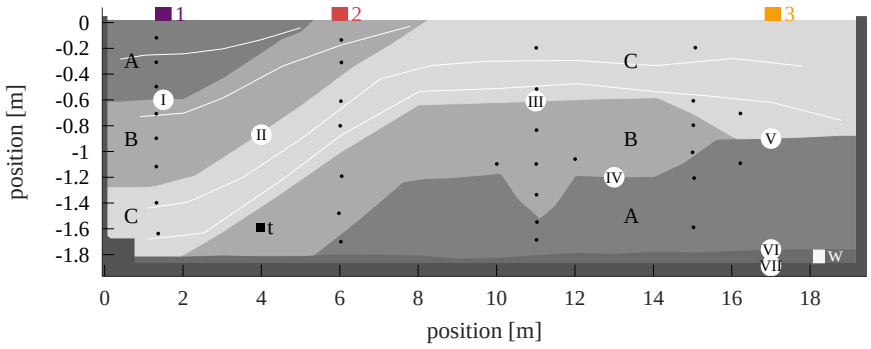

Figure 4.2 ASSESS emulates an effective 2D geometry with three distinct kinds of sand (A, B, and C). The hydraulic state can be manipulated with a groundwater well (white square at 18.3 m) and is monitored with three GPR antennas (1, 2, 3), a tensiometer (black square, at 4.0 m), and 32 TDR sensors (black dots). The gravel layer at the bottom ensures a rapid water pressure distribution over the site. An L-element (left wall, at 0.4 m) and compaction interfaces (white lines) were introduced during the construction. Additionally to those visualized, GPR evidence indicates additional compaction interfaces that were not determined during construction (Fig. 6.12). Roman numeral markers (I)–(VII) indicate material interfaces referred to in the text. Note the different scales on the horizontal and vertical axes.

in the groundwater well and the hydraulic potential in the test site drives the water flux. The largest part of this gradient equilibrates approximately within 5 minutes. Afterwards, the position of the groundwater table still changes which is due to the long-term equilibration of the hydraulic state.

The soil water content was monitored with TDR sensors at particular positions in ASSESS (Fig. 2.2). A mean soil temperature (T_s = 8.5 °C) and a mean electrical

conductivity ($\sigma = 0.003\ \mathrm{S\,m^{-1}}$) was estimated from TDR related measurements. The electrical conductivity was evaluated from the TDR pulse shape and thus includes the direct current conductivity as well as dielectric losses (Sect. 3.4.1). The acquired TDR data are shown and analyzed in more detail in Sect. 5.2.

The soil water content was also monitored with GPR measurements using three shielded bi-static single-channel 400 MHz antennas from Ingegneria dei Sistemi S.p.A., Italy (IDS). These antennas are referred to as antenna 1, 2, and 3, respectively. The measurement resolution was set to 2048 samples for 60 ns. In order to analyze the initial state of the test site, a multi-channel CO measurement was acquired with antennas 1 and 2. The internal separation of the transmitter and receiver of these antennas is 0.14 m. During the experiment, the antennas were used to measure three time-lapse radargrams. In this work, the data acquired with GPR antenna 3 (Fig. 4.2) are evaluated quantitatively Sect. 6.3.2.2.

5 Analysis of TDR data

The TDR data acquired during the fluctuating groundwater table experiment described in Sect. 4 is evaluated subsequently. Note that this section is essentially copied from Jaumann and Roth (2017).

5.1 Introduction

Soil hydraulic material properties are essential to advance quantitative understanding of soil water dynamics. Despite decades of research, direct identification of these properties is time-consuming and near to impossible at larger scales. Therefore, indirect identification methods, such as inversion (Hopmans et al., 2002; Vrugt et al., 2008a), have been successfully applied to evaluate experiments starting from lab-scale (e.g., Parker et al., 1985; Van Dam et al., 1994; Šimůnek et al., 1998; Schneider et al., 2006) up to field-scale studies (e.g., Wollschläger et al., 2009; Huisman et al., 2010).

Due to the multi-scale heterogeneity of the soil hydraulic material properties (Nielsen et al., 1973; Gelhar, 1986; Cushman, 1990; Vogel and Roth, 2003), effective material properties have to be identified directly at the scale of interest. Yet, most studies focus on 1D subsurface architectures with homogeneous layers, e.g., Abbaspour et al. (2000); Ritter et al. (2003); Mertens et al. (2006); Wöhling et al. (2008); Wollschläger et al. (2009).

Only a few studies, e.g., Abbasi et al. (2004); Palla et al. (2009); Huisman et al. (2010), estimate material properties of effectively 2D subsurface architectures. Abbasi et al. (2004) conducted an irrigation experiment to estimate soil hydraulic and solute transport properties for a 2D furrow architecture. Palla et al. (2009) estimated effective soil hydraulic properties for a 2D layered coarse grained green roof based on hydrographs. Huisman et al. (2010) estimated soil hydraulic properties of a homogeneous dike exploiting flat wire TDR and electrical resistance tomography (ERT) data recorded during a fluctuating groundwater table experiment.

With increasing computational power in recent years, 1D subsurface architectures were analyzed with ensemble-based parameter estimation methods reaching from Markov chain Monte Carlo (MCMC) (e.g., Vrugt et al., 2008b; Scharnagl et al., 2011; Wöhling and Vrugt, 2011) and data assimilation (e.g., Wu and Margulis, 2011; Li and Ren, 2011; Erdal et al., 2014) to data driven modeling (e.g., Over et al., 2015).

Most studies describe the given data with models chosen upfront with restricted complexity and a minimum number of parameters. If the models are too simple, critical

uncertainties and processes may be neglected, leading to suboptimal results. If the models are too complex, the resulting material properties are likely to be application-dependent. In general, the required model complexity is unknown a priori (Vereecken et al., 2015).

Quantitative learning about complicated systems is an iterative process (Gupta et al., 2008; Box et al., 2015). It starts from the current understanding of the system that is represented with a model (Clark et al., 2011; Gupta et al., 2012). The optimal experimental design is then based on the model and the resulting data are, figuratively speaking, answer of reality to the questions asked through the experiment. Disagreement between the model and the data reveals incorrect understanding of the system. Consequently, the concepts, decisions, and hypotheses integrated into the model (including evaluation procedures of the data) and the data themselves are revised. If the model predicts the data accurately and precisely enough, the research objectives are expanded, such that the data cover a larger part of the state space. Ultimately, this iterative procedure leads to data covering the whole state space and a statistical model-data mismatch corresponding to the data error model. In general, such data are not available and the application merely requires a limited accuracy and precision. Hence, the crux is to determine the sufficient complexity of both the model and the data for the required accuracy and precision.

This problem can be quantified with a Bayesian total error analysis (BATEA) (Kavetski et al., 2002, 2006) investigating the total uncertainty space which includes uncertainty in the observed input and responses as well as uncertainty in the model hypothesis. However, this analysis is computationally intensive if the number of uncertainties is large and required models may not be available, e.g., for hysteresis. For instance, Bauser et al. (2016) categorized the uncertainties a priori and estimated the most important ones along with effective material properties using an EnKF aiming for a consistent representation of reality. The temporal fluctuation of the estimated hydraulic parameters was used to identify a situation in which the representation of the dynamics is inconsistent. Hence, measurement data acquired during this period of time were merely used for state estimation and excluded from parameter estimation to prevent the incorporation of uncertainties in the dynamics into the estimated parameters.

In this study, the perspective is changed and the model is associated with the current quantitative understanding of reality that is tested against the given measurement data. The analysis of the required model complexity comprises three steps: (i) assume temporally constant material properties, (ii) calculate the maximum likelihood of increasingly complex models, (iii) and analyze the corresponding structural model-data mismatch. It is shown that this structural error analysis indicates limitations of these models and quantifies the effect of the respective unrepresented model errors on the inversely estimated material properties. This procedure is applied to measurement data acquired at ASSESS (Sect. 2) while it was forced with a fluctuating groundwater table which ensures a high dynamical range of the hydraulic state (Sect. 4). Therefore, first a basic representation accounting for uncertainties of the hydraulic material properties and the forcing is set up. Subsequently, shortcomings of this representation are investigated in an

uncertainty analysis. Then, in addition to the properties estimated in the basic representation, the model complexity is increased by additionally estimating the sensor position, the small-scale heterogeneity or both. These increasingly complex models are applied to (i) three 1D profiles in ASSESS with an increasing number of sensors per material and (ii) the full 2D profile to additionally analyze the implications of the restriction to a 1D subsurface architecture and to few sensors per material.

5.2 Data

The TDR measurement data that are evaluated in this study, were acquired in the fluctuating groundwater table experiment described in Sect. 4.

The water content data are based on the measured TDR traces which provide the relative permittivity of the soil bulk $\varepsilon_{\mathrm{r,b}}$ (Sect. 3.4.1). This permittivity is transferred to water content θ_{w} using the CRIM according to Sect. 3.3. Core samples of the materials A, B, and C acquired during the construction of ASSESS (Fig. 2.2). These samples provide the porosities 0.41, 0.36, and 0.38, respectively, which will be assumed for the saturated water content $\theta_{\mathrm{w,s}}$ of the respective materials in the remainder of this analysis.

The water content data of those TDR sensors that were desaturated during the experiment are displayed in Fig. 5.1. The data show that the experiment exhibits complicated flow phenomena. The measured water content increases fast during the imbibition steps as the groundwater table reaches the TDR sensor. This is due to the narrow transition zone of sandy materials during imbibition (Dagenbach et al., 2013; Klenk et al., 2015a) and the small measurement volume of the TDR sensors (Robinson et al., 2003). During the equilibration phases, for example after the last drainage phase (19:15), the measured water content in the unsaturated material either decreases (e.g., sensor 27) or increases (e.g., sensor 2), depending on the hydraulic state at this position with respect to static hydraulic equilibrium. This effect is used in the following evaluation (Sect. 5.5.1.3). The spread of the water content during saturation is mainly attributed to small-scale heterogeneity and quasi saturation due to entrapped air (Christiansen, 1944). In order to avoid effects related to entrapped air and also two-phase flow, all TDR data with an air content below 0.1 (Faybishenko, 1995) are neglected subsequently.

5.3 Methods

In addition to the methods sketched in Sect. 3, other methods have been used and developed by Jaumann and Roth (2017) specifically for the evaluation of TDR data. These methods are outlined subsequently.

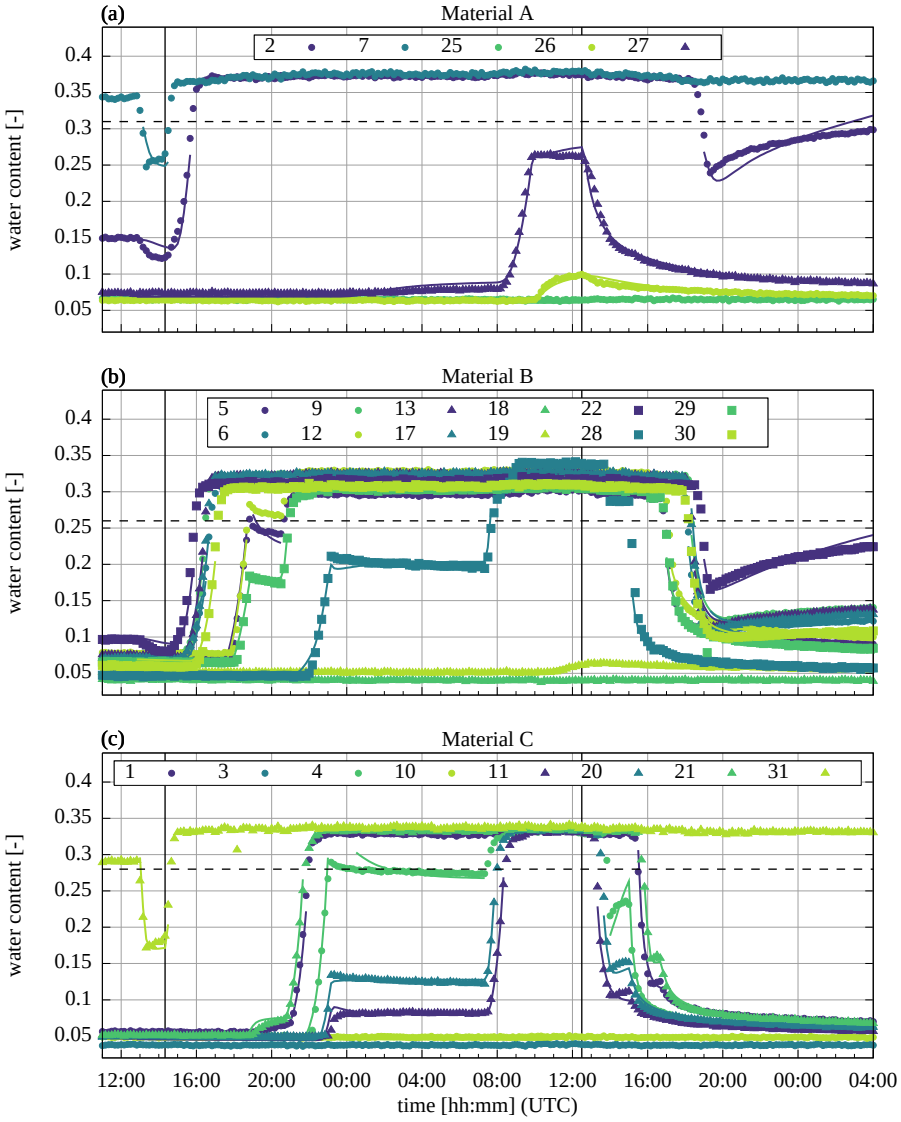

Figure 5.1 The measured water content data for the three different phases (initial drainage, multistep imbibition, and multistep drainage – separated by the solid vertical black lines in the figure) show a high variability up to and beyond the validity limits of the Richards equation due to the fluctuating groundwater table (Fig. 4.1). Hence, in order to avoid effects related to entrapped air and two-phase flow phenomena, all data with a volumetric air content smaller than 0.1 (all values above the dashed horizontal lines) are neglected based on measured porosities from core samples. The colored solid lines show the results of the setup *miller and position* of the 2D study (Sect. 5.5.2). The data measured before 12:50 are only used for the initial state estimation (Sect. 5.3.4).

5.3.1 Orientation of ASSESS

ASSESS is not built completely rectangular. Most importantly, both the surface and the ground are not horizontal but primarily inclined towards the groundwater well with a mean slope of $\approx -\frac{0.1}{20} = -0.005$. Since the applied Richards solver muPhi demands a rectangular structured grid, the geometry was rotated. This rotation was compensated by a counter-rotation of the gravity vector $\boldsymbol{g} \approx (0.0708, -9.8097)^\top$.

5.3.2 Sensor position and small-scale heterogeneity

The numerical solution of the Richards equation (Eq. 3.20) is discretized in space with a rectangular structured grid (Sect. 3.1.6). Generally, the simulated value for the modeled position of a sensor is bilinearly interpolated from the simulated values at the center of the surrounding grid cells. Due to measurement uncertainties and subsidence after the construction, Antz (2010) and Buchner et al. (2012) assess the uncertainty concerning positions of sensors and material interfaces in ASSESS to ± 0.05 m with respect to the model. However, since imbibition fronts can be very steep in sandy soils (Dagenbach et al., 2013; Klenk et al., 2015a) and the measurement volume of the applied sensors is small, fluctuating groundwater table experiments are very sensitive to the sensor position. Hence, (i) the parameter estimation algorithm (Sect. 5.3.5.1) is enabled to estimate the sensor positions and (ii) the measurement volume of the TDR sensors is implemented by averaging the simulation data within a measurement radius of 0.015 m.

In order to represent the heterogeneity of ASSESS which is not covered by describing the different sand types with distinct material properties due to the small-scale variability of the pore space, the center of each grid cell is associated with a Miller scaling factor (Eq. 3.23) that is initialized to 1.0. As the information about this small-scale heterogeneity only enters via the TDR measurement data, the exact position of each TDR sensor in the grid is also associated with a Miller scaling factor. This scaling factor may be estimated with the parameter estimation algorithm (Sect. 5.3.5.1). The scaling factors in the neighborhood of the TDR sensor are determined with a bivariate Gaussian distribution in horizontal and in vertical direction. This distribution is centered at the position of the TDR sensor and its amplitude corresponds to the associated Miller scaling factor. With a standard deviation of 0.015 m in both directions, it approaches 1.0 with increasing distance from the TDR sensor. Finally, this distribution is projected on each grid cell yielding the applied scaling factors which are only different from 1.0 in the neighborhood of the TDR sensors.

5.3.3 Boundary condition

Generally, the boundary of the simulation is implemented with a Neumann no-flow condition. However, during the forcing phases, the measured groundwater table is prescribed

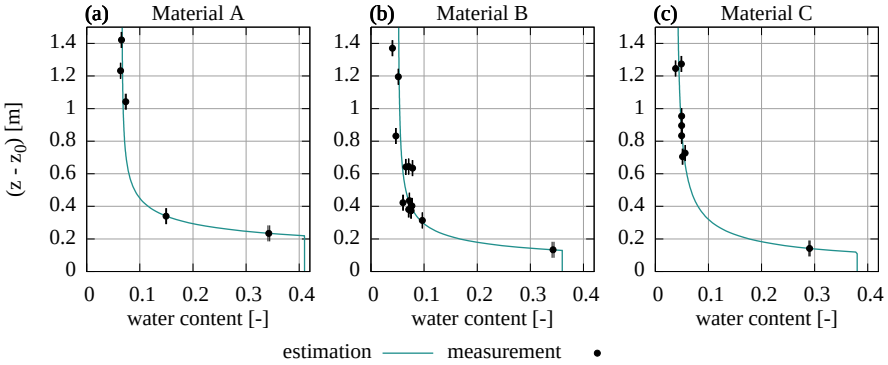

Figure 5.2 The Brooks–Corey parameterization is used to estimate the initial water content distribution between the TDR sensors. Assuming hydraulic equilibrium, the matric potential h_m is approximated with the negative distance to the groundwater table position z_0: $h_\mathrm{m} \approx -(z - z_0)$. For each material, the approximated matric potential at the position of the TDR sensors and the corresponding water content measurement data is used to fit the Brooks–Corey parameters. Each dot depicts the mean of 15 subsequent data points measured in the 4 h preceding the experiment. The standard deviations are all smaller than 0.002, which indicates (i) that the hydraulic system is relatively equilibrated at the beginning of the experiment and (ii) that the deviations from the estimation are statistically significant.

as Dirichlet boundary condition at the position of the groundwater well. Additionally to the orientation of ASSESS (Sect. 5.3.1), the uncertainty of the sensor positions (Sect. 5.3.2) directly translates to an uncertainty in the Dirichlet boundary condition. Since representation errors of the forcing have a large impact on the resulting parameters, an optional offset is implemented to the Dirichlet boundary condition which can be estimated.

5.3.4 Initial state estimation

Since an inversion method for parameter estimation is used, starting as near as possible to the measured initial state is key. Usually, this is achieved with a spin-up phase, which is computationally very expensive, however. Hence, a method to estimate the initial water content distribution based on TDR measurement data was developed.

In the first step, static hydraulic equilibrium is assumed and the matric potential at the measured position of the TDR sensors is approximated with the negative distance of this position to the groundwater table. Subsequently, the approximated matric potential is associated with the measured water content for each sensor. Further, spatially homogeneous and temporally constant material properties are assumed which permits to group the data of the TDR sensors by material, together with the approximated matric potential and the measured water content. Subsequently, the parameters h_0, λ, and $\theta_\mathrm{w,r}$ of the Brooks–Corey parameterization are fitted to the approximated matric

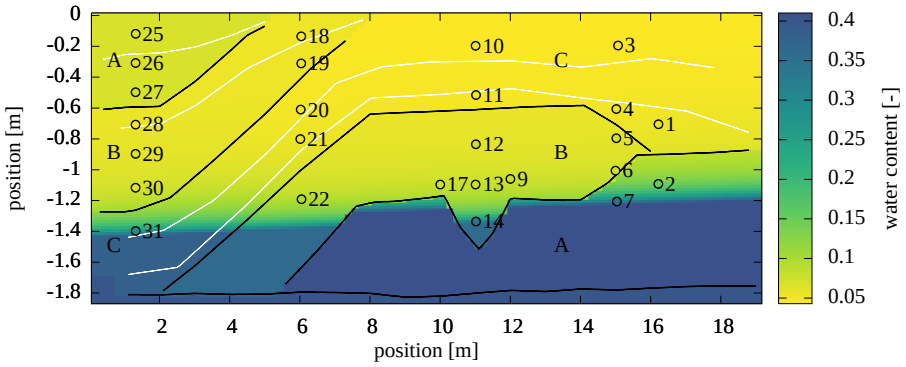

Figure 5.3 The estimated initial water content distribution is based on the TDR measurement data (Fig. 5.2) which are shown as face color of the circled dots. Since the saturated water content $\theta_{w,s}$ is fixed for each material a priori, only TDR sensors in unsaturated material are shown. Due to the orientation of ASSESS (Sect. 5.3.1), the groundwater table is slightly slanted. The black lines indicate material interfaces, whereas the white lines indicate compaction interfaces, which were introduced during the construction of ASSESS. Note the different scales on the horizontal and the vertical axis.

potential and the measured water content for each material (Fig. 5.2). The saturated water content $\theta_{w,s}$ is assumed to be known from core samples (Sect. 5.2). This yields an approximation for the initial water content distribution between the TDR sensors. With the resulting parameter values for each material, the subsurface material distribution, and the position of the groundwater table, an estimation of the initial water content distribution in ASSESS can be calculated (Fig. 5.3).

Since the parameters for the Brooks–Corey parameterization are derived from static measurement data, these may be used as initial parameter values for computationally expensive gradient-based inversions of dynamic measurement data (Sect. 5.4.2). The missing initial parameter values $\tau = 0.5$ and $K_s = 8.3 \cdot 10^{-5}\ \mathrm{m\,s^{-1}}$ are taken from Carsel and Parrish (1988). These parameter sets are referred to as *initial state material functions* in this work.

In particular due to (i) a limited number of TDR sensors, (ii) missing hydraulic potential measurements at the position of the TDR sensors, and (iii) spatial small-scale heterogeneity present in the materials, structural deviations between the estimation and the measurements occur, which indicate limitations of describing ASSESS with effective soil hydraulic material properties.

The water content measured by the TDR sensors 5, 12, and 29 deviates structurally from the estimation of the initial state for material B (Fig. 5.2). GPR measurements (Fig. 6.12, reflection (iii)) indicate that at least TDR sensors 6, 9, 13, 17, and 22 are closely to a compaction interface. Unfortunately, the position of this interface was not measured during the construction process. This indicates that the TDR sensors are monitoring a compacted pore structure. In contrast TDR sensors 5, 12, and 29 are situated in rather undisturbed areas. Hence, as most of the TDR sensors are influenced by the

compaction interfaces, the analysis of this measurement data is likely to underestimate the effective water content leading to a biased soil water characteristic for material B. This is a typical situation encountered with point-like sensors in heterogeneous media.

5.3.5 Structural error analysis

As outlined in Sect. 5.1, the structural error analysis rests on a basic representation and a general assessment of the respective representation errors. Those representation errors, which are investigated in detail, are parameterized and implemented leading to a number of distinct representations with increasing complexity. Using inversion to estimate optimal parameters for each of the representations allows to analyze (i) the resulting residuals to improve the representations and (ii) effect of unrepresented model errors on the resulting material properties. Preparing the tools for the method, this section is started with the Levenberg–Marquardt algorithm (Sect. 5.3.5.1) and discusses the assessment of the representation errors (Sect. 5.3.5.2) as well as the analysis of the resulting residuals (Sect. 5.3.5.3) afterwards.

5.3.5.1 Levenberg–Marquardt

The basic implementation of the Levenberg–Marquardt algorithm is given in Sect. 3.5.2.1. This algorithm heuristically balances performance and stability. Expanding the stability measures, a damping vector $\boldsymbol{d}$ with entries $\in (0, 1]$ is introduced to decrease the correction of particular parameters via

$$\boldsymbol{p}^{i_{\mathrm{iter}}+1} = \boldsymbol{p}^{i_{\mathrm{iter}}} + \boldsymbol{d} \odot \delta \boldsymbol{p}^{i_{\mathrm{iter}}}, \tag{5.1}$$

where $\odot$ denotes the element-wise Hadamard product. Generally, the entries of the damping vector are set to 1. In order to delay the improvement for parameters which represent additional model components, those entries are chosen < 1.

The damping vector is used in particular to estimate sensor positions and Miller scaling factors along with effective soil hydraulic properties (Sect. 5.3.2). First, these parameters are initialized to neutral values: The modeled sensor positions are initialized to the measured sensor positions and the Miller scaling factors to 1.0. Subsequently, the damping vector for the associated parameters is set to 0.1, reducing the applied correction of these parameters to 10% of the proposed correction by the Levenberg–Marquardt algorithm. Hence, the main focus of the algorithm is to estimate consistent effective soil hydraulic properties, whereas the sensor positions and Miller scaling factors are adjusted more gradually.

5.3.5.2 Assessment of representation errors

With the application of the cost function given in Eq. 3.88, it is assumed implicitly that the model is perfect aside from white Gaussian noise. This corresponds to complete quantitative understanding of reality and a Gaussian error model for the measurement data. Structural model-data mismatch indicates that this assumption is invalid. For the presented study, a Bayesian analysis of the total uncertainty space is not feasible, primarily due to a lack of models, e.g., for hysteresis. Hence, such representation errors are neglected and it is trusted that the structural model-data mismatch will reveal any inadequacy. Table 5.1 gives an overview over the treatment of the representation errors considered in this work. The contribution of representation errors, which could not be quantified or excluded from the measurement data a priori, is parameterized and explicitly estimated. Remaining structural model-data mismatch or deviation from the prior for the parameters hint at representation errors which should be corrected in the subsequent iteration of the analysis

The structural error analysis and the assessment of uncertainties results from iterative evaluations. To illustrate the method, an iteration where the orientation of ASSESS was not yet compensated by rotating the geometry and the gravitation vector (Sect. 5.3.1) is presented subsequently. Considering the structural error analysis, uncertain components in the representation were parameterized and estimated. Hence, not only the Mualem–Brooks–Corey parameters, an offset to the Dirichlet boundary condition (Sect. 5.3.3) and the saturated hydraulic conductivity of the gravel layer, but also the position of the TDR sensors were estimated (Sect. 5.3.2). The results presented in Fig. 5.4 show that the estimated TDR positions display a consistent deviation from the positions, which were measured relative to the site's walls, as they compensate for the orientation of ASSESS. Thus, the position of most TDR sensors on the right is estimated to be higher

Table 5.1 This overview includes specification whether the considered model error is represented and explicitly estimated within the scope of this study.

model error	represented	estimated
local non-equilibrium	✗	✗
hysteresis	✗	✗
numerical error	✗	✗
orientation of ASSESS	✓	✗
initial state	✓	✗
entrapped air	✓	✗
boundary condition	✓	✓
sensor position	✓	✓
small-scale heterogeneity	✓	✓
material properties	✓	✓

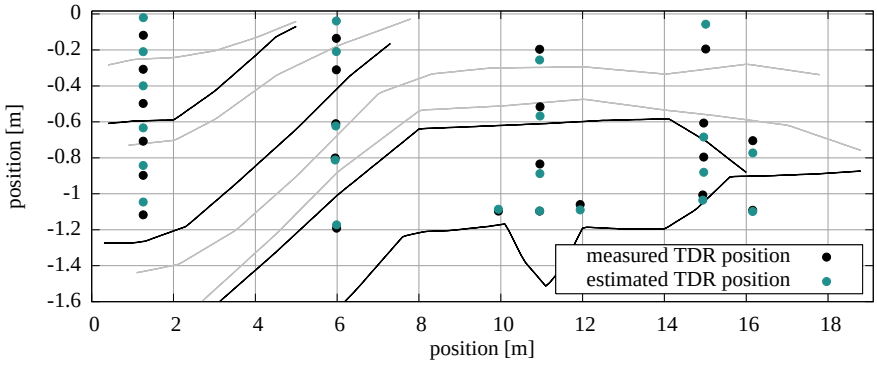

Figure 5.4 The subsurface architecture of ASSESS (Fig. 2.2) is shown with a comparison of measured and estimated TDR sensor positions based on a first evaluation of the hydraulic measurement data. The consistent deviation of the estimated TDR sensor positions reveal an unrepresented model error: the orientation of ASSESS (Sect. 5.3.1).

and the position of most TDR sensors on the left is estimated to be lower than the measured ones. By estimating the TDR sensor position, also other representation errors are incorporated into the resulting parameters, such as small-scale heterogeneities and eventually a non-represented evaporation front mostly affecting the estimated position of the upper TDR sensors (3, 11, 18, and 25). Hence, this analysis (i) demonstrates the difficulty to separate representation errors and (ii) is able to identify representation errors which have to be improved subsequently.

5.3.5.3 Residual analysis

A visual analysis of the standardized residual increases the intuitive understanding of the model-data mismatch (e.g., Legates and McCabe, 1999; Ritter and Muñoz-Carpena, 2013). The standardized residual is analyzed in two ways: (i) The visualization over time highlights the temporal development of the structural model-data mismatch. (ii) The visualization over theoretical quantiles corresponding to a Gaussian distribution with the standard deviation of the measurement data facilitates the comparison of the standardized residual distribution to the expected Gaussian distribution of the measurement data. Hence, if the perfect model assumption is true, the probability plot will show a straight line with slope 1. Yet, probability plots often show a characteristic S-shape (e.g., Fig. 5.6f): The slope < 1 for small residuals indicates that these residuals are smaller than expected for a Gaussian distribution with the standard deviation of the measurements. The slope > 1 for large residuals shows that these residuals are larger than expected for the presumed Gaussian distribution. Since in this work the theoretical quantiles are based on a Gaussian distribution, the S-shape generally indicates non-Gaussian distributions.

Additionally to the visual analysis of the standardized residual, statistical measures help to quantify the model-data mismatch. Since a single measure might be misleading (Legates and McCabe, 1999), the root mean square error (e_{RMS}) and the mean absolute error (e_{MA}) are calculated.

5.4 Setup

The setup of the parameter estimation is explained with Fig. 5.5. For each of the three materials, the Mualem–Brooks–Corey parameters h_0, λ, K_{s}, τ, and $\theta_{\mathrm{w,r}}$ are estimated (Sect. 3.1.5). The saturated water content $\theta_{\mathrm{w,s}}$ is assumed to be equal to an estimate for the porosity ϕ based on core samples (Sect. 5.2). In order to avoid parameter bias due to representation errors, (i) measurement values with volumetric air content smaller 0.1 are neglected (Sect. 5.2), (ii) a constant offset to the Dirichlet boundary condition (Sect. 5.3.3) as well as the saturated hydraulic conductivity of the gravel layer is estimated, and (iii) a method to estimate the initial water content distribution based on TDR measurement data is developed (Sect. 5.3.4), because a spin-up phase would increase the computation time by up to a factor of 17. The details concerning the implementation of the TDR sensors and the small-scale heterogeneity with Miller scaling factors at the position of the TDR sensors are explained in Sect. 5.3.2.

In order to analyze the effect of the uncertainty of the sensor position, small-scale heterogeneity, and lateral flow on the estimated material properties along the lines presented in Sect. 5.3.5, a 1D and a 2D study was implemented with four different setups: (i) ***basic***: The hydraulic material properties, an offset to the Dirichlet boundary condition, and the saturated hydraulic conductivity of the gravel layer are estimated. (ii) ***position***: In addition to the parameters estimated in the *basic* setup, also the sensor positions are estimated. (iii) ***miller***: In addition to the parameters estimated in the *basic* setup, one Miller scaling factor is estimated for each TDR sensor. (iv) ***miller and position***: In addition to the parameters estimated in the *basic* setup, the sensor positions and one Miller scaling factor for each TDR sensor are estimated.

5.4.1 1D study

In order to investigate the extent to which the experiment at ASSESS can be described with a 1D model, three different cases with an increasing number of TDR sensors per material were set up (Table 5.2): ***Case I*** includes the measurement data of sensor 1 in material C and sensor 2 in material A, and thus comprises one sensor per material. ***Case II*** includes two sensors per material, sensors 10 and 11 in material C and sensors 12 and 13 in material B. ***Case III*** includes three sensors per material, sensors 25, 26, 27 in material A and sensors 28, 29, 30 in material B. Note (i) that the cases are located at different positions in ASSESS (Fig. 2.2) and (ii) that since the hydraulic potential is not

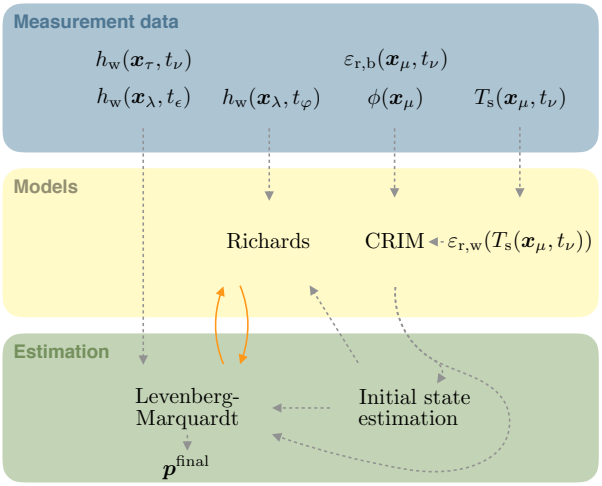

Figure 5.5 The available hydraulic potential h_w is measured at the bottom of the groundwater well $\boldsymbol{x}_\lambda$ and at the position of the tensiometer $\boldsymbol{x}_\tau$. The data set, which is measured in the groundwater well, is split according to the measurement times: The data measured during the equilibration phases t_ε enter the Levenberg–Marquardt algorithm (Sect. 5.3.5.1) directly, whereas the data measured during the forcing phases t_φ are only used as boundary condition for the Richards equation (Sect. 3.1.4). The bulk relative permittivity $\varepsilon_{r,w}(\boldsymbol{x}_\mu, t_\nu)$ and the bulk soil temperature $T_s(\boldsymbol{x}_\mu, t_\nu)$ are measured at the position of the TDR sensors $\boldsymbol{x}_\mu$ at times t_ν. Additionally using the porosity $\phi(\boldsymbol{x}_\mu)$, the bulk permittivity is transferred to water content (Sect. 3.3). The water content data enter the initial state estimation (Sect. 5.3.4) yielding an initial water content distribution and optional initial parameter values for the Levenberg–Marquardt algorithm. The water content data are also directly used in the Levenberg–Marquardt algorithm. Dashed grey arrows represent one-time preparation steps, whereas solid orange arrows represent the iterative steps of the Levenberg–Marquardt algorithm yielding the final material parameters $\boldsymbol{p}^{final}$.

measured in the domain covered with these 1D studies, the respective inversions are only based on the TDR water content measurements.

As described above, the analysis is organized in four different setups (*basic*, *position*, *miller*, and *miller and position*). The *basic* setup is adjusted for the 1D studies, such that not only the material functions of the materials with sensors, but also the saturated conductivity of the third material (material A in *case II* and material C in *case III*) are estimated for *case II* and *case III*. The other setups remain accordingly. For each of the different setups, an ensemble of 20 inversions is initialized with Latin hypercube sampled initial parameter sets in order to analyze the convergence behavior. Note that only the ensemble member with minimal cost is analyzed for each setup in the subsequent discussion (Sect. 5.5.1).

The forward simulations were calculated with a grid resolution of 0.005 m and 10^{-8} as limit of the Newton solver (Sect. 3.1.6). Following Jaumann (2012), the standard deviation of the TDR measurements is assumed as 0.007. The manually measured ground-

water table data are used as Dirichlet boundary condition. Uncertainties concerning the position of the sensors and the subsurface material interfaces directly translate to uncertainties in the boundary condition (Sect. 5.3.3). Accounting for the orientation of ASSESS (Sect. 5.3.1), a constant offset to the Dirichlet boundary condition is added for each case (*case I*: −0.02 m, *case II*: −0.05 m, *case III*: −0.12 m). In order to minimize the input error, this offset is also estimated in the inversion. If TDR sensor positions are estimated, these are initialized to the measured position. Similarly, the Miller scaling factors are initialized to 1.0.

5.4.2 2D study

In this study, the investigated domain is expanded to 2D and the performance of the improved representation is analyzed. To this end, four different setups *basic*, *position*, *miller*, and *miller and position* were set up as described above. Since the position of both the tensiometer and the groundwater well is in the modeled domain, the hydraulic potential measurement data as well as the TDR measurement data can be used in this study. Thus, the *position* setup is adjusted, such that both the positions of TDR sensors and the tensiometer are estimated. All inversions for the 2D study are initialized with the initial state material functions (Sect. 5.3.4) in order to bring out the quantitative effect of the different representations on the resulting material properties.

The 2D simulations in this work are calculated with a grid resolution of 0.2 m × 0.02 m. The limit of the Newton solver is set to 10^{-8} (Sect. 3.1.6). Like for the 1D studies, the standard deviation of the TDR measurements is set to 0.007. The standard deviation of the tensiometer (0.025 m) is assessed from the accuracy (±5 hPa) as specified by the manufacturer. In order to transfer the given uniform distribution with range ±5 hPa ≈ ±0.05 m to a Gaussian distribution, this range is associated with the 2σ interval of a Gaussian (5 % to 95 %). This leads to an approximate standard deviation of $(0.05\ \text{m} \cdot 2)/4 = 0.025$ m. Lacking an independent estimate for the accuracy of the manual groundwater table position measurement, the accuracy of material interfaces in ASSESS is employed (Sect. 5.3.3). Same as for the tensiometer, this leads to a standard deviation of 0.025 m. Some TDR sensors are located close to or even below the groundwater table.

Table 5.2 The 1D study comprises three different cases which investigate the three materials with increasing number of TDR sensors per material at different locations in ASSESS (Fig. 2.2). Note that each material is covered twice.

case	sensors	materials	position [m]
I	1 & 2	C, A	16.16
II	10, 11 & 12, 13	C, B	10.95
III	25, 25, 27 & 28, 29, 30	A, B	1.26

Therefore, the position and the Miller scaling factor could not be estimated for TDR sensors. Hence, no position was estimated for sensors 7, 8, 14, 15, 16, 23, 24, 31, and 32 and no Miller scaling factor was estimated for sensors 8, 14, 15, 16, 17, 23, 24, 31, and 32.

5.5 Results and discussion

In order to improve the quantitative understanding of the hydraulic behavior of ASSESS (Sect. 2), a basic representation (Sect. 3.5) is evaluated with a structural error analysis (Sect. 5.3.5) that is implemented as outlined in Sect. 5.4. The discussion of the results is done separately for the 1D study (Sect. 5.5.1) and the 2D study (Sect. 5.5.2).

5.5.1 1D study

5.5.1.1 Objectivity of the measurement data

The standardized residual for each case is presented in Fig. 5.6 combining the resulting data of all applied TDR sensors. Investigating them for *case I*, it is striking that all setups describe the data qualitatively equally well. Since the estimation of the material properties is only based on one sensor per material in this case, the parameterization offers enough freedom to describe the data. Hence, it also accommodates unrepresented model errors, such as the sensor position and small-scale heterogeneities. Therefore, additional representation and estimation of TDR sensor positions or Miller scaling factors do not lead to further improvement. The largest residuals occur during highly transient phases. Compared to the data, the simulated imbibition phase is too slow for sensor 1 and too fast for sensor 2. Also the simulated drainage phase is too slow for sensor 1 and drainage behavior of sensor 2 is consistently wrong. This structural model-data mismatch hints at unrepresented model errors due to the restriction to a 1D domain, which is further discussed in Sect. 5.5.1.3. Still, the residuals of all setups are smaller than 5 standard deviations, which translates to a volumetric water content of 0.035.

The large residuals are not random and preferably occur in transient phases. These are attributed to missing processes in the dynamics or to biased parameters. As the curves in the probability plot are basically centered at the origin, a significant constant bias in the residuum can be excluded. The resulting statistical measures are given in Table 5.3.
The e_{MA} of the *basic* setup increases in *case II*, because there are two sensors per material and the effective material parameterization cannot completely compensate for the small-scale heterogeneity at the position of both sensors simultaneously. Consequently, representing the small-scale heterogeneity improves the description of the data. As before, the largest residuals occur during highly transient phases, especially during the drainage phase. Except for two outliers, the residuals stay smaller than 5 standard devi-

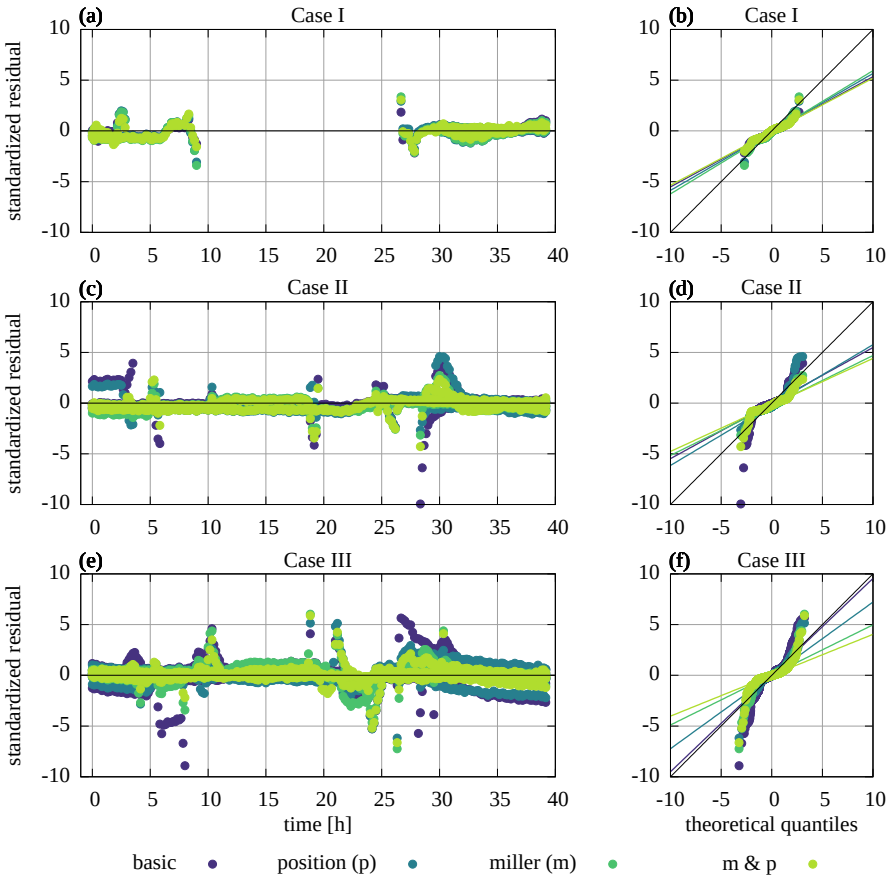

Figure 5.6 For the 1D study, the standardized residuals of the best ensemble member are visualized over time (left) and over the theoretical quantiles of a Gaussian with the estimated standard deviation of the TDR measurements (0.007) (right). The cases are analyzed with four setups ***basic***, ***position***, ***miller***, and ***miller and position***. The more sensors per material are used in the inversion, the worse the representation of the *basic* setup gets. In this case, representing uncertainties with respect to the sensor position and small-scale heterogeneities improves the representation substantially. The decreasing slope of a linear fit (thin lines in the probability plots), which is based on the standardized residuals within $[-2, 2]$ theoretical quantiles, also indicates this improvement.

ations here as well. Considering three sensors per material in *case III*, the e_{MA} increases even further in the *basic* setup. Consequently, representing small-scale heterogeneities and uncertainties in the sensor position in the *miller and position* setup improves the e_{MA} by more than a factor of 2.

5.5.1.2 Separation of uncertain model components

Comparing the resulting material properties of the evaluated ensemble members for the different cases and setups (Fig. 5.7), it is noticeable that the resulting soil water characteristic functions are shifted within each material. During static phases and if only few measurement sensors are available, the parameters for the estimated uncertain model components (Sect. 5.4) can be correlated. However, during transient phases and if a larger number of measurement sensors is available, the distinct properties of these uncertain model components are more clearly pronounced (see e.g., Fig. 5.8 and Sect. 5.5.2.3).

The inversions were also run without estimating the offset to the Dirichlet boundary condition (Sect. 5.3.3). However, the results are not shown here. Besides destabilizing the convergence of the Levenberg–Marquardt algorithm, not estimating this offset fully transfers the uncertainty in the boundary condition to the sensor position. Hence, setups that estimate the sensor position clearly outperform the others. Additionally, this does not remove the shift of the soil water characteristics.

Table 5.3 In order to analyze the results of the 1D study, the performance of the best ensemble members for each case and for each setup are benchmarked with statistical measures. With an increasing number of included TDR sensors per material, the statistical measures for the *basic* setup indicate worse description of the measured water content data. However, estimating the position and the Miller scaling factor for each TDR sensor, improves description of the measurement data significantly according to the statistical measures.

case	setup		e_{RMS}	e_{MA}
I	basic		0.004	0.003
	position	(p)	0.004	0.003
	miller	(m)	0.005	0.004
	m & p		0.004	0.003
II	basic		0.007	0.003
	position	(p)	0.005	0.003
	miller	(m)	0.004	0.003
	m & p		0.004	0.003
III	basic		0.009	0.006
	position	(p)	0.006	0.004
	miller	(m)	0.005	0.003
	m & p		0.004	0.002

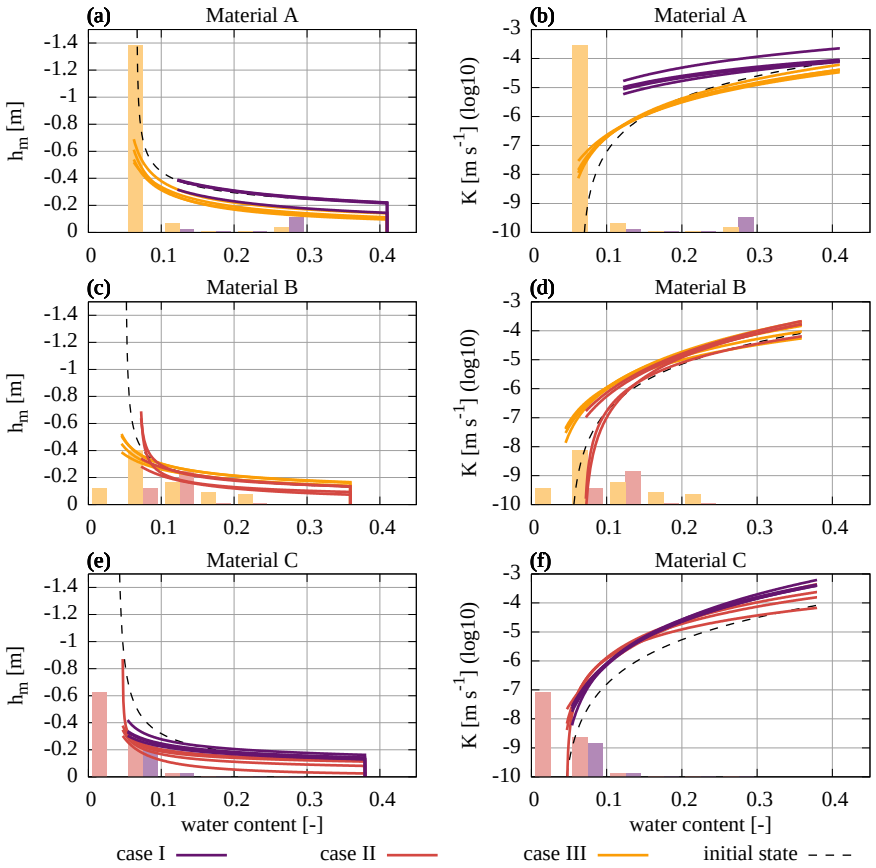

Figure 5.7 The estimated material functions of the best ensemble member are shown for each of the three cases (***case I***, ***case II***, and ***case III***) and the four setups of the 1D study. Additionally, the material functions resulting from the ***initial state estimation*** (Sect. 5.3.4) are presented. The plot range is adjusted to the available water content range for all inversion results. The number of water content measurements within intervals of 0.05 is indicated with histogram bars for each case. The height of these bars is normalized over all figures in this work. The main message of this figure is, that unrepresented model errors may lead to biased hydraulic parameters. In particular, this can be seen by comparing the hydraulic conductivity K_s of material A for the cases I and III.

5.5.1.3 Lateral flow

The three cases cover the three materials at different locations in ASSESS and are based on distinct data with respect to both quantity and data range. This is most evident for material A which is located at the bottom of ASSESS and nearly saturated in *case I* whereas it is at the top and rather dry in *case III* (colored dots in Fig. 2.2). To illustrate that this leads to a different sensitivity to the unrepresented model errors, one example is highlighted that is most pronounced during the final equilibration phase.

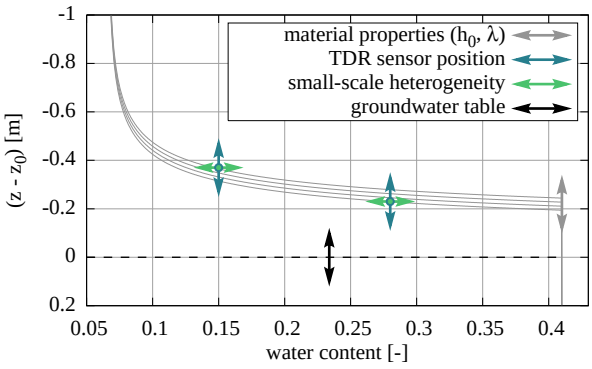

Figure 5.8 The estimation of uncertain model components can lead to correlated estimated parameters, e.g., as an incorrect position of the groundwater table (z_0) can be compensated by changing h_0 *and* λ during static phases. During transient phases, however, the components have distinct effects, e.g., as λ also changes the conductivity function. Hence, the ability of the parameter estimation algorithm to separate these uncertainties depends on the available measurement data. Also, the more sensors are available, the fewer uncertain model components can be compensated simultaneously by the parameterization.

In *case III*, the water content at position of the TDR sensors 25, 26, and 27 is higher than in static hydraulic equilibrium, leading to a drainage flux and a decrease in water content (Fig. 5.1). However, in *case I*, at the position of TDR sensor 2, the water content increases as the sensor monitors the relaxation of the capillary fringe. Due to the different hydraulic properties of the materials in ASSESS, this relaxation also includes unrepresented lateral flow. In order to minimize the structural model-data mismatch during this equilibration phase, the parameter estimation algorithm increases the hydraulic conductivity to compensate for the non-represented lateral flow with additional vertical flow from above the sensor. Hence, the hydraulic conductivity of *case I* is larger than the hydraulic conductivity for both the *case III* and the 2D study which is discussed in the following (Sect. 5.5.2.4).

The measurement data of material B used in the inversions of *case II* and *case III* do not emphasize the relaxation of the capillary fringe strongly. Hence, it is expected that the effect of the unrepresented lateral flow is not as significant as for material A leading to relatively congruent resulting material functions. This expectation is confirmed by the results, except for those setups of *case II*, in which no Miller scaling factor was estimated. Those setups show a larger curvature of the soil water characteristic and of the hydraulic conductivity function. This is explained in more detail subsequently in Sect. 5.5.2.4. Additionally, the previously discussed shift of the soil water characteristic can be identified (Sect. 5.5.1.2).

Similarly as for material B, the inversions for material C are not strongly influenced by the relaxation of capillary fringe. The large uncertainty in the saturated hydraulic conductivity reflects the low sensitivity of the measurement data on this parameter due to the lack of measurements influenced by the saturated material C.

5.5.1.4 Quality of the initial state material functions

The curvature of the soil water characteristic for the inversion results is reasonably close the initial state material functions (Sect. 5.3.4), although the 1D inversions were started from Latin hypercube sampled initial parameter sets. This allows to use the initial state material functions to initialize gradient-based inversion methods. The estimate of the initial state material function for material C deviates strongest from the inversion results compared to the other two materials, since in material C only few sensors are available to assess the form of the capillary fringe. Naturally, the better the available number of TDR sensors is spread over the water content range, the better the fit of the initial state parameters gets. Iteratively restarting the inversion using the previous inversion results as initial state material functions is likely to improve the representation. Since K_s and τ are not estimated along with the initial water content distribution but prescribed a priori, the hydraulic conductivity functions associated with the initial state show large deviations from the inversion results.

5.5.2 2D study

5.5.2.1 Objectivity of the measurement data

For the 2D study, the number of sensors is comparable to the number of hydraulic material parameters. Therefore, estimating sensor positions and Miller scaling factors increases the total number of the parameters and thus the computational cost considerably (number of estimated parameters: *basic*: 17, *position*: 41, *miller*: 41, *miller and position*: 65). The total number of analyzed TDR sensors increased to 25, corresponding to 5, 12, 8 TDR sensors for the materials A, B, C, respectively. In the 1D study, the residuals increased considerably during transient phases reaching up to 5 standard deviations in the *miller and position* setup (except for 3 outliers). Due to the larger number of considered TDR sensors in the 2D study, the measurement data cover more architectural situations and thus more complicated flow phenomena. In particular, there are more transient phases observed than in the 1D studies. Therefore, it is expected that (i) the resulting parameters are more objective (not shown, however), (ii) the standardized residuals increase at least in the *basic* setup, and (iii) estimating sensor positions and Miller scaling factors improves the description of the TDR data significantly. The standardized residuals shown in Fig. 5.9 confirm the last two expectations. However, similar to the 1D study, even the residuals of the *miller and position* setup still reach more than 5 standard deviations for the 2D representation.

In order to understand this deviation in more detail, the remaining structural model-data mismatch is investigated for the final drainage and equilibration phases between 30–40 h. The largest residuals occurring during the drainage phase around 30 h come from the TDR sensors 6, 9, 13, and 17. Note that these sensors are located close to a compaction interface (Sect. 5.3.4). Hence, the large residuals indicate that this mostly horizontal compaction layer is not correctly represented with a point-scale representation

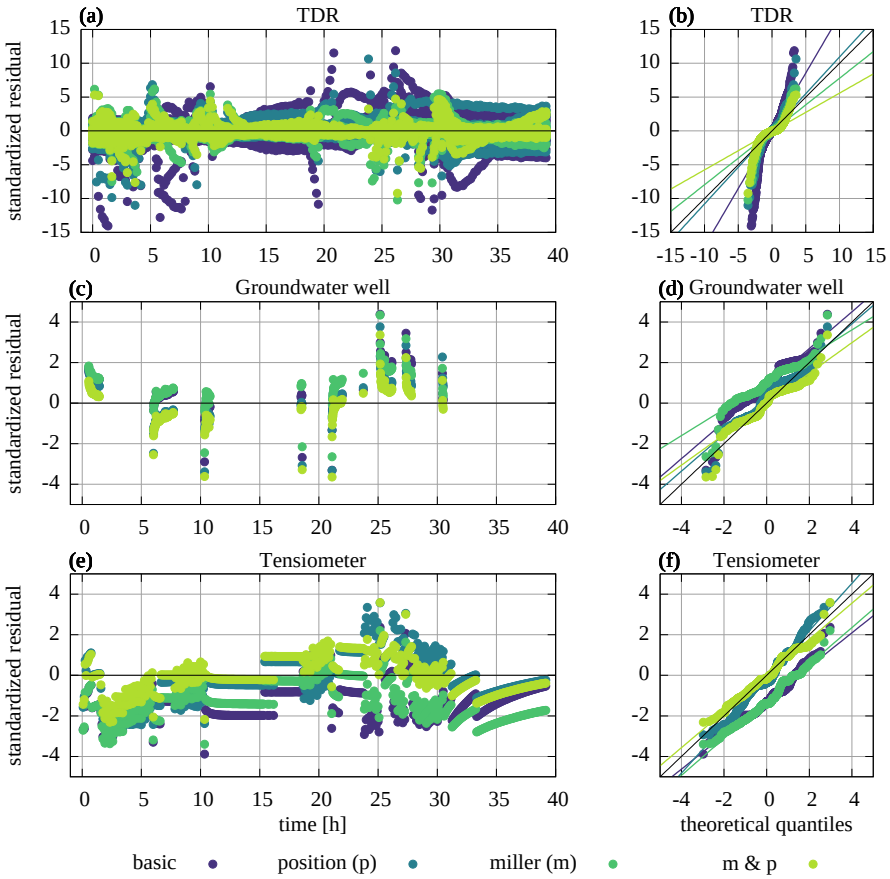

Figure 5.9 The standardized residuals of the 2D study are visualized over time (left) and in a probability plot (right) for all TDR and hydraulic potential sensors. The color associates the results with the four setups of the study (***basic***, ***position***, ***miller***, and ***miller and position***). Same as for the 1D study, the standard deviation for the TDR measurement data is chosen as 0.007. The standard deviation for both the manual measurements in the groundwater well and the tensiometer measurement data is chosen as 0.025 m. The representation of uncertainties with respect to the sensor positions and small-scale heterogeneities improves the description of the TDR data quantitatively. The decreasing slope of a linear fit (thin lines in the probability plots), which is based on the standardized residuals within $[-2, 2]$ theoretical quantiles, also indicates this improvement. The structural model-data mismatch for the hydraulic potential data is mainly due to (i) uncertainties concerning the position of the tensiometer and (ii) unrepresented 3D water flux phenomena.

of the small-scale heterogeneity. The largest residuals during the final equilibration phase between 30–40 h come from TDR sensors 2 and 22 close to the capillary fringe. These are attributed to unrepresented processes in the dynamics, such as hysteresis or 3D water flux (Sect. 5.5.2.2).

Due to the persisting large residuals during transient phases, the probability plot given in

Fig. 5.9b displays a characteristic S-shaped curve for the TDR data (Sect. 5.3.5.3). The large residuals during transient phases are evidently different from the small residuals during static phases. This is corroborated by a linear fit based on the residuals within $[-2, 2]$ theoretical quantiles. For both the *miller* and the *miller and position* setup, the fits yield a slope < 1, indicating that distribution of the small residuals is more narrow than a Gaussian with a standard deviation of 0.007. This standard deviation is a measure that includes both precision and accuracy. The precision of the evaluated measurement data was calculated with a cubic spline fit yielding 0.001, 0.007 m, 0.006 m for the water content, tensiometer, manual groundwater position data, respectively. With complete quantitative understanding (Sect. 5.3.5), the standard deviation of the residuals would correspond to this precision. Lacking ground truth, the accuracy of the measurement data is unknown a priori and may depend on the hydraulic state. In this study, its estimated contribution dominates the size of the standard deviations. The results show that the model can represent static phases better than highly transient phases and that the accuracy of the measurement data is higher than estimated a priori. The statistical measures for the water content data given in Table 5.4 reveal that the e_{MA} of the *basic* setup merely increases by less than a factor of 2 compared to *case III* of the 1D study. Estimating sensor positions and Miller scaling factors improves the description of the TDR measurement data by more than a factor of 2 leading to a e_{MA} of 0.004.

5.5.2.2 Hydraulic potential

The description of the hydraulic potential data only improves in those setups, in which the sensor position is estimated (Fig. 5.9 and Table 5.4). Also the temporal structure of the model-data mismatch does not change significantly with the different setups. The data show a gradient of the hydraulic pressure between the tensiometer and the groundwater well during the forcing phases (Fig. 4.1). Considering symmetry, this gradient of the hydraulic potential is also assumed in the neglected third dimension. Hence, the forcing via the groundwater well leads to a 3D water flux during the experiment.

Table 5.4 For each setup of the 2D study, the results are benchmarked with statistical measures. Similar to the 1D study, estimating the sensor position and the Miller scaling factors improves the statistical measures related to the water content significantly. The statistical measures for the position of the groundwater table including both the tensiometer and the groundwater well data improve only for setups in which the sensor positions are estimated.

		water content		water table	
setup		e_{RMS}	e_{MA}	e_{RMS}	e_{MA}
basic		0.017	0.011	0.04	0.03
position	(p)	0.011	0.006	0.02	0.02
miller	(m)	0.008	0.005	0.03	0.03
m & p		0.006	0.004	0.02	0.02

This makes a correct representation of the groundwater table in 2D impossible. Consequently, the simulation should predict a higher position of the groundwater table in the well during imbibition phases and a lower groundwater table during the drainage phases. This expectation is confirmed by the standardized residuals shown in Fig. 5.9. Thus, the structural model-data mismatch of the tensiometer data indicates that employing the groundwater table as Dirichlet boundary condition overestimates the forcing in the simulation. Therefore, the simulated hydraulic pressure during the imbibition is larger than the measured one which leads to negative residuals. As expected, this behavior reverses during drainage phases.

5.5.2.3 Separation of uncertain model components

Compared to the previously discussed 1D study (Sect. 5.5.1), the 2D study is based on a larger number of water content measurements, additional hydraulic potential measurements, and more complicated flow phenomena. This improves the ability of the Levenberg–Marquardt algorithm to separate uncertain model components (Sect. 5.5.1.2) and decreases the shift in the soil water characteristics of the different setups compared to the 1D study (Fig. 5.10).

5.5.2.4 Effect of unrepresented model errors

Each setup is started from the same initial material functions (Sect. 5.3.4). Therefore, the difference between the resulting material properties of the setups (Fig. 5.10) is a direct consequence of the representation of uncertainties in the sensor position and small-scale heterogeneities.
To investigate this, consider the initial state estimation for material B shown in Fig. 5.2. The measurement data of the sensors 5, 12, and 29 which are approximately 0.6 m above groundwater table deviate from the estimated function considerably. In order to cope with this deviation, the least-squares fit for the initial state draws the estimated soil

Table 5.5 The effective hydraulic material parameters obtained with the setup *miller and position* of the 2D study are presented for the materials A, B, and C. The formal standard deviations of the parameter estimation are given with the understanding that these are specific to the applied algorithm and will change for different algorithm parameters. The estimation for the saturated hydraulic conductivity of the gravel layer and for the offset to the Dirichlet boundary condition are $10^{-0.728\pm0.006}$ m s^{-1} and -0.034 ± 0.001 m, respectively.

	h_0 [m]	λ [−]	K_s [m s^{-1}]	τ [−]	$\theta_\mathrm{w,r}$ [−]	$\theta_\mathrm{w,s}$ [−]
A	-0.184 ± 0.005	1.94 ± 0.07	$10^{-4.212\pm0.004}$	0.33 ± 0.07	0.025 ± 0.004	0.41
B	-0.174 ± 0.004	2.54 ± 0.06	$10^{-3.77\pm0.02}$	0.78 ± 0.05	0.035 ± 0.001	0.36
C	-0.159 ± 0.004	3.28 ± 0.02	$10^{-3.70\pm0.02}$	0.74 ± 0.06	0.026 ± 0.002	0.38

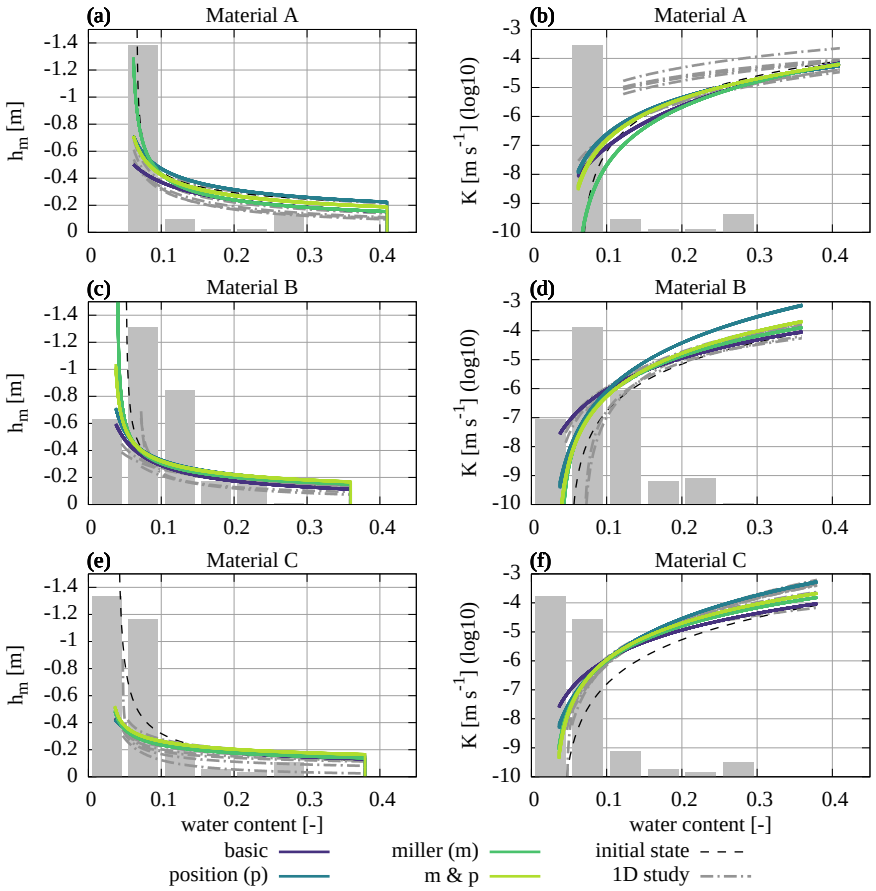

Figure 5.10 The resulting material functions are shown for all three materials involved in the 2D study which is analyzed with the four setups ***basic***, ***position***, ***miller***, and ***miller and position***. The plot range is adjusted to the available water content range for each material. The height of the histogram bars denotes the number of available water content measurements and is normalized over all figures in this work. Since the inversions for all setups are initialized with the material functions resulting from the ***initial state estimation*** (Sect. 5.3.4), the difference between the results is directly linked to the estimation of sensor positions and small-scale heterogeneities. For direct comparison, the results of the ***1D study*** (Sect. 5.5.1) are also shown.

water characteristic to higher water contents. Due to the rigidity of the Brooks–Corey parameterization, this causes an overestimation of the water content at the position of the sensors 0.8 and 1.4 m above the groundwater table (sensors 28 and 18). If the uncertainty in sensor position and small-scale heterogeneities are represented in the model, the outlying measurement data can be described without altering the effective material properties.

It is worth noting, that although the uncertainty of the measured grain size distribution (Table 2.1) is large, the resulting material properties confirm the measurements in that material A is the finest and the properties of materials B and C are similar. The final

best estimates for the effective hydraulic material properties for the *miller and position* setup are given in Table 5.5.

5.6 Summary and conclusions

A basic representation of the effectively 2D architecture ASSESS was investigated with a structural error analysis. This representation included TDR and hydraulic potential measurement data which were acquired during a fluctuating groundwater table experiment. Based on the assumption that structural model-data mismatch indicates incomplete quantitative understanding of reality, a 1D and a 2D study was implemented with different setups using increasingly complex models. Starting with the estimation of effective hydraulic material properties, the complexity of the setups was increased by adding the estimation of sensor positions, small-scale heterogeneity, or both. It was demonstrated that the structural error analysis can indicate significant unrepresented model errors, such as the slope of the ASSESS test site.

The analysis showed that the estimated material properties resulting from a 1D study are biased due to unrepresented lateral flow. Analyzing representations with increasing data quantity, it was found that the fewer sensors are available per material, the stronger is the influence of unrepresented model errors on the estimated material properties. It was illustrated, that the more complicated flow phenomena are represented, the better uncertain model components can be separated by the parameter estimation algorithm leading to more reliable material properties. Generally, representing sensor position uncertainty and small-scale heterogeneity improved the description of the water content data quantitatively in setups with many sensors. Yet, the residuals of the water content data still reach more than 5 standard deviations during transient phases. This was attributed to remaining representation errors in the dynamics, forcing, and compaction interfaces.

In order to minimize the error in the initial state, a method to estimate the initial water content distribution was developed which is based on TDR measurements and an approximation of hydraulic head which additionally yields an approximation of the soil water characteristic. It was found that this approximation is reasonably close to inversion results and that the estimated parameters can be used as initial parameters for gradient-based optimization. As all the inversions of the 2D study are initialized with these parameters, the comparison of the results directly displays the quantitative effect of the unrepresented model errors on the estimated material properties.

Since the three approaches (i) initial state estimation, (ii) 1D inversion, and (iii) 2D inversion allow to estimate effective hydraulic material parameters, their levels of improving the quantitative understanding of soil water dynamics is discussed finally.

The initial state estimation requires at least three water content measurements per material over the full water content range and the position of the groundwater table

to estimate the parameters for soil water characteristic for one specific equilibrated hydraulic state. Lacking direct measurements of the unsaturated hydraulic conductivity, the method cannot estimate the remaining parameters K_s and τ required to model soil water dynamics. Additionally, it is highly susceptible to uncertainties related to the sensor position and small-scale heterogeneities. Yet, the method is fast (few seconds on a local machine) and suitable to provide initial parameters for gradient-based inversion methods.

The 1D inversions are comparably fast (minutes up to hours on a local machine) and can represent transient states. In contrast to the initial state estimation, 1D inversions can estimate all parameters of the material functions. However, more complicated flow phenomena including lateral flow cannot be represented. This leads to biased parameters.

The unique characteristic of the 2D inversions (days on a cluster using the same number of cores as parameters) is the ability to represent lateral flow phenomena which are typically monitored with a high number of sensors. Hence, the consistency of the representation is implicitly checked. Therefore, it is expected that of the three approaches discussed, this one yields the most reliable material properties. Still, unrepresented model errors including 3D water flux phenomena influence the results.

6 Analysis of GPR data

The GPR data acquired during the fluctuating groundwater table experiment described in Sect. 4 is evaluated subsequently. Note that this section is essentially copied from Jaumann and Roth (2018).

6.1 Introduction

Quantitative understanding of soil water movement is in particular based on accurate knowledge of the subsurface architecture and the hydraulic material properties. As direct measurements are time-consuming and near to impossible at larger scales, soil hydraulic material properties are typically determined with indirect identification methods, such as inversion (Hopmans et al., 2002; Vrugt et al., 2008a). TDR is a standard method to acquire the required measurement data since it is sensitive to hydraulic processes (e.g., Robinson et al., 2003). Yet, being an invasive method, the TDR sensors disturb the soil texture of interest and require the maintenance of a local measurement station. Hence, it is difficult to apply the method at larger scales or to transfer the sensors to another field site. GPR is an established noninvasive method for subsurface characterization (e.g., Daniels, 2004; Neal, 2004) and has the potential to become a standard method for efficient, accurate and precise determination soil hydraulic material properties.

Available research studies regarding estimation of hydraulic properties from GPR measurements may be categorized according to the applied methods for the different components of the research study, such as the (i) GPR measurement procedure, (ii) experiment type, (iii) GPR simulation method, (iv) optimization method, and (v) evaluation method of the GPR signal. Most of these studies either use on-ground, off-ground, or borehole GPR measurements.

On-ground measurements (e.g., Buchner et al., 2012; Busch et al., 2012; Léger et al., 2015) offer the most flexible approach. They have the disadvantage, however, that the antenna characteristics are influenced by coupling to the ground. Off-ground measurements (e.g., Lambot et al., 2009; Jadoon et al., 2012; Jonard et al., 2015) avoid these effects, but the measurements are influenced by surface roughness. Cross-borehole measurements allow for high-resolution tomography of the subsurface (e.g., Ernst et al., 2007; Looms et al., 2008; Scholer et al., 2011) but require boreholes which are destructive and expensive.

The applied experiment types range from infiltration, fluctuating groundwater table, to evaporation. Infiltration experiments (e.g., Léger et al., 2014; Thoma et al.,

2014; Rossi et al., 2015) are fast (hours) and provide indirect information about the near-surface material properties. Through its dependence on the form of the infiltration front or plume, the resulting GPR signal can get rather complicated to reproduce when used for quantitative evaluation. Difficulties arise from multiple reflections in the plume, waveguides in the infiltration front, and from noise originating for small-scale heterogeneity or fingering. In particular, if the infiltration is done artificially, accurate knowledge of the spatial distribution of the infiltration flux is required. Simultaneous GPR measurements during the infiltration process are difficult as the antenna coupling to the subsurface is influenced by the changing water content close to the surface. Fluctuating groundwater table experiments (e.g., Bradford et al., 2014; Léger et al., 2015) require intermediate timescales (hours to days) and provide information about the material properties close to the groundwater table. These experiments are typically limited to fluvial or coastal areas or are induced artificially in test sites. Evaporation experiments (e.g., Moghadas et al., 2014) demand long timescales (weeks) as the hydraulic dynamics are slow at low water contents. Yet, this kind of experiment is important to understand the coupling of the pedosphere with the atmosphere.

The applied models to simulate the GPR signal are faced with an inherent tradeoff between performance and accuracy. Ray tracing (Léger et al., 2014, 2015) is fast but merely yields an approximate solution of Maxwell's equations. These equations can be solved analytically with Green's function (e.g., Lambot et al., 2009; Busch et al., 2012; Jonard et al., 2015) assuming a layered subsurface architecture. Alternatively, Maxwell's equations can be solved numerically with the FDTD method (e.g., Lampe et al., 2003; Giannopoulos, 2005; Buchner et al., 2012). This method is computationally expensive, but grants full flexibility concerning the source wavelet and the subsurface architecture.

Due to the inherent oscillating nature of the electromagnetic signal, inversion of GPR data generally demands globally convergent and robust optimization techniques. Sequentially coupling a globally convergent search algorithm, e.g., the global multilevel coordinate search (GMCS) algorithm (Huyer and Neumaier, 1999), with the gradient-free locally convergent Nelder–Mead simplex (NMS) algorithm (Nelder and Mead, 1965) was successfully applied to estimate hydraulic material properties from GPR measurements (e.g., Lambot et al., 2004; Busch et al., 2012; Moghadas et al., 2014). The NMS was further developed to the SCE-UA (Duan et al., 1992) which has become a standard tool in hydrology and was also applied on GPR measurements (e.g., Léger et al., 2014, 2015; Jadoon et al., 2012). Additionally, MCMC methods (e.g., Scholer et al., 2011; Thoma et al., 2014; Jonard et al., 2015) and data assimilation approaches (e.g., Tran et al., 2014; Manoli et al., 2015; Rossi et al., 2015) have been successfully applied so far.

The GPR signal has to be processed automatically for parameter estimation. Many full waveform inversion approaches directly use the resulting Green's function (e.g., Lambot et al., 2009; Busch et al., 2012; Jadoon et al., 2012) in the cost function. Using the full antenna signal may lead to many local minima prohibiting a reliable identification of the global minimum (e.g., Bradford et al., 2014). In contrast, filtering the radargram with convolution approaches to determine travel time and amplitude of a limited number of

events leads to better convergence and may even allow the application of efficient locally convergent algorithms (e.g., Buchner et al., 2012).

In homogeneous materials, the transition zone above the groundwater table exhibits a smooth variation of the relative permittivity. Since the resulting GPR reflection is a superposition of a series of infinitesimal contributions along the transition zone, the detailed form of this reflection is sensitive to the variation of the relative permittivity. For simplicity, this reflection is referred to as *transition zone reflection*. Dagenbach et al. (2013) showed that this reflection is sensitive to the hydraulic material parameterization model. Bradford et al. (2014) measured the transition zone reflection of a drainage pumping test in a fluvial area with an antenna center frequency of 200 MHz and estimated hydraulic material properties. Klenk et al. (2015a) employed numerical forward simulations and experiments using GPR antennas with higher antenna center frequency (400 and 600 MHz) for a more-detailed explanation of the transition zone reflection for imbibition, relaxation, and drainage. They also concluded that the transition zone reflection is sensitive to hydraulic material properties.

This work builds upon previously published methods for simultaneous estimation of the subsurface architecture and the effective water content based on on-ground multi-offset GPR measurement data (e.g., Gerhards et al., 2008; Buchner et al., 2012). In order to develop methods to additionally estimate hydraulic material properties, the ASSESS test site was forced with a fluctuating groundwater table ensuring large hydraulic dynamics. In this study, the resulting transition zone reflection is evaluated together with reflections originating from material interfaces to estimate the subsurface architecture and the corresponding soil hydraulic material properties. To this end, two studies are implemented. The first study is based on both synthetic and measured time-lapse CO GPR data acquired at a stationary position. Thus, merely the position of subsurface layers can be estimated with this data. The second study is based on synthetic data which are acquired with time-lapse CO measurements on a subsurface architecture that resembles the one of ASSESS. Hence, these data allow to estimate the 2D structure of the subsurface architecture. To evaluate these GPR data, a new semi-automatic heuristic approach is developed which allows to extract the travel time and amplitude of relevant reflections. Subsequently, this information is evaluated with the Levenberg–Marquardt algorithm and the simulated annealing algorithm. Before discussing the two studies in more detail (Sects. 6.3–6.4), the applied methods are sketched first (Sect. 6.2).

6.2 Methods

In addition to the methods sketched in Sect. 3, other methods have been used and developed by Jaumann and Roth (2018) specifically for the evaluation of GPR data. These methods are outlined subsequently.

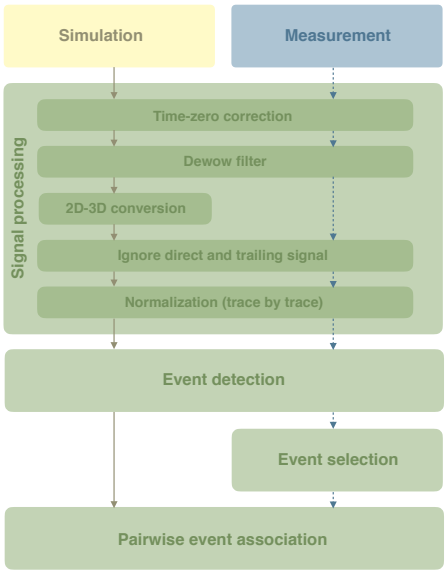

Figure 6.1 The GPR data evaluation method presented in this section consists of four main steps. In the first step, the signal is processed (Sect. 6.2.1.1). The 2D to 3D conversion in this step is applied to the simulated data, if they are either compared to real measured data or to synthetic measurement data to which this conversion was applied (Sect. 6.3). In the second step, extrema in the GPR signal (events) are detected (Sect. 6.2.1.2). The detected events in the measurement data can be selected manually for the subsequent evaluation (Sect. 6.2.1.3). This ensures that the optimization focuses only on the most relevant information in the data. Finally, the most plausible association of simulated and measured events is determined (Sect. 6.2.1.4). Note that for each parameter set that is tested during the optimization procedure, the simulation data are evaluated automatically (solid lines). In contrast, the measurement data are only evaluated once before starting the optimization procedure (dashed lines).

6.2.1 GPR analysis

Following Buchner et al. (2012), the travel time t and the corresponding amplitude A for N_m samples of the GPR signal (events)

$$E_x \mapsto \left\{ \begin{pmatrix} t_1 \\ A_1 \end{pmatrix} \dots \begin{pmatrix} t_{N_\mathrm{m}} \\ A_{N_\mathrm{m}} \end{pmatrix} \right\} \tag{6.1}$$

are extracted with a heuristic approach. Hence, this allows us to focus on the phenomena that are represented in the model. However, this procedure demands an automatic event association algorithm to associate events extracted from the measured signal with events extracted from the simulated signal. As outlined in Fig. 6.1, the evaluation method presented in this section consists of four steps: (i) signal processing (Sect. 6.2.1.1), (ii) event detection (Sect. 6.2.1.2), (iii) event selection (Sect. 6.2.1.3), and (iv) pairwise event association (Sect. 6.2.1.4).

6.2.1.1 Signal processing

The GPR signal is processed for further evaluation according to the following steps: (i) time-zero correction, (ii) dewow filter, (iii) 2D to 3D conversion, (iv) ignore direct and trailing signal, and (v) normalization (Fig. 6.1).

Since the time-zero of the GPR antennas changes over time, the direct signal is picked and the evaluated travel time is subtracted from the radargram for time-zero correction.

Subsequently, a dewow filter is applied to subtract inherent low-frequency wow noise of the GPR signal. Because the observation is in 3D and the simulation in 2D, the simulated signal is converted to 2.5D, meaning to 3D with translational symmetry perpendicular to the survey line and parallel to the ground surface (Bleistein, 1986). The ASSESS site conforms to this 2D requirement (Sect. 2). For the conversion, each trace is transformed to the frequency domain with the fast Fourier transform (FFT), which is denoted by $\widehat{\ }$. Afterwards, the electric field is modified depending on the angular frequency ω:

$$\widehat{E}_x^{3D} = \widehat{E}_x^{2D} \cdot C_i \cdot \sqrt{\frac{|\omega_{k'}|}{2\pi\sigma_c}} \exp\left(-\frac{\mathrm{i}\pi}{4}\mathrm{sign}(\omega)\right), \tag{6.2}$$

where i is the complex unit, C_i is a constant [m], and σ_c denotes the integral of the velocity with respect to the length s of the ray trajectory. Assuming a direct ray path and horizontal reflector with the reflector distance d as well as the mean square root of dielectric permittivity $\overline{\sqrt{\varepsilon_r}}$ along the ray path, this is leads to

$$\sigma_c = \int c(s)\mathrm{d}s = \frac{c_0 d}{\overline{\sqrt{\varepsilon_r}}}. \tag{6.3}$$

Subsequently, all traces are transformed back to the time domain with the inverse FFT. Due to the frequency conversion and the manipulation, a high-frequency noise remains on the signal which is smoothed with a fourth-order Savitzky–Golay filter (e.g., Press, 2007, here the implementation of the *signal* package for Gnu Octave is employed: `https://octave.sourceforge.io/signal/`) using a window width of 41 samples. Subsequently, the direct signal and the trailing signal of the dewow filter are set to zero. Finally, each trace is normalized to its maximum absolute amplitude since the absolute power of the GPR source is typically unknown. Thus, the value of the constant C_i in Eq. 6.2 also becomes irrelevant.

6.2.1.2 Event detection

In this step, events are detected in each trace separately (Fig. 6.2). To facilitate the detection of relevant events at large signal travel times, the amplitude of the processed signal (Sect. 6.2.1.1) is amplified quadratically with travel time using an arbitrary gain function that was shown to work well. Subsequently, the extrema of the amplified amplitude are detected with a local neighborhood search. We keep a predefined number of events (15) with the largest amplified absolute amplitude. If the non-amplified amplitude of a detected extremum is below a predefined amplitude threshold (0.006), the event is discarded in any case. In order to correct the perturbation in travel time due to the amplification and to cope with the discrete measurement resolution, a Gaussian curve centered at the travel time of the detected event with width of ±5 samples is fitted to the non-amplified amplitude of the processed signal. The travel time of the resulting extremum of the Gaussian fit is directly used as the amplitude of this event. This procedure makes the form of the previously applied gain function irrelevant. The

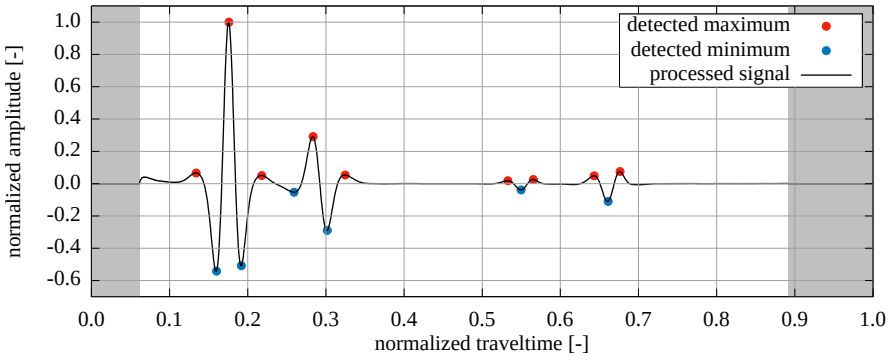

Figure 6.2 The detected events of the first trace of the synthetic radargram are analyzed in Sect. 6.3.2.1. The amplitude of a trace is searched for extrema with a neighborhood search algorithm. For the subsequent evaluation, the amplitude of the detected events is normalized to the maximum absolute amplitude of all events detected in the trace. The direct signal and the trailing signal of the dewow filter with normalized travel times < 0.06 and > 0.89, respectively, are set to zero in a processing step (Sect. 6.2.1.1) and possible events close to these signals are ignored.

amplitude of all detected events is normalized with the absolute maximal amplitude of all detected events within the same trace.

6.2.1.3 Event selection

After the event detection, the measured signal and the detected events (Sect. 6.2.1.2) are inspected manually. In this one-time processing step, events can either be deleted or added manually. Thus, it can be ensured, that only those events that are also represented in the model enter the parameter estimation. This step is skipped for the analysis of the simulated data. The amplitude of all selected events is normalized with the absolute maximal amplitude of all selected events within the same trace.

6.2.1.4 Pairwise event association

The selected events extracted from the measured data have to be associated with the detected events extracted from the simulated data for the parameter estimation. To this end, Buchner et al. (2012) tested all possible combinations of events, using the one with the minimal summed absolute travel time difference. However, this is only feasible for a small number of events. As no Gaussian convolution of the data but the data themselves is used, the number of events increases. Hence, testing all combinations is often prohibitively expensive.

In order to exclude combinations a priori, the detected events are aggregated in clusters (Fig. 6.3a). Then, these clusters are associated by testing all possible combinations and

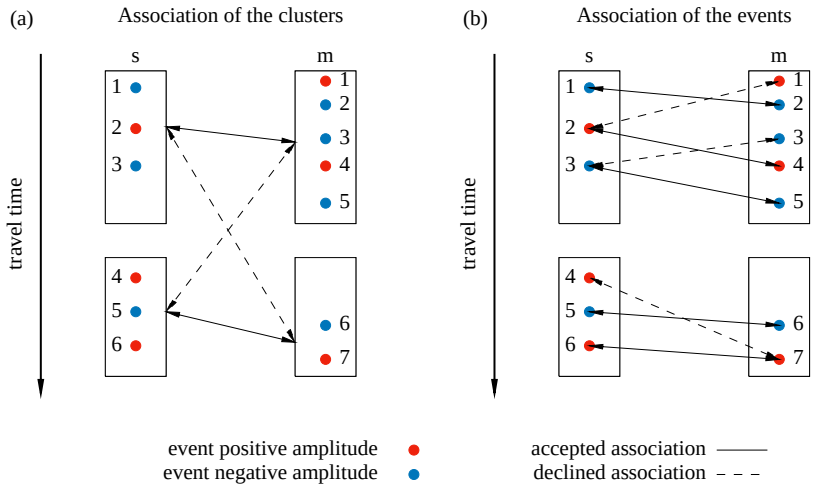

Figure 6.3 Example of the association of simulated (s) and measured (m) events with indices 1–6 and 1–7, respectively. The color of the dots indicates the amplitude sign of the events. (a) The detected events (Fig. 6.2) are aggregated in clusters to minimize the number of possible event combinations. The clusters are associated such that the summed absolute travel time difference of the mean travel time of the events in the cluster is minimal. (b) The events in the clusters are associated according to consistent temporal order and amplitude sign. Hence, if $(t_{s,1}, A_{s,1})$ is associated with event $(t_{m,2}, A_{m,2})$, event $(t_{s,2}, A_{s,2})$ cannot be associated with event $(t_{m,1}, A_{m,1})$, if $t_{m,1} < t_{m,2}$ or $\text{sign}(A_{s,2}) \neq \text{sign}(A_{m,1})$. Solid (dashed) arrows indicate some of the accepted (declined) association combinations. The combination with the maximal number of associations and the minimal summed absolute travel time difference is used for evaluation. Thus, for example $(t_{s,1}, A_{s,1})$ is associated with $(t_{m,2}, A_{m,2})$ and not with $(t_{m,3}, A_{m,3})$.

finally using the combination with the minimal summed absolute travel time difference. Afterwards, those events that are aggregated in the associated clusters are associated themselves. The applied association procedure requires the events to have an identical amplitude sign and a consistent temporal order which reflects the principle of causality (Fig. 6.3b). After iterating over all allowed combinations, the association with the maximal number of associated events and the minimal summed absolute travel time difference is used. It is critical to also consider combinations where some intermediate events (e.g., $(t_{s,2}, A_{s,2})$ in Fig. 6.3) cannot be associated.

After the association of the events, outliers are detected by calculating the mean and standard deviation of the travel time differences. All associations that exhibit an absolute travel time difference larger than 3 standard deviations of all absolute travel time differences are discarded. Finally, the amplitude of the associated events is normalized to the maximal absolute amplitude of the associated events of each trace separately for the simulation and the measurement.

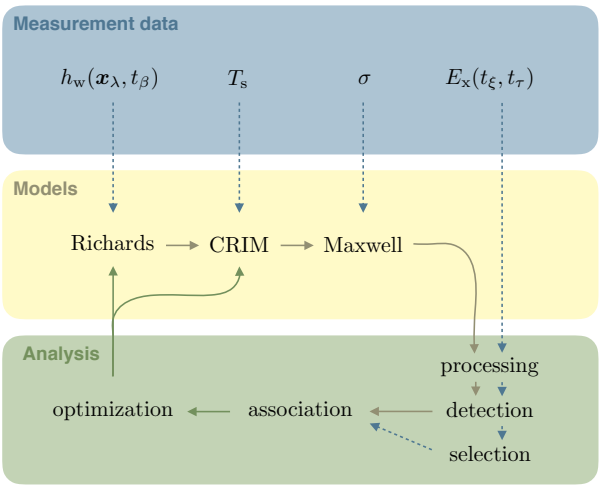

Figure 6.4 The general setup of the optimization is sketched with this figure. The hydraulic potential h_w is measured at the position of the groundwater well x_λ at times t_β. These measurements are used as boundary condition for the Richards equation (Sect. 3.1.4). Estimates for the soil temperature T_s and the electrical conductivity σ are derived from TDR related measurements. The actual signal of the GPR system is proportional to the x dimension of the electric field E_x and is measured discretely at experiment time t_ξ and signal travel time t_τ. This signal is processed (Sect. 6.2.1.1) and used for event detection (Sect. 6.2.1.2). Based on the detected events in the measurement data, events can be either added or deleted in the subsequent event selection step (Sect. 6.2.1.3). The simulated water content distribution is converted to relative permittivity distribution with CRIM and used to solve Maxwell's equations (Sect. 3.2.1). After the processing step and the event detection, the simulated events are associated with the measured events (Sect. 6.2.1.4). The resulting mapping of the events is used to calculate the cost in the optimization step (Sect. 6.2.2). Dashed arrows indicate initial processing steps, whereas solid arrows indicate iterative steps required for the optimization.

6.2.2 Optimization

The general setup of the parameter estimation is explained with Fig. 6.4. Optimization based on GPR data requires modifications of (i) the cost function (Sect. 6.2.2.1), (ii) the Levenberg–Marquardt algorithm (Sect. 6.2.2.2), and (iii) the simulated annealing algorithm (Sect. 6.2.2.3). These modifications are outlined subsequently.

6.2.2.1 Cost function

Assuming N_{param} parameters and N_{m} associations of measured events $(t_{i_{\mathrm{meas}},\mathrm{m}}, A_{i_{\mathrm{meas}},\mathrm{m}})$ with simulated events $(t_{i_{\mathrm{meas}},\mathrm{s}}(\boldsymbol{p}), A_{i_{\mathrm{meas}},\mathrm{s}}(\boldsymbol{p}))$, the cost function is given by

$$\begin{aligned} S(\boldsymbol{p}) &= \frac{1}{2} \sum_{i_{\mathrm{meas}}=1}^{N_{\mathrm{m}}} \left(\frac{t_{i_{\mathrm{meas}},\mathrm{s}}(\boldsymbol{p}) - t_{i_{\mathrm{meas}},\mathrm{m}}}{\sigma_{t,i_{\mathrm{meas}}}} \right)^2 + \left(\frac{A_{i_{\mathrm{meas}},\mathrm{s}}(\boldsymbol{p}) - A_{i_{\mathrm{meas}},\mathrm{m}}}{\sigma_{A,i_{\mathrm{meas}}}} \right)^2 \\ &= \frac{1}{2} \sum_{i_{\mathrm{meas}}=1}^{N_{\mathrm{m}}} r_{t,i_{\mathrm{meas}}}^2 + r_{A,i_{\mathrm{meas}}}^2 \end{aligned} \tag{6.4}$$

with the constant standard deviation of the measured normalized travel times $\sigma_{t,i_{\mathrm{meas}}} = \sigma_t$ and the measured normalized amplitudes $\sigma_{A,i_{\mathrm{meas}}} = \sigma_A$. This leads to the standardized residuals in travel time $r_{t,i_{\mathrm{meas}}}$ and amplitude $r_{A,i_{\mathrm{meas}}}$.

Due to the oscillating nature of the GPR signal and due to the applied GPR data evaluation method (Sect. 6.2.1), the cost function is not necessarily convex and may even be discontinuous at some points, in particular as the number of associated events N_{m} may change during the minimization process. Hence, adding and removing associations of events requires a compensation to prevent the cost function from becoming discontinuous. To this end, Buchner et al. (2012) introduced *tagging*. If the number of the measured events is smaller than the number of the simulated events, those simulated events that are not associated are excluded. Alternatively, if there are more measured events than simulated events, measured events without a partner are tagged as partnerless. If a reflection event has been tagged and becomes untagged after the parameter update, the contribution of the event and its new partner to the cost function is added to the previous cost. If an event has not been tagged and becomes tagged after the parameter update, the contribution to the cost function is subtracted from the previous cost.

6.2.2.2 Levenberg–Marquardt

The Levenberg–Marquardt algorithm is implemented as described in Sect. 3.5.2.1. The application of this gradient-based algorithm on GPR data requires the implementation of tagging (Sect. 6.2.2.1) and additional regularization of the optimization. This regularization can be achieved by focussing in particular on the improvement of small residuals, because if the small residuals improve, the larger residuals are likely to also improve in subsequent iterations due to the temporal correlation of the time-lapse data. Therefore, events with $r_{t,i_{\mathrm{meas}}} > 100$ or $r_{A,i_{\mathrm{meas}}} > 100$ are tagged. Tagged events are excluded from the optimization by setting these entries in the Jacobian matrix $(J_{i_{\mathrm{meas}},i_{\mathrm{param}}} = \partial r_{i_{\mathrm{meas}}} / \partial p_{i_{\mathrm{param}}})$ to zero. The event association may also change during the perturbation of the parameters for the numerical assembly of the Jacobian matrix. This can lead to large changes in the residuals, which in turn may lead to a disturbed parameter update. Hence, corresponding entries of large changes in the resid-

ual $|r_{i_{\mathrm{meas}}}(\boldsymbol{p}_{\mathrm{perturbed}}) - r_{i_{\mathrm{meas}}}(\boldsymbol{p})| > 50$ are also set to zero together with entries of the Jacobian matrix that are larger than 10^4.

The weighting parameter λ_{LM} (Eq. 3.91) is initialized with 5 and changed according to the delayed gratification method by decreasing (increasing) λ_{LM} by a factor of 2 (3) if the parameter update is successful (not successful). This ensures that the algorithm takes small steps, such that the association and the Jacobian matrix can adapt smoothly.

6.2.2.3 Simulated annealing

The simulated annealing algorithm is implemented as described in Sect. 3.5.2.1. In addition to the implementation of tagging (Sect. 6.2.2.1), no further regularization is required for this algorithm due to its random parameter update (Eq. 3.93). Hence, this algorithm is in particular suitable for initial iterations, where the association of the single events does typically not lead to a consistent association of the reflections. Once the reflections are consistently associated, the Levenberg–Marquardt algorithm is typically more efficient than the simulated annealing algorithm.

6.3 Study 1: Transient hydraulic state and stationary antenna

The time-lapse GPR data that were acquired during the fluctuating groundwater table experiment described in Sect. 4, are evaluated subsequently for their suitability to determine the subsurface architecture and the corresponding soil hydraulic material properties.

Since the GPR antenna was stationary during the experiment, the evaluation is limited to 1D. As lateral flow in ASSESS is most significant during drainage phases, this evaluation focusses on the imbibition phase of the experiment (Fig. 4.1). However, the evaluation also includes the initial drainage phase, because otherwise the error of assuming an initially equilibrated state would be large. To limit the effect of lateral flow on the resulting estimates, the events measured during the drainage phase and the beginning of the imbibition phase are excluded from the evaluation.

In the following, the implementation of the evaluation and optimization methods is outlined (Sect. 6.3.1). Afterwards in Sect. 6.3.2, the suitability of those methods to simultaneously estimate the subsurface architecture and the corresponding soil hydraulic material properties of ASSESS is tested with synthetic data (Sect. 6.3.2.1). Subsequently, the methods are applied to the measured data (Sect. 6.3.2.2).

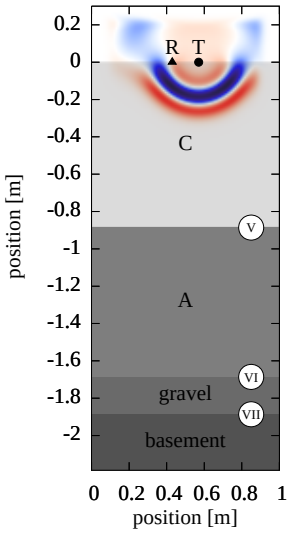

Figure 6.5 For the simulation of the GPR signal of antenna 3, a layered subsurface architecture is assumed (Fig. 4.2). The transmitter of the antenna is represented with an infinitesimal dipole (T) and the electric field is read at the position of the receiver antenna (R). A perfectly matched layer is used as boundary condition. The x component of the resulting electric field after 5 ns is shown. The markers for the material interfaces are introduced in Fig. 6.12 and are used consistently in this work. The position of the interface of materials C and A (V) as well as the position of the interface of materials A and gravel (VI) are parameterized (d^{V} and d^{VI}) and can be estimated.

6.3.1 Setup

6.3.1.1 Implementation

In this study, the subsurface architecture of ASSESS is represented with layers. The position of these layers is parameterized and can be estimated. For illustration, the setup of the simulation is shown in Fig. 6.5.

The Richards equation is solved numerically with muPhi (Sect. 3.1.6) on a structured grid with a resolution of ≈ 0.005 m. The CRIM (Sect. 3.3) is used to transfer the simulated water content to relative permittivity using the measured mean soil temperature $T_{\mathrm{s}} = 8.5$ °C (Sect. 4). Since Maxwell's equations are solved in 2D, the simulated 1D permittivity distribution is extruded in the y dimension using the same spatial resolution. The total size of the represented subsurface architecture is 1.0 m × 1.9 m. To simulate the temporal propagation of the electromagnetic signal, Maxwell's equations

(Sect. 3.2.1) are solved in 2D with MEEPGPR (Sect. 3.2.3.2). One-tenth of the minimal wavelength λ_{wmin} is typically chosen as upper limit for the spatial resolution

$$\Delta z \leq \frac{\lambda_{\mathrm{wmin}}}{10} = \frac{\frac{c_0}{\sqrt{\varepsilon_{\mathrm{rmax}}}}}{10 f_{\mathrm{wmax}}} \approx 0.007 \text{ m} \tag{6.5}$$

for the electromagnetic simulation, with the maximal frequency $f_{\mathrm{wmax}} = 2 \cdot 400$ MHz and the maximal relative permittivity $\varepsilon_{\mathrm{rmax}} = 31.25$ which corresponds to a maximal saturated water content of 0.5. Accordingly, the numerical resolution for the isotropic structured rectangular grid is chosen as $\Delta z = 0.005$ m.

Generally, the boundary condition is implemented with a Neumann no-flow condition. However, during the forcing phases, the measured groundwater table (Fig. 4.1) is prescribed as Dirichlet boundary condition at the bottom boundary. The electromagnetic simulation is initialized with static hydraulic equilibrium based on the measured groundwater table position. To avoid multiple reflections at the air–soil boundary, the relative permittivity above the soil is set to 3.5, which is typical for dry sand. This is justified, since no evaluation of air wave or ground wave is done and the amplitude is normalized according to the detected events. The permittivity of the basement below ASSESS is set to 23.0, based on previous simulations. The electrical conductivity of the subsurface σ is set to 0.003 $\mathrm{S\,m^{-1}}$ (Sect. 4).

The GPR data are evaluated according to Sect. 6.2.1. The detection of the clusters is chosen to be identical for the measured and simulated data. The characteristic shape time-lapse radargram allows separating the clusters at a specific normalized travel time ($t_{\mathrm{split}} = 0.5$) for all traces. Hence, all events with a travel time $t \leq t_{\mathrm{split}}$ are in cluster 1, and the others are in cluster 2.

6.3.1.2 Setup of the parameter estimation

Inversion of GPR data typically requires globally convergent parameter estimation algorithms which are computationally expensive. In order to keep the parameter estimation procedure efficient, an iterative strategy is used (Fig. 6.6). The optimization procedure is started by drawing an ensemble of initial parameter sets with the Latin hypercube algorithm (Sect. 3.6.5.5).

The most expensive operation of the forward simulation is the calculation of the observation operator, which includes the solution of Maxwell's equations and the subsequent event association (Sect. 6.2.1). Since time-lapse GPR data are highly correlated in experiment time, the number of traces in the time-lapse GPR radargram are subsampled equidistantly generating a data set with lower temporal resolution. Those data are used to improve the distribution of the initial parameters (preconditioning). Therefore, the drawn parameter sets are used to initialize the simulated annealing algorithm (Sect. 6.2.2.3) which allows for a robust and fast parameter update. The resulting parameters then serve as initial parameters for the Levenberg–Marquardt algorithm (Sect. 6.2.2.2) which concludes the preconditioning step. The resulting parameters of

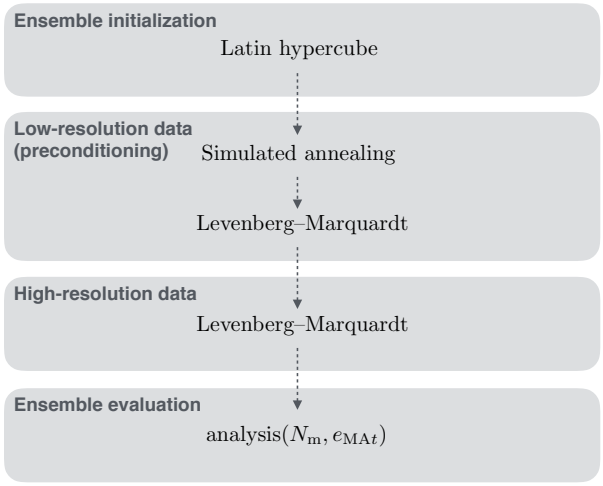

Figure 6.6 For the GPR data analysis, a sequentially coupled parameter estimation procedure is chosen that (i) allows to minimize the computational cost and (ii) facilitates the implementation of tagging (Sect. 6.2.2.1). Therefore, Latin hypercube sampled parameter sets are preconditioned with a data set with reduced number of traces (low-resolution data) by sequentially coupling the simulated annealing algorithm and the Levenberg–Marquardt algorithm. The preconditioned parameter sets for each ensemble member serve as initial parameters for the final parameter estimation based on high-resolution data. The subsequent evaluation of the ensemble is based on the number of associated events N_m and the mean absolute error in travel time $e_{\mathrm{MA}t}$ (Sect. 6.3.1.2).

the preconditioning step are used as the initial parameter sets for the more expensive optimization of the high-resolution data set with the Levenberg–Marquardt algorithm.

The data set with high (low) resolution includes 86 (9) traces corresponding to one trace per 15 (150) min. Hence, both data sets subsample the actually measured number of traces (one trace per $\approx$ 30 s) equidistantly in time. Within the sample range given in Table 6.1, 60 initial parameter sets are drawn with the Latin hypercube algorithm and the data set with the low temporal resolution is used to improve these parameter sets running 200 iterations of the simulated annealing algorithm. Notice that the parameter fit range given in Table 6.1 determines the parameter update via $p_{i_\mathrm{param},\mathrm{max}}$ and $p_{i_\mathrm{param},\mathrm{min}}$ according to Eq. 3.93. After the application of the simulated annealing algorithm, maximally 15 iterations of the Levenberg–Marquardt algorithm are run. This optimization completes the preconditioning step. The resulting parameter sets serve as initial parameters for the Levenberg–Marquardt algorithm which is applied to the high-resolution data.

In order to evaluate the performance of the ensemble members, the mean absolute error in travel time $e_{\mathrm{MA}t}$ is used since this statistical measure is independent of the number of associated events. The number of associated events is accounted for by evaluating those 10 members with minimal $e_{\mathrm{MA}t}$ that associated at least 85% of the measured events.

Each of these members has locally optimal parameters. However, the exact position of these local minima typically depends on the initial parameters and the random numbers drawn in the simulated annealing algorithm. There is also no guarantee that the global optimum was found by one of the ensemble members. However, the distribution of these 10 best ensemble members contains valuable information about the shape of the cost function. To account for this information, (i) the mean parameter set of the best members is analyzed and (ii) the standard deviation is used to indicate the uncertainty of the parameters. Notice that the mean parameter set is not necessarily optimal. However, if the standard deviation of the resulting parameters is small, the mean parameter set is typically more reliable than the parameter set of the best ensemble member.

The standard deviations of the measured data, $\sigma_t \approx 6 \cdot 10^{-4}$ and $\sigma_A \approx 5 \cdot 10^{-3}$ for the normalized travel times and amplitudes, respectively, are used to standardize the residuals in the cost function (Eq. 6.4). These standard deviations were calculated from travel time and amplitude data acquired by picking different reflections with approximately constant travel time. In order to perturb the travel time and the amplitude of the selected events of the synthetic measurement data, a realization of white Gaussian noise with this standard deviation is added to the data.

Table 6.1 The fit range limits the parameter space available for parameter estimation and is in particular used by the simulated annealing algorithm to update the parameters (Sect. 3.5.2.2). The sample range is used to generate an ensemble of initial parameter sets with the Latin hypercube algorithm.

material	parameter	fit range		sample range	
		min	max	min	max
C	h_0 [m]	-0.25	-0.05	-0.20	-0.10
	λ [−]	1.0	5.0	2.0	4.0
	K_s [m s^{-1}]	$10^{-4.1}$	$10^{-2.9}$	10^{-4}	10^{-3}
	τ [−]	-1.0	2.0	0.0	1.0
	$\theta_{\mathrm{w,s}}$ [−]	0.33	0.43	0.36	0.40
	$\theta_{\mathrm{w,r}}$ [−]	0.00	0.10	0.02	0.08
A	h_0 [m]	-0.30	-0.10	-0.25	-0.15
	λ [−]	1.0	5.0	2.0	4.0
	K_s [m s^{-1}]	$10^{-5.1}$	$10^{-3.9}$	10^{-5}	10^{-4}
	τ [−]	-1.0	2.0	0.0	1.0
	$\theta_{\mathrm{w,s}}$ [−]	0.36	0.46	0.39	0.43
	$\theta_{\mathrm{w,r}}$ [−]	0.00	0.10	0.02	0.08
gravel	$\theta_{\mathrm{w,s}}$ [−]	0.30	0.50	0.38	0.42
architecture	d^{V} [m]	0.90	1.10	0.95	1.05
	d^{VI} [m]	0.10	0.30	0.15	0.25

6.3.2 Discussion

The suitability of the presented methods to estimate the subsurface architecture and the corresponding soil hydraulic material properties is first tested with synthetic data (Sect. 6.3.2.1). Subsequently, the methods are applied to measured data (Sect. 6.3.2.2). In each section, the phenomenology of the data sets is first discussed qualitatively. Afterwards, the inversion results are evaluated.

6.3.2.1 Synthetic data

Phenomenology The phenomenology of the transition zone reflection for characteristic times during imbibition, equilibration, and drainage was discussed by Klenk et al. (2015a) for coarse sand. In this study, the focus is on the temporal development of this reflection during imbibition and equilibration. To this end, the water content distribution of the 1D profile located at 17.05 m of the ASSESS site (Fig. 4.2) was simulated using typical parameters for coarse-textured sandy soils. These parameters are given together with the estimated parameters in Table 6.2. The resulting simulation is visualized over time and over water content in Fig. 6.7.

Initialized with static hydraulic equilibrium, the simulation starts with an initial drainage step where the groundwater table is lowered. Hence, the material at the upper end of the capillary fringe with high initial water content is desaturated. After the subsequent equilibration step, the groundwater table is raised during the subsequent imbibition step. The Brooks–Corey parameterization (Eq. 3.21) features a sharp kink where air enters the material at the upper end of the capillary fringe. Furthermore, the imbibition introduces an additional kink in the water content distribution (marker (2) in Fig. 6.7b), because the relaxation time from hydraulic non-equilibrium is much shorter for high water contents compared to the relaxation time for low water contents. This is due to the nonlinear dependency of the hydraulic conductivity (Eq. 3.22) on the water content and leads to the differences in hydraulic conductivity of several orders of magnitude. Hence, the width of the transition zone is decreased during the imbibition phase.

During the equilibration step after the first imbibition, the additional kink smoothes. Thus, the water content increases in the material with low water content (3) and decreases in the material at the upper end of the capillary fringe (4). This smoothing depends on both the soil water characteristic and the hydraulic conductivity function. Sharpening and smoothing of the transition zone are repeated consistently for the other subsequent imbibition and equilibration phases ((5), (6) and (7), (8)).

According to the CRIM (Sect. 3.3), the relative permittivity distribution has the same shape as the water content distribution. Hence, kinks in the water content distribution directly lead to partial reflections of the GPR signal (Fig. 6.7c). Shortly after starting the imbibition, the amplitude of the reflection originating from the additional kink (2) increases. After passing the material interface (V), the spatial distance between the

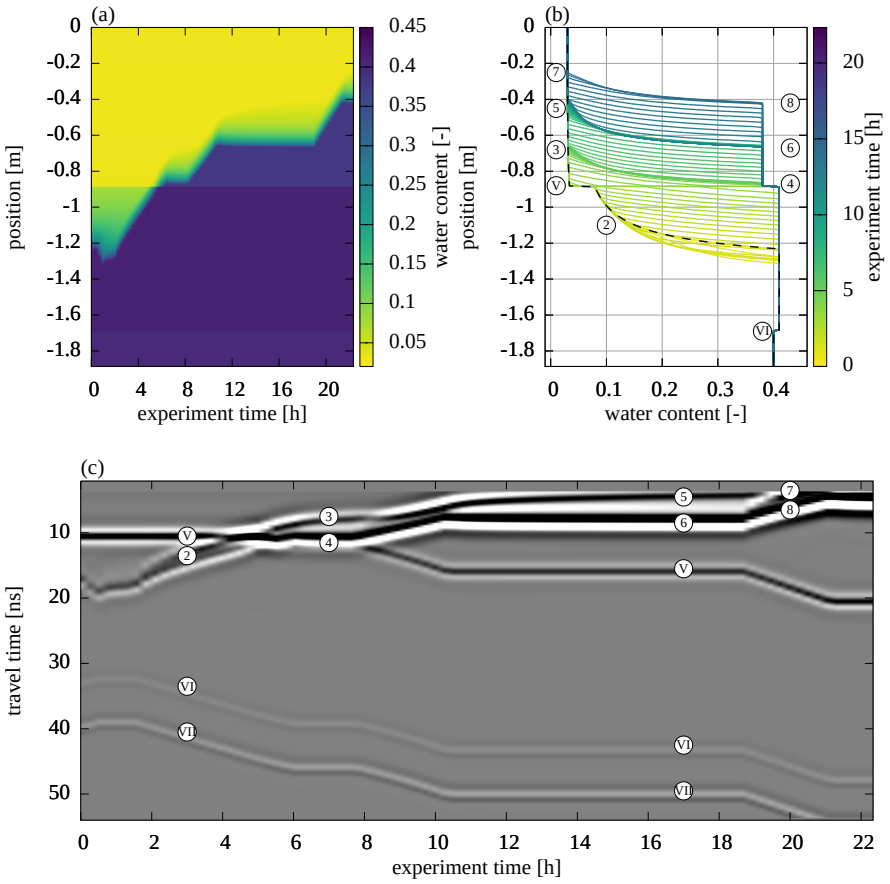

Figure 6.7 The true synthetic data are simulated with hydraulic parameters that represent coarse-textured sandy soils (Table 6.2). (a) and (b) show different representations of the simulated water content. In (b) the initial water content distribution is marked with a black dashed line. (c) shows the simulation of the GPR signal. The imbibition leads to a characteristic transition zone reflection (marker (2)). The temporal evolution of this reflection is sensitive to the initial water content distribution, the soil water characteristic and the hydraulic conductivity function. The data shown are processed according to Sect. 6.2.1 except for the normalization. In contrast to the data that are evaluated, the shown radargram is normalized to the maximum absolute amplitude of all traces, facilitating the visual comparison of the traces. The markers are defined in Fig. 6.12.

kinks increases, such that the two reflected wavelets (3) and (4) are separable. Since the water content changes continuously, the signal in-between these wavelets is a superposition of infinitesimal reflections which also contain detailed information about the form of the transition zone. Additionally, the reflection (3) scans the initial water content distribution, which in steady state corresponds to the soil water characteristic. With progressing equilibration, the amplitude of reflection (3) decreases as the transition zone smoothes. The GPR signal of the subsequent imbibition and equilibration phases ((5),

(6) and (7), (8)) show similar behavior and emphasize the relatively long time scale for equilibration of sandy materials.

In summary, this numerical simulation confirms qualitatively (i) that the dynamics of the fluctuating groundwater table are sensitive to both the soil water characteristic and the hydraulic conductivity function and (ii) that the transition zone reflection leads to tractable reflections during the imbibition step.

Results and discussion After the inversion of the synthetic data, the soil water characteristics estimated for material A (Fig. 6.8a) exhibit a similar curvature but are shifted. Both the parameters h_0 and λ influence the shape of the desaturated transition zone. Hence, merely evaluating the shape of the desaturated part of the transition zone is not necessarily sufficient to uniquely identify both parameters leading to large correlation coefficients. However, parameter h_0 additionally determines the extent of the capillary fringe. If the evaluation is also sensitive to the extent of the capillary fringe, h_0 can be uniquely identified which significantly decreases the correlation between h_0 and λ. Hence, the strong correlation of the parameters ${h_0}^{\mathrm{C}}$ and ${\lambda}^{\mathrm{C}}$ (-0.7, Fig. 6.9) indicates that the evaluation is more sensitive to the shape of the transition zone than to the extent of the capillary fringe.

Table 6.2 The mean and the standard deviation are calculated using the resulting parameters of the 10 best ensemble members estimated from synthetic data (Sect. 6.3.1.2). The corresponding material functions are given in Fig. 6.8. Notice that the true parameter set is within the standard deviation of the mean parameter set.

material	parameter	truth	mean results
C	h_0 [m]	-0.15	-0.13 ± 0.02
	λ [−]	3.5	3.2 ± 0.3
	K_s [m s^{-1}]	$10^{-3.5}$	$10^{-3.4 \pm 0.2}$
	τ [−]	0.5	0.6 ± 0.2
	$\theta_{\mathrm{w,s}}$ [−]	0.38	0.38 ± 0.01
	$\theta_{\mathrm{w,r}}$ [−]	0.03	0.027 ± 0.006
A	h_0 [m]	-0.20	-0.199 ± 0.008
	λ [−]	2.5	2.8 ± 0.7
	K_s [m s^{-1}]	$10^{-4.5}$	$10^{-4.47 \pm 0.05}$
	τ [−]	0.5	0.4 ± 0.5
	$\theta_{\mathrm{w,s}}$ [−]	0.41	0.41 ± 0.02
	$\theta_{\mathrm{w,r}}$ [−]	0.05	0.06 ± 0.02
gravel	$\theta_{\mathrm{w,s}}$ [−]	0.40	0.40 ± 0.03
architecture	d^{V} [m]	1.00	0.99 ± 0.02
	d^{VI} [m]	0.20	0.20 ± 0.01

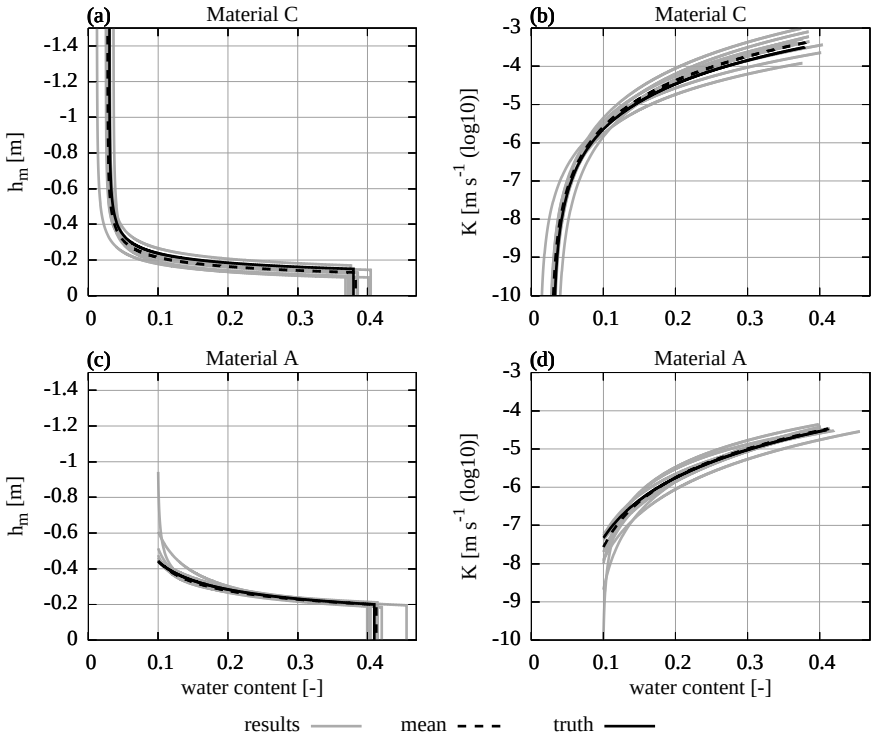

Figure 6.8 The resulting material parameters estimated from synthetic data are shown for the 10 best ensemble members (Sect. 6.3.1.2) together with the mean of these parameter sets and the true parameter set (Table 6.2). The plot range of the material functions is adjusted to the water content range of the data.

Since the architecture is a layered structure where material C is located above material A (Fig. 6.5), the water content in material C contributes to the travel time of the other reflections. This introduces correlations of ${\theta_{\mathrm{w,s}}}^{\mathrm{A}}$ with all the parameters associated with the soil water characteristic of material C. A high correlation of parameters indicates that the inverse problem is not well-posed. This typically increases the number of local minima and thus the uncertainty of the parameters.

The saturated hydraulic conductivity of material A (Fig. 6.8d) is approximately 1 order of magnitude smaller than the saturated hydraulic conductivity of material C (Table 6.2). Since the 1D architecture is forced at the lower boundary, the hydraulic conductivity of material A limits the water flux into material C. Hence, the data are not sensitive to ${K_{\mathrm{s}}}^{\mathrm{C}}$. Consequently, the uncertainty of the hydraulic conductivity in material C decreases for low water contents as the reflection at the additional kink (markers 3 and 5 in Fig. 6.7) is sensitive to the hydraulic conductivity. The hydraulic conductivity function (Eq. 3.22) is not unique if K_{s} is not fixed. This leads to a strong correlation of the parameters ${K_{\mathrm{s}}}^{\mathrm{C}}$ and τ^{C} (0.6, Fig. 6.9). Note that the uncertainty of the saturated

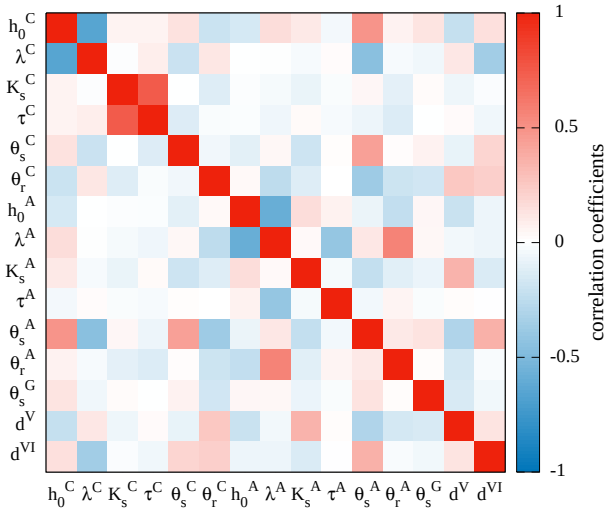

Figure 6.9 The correlation coefficients for the mean parameter set show in particular that the porosity of the gravel ($\theta_{\mathrm{w,s}}{}^{\mathrm{G}}$) as well as the position of the material layers (d^{V} and d^{VI}) can be reliably estimated from single-channel CO GPR when evaluating both signal travel time and amplitude.

hydraulic conductivity of material A also influences the uncertainty of the hydraulic conductivity of material C.

The uncertainty of the soil water characteristic of material A (Fig. 6.8c) is largest for low water contents, because there are only few data points available. In particular, this increases the uncertainty of λ^{A} (± 0.7, Table 6.2). The material properties of the unsaturated material A are only monitored during the first ≈ 5 h of the experiment and are independent of the largest part of the other data. This regularizes the optimization leading to fewer local minima. Similar to material C, the parameters ${h_0}^{\mathrm{A}}$ and λ^{A} are strongly correlated (-0.6). Yet, the uncertainty in ${h_0}^{\mathrm{A}}$ is relatively small (± 0.008, Table 6.2), mainly because it is essentially uncorrelated to other parameters. In contrast, the parameter $\theta_{\mathrm{w,s}}{}^{\mathrm{A}}$ is correlated to the parameters ${h_0}^{\mathrm{C}}$, λ^{C}, $\theta_{\mathrm{w,s}}{}^{\mathrm{C}}$, and $\theta_{\mathrm{w,r}}{}^{\mathrm{C}}$, because wrong parameters for material C introduce changes in the total water content which can be partially balanced out by adjusting $\theta_{\mathrm{w,s}}{}^{\mathrm{A}}$.

The uncertainty of the saturated hydraulic conductivity of material A (Fig. 6.8d) is comparably small, because a large fraction of the data are influenced by this parameter. Hence, the parameters τ^{A} and ${K_{\mathrm{s}}}^{\mathrm{A}}$ are only very weakly correlated.

The correlation coefficients (Fig. 6.9) also show that both the permittivity and the thickness of the gravel layer can be estimated reliably with the presented evaluation method using travel time and amplitude information of a single-channel time-lapse CO radargram. Evaluation methods that merely exploit the signal travel time (e.g., Gerhards et al., 2008) require a multi-channel CO approach to achieve this goal.

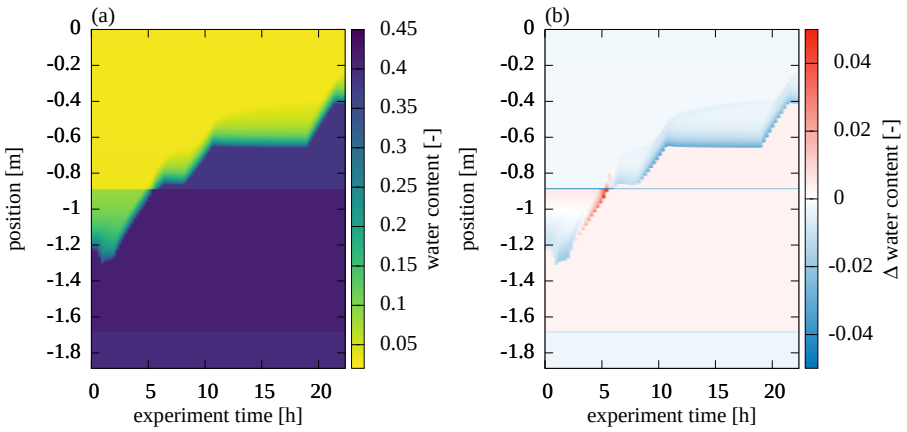

Figure 6.10 This figure shows (a) the water content distribution simulated with the resulting mean parameter set and (b) the difference to the true water content distribution (Fig. 6.7). The mean absolute deviation of the volumetric water content is 0.004. The overall balance of the volumetric water content can be characterized by calculating the mean of the summed difference per grid cell over all measurement times which yields -0.003. Hence, the mean parameter set generally underestimates the water content in the profile. The constant deviations above as well as below the groundwater table and in the gravel layer are due to small deviations in the estimated parameters ${\theta_{\mathrm{w,r}}}^{\mathrm{C}}$, ${\theta_{\mathrm{w,s}}}^{\mathrm{C}}$, ${\theta_{\mathrm{w,s}}}^{\mathrm{A}}$, and ${\theta_{\mathrm{w,s}}}^{\mathrm{G}}$. Still, the standard deviation of the estimated parameters contains the true parameter values (Table 6.2).

In order to further investigate the quality of the mean parameter set, the resulting water content distribution was simulated and the true water content distribution was subtracted (Fig. 6.10). Due to the narrow pore size distribution of the sandy material, small deviations in the parameters h_0 and λ lead to large differences in the volumetric water content above the capillary fringe ($\approx \pm 0.04$). Combined with deviations in the position of the material interface, the largest differences in volumetric water content reach up to 0.17. Still, the mean absolute deviation of the volumetric water content is 0.004.

The remaining deviations in soil water content after the parameter estimation cause residuals in the GPR signal (Fig. 6.11). These residuals are most evident for the reflection at the gravel layer (VI). The bias of its travel time shows that the total water content above the gravel layer is underestimated with the mean parameter set. This bias is essentially balanced out with the properties of the gravel layer. However, the reflection originating from the basement of ASSESS (VII) reveals residuals that decrease as soon as the groundwater table is above the initial groundwater table. This indicates (i) deviations in the initial water content distribution and (ii) that the hydraulic dynamics during the initial drainage phase are not correctly represented.

Similar to the analysis of the deviation in water content (Fig. 6.10), the largest residuals in the unsaturated part of the domain are found where the groundwater table is crossing the interface of materials A and C. This indicates that the interference of the

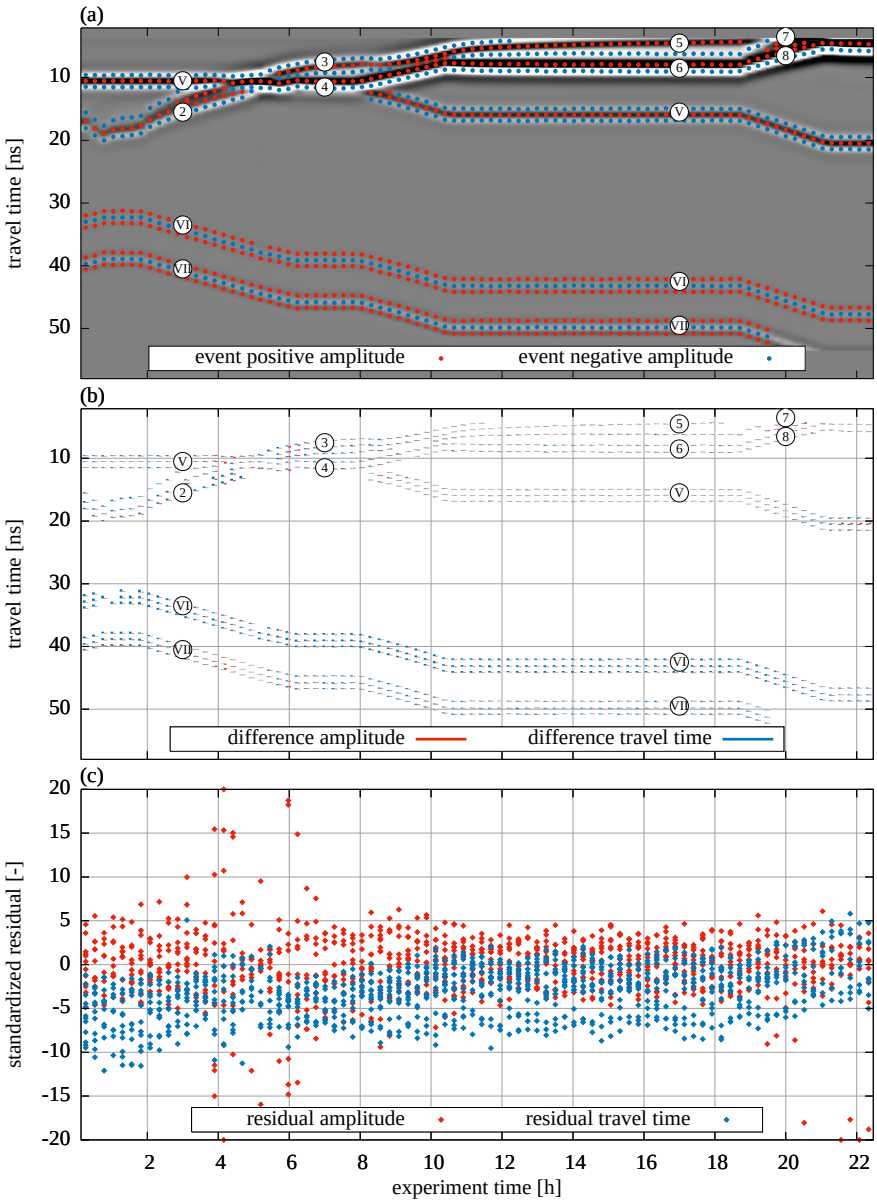

Figure 6.11 The evaluation of the synthetic GPR data is separated into three parts: (a) shows the selected events (Sect. 6.2.1.3) which are evaluated with the optimization. The data shown are processed according to Sect. 6.2.1 except for the normalization. In contrast to the data that are evaluated, the shown radargram is normalized to its maximum absolute amplitude, facilitating the visual comparison of the traces. (b) shows the resulting differences in travel time and amplitude of the mean parameter set. The differences of the amplitude are given in arbitrary units which are consistently used in this study. For the synthetic data, these differences are practically invisible. For the measured data, however, they are more clearly recognizable (Fig. 6.11). (c) shows the standardized residuals, essentially zooming into the small differences given in (b). Note that outliers are set onto the boundary. The markers are defined in Fig. 6.12.

reflection still contains information that could not be exploited with the used parameter estimation procedure.

6.3.2.2 Measured data

Phenomenology Before starting the experiment, a single-channel CO GPR measurement was acquired that allows to analyze the initial state of ASSESS revealing material interfaces as well as compaction interfaces (Fig. 6.12). Typically, it is difficult to associate the reflections based on an individual radargram. In particular the reflection of the compaction interface (iv) close to the reflection of the initial position of the groundwater table (1) is difficult to distinguish from reflections originating from material interfaces.

ASSESS is confined by walls at all four sides. Reflections from confining walls are most visible around 1 m (W) but influence the signal for more than 2 m. The walls parallel to the measurement direction are approximately 4 m apart from each other. Thus, it is assumed that the measurement is also influenced by reflections originating from those walls. The reflection of the edge of the L-element (L) is particularly prominent.

As an aside, closer scrutiny of the radargrams reveals that the CO and the time-lapse CO data were measured with different but structurally identical antennas. Thus, in particular the measured GPR signals of the direct wave and the ground wave are slightly different.

The single-channel time-lapse CO GPR measurement (Fig. 6.12) was recorded at 17.05 m (Fig. 4.2). As the groundwater table is raised, the reflection originating from the groundwater table (2) separates from the reflection of the compaction interface (iv). After passing the material interface (V), the reflection (2) splits into two separate reflections (3) and (4). This is due to the dependency of the hydraulic conductivity on the water content and was also identified for the synthetic data (Sect. 6.3.2.1). Since the transition zone is smoothing during the equilibration phase, the amplitude of reflection (3) decreases and the distance of the reflections (3) and (4) increases. During the subsequent imbibition step, the reflections are separated.

Corresponding to the analysis of the synthetic data (Sect. 6.3.2.1), the effects of the smoothing water content distribution are most clearly visible during the equilibration phase for the reflections (5) and (6). However, the associated measured signals interfere with the direct wave, the ground wave, and the reflection from the compaction interface (i) which makes the identification of the hydraulic effects difficult. The reflections (7) and (8) measured during the final imbibition phase confirm the previous observations.

Together with the water content distribution, the time-lapse GPR data also contain information about the subsurface architecture. However, separating the signal contribution from the subsurface architecture and the hydraulic dynamics is not always possible. Here, this is most prominent for the reflection of the material interface (V). Initially, the amplitude of this reflection is large, because the water content in material C is near the residual water content, whereas the water content in material A is significantly higher

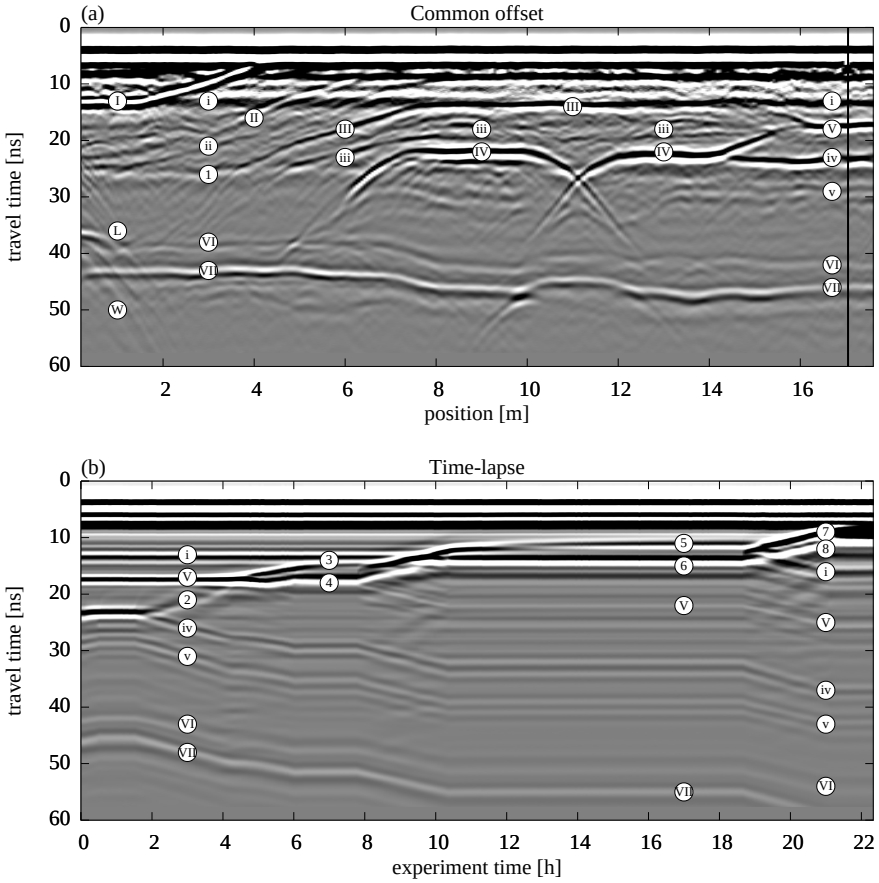

Figure 6.12 (a) shows a CO measurement of the hydraulic state of ASSESS at the beginning of the experiment. For this measurement, the antenna was moved over the site at one point in time. The temporal evolution of the subsequent hydraulic dynamics was monitored with a stationary antenna at the position indicated with the vertical black line. The resulting time-lapse measurement data are shown in (b). Both radargrams are measured with internal channels with an antenna separation of 0.14 m. Except for the normalization, the data are processed according to Sect. 6.2.1. In contrast to the quantitative evaluation, the radargrams are normalized to their maximal absolute amplitude, facilitating the visual comparison of the traces. The markers – uppercase Roman numeral markers for material interfaces (I, II, III, IV, V, VI, and VII), lowercase Roman numeral markers for compaction interfaces (i, ii, iii, iv, and v), and Arabic numeral markers for reflections originating from the water content distribution – are used consistently in this paper and are further explained in the text.

at the material interface. As soon as both materials are water saturated, the amplitude of the material interface reflection (V) is low, because the effective porosities of the two materials are similar. Thus, the amplitude of the reflected signal originating from the material interfaces may change depending on the hydraulic state. Additional information about the subsurface architecture can be inferred from the reflection at the material

interface between material A and the gravel layer (VI) and from the reflection at the material interface of the gravel layer and the concrete basement (VII). These reflections are in particular suitable to analyze the total change of water content over time.

In summary, the characteristic properties of the transition zone reflection during the imbibition and equilibration steps that were identified in the simulation (Fig. 6.7) can also be identified in the measured data (Fig. 6.12).

Results and discussion Since the GPR measurements cover only a small portion of the subsurface architecture, the hydraulic representation is restricted to 1D (Sect. 6.3.1.1). Hence, 2D effects such as lateral flow are neglected. This has to be considered during the event selection of the measured data (Sect. 6.2.1.3). Therefore, the focus of this study is on the evaluation of the imbibition phase of the experiment, because the effect of lateral flow in fluctuating groundwater table experiments is largest during drainage and close to the capillary fringe (Sect. 5.5.1.3).

Investigating the resulting material properties of the inversion (Fig. 6.13), the main findings, which were discussed previously for the mean parameters for the synthetic data (Sect. 6.3.2.1) can also be identified for the measured data. These findings comprise (i) the shift in the soil water characteristic of material C, (ii) the large uncertainty of the saturated hydraulic conductivity of material C, (iii) the high uncertainty of the soil water characteristic of material A for low water contents, and (iv) the high sensitivity to ${K_\mathrm{s}}^\mathrm{A}$.

Compared to the uncertainties based on synthetic data (Table 6.2), the uncertainty of the resulting mean parameters (Table 6.3) mostly increased. Except for four parameters, the parameters estimated from TDR measurements (Table 5.5) are within 1 standard deviation of the mean parameter set. The deviations of the other four parameters are clearly visible in Fig. 6.13 and will be analyzed in the following.

The parameter ${\theta_\mathrm{w,r}}^\mathrm{C}$ estimated from the GPR data is approximately a factor of 3 larger than the estimated value based on the TDR data (Table 6.3). Essentially, there are three main reasons for this. First, by evaluating the travel time of reflection (V), the integral water content is included in the inversion. This also comprises the compaction interface (i) which is not represented in the model. At the beginning of the experiment, the amplitude of this reflection is comparable to the amplitude of the reflection originating from the interface of material A and C (V). Notice that the amplitude of the reflection (i) does not vanish, but merely decreases when the material is saturated at the end of the experiment (Fig. 6.12). This indicates that this reflection originates from changes in both the small-scale texture of the material and the stored water content at the beginning of the experiment. Hence, since this compaction interface is not represented in the model, the resulting ${\theta_\mathrm{w,r}}^\mathrm{C}$ is increased coping for this representation error. Second, a deviation in the position of the groundwater table with reference to the antenna position at the surface can be partially adapted by changing ${\theta_\mathrm{w,r}}^\mathrm{C}$. As the position of the surface is subject to change over the years, the measurements of the groundwater table are referenced to a fixed point at the end of the groundwater well, leaving the exact position of the surface relative to the groundwater table uncertain. According to Buchner et al.

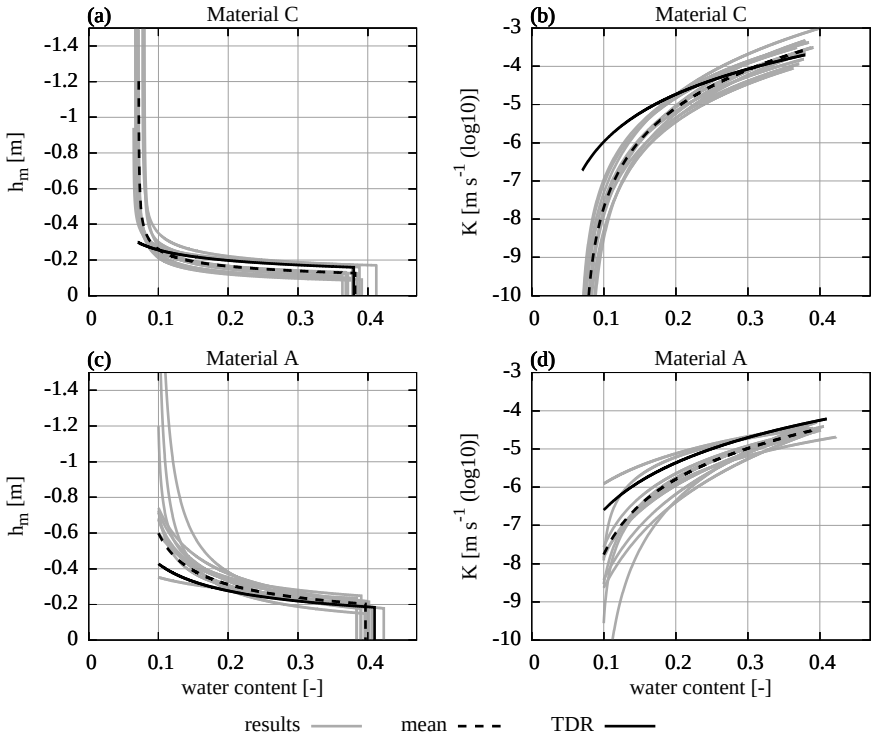

Figure 6.13 The resulting material parameters estimated from measured data are shown for the 10 best ensemble members (Sect. 6.3.1.2) together with the mean of these parameter sets (Table 6.3) and a reference parameter set determined from TDR data acquired during the same experiment (Table 5.5). The deviation from the reference parameters can be explained with representation errors in GPR analysis (e.g., neglecting compaction interfaces) and missing data (e.g., for low water contents in material A). The plot range of the parameters is adjusted to the water content range of the corresponding data.

(2012), the accuracy of the ASSESS architecture when compared to GPR measurements is ±0.05 m. The estimation of an offset to the Dirichlet boundary could mitigate this problem, but would in any case increase the number of local minima significantly making the optimization process less stable. Third, analyzing the TDR data, it is found that an underestimation of ${\theta_{\mathrm{w,r}}}^{\mathrm{C}}$ is likely due to the lack of TDR measurements at low hydraulic potential. Hence, the sensitivity of the TDR data to ${\theta_{\mathrm{w,r}}}^{\mathrm{C}}$ is low.

The resulting value for parameter τ^{C} for the GPR evaluation is a factor of 2 larger compared to the evaluation of the TDR data. This parameter adjusts the hydraulic conductivity for the unsaturated material and is mainly determined with the reflections (3) and (5) originating from the additional kink during imbibition (Fig. 6.12). These reflections exhibit a small amplitude for low water contents. However, both reflections interfere with the rather prominent reflection originating from the compaction interface (i). Additionally, the reflection (5) also interferes with parts of the direct and the ground wave. Hence, the travel time of these reflections hardly changes leading to an

underestimation of the hydraulic conductivity for low water contents resulting in an overestimation of parameter τ^{C}.

Similar to parameter ${\theta_{\mathrm{w,r}}}^{\mathrm{C}}$, the parameter ${\theta_{\mathrm{w,r}}}^{\mathrm{A}}$ estimated from the GPR evaluation is approximately a factor of 3 smaller than the result from the TDR evaluation. However, this parameter can only be approximated evaluating the GPR data, because they lack events that are influenced by low water content.

The resulting value for parameter ${K_{\mathrm{s}}}^{\mathrm{A}}$ is smaller by a factor of 2 for the GPR evaluation compared to the result from the TDR evaluation. This parameter limits the flux through the lower boundary, because the domain is forced with a Dirichlet boundary condition. Hence, the parameter can be used to cope with errors in the boundary condition. Forcing ASSESS with a groundwater well instantiates a 3D flux (Sect. 5.5.2.2).

Table 6.3 The mean and the standard deviation are calculated using the resulting parameters of the 10 best ensemble members estimated from measured data (Sect. 6.3.1.2). The corresponding material functions are shown in Fig. 6.13. The reference parameters for the materials A and C are determined from TDR data acquired during the same experiment (Table 5.5). Note that the standard deviation for these reference parameters are determined from a single Levenberg–Marquardt run and thus are only representative for one local minimum. Also, these standard deviations are given with the understanding that they are specific to the applied algorithm and will change for different algorithm parameters. Hence, these standard deviations are in particular not suitable to compare the precision of the TDR and GPR evaluation. Notice that for the TDR evaluation the porosity of the materials is assumed to be known from core samples. The reference parameters for the subsurface architecture are calculated from ground truth measurements acquired during the construction of ASSESS. The corresponding standard deviations are given according to Buchner et al. (2012).

material	parameter	reference	mean results
C	h_0 [m]	-0.159 ± 0.004	-0.13 ± 0.03
	λ [−]	3.28 ± 0.02	3.3 ± 0.7
	K_{s} [m s^{-1}]	$10^{-3.70\pm0.02}$	$10^{-3.6\pm0.3}$
	τ [−]	0.74 ± 0.06	1.4 ± 0.4
	$\theta_{\mathrm{w,s}}$ [−]	0.38	0.38 ± 0.01
	$\theta_{\mathrm{w,r}}$ [−]	0.026 ± 0.002	0.071 ± 0.005
A	h_0 [m]	-0.184 ± 0.005	-0.20 ± 0.03
	λ [−]	1.94 ± 0.07	2.1 ± 0.7
	K_{s} [m s^{-1}]	$10^{-4.212\pm0.004}$	$10^{-4.5\pm0.1}$
	τ [−]	0.33 ± 0.07	0.4 ± 1.0
	$\theta_{\mathrm{w,s}}$ [−]	0.41	0.40 ± 0.01
	$\theta_{\mathrm{w,r}}$ [−]	0.025 ± 0.004	0.07 ± 0.03
gravel	$\theta_{\mathrm{w,s}}$ [−]		0.41 ± 0.02
architecture	d^{V} [m]	0.99 ± 0.05	0.97 ± 0.02
	d^{VI} [m]	0.13 ± 0.05	0.17 ± 0.02

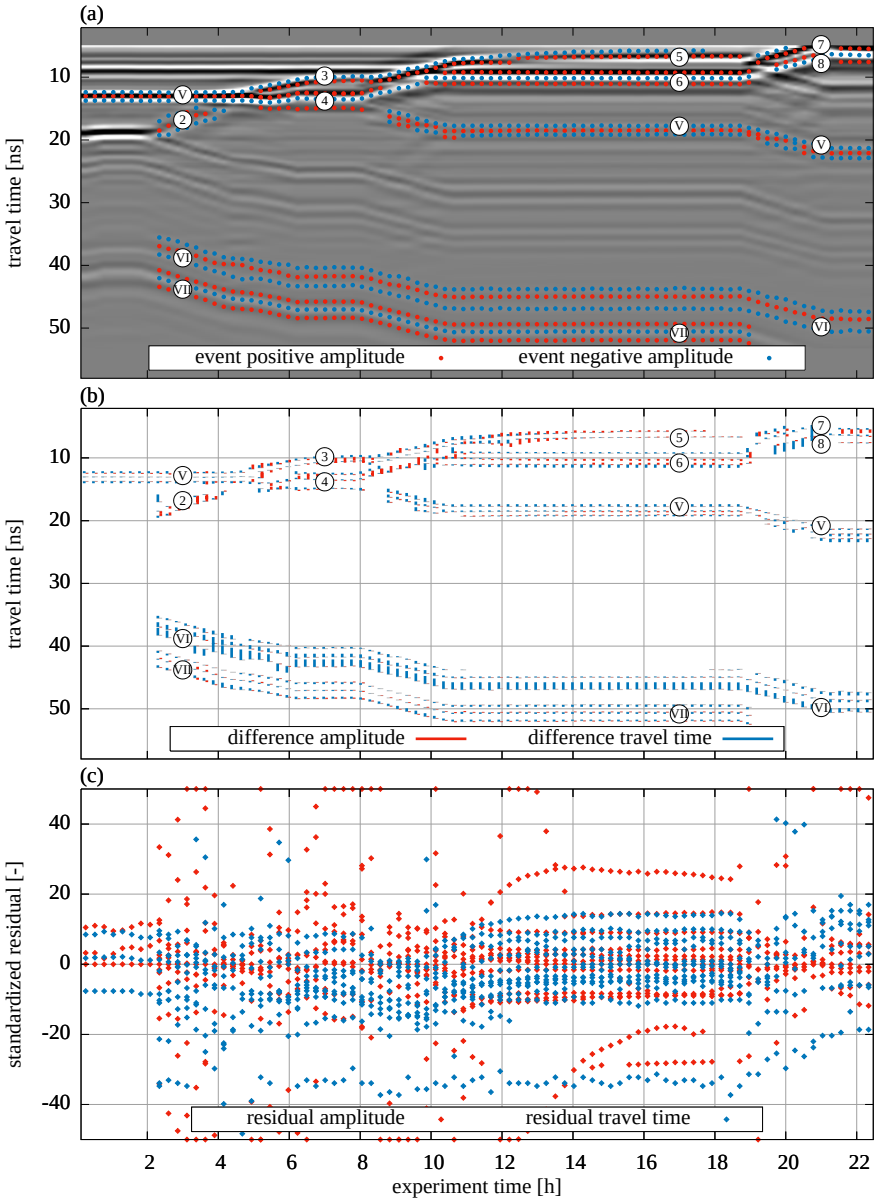

Figure 6.14 Analogous to Fig. 6.11 but for measured data. Since the measurement data acquired with a stationary antenna cannot spatially resolve the lateral flow present in the initial drainage phase, the measured events of the hydraulic dynamics during the first 2 h are neglected.

Since this 3D water flux is not represented, the hydraulic potential at the bottom and thus also the water flux are too large. This is compensated by the parameter estimation procedure with decreasing $K_s{}^A$.

Concerning the position of the material interfaces, it is found that the estimated interface position of materials A and C (d^V) corresponds well to the ground truth mea-

surements acquired during the construction of the ASSESS site (Table 6.3). In contrast, the estimated position of the gravel layer (d^{VI}) deviates from the ground truth measurements. However, the estimate is still within the uncertainty of the ground truth measurements when compared to GPR measurements.

An analysis of the remaining residuals in travel time after the optimization (Fig. 6.14) shows that deviations in the width of the reflected wavelet contribute to the residuum significantly, in particular for reflections (V), (VI), and (VII). At the beginning of the experiment, the simulated wavelet is too broad for reflection (V), whereas it is too narrow for reflections (VI) and (VII). This is in particular noticeable for the residuals for reflection (VI) which are the major contribution to the cost function. Of all the events in this wavelet, the events with the longest travel time exhibit the largest residuals. The difference in the width of the reflected wavelet can be explained with the roughness of the material interfaces (Dagenbach et al., 2013). Due to the large grain size of the gravel, the real material interface is rougher than its representation. This also explains the partly non-symmetric broadening of the measured compared to the simulated wavelet of reflection (VI).

The measured reflection (6) interferes with the reflection of the compaction interface (i) leading to a compressed reflected wavelet in the measurement. Similarly, reflections (3) and (5) also interfere with the compaction interface (i). Since interferences cannot be correctly evaluated if not all contributions are represented, this analysis shows that representing compaction interfaces is relevant in ASSESS.

As a side remark, note that the error originating from assuming a constant soil temperature for the calculation of the relative permittivity of water is relatively small regarding the total residuum. However, it is worth noting that the corresponding residuals easily exceed 1 standard deviation in signal travel time (Fig. 3.23).

The distribution and the support of the measurement data (i) differs between the TDR sensors and GPR measurements (Fig. 4.2), (ii) relates directly to the applicability of the resulting parameters for the different evaluations, and (iii) influences the quantitative effect of different representation errors. In the reference analysis, the TDR sensors are distributed over a 2D slice of ASSESS measuring in all available materials (Fig. 4.2). Yet, their measurement volume is limited to the position of the sensors yielding the average permittivity along the TDR rods. Hence, these measurements are subject to representation errors such as small-scale heterogeneity or uncertainty in the sensor position (Sect. 5). In contrast, the GPR measurement data do not cover the whole ASSESS site and their support is dependent on the evaluated events of the wavelet. This includes the whole depth average (travel time) and the contrast (amplitude) of both permittivity and electrical conductivity. Hence, these measurement data are subject to representation errors such as neglected compaction interfaces and the roughness of the material interfaces. Hence, the previous analysis illustrates how GPR-determined parameters can differ from TDR-determined ones making joint evaluation procedures both challenging and promising, since they open a window to the soils' multi-scale nature.

6.4 Study 2: Transient hydraulic state and moving antenna

In the previous section, the evaluation and optimization methods presented in Sect. 6.2.1 and Sect. 6.2.2 have been applied to time-lapse GPR measurement data acquired with a stationary antenna, in order to determine the subsurface architecture and the corresponding soil hydraulic material properties. In this section, these methods are used to estimate the positions of material interfaces in a 2D subsurface architecture and the corresponding soil hydraulic material properties based on synthetic time-lapse GPR measurement data acquired with a moving antenna. Therefore, a parameterization model was implemented that generates a subsurface architecture that is similar to the one in ASSESS. As in the previous sections, this subsurface architecture is forced with a fluctuating groundwater table in order to provide the necessary data for the optimization. After the presentation of the setup of the study (Sect. 6.4.1), the results are discussed subsequently in Sect. 6.4.2.

6.4.1 Setup

6.4.1.1 Implementation

The estimation of a 2D subsurface architecture requires a suitable parameterization. The subsurface architecture that is the basis for this study is shown in Fig. 6.15. The vertical position of the material interfaces is essentially parameterized with the parameters d^{III}, d^{V}, d^{IVa}, and d^{IVb}. The structured grid with 100×100 grid cells for the hydraulic simulation is generated automatically based on these parameters. The true position of these synthetic material interfaces is approximately 0.1 m lower than their counterparts in the real ASSESS site in order to avoid interferences of reflections originating from these interfaces with the direct signal. The gravel layer at the bottom of the site has an extent of 0.15 m. In contrast to the previous study (Sect. 6.3), the extent of the gravel layer is not estimated in this study. Note that only the materials required for the hydraulic model are shown in Fig. 6.15. For the electromagnetic model, (i) a 0.3 m thick concrete basement is added below, (ii) 0.2 m thick concrete walls are added at the sides, and (iii) a 0.3 m thick layer of air is added above the subsurface architecture. The spatial resolution of the electromagnetic simulation is set to ≈ 0.007 m.

The initial hydraulic state is modeled using static hydraulic equilibrium with a groundwater table 0.1 m above the concrete layer. Corresponding to Sect. 3.2.3.2, the source current density at the transmitter generates a Ricker wavelet with a center frequency of 400 MHz. The antenna separation a between the transmitter and the receiver is set to 0.14 m.

The boundary condition for the hydraulic simulation is implemented using a Dirichlet boundary condition during the forcing phases at the position of the groundwater well (between 18.0 m and 18.5 m in Fig. 6.15). The other boundaries are set to a Neumann no-flow boundary condition. The Dirichlet boundary condition in the well is raised

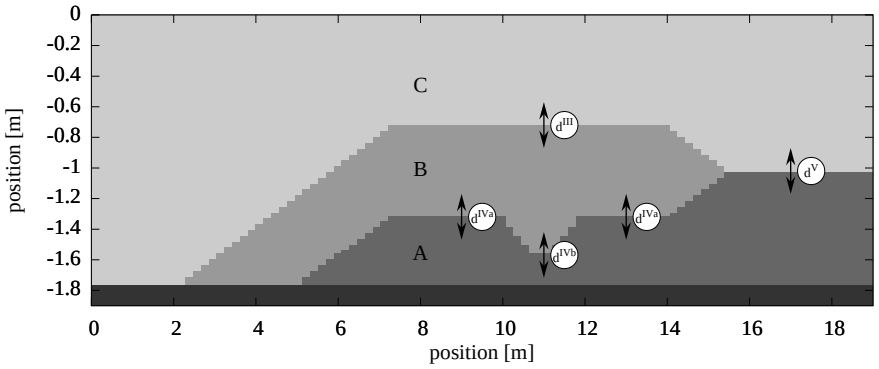

Figure 6.15 Based on this simplified subsurface architecture, the suitability of the proposed methods (Sect. 6.2) to simultaneously estimate the subsurface architecture and the corresponding soil hydraulic material properties based on synthetic time-lapse CO radargrams is investigated. This subsurface architecture is created with support points that are connected linearly. In this study, the horizontal position of these support points remains constant. Only their vertical position and thus the vertical position of the material interfaces d is changed. The figure shows the resulting structured grid which is used for the hydraulic simulation. For the electromagnetic simulation, this architecture is extended with a concrete basement below, concrete walls at the sides, and an air layer at the top.

linearly from 0.1 m to 1.3 m over the course of 10 h. Afterwards, the hydraulic state equilibrates for 2 h using a Neumann no-flow boundary condition at the position of the groundwater well. During the subsequent drainage phase, the groundwater table is lowered to 1.3 m linearly over the course of another 10 h. Finally, the hydraulic state equilibrates again for 2 h using a Neumann no-flow boundary condition at the position of the groundwater well.

In order to keep this synthetic experiment close to reality, the true soil hydraulic material properties are chosen to be close to the results of the 2D TDR study (Table 5.5). The initial parameters are given subsequently together with the resulting parameters in Table 6.4. For the gravel layer, $\theta_{w,s}$ is set to 0.4 and K_s is set to the value estimated in the TDR study (Table 5.5). The remaining parameters are set to generic material properties for sand given in Carsel and Parrish (1988). However, since the gravel layer is completely saturated during this simulation, the parameters for the unsaturated hydraulic material properties are irrelevant for this simulation. For the electromagnetic model, the electrical conductivity of the domain is set to 0.0 $\mathrm{S\,m^{-1}}$ and the relative permittivity of the basement and the walls is set to 11.

6.4.1.2 Data generation

In order to generate the true synthetic radargrams, the Richards equation is solved with muPhi (Sect. 3.1.6) and the simulated hydraulic state is written in equidistant temporal steps of 4 h. The relative permittivity distributions are then used to simulate

the time-lapse CO radargrams with MEEPGPR (Sect. 3.2.3.2). Therefore, the initial position of the transmitter is set to 1.5 m and the final position of the receiver is set to 18.5 m. This distance is equidistantly partitioned, such that 20 traces are measured. The measurement time of 60 ns is resolved with 2048 samples.

The evaluation of the GPR data is realized as described in Sect. 6.2.1, except for (i) the 2D to 3D conversion which was not applied in order to reduce the computational cost and (ii) the cluster detection. In the previous study, the events are grouped into clusters by separating them at a single travel time (Sect. 6.3.1.1). This is possible due to the comparably simple shape of the radargram. However, time-lapse CO radargrams are typically more complicated. This requires the application of a different cluster detection algorithm. In this study, the clusters are detected with a binning algorithm that gathers all events within a bin width of 6 ns. The resulting cluster contains all neighboring bins that include events. This algorithm is applied for each trace separately.

According to the GPR evaluation method described in Sect. 6.2.1, the most important events are selected manually from those events that are detected in the true synthetic radargrams. Afterwards, the normalized travel time and amplitude of the selected events are perturbed with white Gaussian noise with a standard deviation of $\sigma_t = 5 \cdot 10^{-4}$ and $\sigma_A = 5 \cdot 10^{-3}$, respectively.

6.4.1.3 Parameter estimation

Compared to the previous study with a stationary antenna, the required computation time for the parameter estimation is larger due to (i) the increased domain size for the hydraulic and the electromagnetic simulation, (ii) the increased number of events to associate, and (iii) the increased total number of parameters describing the soil hydraulic material properties of the three materials as well as the subsurface architecture. Consequently, one iteration of the Levenberg–Marquardt algorithm takes approximately one day using 48 CPU cores.

The available computation time using the standard queue of the *bwforcluster* is limited to 6 h. The maximal number of jobs per user for another queue, that allows for jobs that run for up to 10 days, was limited to 2. Hence, it was not possible to run an ensemble analysis for this study on the *bwforcluster*. Alternatively, the convergence properties of a single run of the Levenberg–Marquardt algorithm (Sect. 6.2.2.2) and the simulated annealing algorithm (Sect. 6.2.2.3) are investigated for this data set.

The optimization algorithms are initialized with the same parameter set. This initial parameter set is chosen to be comparably close to the true parameter set in order to investigate the applicability of these locally convergent optimization methods. Except for $\theta_{\mathrm{w,s}}$ which is assumed to be known a priori, the same initial parameter set is used for all materials. This was done in order to (i) simplify the parameter estimation due to the limited computational resources available and (ii) investigate the ability of the algorithms to distinguish between the different materials based on the given data. The initial parameters for the subsurface architecture are disturbed in a structural manner.

Except for the position of the synclinal structure, the position of all material interfaces is initialized 0.1 m below the corresponding true position. The position of the synclinal structure is initialized 0.1 m above its true position. The true and the initial parameters are given together with the estimated parameters in Table 6.4.

6.4.2 Discussion

Phenomenology The true synthetic spatiotemporal water content distribution is shown in Fig. 6.16. The characteristic phenomena of the fluctuating groundwater table experiment described in Sect. 3.1.7 for a 1D simulation can also be identified in this 2D simulation. In particular, the vadose zone is more narrow (wider) during imbibition (drainage) compared to the equilibrium state due to the nonlinear dependency of the hydraulic conductivity on the water content. Thus, the water content remains relatively high after the drainage. Note that the hydraulic dynamics are differently pronounced in the three materials. Material A is mainly saturated and the minimal water content in this material is higher than for all other materials (≈ 0.05). In contrast, material B sees more of the hydraulic dynamics which uses nearly the full range of possible water contents ($[\theta_{\mathrm{w,r}}, \theta_{\mathrm{w,s}}]$). Material C is prevalent within the domain. Thus, the hydraulic dynamics in material C essentially uses the full range of available water contents. Also, the equilibration of the additional kink (Sect. 3.1.7) exclusively takes place in material C. Note that the groundwater table is close to the material interfaces for most measurement times to challenge the GPR data evaluation algorithm.

Results and discussion Although the initial parameter set is very close to the true parameter set, the resulting material properties (Fig. 6.17) show that the true material properties could not be identified reliably for all materials. This deviation is clearly visible for the individual material parameters in Table 6.4. The ability of the simulated annealing algorithm to identify the parameters precisely is limited due to its random parameter update (Eq. 3.93). In contrast, the Levenberg–Marquardt algorithm essentially exploits the sensitivity of the GPR evaluation to the parameters to propose parameter updates. Hence, the following evaluation essentially focuses on the results of the Levenberg–Marquardt algorithm.

From the 19 parameters estimated with the Levenberg–Marquardt algorithm, only 11 converged towards the right direction. This indicates local minima even this close to the true parameters. This interpretation is also supported by the resulting correlation coefficients from the final iteration (Fig. 6.18). The higher the number of correlation coefficients with large absolute values, the more difficult an accurate identification of the true parameters gets, because the inverse problem becomes increasingly ill-posed. This problem can be approached in at least two ways. The first way could be to simply apply different globally convergent optimization algorithms. These should be efficient and probably also gradient-free. Thus, optimization algorithms such as the NMS or the SCE-UA are likely to yield more favorable results. Following the second way is based

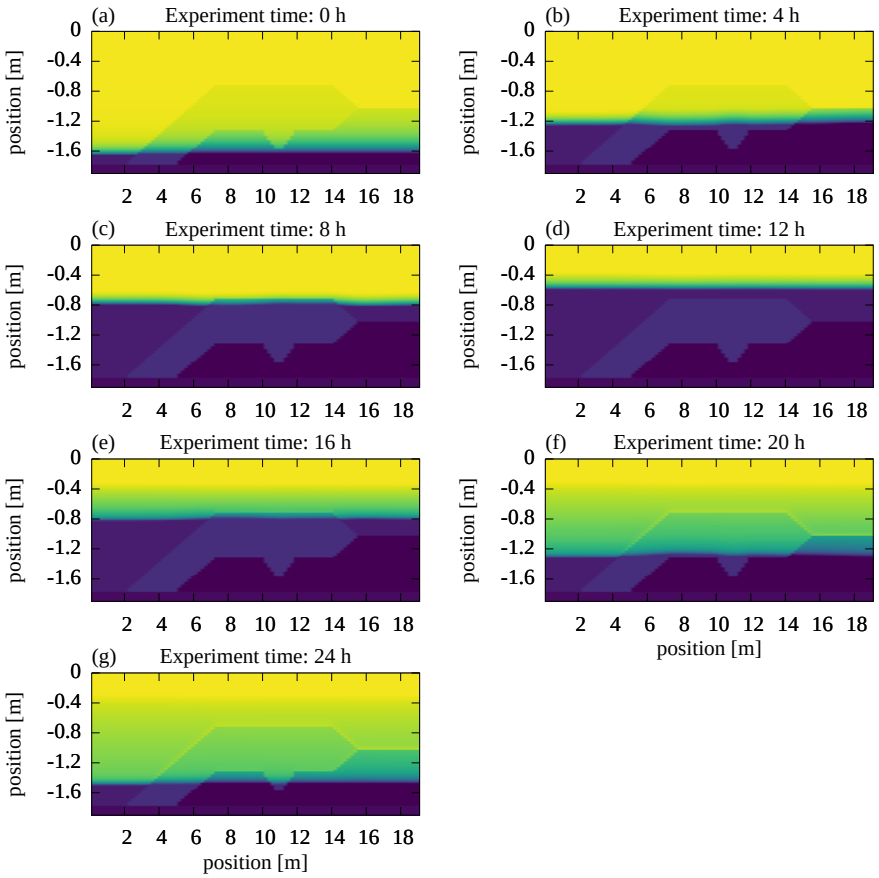

Figure 6.16 The true water content distribution for the synthetic study is shown in color code ranging from 0.02 (yellow) to 0.41 (blue) for all measurement times. Each of these water content distributions is used for the simulation of corresponding CO radargrams. The underlying subsurface architecture is given in Fig. 6.15. The hydraulic boundary condition of the experiment follows a rather simple three-step scheme, where groundwater table is (i) raised, (ii) kept constant, and (iii) finally set back to the initial value (Sect. 6.4.1.1).

on the understanding that the correlations also may originate at least partly from the formulation of the parameterization of the material properties. For the Mualem–Brooks–Corey parameterization, different parameter combinations can lead to similar material functions. This is in particular true, if the measurement data range does not cover the full water content range ($[\theta_{w,r}, \theta_{w,s}]$) and includes uncertainties in the hydraulic head and in the hydraulic conductivity. Thus, extending the data set with measurements that are more sensitive to the estimated parameters, could be a different approach. Hence, the choice of the optimal algorithm typically depends on the sensitivity of the available measurement data to the estimated parameters. The less sensitive the measurement data are to the parameters, the more an expensive search algorithm is required for finding the global minimum.

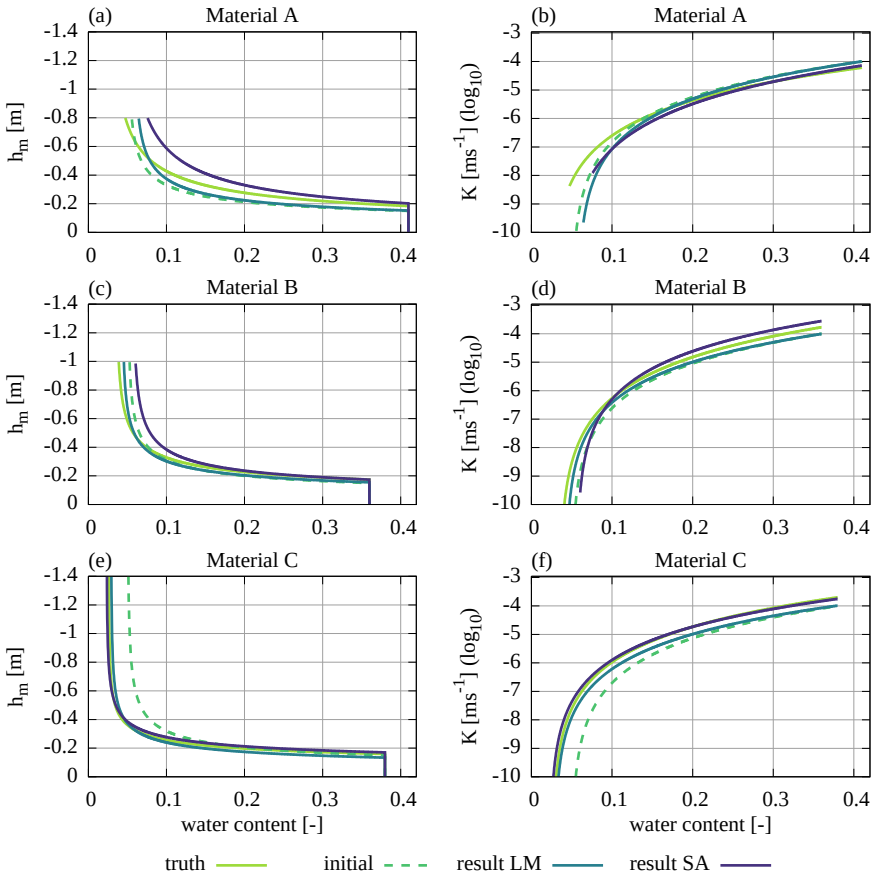

Figure 6.17 The initial material functions for the Levenberg–Marquardt algorithm (LM) and the simulated annealing algorithm (SA) are chosen to be close to the true material functions in order to investigate the convergence behavior of the two algorithms. Although the resulting parameter functions of the Levenberg–Marquardt algorithm are close to the true ones, the algorithm converges to a local minimum. This is in particular true for material A where the data are comparably sparse. Note that (i) the material functions of the Levenberg–Marquardt algorithm are not always between the initial and the true curve and (ii) the resulting parameters of the simulated annealing algorithm are drawn randomly and do not necessarily represent the sensitivity of the data to the parameters. In order to account for the available range of the measurement data, the material functions are only shown for a limited range of matric head.

The measurements in material A do not fully cover the dry part of the water content range. Hence, the resulting uncertainty is highest for those parameters that are sensitive to the material properties at low water content. Note that the evaluation of the extrema of two reflections, e.g., one originating from a material interface and another from the capillary fringe, is not necessarily sensitive to the form of the soil water characteristic, but merely to the integral water content between the reflectors. Hence, underestimation of the water content for high hydraulic head can be compensated with an overestimation

of the water content for low hydraulic head and vice versa. Note that this explains the crossing of the true and the estimated soil water characteristic using the Levenberg–Marquardt algorithm, which can be identified for materials A and B. This can explain the correlation between the parameters h_0 and λ which is evident for material B in this case (Fig. 6.18), but was also identified in the previous case study (Fig. 6.9).

The residuals remaining after the parameter estimation are given in the appendix for all radargrams (Figs. A.9–A.15 for the Levenberg–Marquardt algorithm and Figs. A.16–A.22 for the simulated annealing algorithm). Most of these residuals can be associated with errors in the hydraulic dynamics. Hence, it is assumed that an improved optimization procedure may provide better parameter estimates.

Table 6.4 Together with the true Mualem–Brooks–Corey material parameters for the synthetic study, the initial as well as the resulting parameters of the Levenberg–Marquardt algorithm (LM) and the simulated annealing algorithm (SA) are given. The saturated water content of the materials $\theta_{w,s}$ [−] is assumed to be known and 0.41, 0.36, 0.38 for the materials A, B, C, respectively. Note that the Levenberg–Marquardt algorithm converged only for 11 of the 19 parameters forwards the right direction. This indicates the existence of local minima. However, the parameters which contribute significantly to the residuum (e.g, ${\theta_{w,r}}^{C}$, d^{III}, d^{V}, and d^{IVa}) have been estimated correctly by the Levenberg–Marquardt algorithm. Due to the random parameter update, the individual resulting parameters of the simulated annealing algorithm do not necessarily reflect the sensitivity to the data.

material	parameter	truth	initial	result LM	result SA
A	h_0 [m]	−0.184	−0.150	−0.152	−0.202
	λ [−]	1.94	2.50	2.35	1.72
	K_s [m s^{-1}]	$10^{-4.2}$	$10^{-4.0}$	$10^{-4.0}$	$10^{-4.1}$
	τ [−]	0.33	0.50	0.50	0.52
	$\theta_{w,r}$ [−]	0.025	0.050	0.057	0.041
B	h_0 [m]	−0.174	−0.150	−0.155	−0.174
	λ [−]	2.54	2.50	2.56	2.44
	K_s [m s^{-1}]	$10^{-3.8}$	$10^{-4.0}$	$10^{-4.0}$	$10^{-3.6}$
	τ [−]	0.78	0.50	0.47	0.46
	$\theta_{w,r}$ [−]	0.035	0.050	0.043	0.056
C	h_0 [m]	−0.159	−0.150	−0.134	−0.170
	λ [−]	3.28	2.50	2.74	3.16
	K_s [m s^{-1}]	$10^{-3.7}$	$10^{-4.0}$	$10^{-4.0}$	$10^{-3.7}$
	τ [−]	0.74	0.50	0.48	0.59
	$\theta_{w,r}$ [−]	0.026	0.050	0.029	0.023
	d^{III} [m]	1.20	1.10	1.21	1.21
	d^{V} [m]	0.90	0.80	0.90	0.73
	d^{IVa} [m]	0.60	0.50	0.61	0.61
	d^{IVb} [m]	0.30	0.40	0.37	0.44

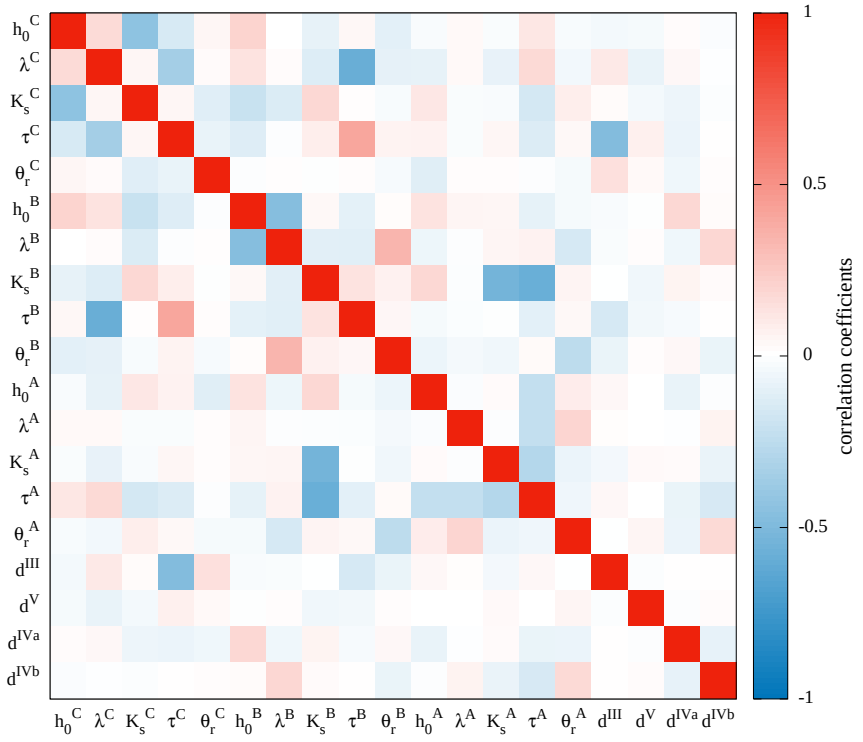

Figure 6.18 The correlation coefficients of the final iteration of the Levenberg–Marquardt algorithm also show off-diagonal entries with absolute values > 0.5. Strong correlations between parameters makes the accurate identification of the global minimum of the cost function more difficult.

The positions of the material interfaces are identified reasonably well by the Levenberg–Marquardt algorithm, except for the position of the synclinal structure (d^{IVb}). This highlights critical points concerning the GPR evaluation method proposed in Sect. 6.2.1. The synclinal structure is acquired with three traces and its signal does interfere with other reflections in two of the three traces. Additionally, the contrast in relative permittivity as well as the incoming energy are comparably low, as soon as the synclinal structure is below the groundwater table. This leads to a low amplitude of the reflection originating from the synclinal structure. Hence, this reflection is not detected for all parameter combinations during the parameter estimation. Additionally, the number of detected clusters can change for certain parameter combinations. If the number of clusters in the simulation does not match the number of clusters in the measurement, the information of the events of the cluster that could not be associated will not be used for parameter estimation. If only few data points are available and if the signal cannot be clearly separated, then it is likely that this information can't be used by the evaluation method (Sect. 6.2.1). This is the case for the position of the synclinal structure. Hence, in order to identify this parameter correctly, this part of the subsurface architecture should be covered with more traces. Additionally, the cluster and possibly also the event detection

algorithm have to be adjusted, e.g., by changing the hyperparameters of the algorithm, such that the required information can be extracted more reliably.

In summary, it was demonstrated that if (i) the parameterization function is unique and (ii) the signal required for the parameter estimation can be clearly identified and separated from other signals, then the correct parameters may be identified even with the Levenberg–Marquardt algorithm. This is in particular true for the parameters of the subsurface architecture d^{III}, d^{V}, and d^{IVa}. For the additional estimation of the soil hydraulic material properties, however, globally convergent optimization methods are required.

6.5 Summary and conclusions

In this study, a new heuristic semiautomatic approach to identify, extract, and associate relevant information from GPR data was proposed. Its suitability to accurately identify the subsurface architecture and the soil hydraulic material properties based on time-lapse GPR measurement data was analyzed. This was done with the help of two different studies of hydraulic systems that were forced with a fluctuating groundwater table. In study 1 (2), the resulting transient hydraulic state was observed with a stationary (moving) antenna.

In study 1, synthetic and measured time-lapse CO GPR data were first analyzed qualitatively. It was confirmed that a fluctuating groundwater table experiment introduces characteristic transition zone reflections that are likely to provide valuable information for the parameter estimation. Subsequently, the GPR data were analyzed using a sequentially coupled global–local optimization approach with preconditioning.

Starting from an ensemble of 60 Latin hypercube sampled initial parameter sets, a preconditioning step was implemented in which the simulated annealing algorithm and the Levenberg–Marquardt algorithm were sequentially applied to optimize the parameters based on a subsampled data set. Only a limited amount of iterations were allowed for both algorithms. The resulting parameters are then used as initial parameters for a final run of the Levenberg–Marquardt algorithm based on the full data set. Finally, the mean parameter set of the 10 best ensemble members is evaluated in detail.

Employing the presented GPR data evaluation method and optimization procedure on synthetic data shows that the true parameters are within 1 standard deviation of the evaluated mean parameter set. This parameter set also describes the true hydraulic dynamics with a mean absolute error in volumetric water content of 0.004. Additionally, it was found that the parameter correlations are mostly specific to the experiment type and the subsurface architecture. Using travel time and amplitude information in the evaluation allowed to estimate the effective permittivity and layer depth simultaneously with a single GPR channel.

The methods were also applied to the time-lapse GPR data measured at ASSESS. The GPR-determined subsurface architecture corresponds well to the ground truth. The resulting soil hydraulic material properties compare reasonably well to material properties determined from an independent analysis of TDR measurements which were acquired during the same experiment. Deviations of the parameters were discussed and basically associated with representation errors as well as the lack of available data. Critical representation errors comprise the neglected compaction interfaces as well as the roughness of certain material interfaces.

In study 2, synthetic time-lapse CO GPR data acquired with a moving antenna during a fluctuating groundwater table experiment were analyzed in order to estimate the 2D subsurface material distribution as well as the corresponding soil hydraulic material properties. The computational effort to simulate the time-lapse CO measurements is large. Hence, it was not possible to run an ensemble analysis on the *bwforcluster*. As a result, the investigation of this study was limited to a convergence analysis where the locally convergent algorithms were started close to the true parameters. It was found that in order to provide accurate parameters, the proposed methods require (i) a unique parameterization and (ii) a clearly identifiable and separable GPR signal. These requirements were met for the position of three of the four material interfaces. Thus, these positions were identified reasonably well. In contrast, a subsurface water content distribution can be described within a small error band using a multitude of different Mualem–Brooks–Corey parameters, if the water content range is not completely covered. In this sense, the Mualem–Brooks–Corey parameterization is not unique. Hence, exclusively using locally convergent optimization algorithms to estimate soil hydraulic material properties improves the residuum, however, these algorithms are likely to converge to a local minimum.

The three major drawbacks of the presented approach comprise (i) the computational effort which is required to solve the Richards equation and Maxwell's equations, (ii) the limited number of events which can be analyzed due to the pairwise event association which investigates all plausible combinations of simulated and measured events, and (iii) the fact that the hyperparameters for the GPR evaluation algorithm have to be determined a priori. The latter is difficult and requires expert knowledge, especially since the shape of the radargram is likely to change considerably during the optimization procedure.

Previous work showed that the location of moderately complicated layer interfaces and the mean water content between them can be obtained from multi-channel CO measurements (Buchner et al., 2012). Together with the demonstrations in this work that the effective hydraulic material properties of layers can be estimated from time-lapse CO GPR data measurements, we now have the methods to determine the subsurface architecture and its hydraulic properties for moderately complicated situations. This obviously demands quite a significant experimental effort together with subsequent massive computations, as spatially resolved time-lapse measurements of the region of interest are required which then have to be inverted.

7 Summary and way forward

In this study, methods were developed to improve the quantitative understanding of soil water movement. Soil water movement is typically described with the Richards equation and the associated soil hydraulic material properties. These properties are highly nonlinear, vary over many orders of magnitude, and are unknown a priori. Due to the multi-scale heterogeneity of soils, these properties have to be determined directly at the scale of interest. Hence, methods are required that allow for fast, efficient, and noninvasive identification of the subsurface material distribution and the corresponding soil hydraulic material properties.

The methods developed in this study are based on data from the ASSESS test site which is essentially a tank filled with a complicated 2D layered structure of three different kinds of sands. During the experiment that is evaluated in this study, the groundwater table in ASSESS was raised and lowered through a groundwater well. The resulting hydraulic dynamics were essentially monitored with TDR and GPR. Both measurement methods are sensitive to the soil water content and use the same measurement principle. However, they differ in their measurement volume, which is $\mathcal{O}(10^{-3}\ \mathrm{m}^3)$ for TDR and $\mathcal{O}(1\ \mathrm{m}^3)$ for GPR. The methods also differ in the type of wave propagation. TDR uses guided electromagnetic pulses, whereas GPR is based on free propagation of electromagnetic pulses. Hence, the measurement data provide a different perspective on the same experiment.

TDR is an accepted standard method to accurately measure soil water content. GPR has the potential to become a standard method to determine the soil water content and the subsurface architecture on the field-scale. However, efficient and accurate evaluation methods are still to be developed. The estimated material properties based on TDR can provide a ground truth reference for the evaluation of GPR data. Consequently, the acquired measurement data were evaluated with different foci: the TDR data are used to analyze the effect of model errors on the estimated soil hydraulic material properties, whereas the GPR data are used to estimate the subsurface material distribution simultaneously with the corresponding soil hydraulic material properties.

The presented analysis of the effect of model errors on the estimated soil hydraulic material properties is based on the assumption, that the model represents the quantitative understanding of the system of interest including the measurement procedure. Hence, structured deviation between the simulation and the measurement data indicates incomplete quantitative understanding and is therefore analyzed with a structural error analysis. This analysis includes the identification of the most important model errors which have to be represented in the model. If this representation is not possible a priori, the effect of the model error is parameterized and estimated with inversion methods.

It is assumed that the structural model-data mismatch that remains after the estimation, indicates unrepresented model errors. In this study, this procedure allowed to (i) identify the slanted orientation of ASSESS and (ii) quantify the effect of unrepresented small-scale heterogeneity and uncertainty in the sensor position. The analysis of 1D and 2D cases demonstrated that 1D models are likely to yield biased parameters due to neglected lateral flow. It was found that the representation of the fluctuating groundwater table experiment in 2D including the estimation of the small-scale heterogeneity and the sensor position improves the description of the water content data by more than a factor of 2, leading to a mean absolute error of 0.004.

In order to evaluate the measured GPR signal quantitatively, it is modeled by solving Maxwell's equations based on the water content distribution which is provided by solving the Richards equation. This allows to estimate the subsurface architecture as well as the corresponding soil hydraulic material properties.

In order to identify and extract the relevant information given in the GPR data, a heuristic evaluation method was developed. First, this method detects the most important extrema of the signal (events) in the measurement and in the simulation. Subsequently, the detected measured events are associated with the detected simulated events. All plausible combinations of simulated and measured events are analyzed to identify the optimal pair association of these events. To decrease the computational effort, the detected events are grouped in clusters. First, the clusters are associated. Then follows the association of the events contained in these clusters. In order to estimate the subsurface architecture and the corresponding soil hydraulic material properties, the difference in signal travel time and amplitude of the associated events is minimized with inversion methods. Using events instead of the full GPR signal regularizes this optimization.

The developed evaluation method was applied to synthetic and measured GPR data acquired with a stationary antenna. In particular comparing the estimated soil hydraulic material properties based on the measured GPR data with those properties based on the measured TDR data shows that the presented GPR evaluation method provides reasonably accurate estimates. The deviation of some of these parameters can be explained with the different sensitivity of the two measurement methods to the data or with the lack of available data. Also the estimated subsurface material distribution compares reasonably well with given ground truth information. Additionally, it was illustrated that the different measurement methods TDR and GPR are sensitive to different model errors. This makes joint evaluation procedures challenging.

The proposed method was also applied to synthetic data acquired with a moving antenna. The estimation of a 2D subsurface material distribution and the corresponding soil hydraulic material properties demonstrated the limits of the method. One major limit of the method is its relatively large computational effort which is mainly required for the solution of the Richards equation and Maxwell's equations. It was also found that, although the focus of the method on events regularizes the optimization, still a globally convergent optimization method is required. Additionally, it was shown that the method requires that the detected events in the data are clearly separable.

More detailed summaries of the results provided by the analysis of the TDR and GPR data are given in Sect. 5.6 and Sect. 6.5, respectively.

Fluctuating groundwater tables are typically limited to fluvial or coastal areas, the active layer in permafrost regions, or pumping experiments. Also their dynamical range is generally limited. Additionally, the estimated material properties are only representative for an area which is close to the groundwater table. However, this type of experiment provides a characteristic GPR signal that is comparably easy to evaluate. Hence, this type of experiment is suitable for the development of GPR data evaluation methods. Yet, in order to fully develop the capabilities of the proposed methods, they have to be applied to infiltration experiments. This type of experiment investigates the soil hydraulic material properties close to the surface and the spatial application is less restricted compared to fluctuating groundwater table experiments. However, there are a number of challenges in this context that have to be addressed first.

Compared to the GPR signal of fluctuating groundwater table experiments, the signal of infiltration experiments is in general more complicated, because it may include multiple reflections, waveguides, and noise originating from small-scale heterogeneity or fingering. Thus, it has to be investigated, if the proposed methods are suitable to evaluate these kind of data. The characteristic GPR signal for infiltration experiments is essentially limited to the position of the infiltration front. In contrast to the fluctuating groundwater table experiment, the reflection signal from the relaxation process is typically less pronounced. Hence, the information about the soil hydraulic properties is less accessible for infiltration experiments. Due to the infiltration, the antenna coupling to the surface changes with the water content. Also, the accurate identification of the spatial distribution of the top boundary condition is in particular challenging for artificial infiltration experiments. Infiltration experiments are typically fast compared to fluctuating groundwater table experiments. Hence, automated measurement procedures may be required to achieve a suitable measurement resolution and precision.

A Appendix

A.1 ASSESS

Over the course of this PhD-project, the author was responsible for several changes at ASSESS. This included the construction of a roof (Sect. A.1.1), infiltration devices (Sect. A.1.2), and the installation of measurement devices to determine the position of the groundwater table (Sect. A.1.3).

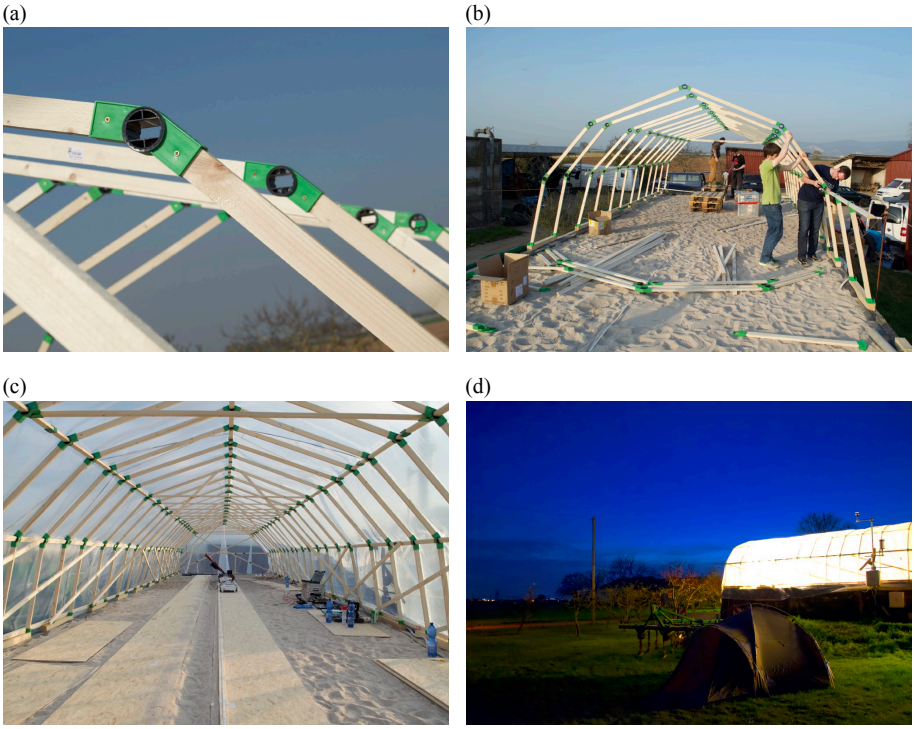

Figure A.1 (a) In order to construct the roof at ASSESS, VarioQuick® elements were used to connect roof battens. (b) The erection of the roof required many helping hands. (c) The roof allowed for long-term fluctuating groundwater table and infiltration experiments, that required continuous measurements for several days and (d) some camping at ASSESS.

A.1.1 Roof

The experiments published in Klenk et al. (2015a,b) required dry weather conditions for many weeks. Since these experiments where organized as field courses within the practical course curriculum, the timeframe for these experiments was limited to the lecture free time. Hence, after one field experiment failed due to bad weather conditions, a roof was planed and constructed in spring 2014. This roof had to be rather lightweight, stabile, and comparably cheap. Furthermore, the amount of metal components had to be minimized. Hence, a wooden construction based on roof battens served as main construction. These battens were connected with VarioQuick® elements that were obtained at GeKaHo GbR. The roof was sealed with a greenhouse film. After several experiments, the roof was disassembled in December 2014.

A.1.2 Infiltration device

The construction of the roof (Sect. A.1.1) allowed for infiltration experiments. Hence, a drip irrigation device was created with a wooden construction using the Micro-Drip-System from GARDENA®. Each of the micro drip devices can be regulated separately.

Figure A.2 The construction of a roof over ASSESS (Fig. A.1) allowed for long-term infiltration experiments. Hence, an infiltration device was created. The successful application of the prototype shown in this figure lead to a more advanced version (Fig. A.3).
[from Klenk et al. (2015b)]

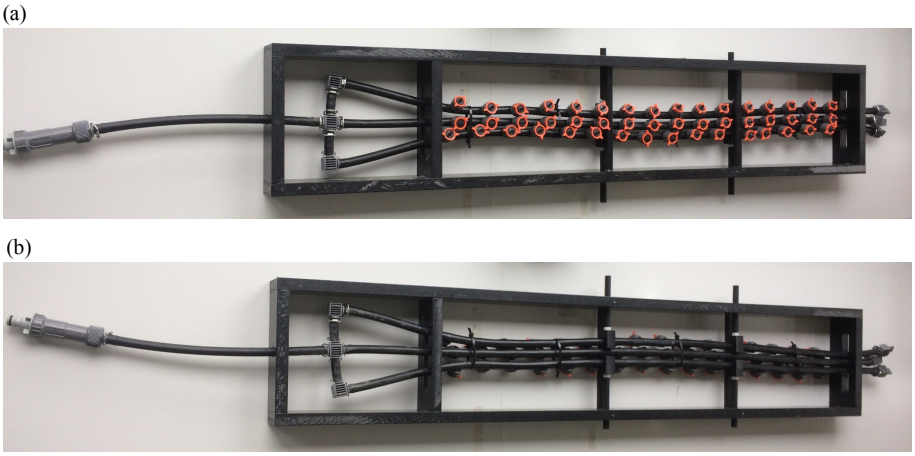

Figure A.3 The final version of the infiltration device was realized by the workshop of the institute. The size of the area to be irrigated is approximately 1.0 m × 0.1 m. The hoses are flexible and have to be adjusted for each experiment separately.

Thus, the micro drips were calibrated before each application. The device shown in Fig. A.2 was used to produce the data that is published in Klenk et al. (2015b). After the successful application of the prototype, a final version was produced by the workshop of the institute (Fig. A.3).

A.1.3 Groundwater table

In order to measure the position of the groundwater table automatically, one ≈ 1.80 m long TDR sensor was created by the workshop of the institute and installed vertically in the groundwater well of ASSESS (Fig. A.4). For the evaluation, the signal travel of

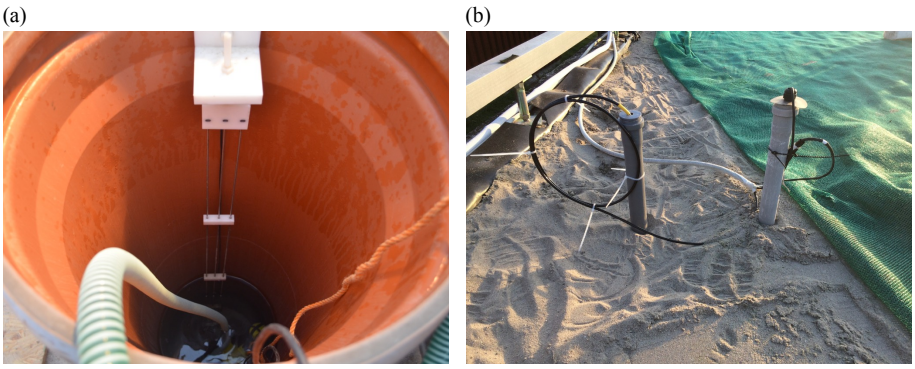

Figure A.4 (a) A long TDR sensor was installed to determine the position of the groundwater table automatically. (b) After the tensiometer (right) failed, a submersible pressure transducer (CS-451, left) was installed at ASSESS.

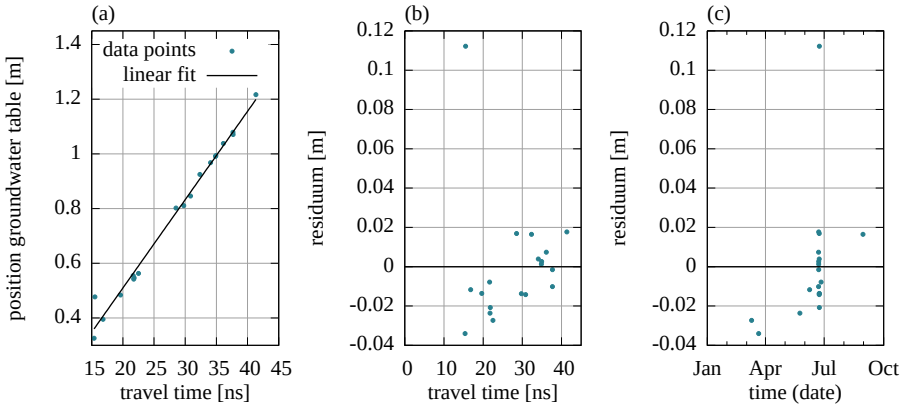

Figure A.5 (a) The TDR sensor is calibrated with manual measurements of the position of the groundwater table. (b) The residuals of the calibration fit are shown over the signal travel time and (c) over the measurement time. Note that a single outlier changes the slope of the fit and leads to biased estimates for the groundwater position. Hence, the evaluation can be further improved by using a more reliable fit algorithm. This also concerns the temperature dependence of the permittivity which could can be corrected for with an estimate for the water temperature.

the TDR sensor is calibrated with manual measurements of position of the groundwater table (Fig. A.5). This yields the position of the groundwater table with a standard deviation of ≈ 0.01 m. The evaluation process can be further improved by implementing (i) a correction for the temperature dependency of the permittivity of water (Eq. 3.53) and (ii) an a more reliable fit algorithm making the calibration more reliable and less susceptible for outliers (Fig. A.5).

After the tensiometer failed, a Campbell Scientific CS-451 submersible pressure transducer was installed close to the position of the tensiometer (Fig. A.4) in collaboration with Hannes Bauser and Lisa Hantschel. The measurement data of the different devices are compared in Fig. A.6.

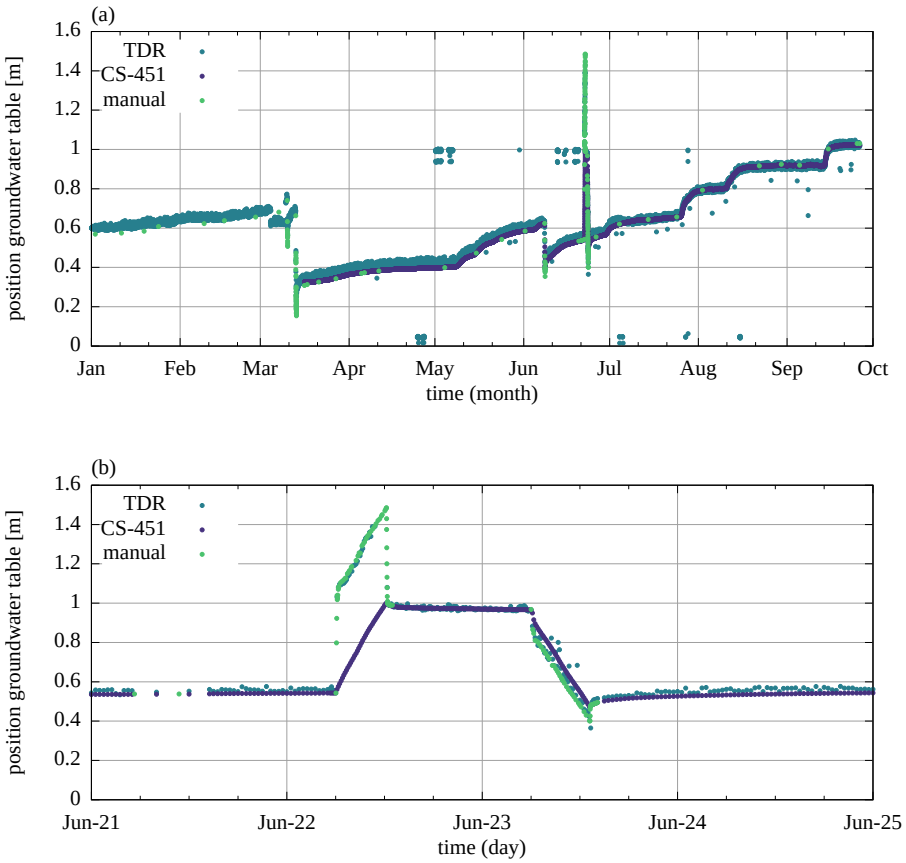

Figure A.6 The position of the groundwater table in ASSESS can be determined with manual measurements, a long TDR, and a CS-451 pressure transducer. (a) The evaluated data for all three methods are given from January to October 2017. The TDR data were calibrated with the data shown in Fig. A.5. (b) The calibration data were mainly acquired during one fluctuating groundwater table experiment. The offset of the TDR data for low positions is mainly due to an outlier in the calibration fit (Fig. A.5). There are some outliers due to a malfunctioning of the TDR100 in particular in the end of April, in the beginning of May, in the mid of June, and in the beginning of July. At these points in time, all the TDR data acquired with this device are corrupted including the water content and the electrical conductivity data. The data of the CS-451 are comparably precise and also quite accurate when compared to the manual measurements in the groundwater well.

A.2 Hydraulic material properties

For the interpretation of the estimation of soil hydraulic material properties, it is advantageous to analyze the dependency of the Mualem–Brooks–Corey parameterization on its parameters. In order to visualize the influence of individual parameters on the shape of the Mualem–Brooks–Corey material functions, single parameters are scanned through the typical parameter range, while the remaining parameters are kept constant at reference values for sand (Table 3.1). The resulting material functions are given in Fig. A.8 and in Fig. A.7.

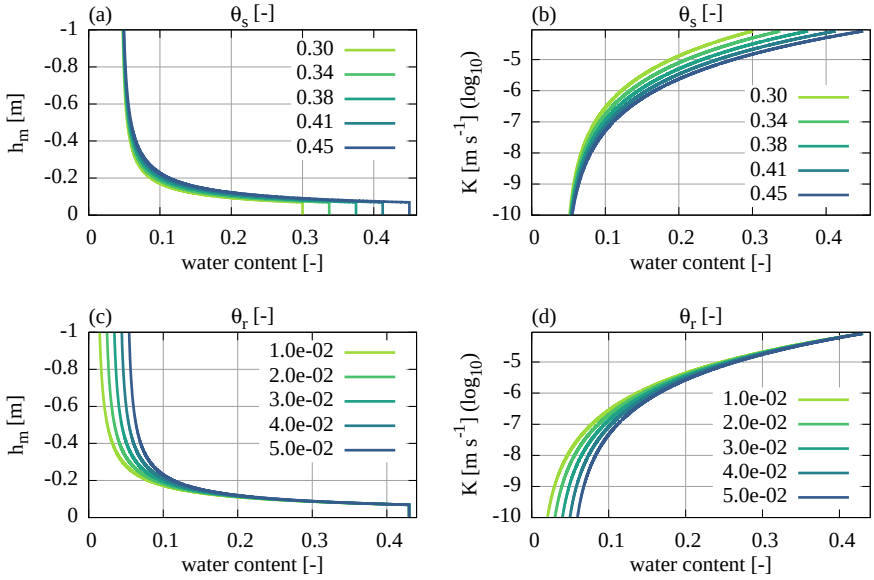

Figure A.7 The influence of single parameters on the shape of the Mualem–Brooks–Corey material functions is investigated by scanning the typical parameter range. The remaining parameters are kept at reference values for sand given in Table 3.1.

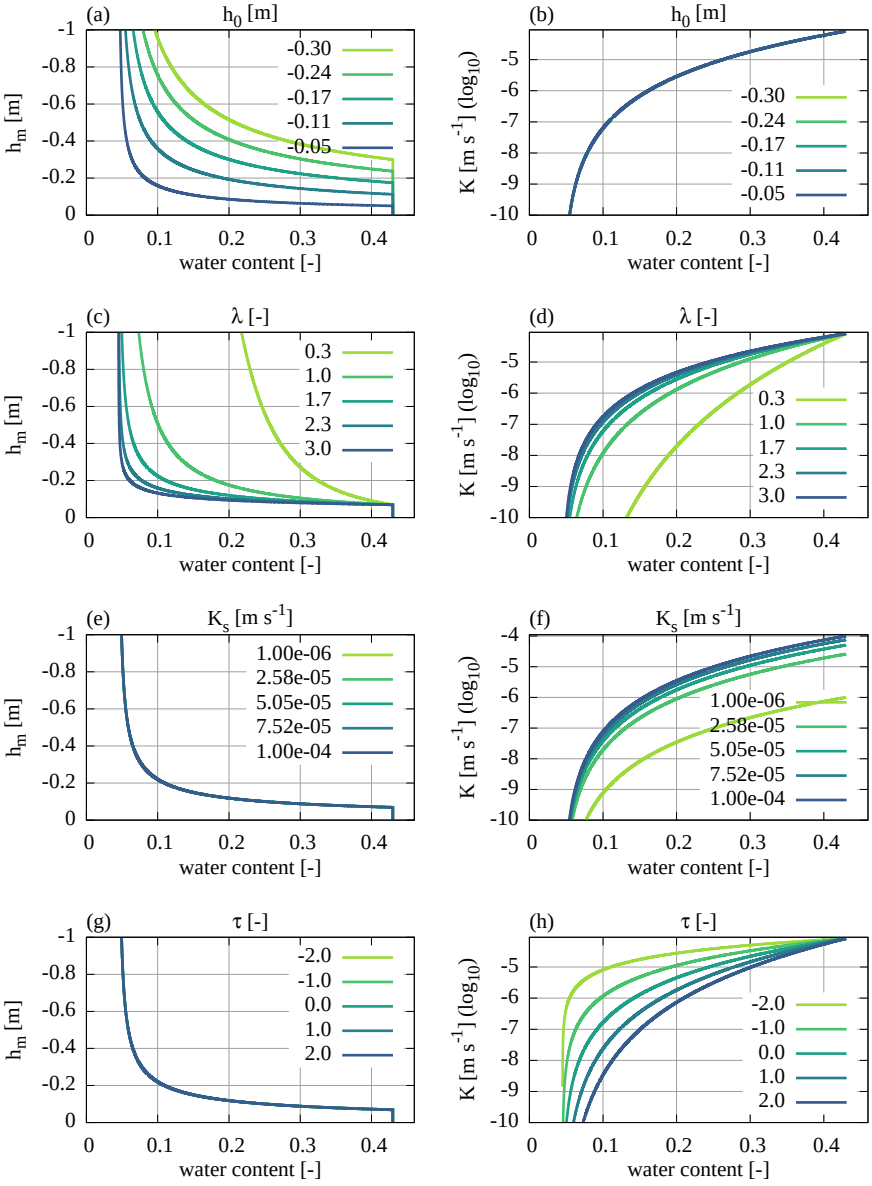

Figure A.8 The influence of single parameters on the shape of the Mualem–Brooks–Corey material functions is investigated by scanning the typical parameter range. The remaining parameters are kept at reference values for sand given in Table 3.1.

A.3 GPR study 2: Transient hydraulic state and moving antenna

In the study presented in Sect. 6.4, soil hydraulic material properties and the 2D subsurface architecture are estimated based on time-lapse CO GPR data measurements. The remaining residuals after the parameter estimation are given for each of these CO radargrams subsequently including the results of the Levenberg–Marquardt algorithm (Sect. A.3.1) and the simulated annealing algorithm (Sect. A.3.2). These residuals are evaluated and discussed in more detail in Sect. 6.4.2.

A.3.1 Levenberg–Marquardt

The residuals for the Levenberg–Marquardt algorithm are shown in Figs. A.9–A.15.

A.3.2 Simulated annealing

The residuals for the simulated annealing algorithm are shown in Figs. A.16–A.22.

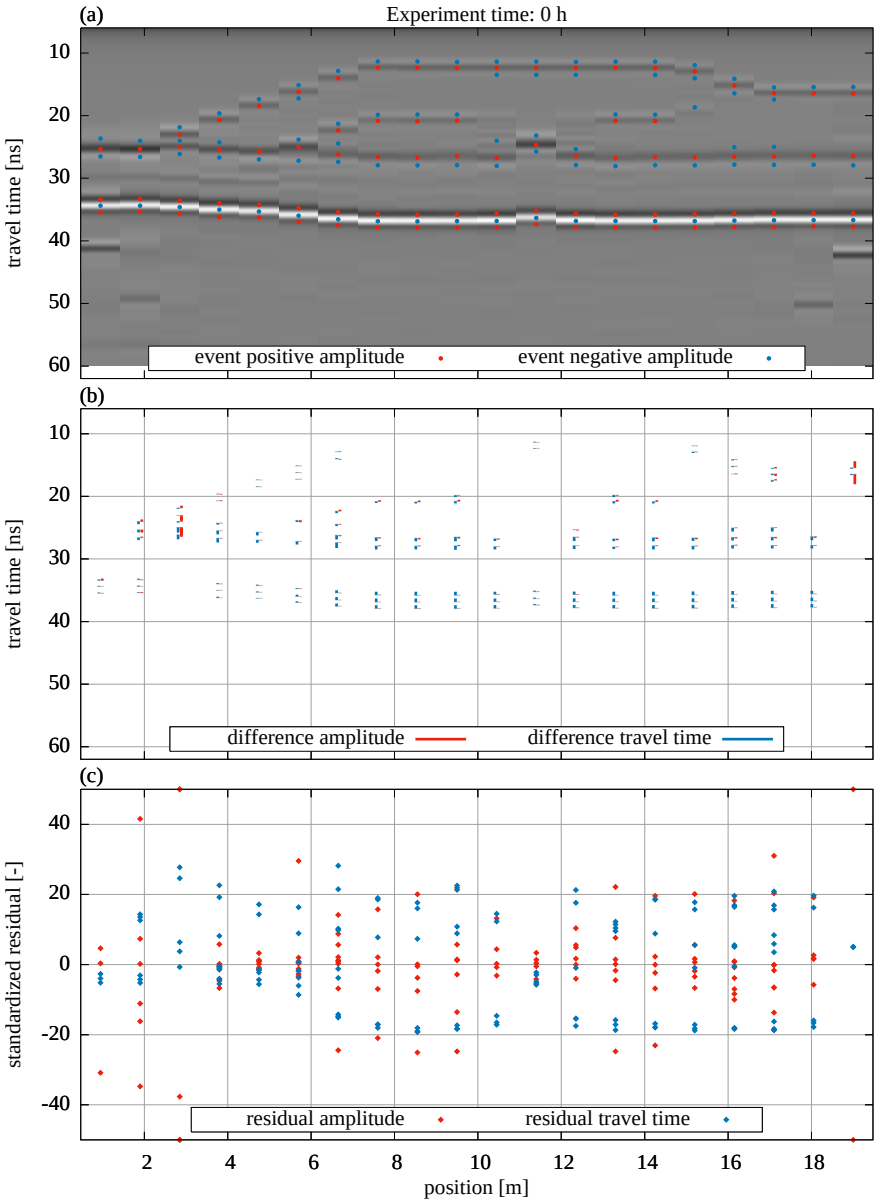

Figure A.9 This evaluation of the synthetic GPR data with the Levenberg–Marquardt algorithm is separated into three parts: (a) shows the selected (Sect. 6.2.1.3) events which are used as synthetic measurement data. Except for the normalization and the 2D to 3D conversion the data are processed according to Sect. 6.2.1. The radargram is normalized to the maximum absolute amplitude, facilitating visual comparison of the traces. (b) shows resulting differences in travel time and amplitude of the mean parameter set. The differences of the amplitude are given in arbitrary units which are consistently used in this study. (c) shows standardized residuals of the differences, essentially zooming into the small differences given in (b). Note that outliers are set onto the boundary.

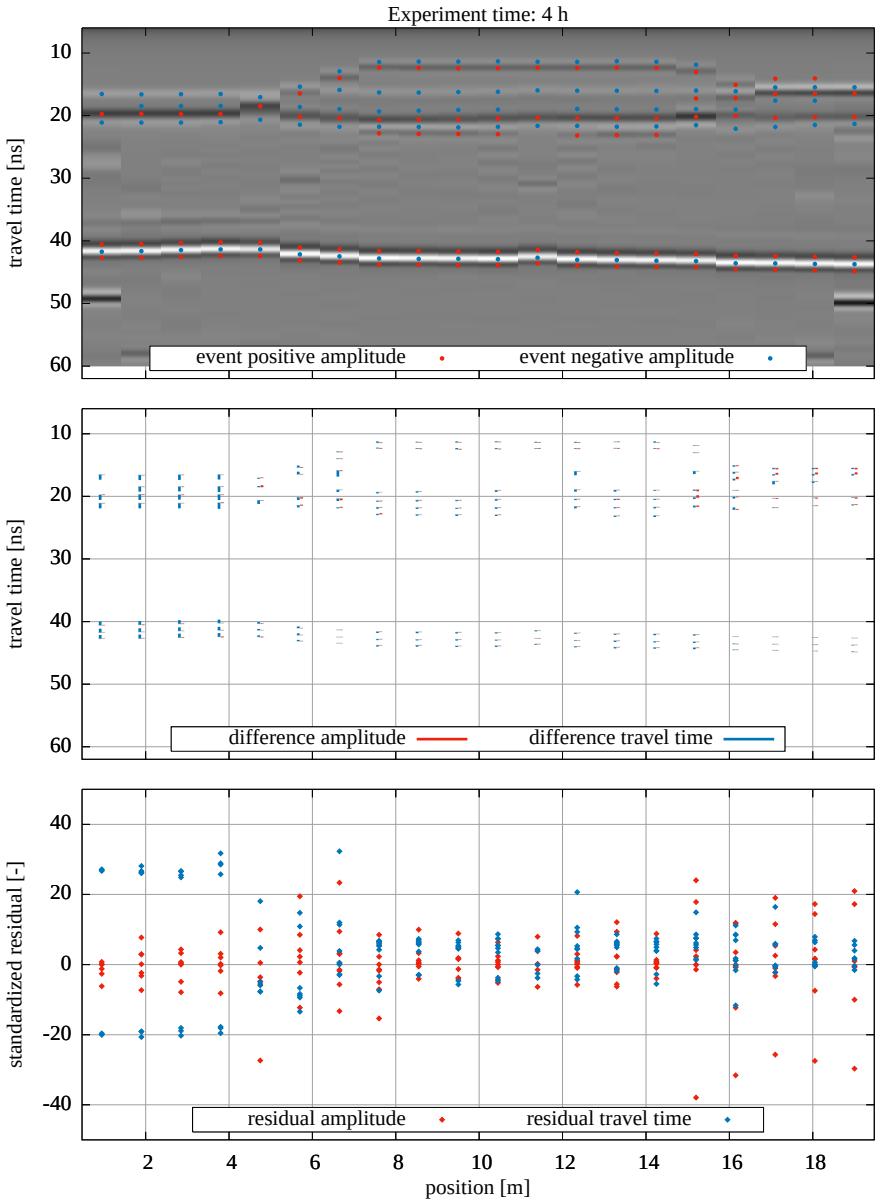

Figure A.10 This evaluation of the synthetic GPR data with the Levenberg–Marquardt algorithm is separated into three parts: (a) shows the selected (Sect. 6.2.1.3) events which are used as synthetic measurement data. Except for the normalization and the 2D to 3D conversion the data are processed according to Sect. 6.2.1. The radargram is normalized to the maximum absolute amplitude, facilitating visual comparison of the traces. (b) shows resulting differences in travel time and amplitude of the mean parameter set. The differences of the amplitude are given in arbitrary units which are consistently used in this study. (c) shows standardized residuals of the differences, essentially zooming into the small differences given in (b). Note that outliers are set onto the boundary.

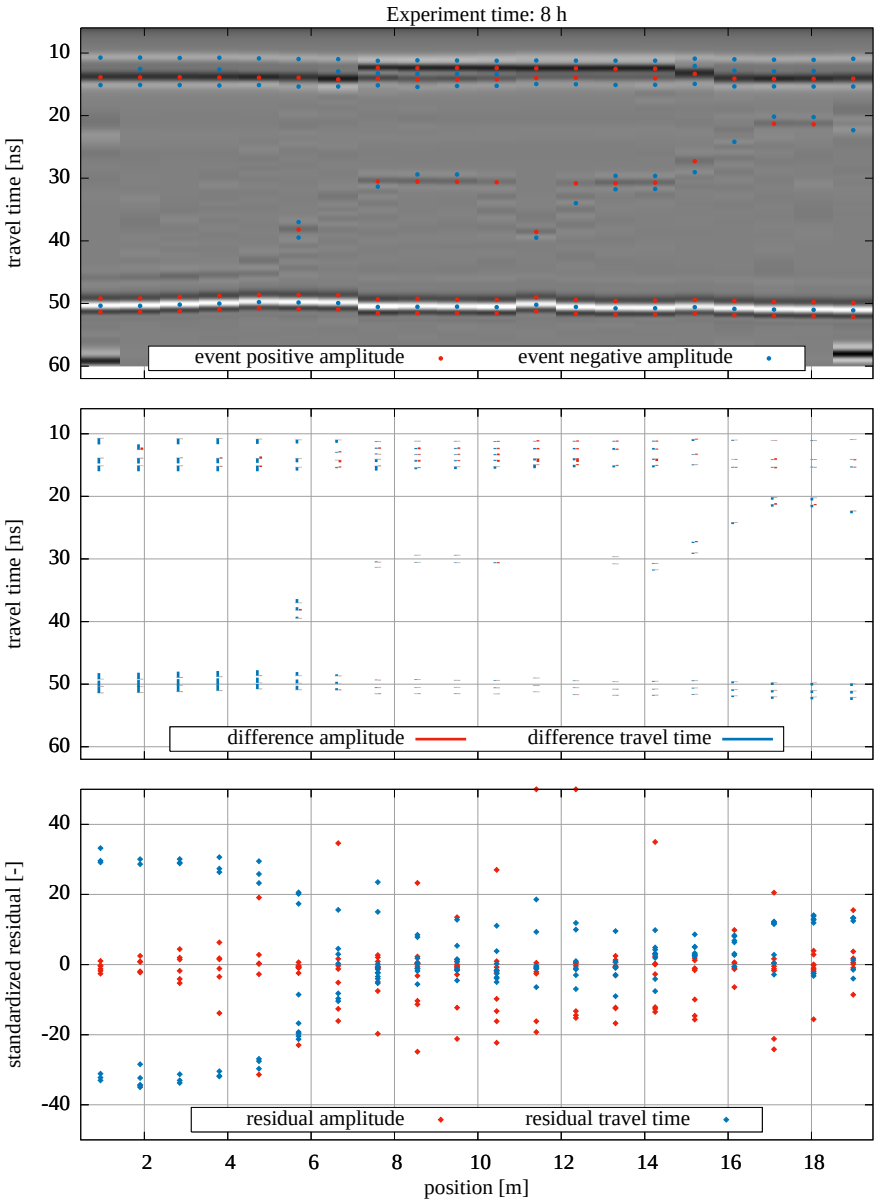

Figure A.11 This evaluation of the synthetic GPR data with the Levenberg–Marquardt algorithm is separated into three parts: (a) shows the selected (Sect. 6.2.1.3) events which are used as synthetic measurement data. Except for the normalization and the 2D to 3D conversion the data are processed according to Sect. 6.2.1. The radargram is normalized to the maximum absolute amplitude, facilitating visual comparison of the traces. (b) shows resulting differences in travel time and amplitude of the mean parameter set. The differences of the amplitude are given in arbitrary units which are consistently used in this study. (c) shows standardized residuals of the differences, essentially zooming into the small differences given in (b). Note that outliers are set onto the boundary.

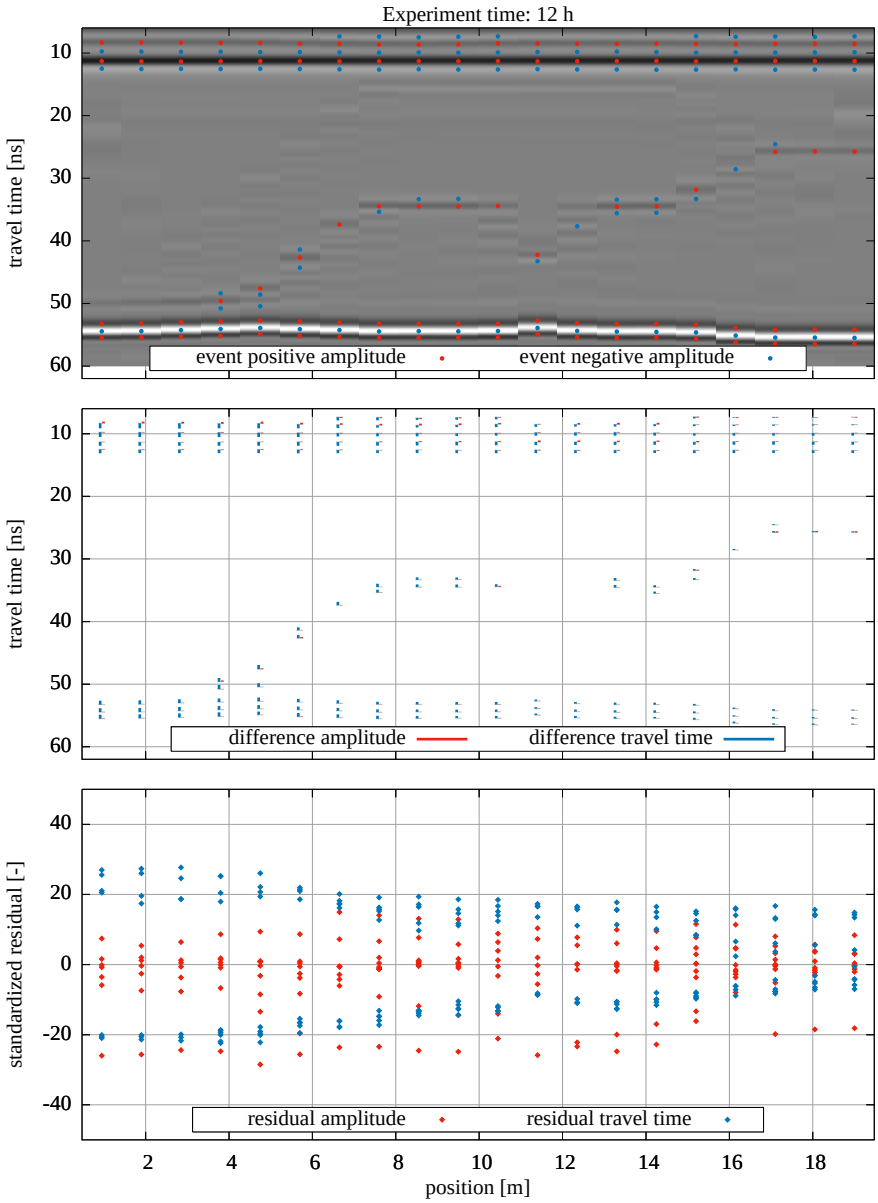

Figure A.12 This evaluation of the synthetic GPR data with the Levenberg–Marquardt algorithm is separated into three parts: (a) shows the selected (Sect. 6.2.1.3) events which are used as synthetic measurement data. Except for the normalization and the 2D to 3D conversion the data are processed according to Sect. 6.2.1. The radargram is normalized to the maximum absolute amplitude, facilitating visual comparison of the traces. (b) shows resulting differences in travel time and amplitude of the mean parameter set. The differences of the amplitude are given in arbitrary units which are consistently used in this study. (c) shows standardized residuals of the differences, essentially zooming into the small differences given in (b). Note that outliers are set onto the boundary.

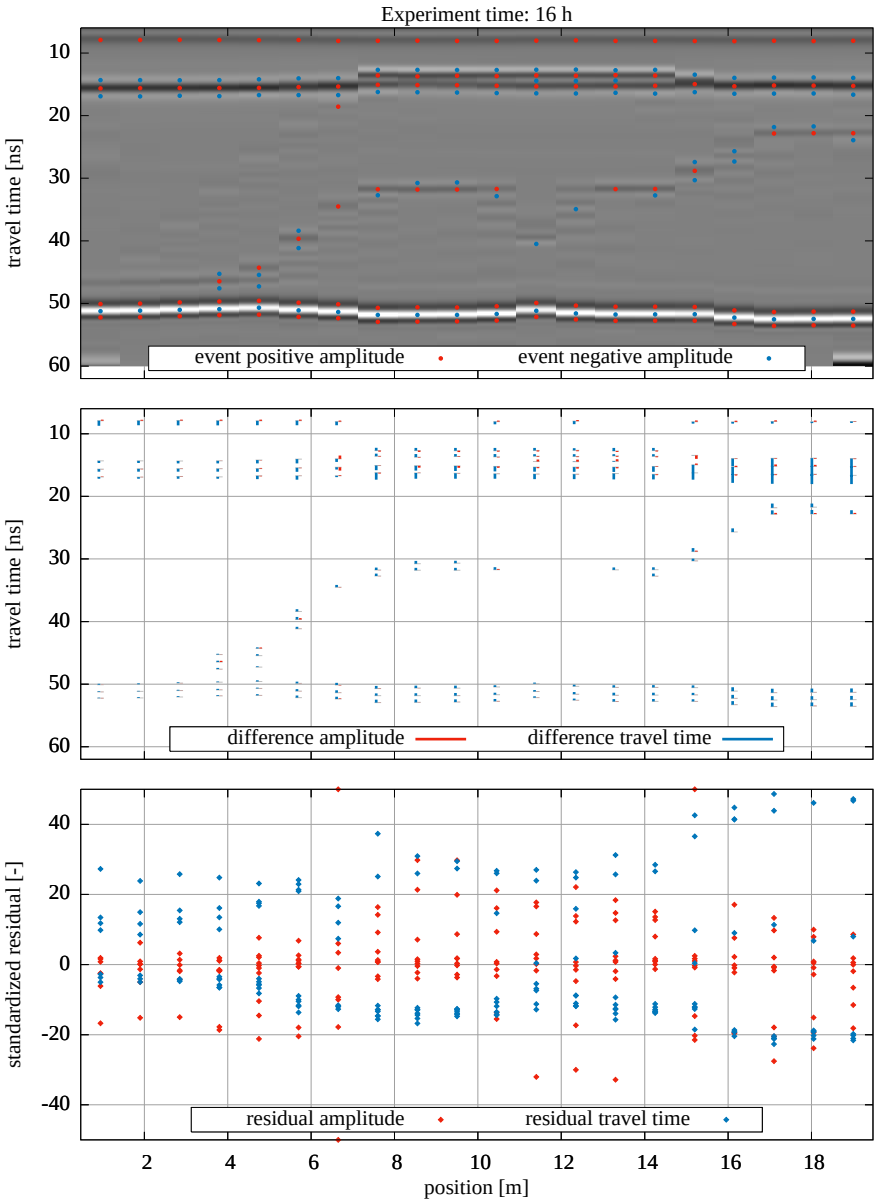

Figure A.13 This evaluation of the synthetic GPR data with the Levenberg–Marquardt algorithm is separated into three parts: (a) shows the selected (Sect. 6.2.1.3) events which are used as synthetic measurement data. Except for the normalization and the 2D to 3D conversion the data are processed according to Sect. 6.2.1. The radargram is normalized to the maximum absolute amplitude, facilitating visual comparison of the traces. (b) shows resulting differences in travel time and amplitude of the mean parameter set. The differences of the amplitude are given in arbitrary units which are consistently used in this study. (c) shows standardized residuals of the differences, essentially zooming into the small differences given in (b). Note that outliers are set onto the boundary.

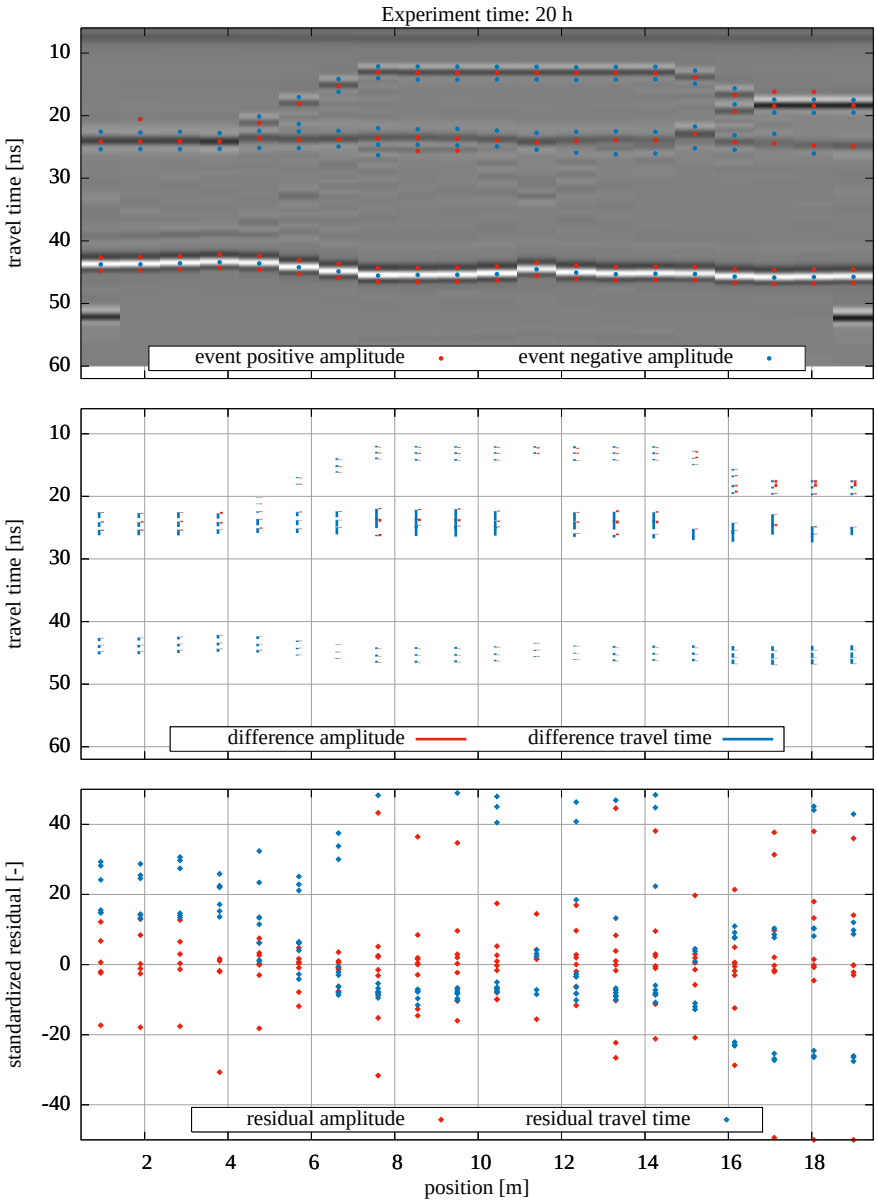

Figure A.14 This evaluation of the synthetic GPR data with the Levenberg–Marquardt algorithm is separated into three parts: (a) shows the selected (Sect. 6.2.1.3) events which are used as synthetic measurement data. Except for the normalization and the 2D to 3D conversion the data are processed according to Sect. 6.2.1. The radargram is normalized to the maximum absolute amplitude, facilitating visual comparison of the traces. (b) shows resulting differences in travel time and amplitude of the mean parameter set. The differences of the amplitude are given in arbitrary units which are consistently used in this study. (c) shows standardized residuals of the differences, essentially zooming into the small differences given in (b). Note that outliers are set onto the boundary.

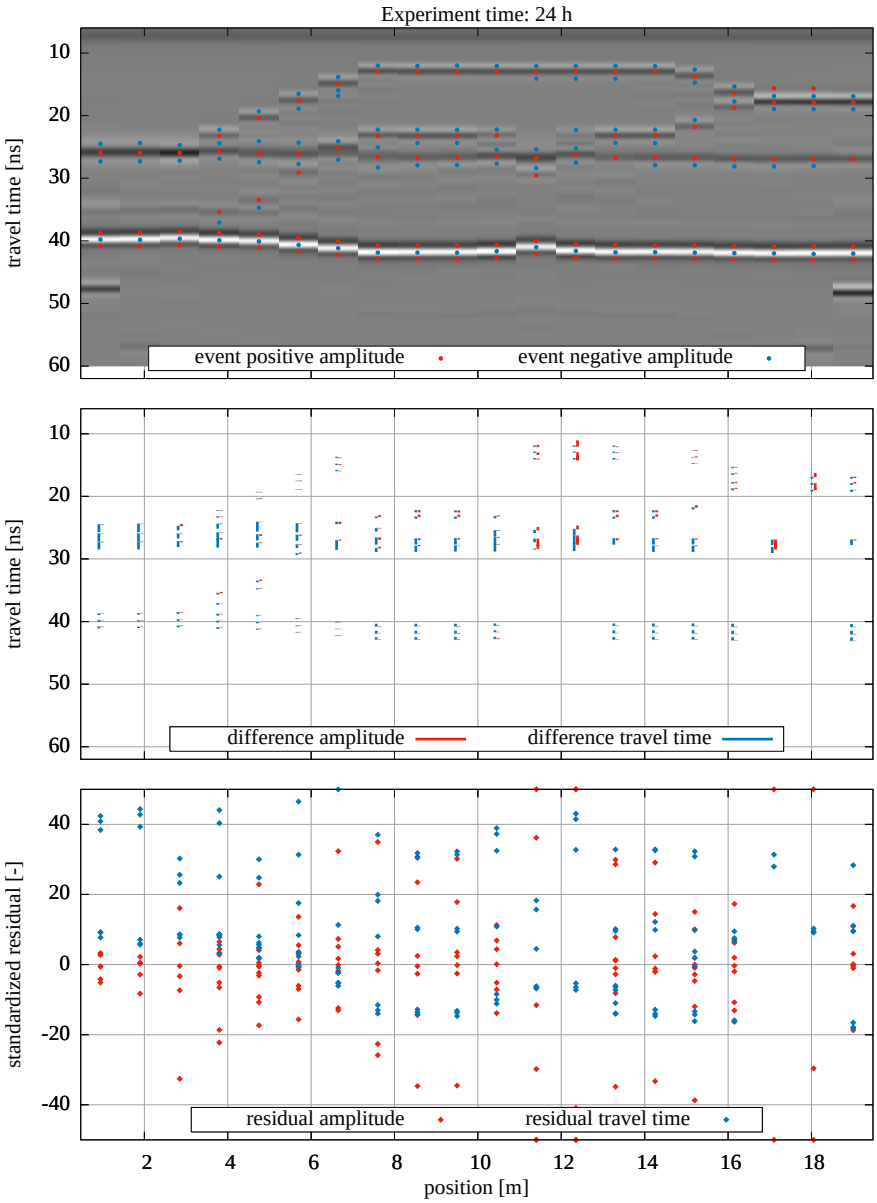

Figure A.15 This evaluation of the synthetic GPR data with the Levenberg–Marquardt algorithm is separated into three parts: (a) shows the selected (Sect. 6.2.1.3) events which are used as synthetic measurement data. Except for the normalization and the 2D to 3D conversion the data are processed according to Sect. 6.2.1. The radargram is normalized to the maximum absolute amplitude, facilitating visual comparison of the traces. (b) shows resulting differences in travel time and amplitude of the mean parameter set. The differences of the amplitude are given in arbitrary units which are consistently used in this study. (c) shows standardized residuals of the differences, essentially zooming into the small differences given in (b). Note that outliers are set onto the boundary.

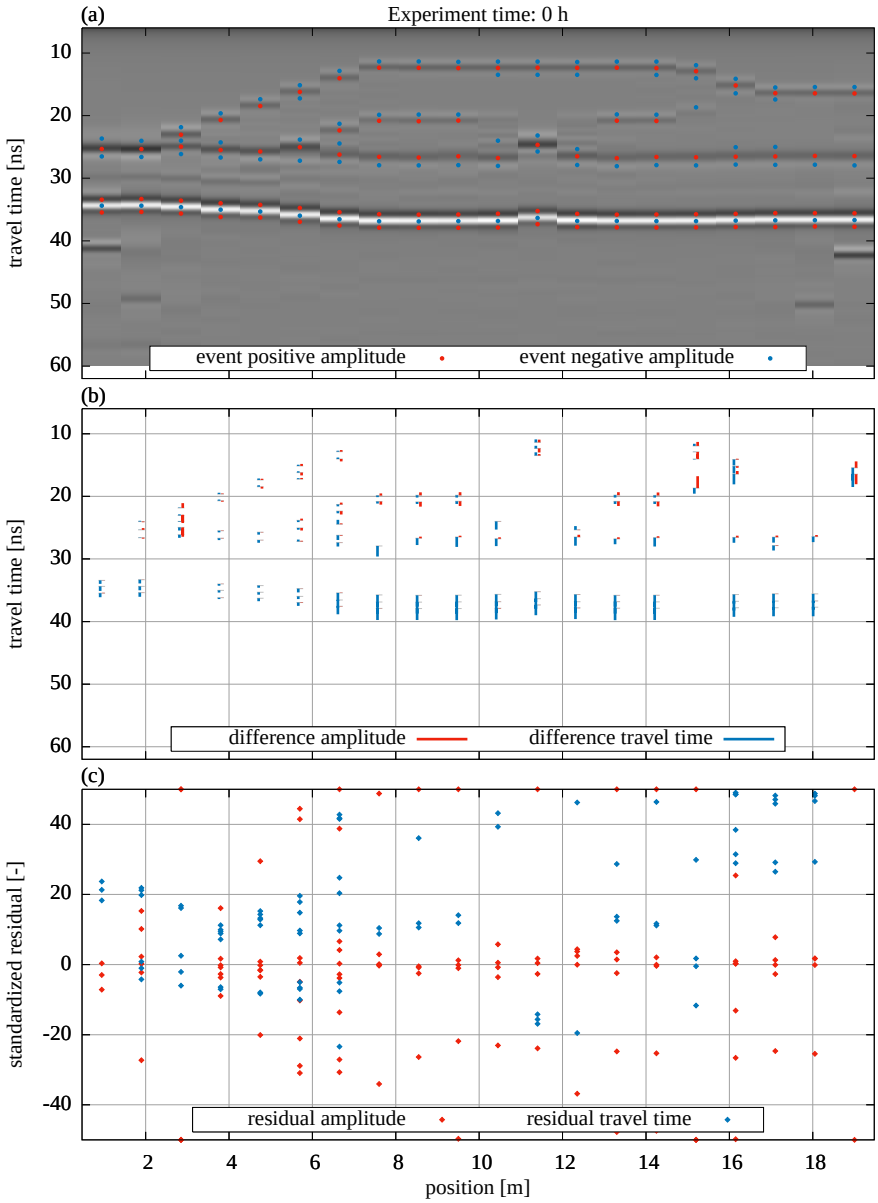

Figure A.16 This evaluation of the synthetic GPR data with the simulated annealing algorithm is separated into three parts: (a) shows the selected (Sect. 6.2.1.3) events which are used as synthetic measurement data. Except for the normalization and the 2D to 3D conversion the data are processed according to Sect. 6.2.1. The radargram is normalized to the maximum absolute amplitude, facilitating visual comparison of the traces. (b) shows resulting differences in travel time and amplitude of the mean parameter set. The differences of the amplitude are given in arbitrary units which are consistently used in this study. (c) shows standardized residuals of the differences, essentially zooming into the small differences given in (b). Note that outliers are set onto the boundary.

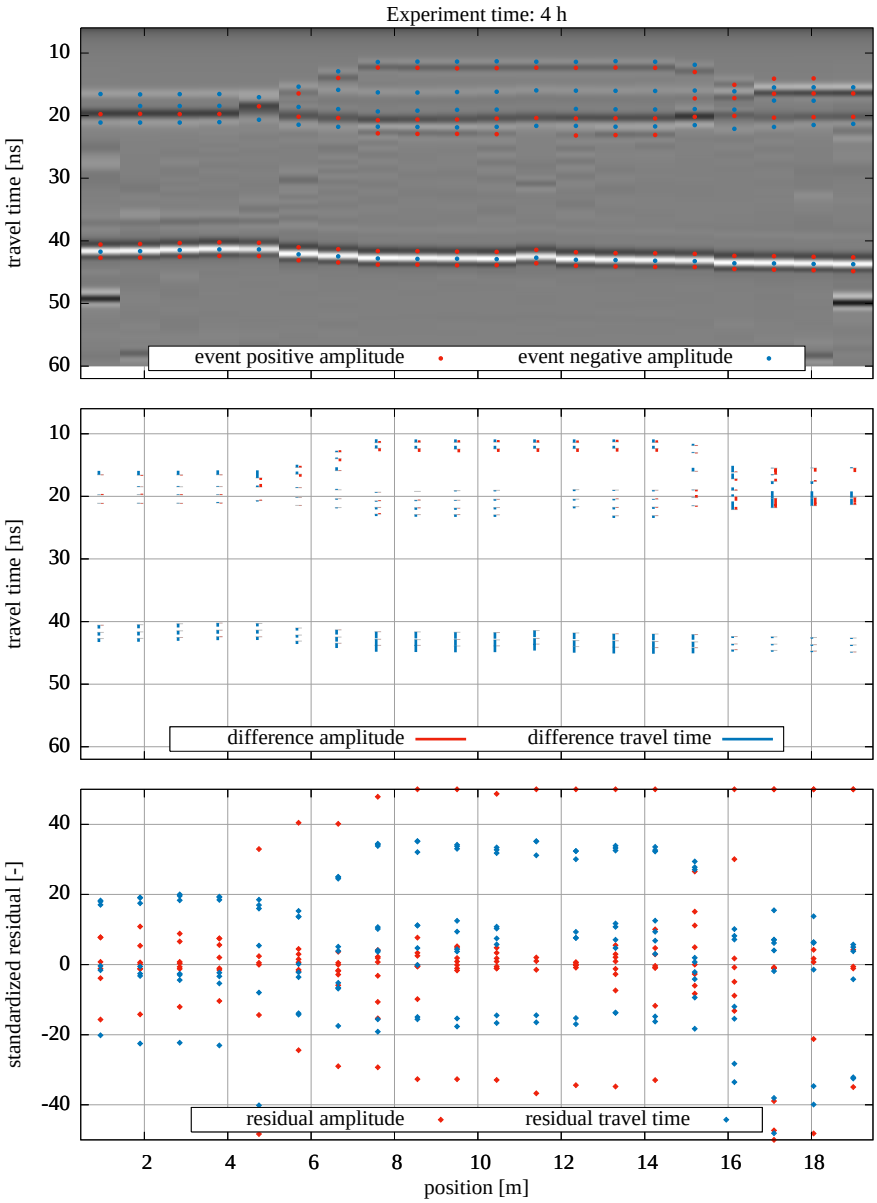

Figure A.17 This evaluation of the synthetic GPR data with the simulated annealing algorithm is separated into three parts: (a) shows the selected (Sect. 6.2.1.3) events which are used as synthetic measurement data. Except for the normalization and the 2D to 3D conversion the data are processed according to Sect. 6.2.1. The radargram is normalized to the maximum absolute amplitude, facilitating visual comparison of the traces. (b) shows resulting differences in travel time and amplitude of the mean parameter set. The differences of the amplitude are given in arbitrary units which are consistently used in this study. (c) shows standardized residuals of the differences, essentially zooming into the small differences given in (b). Note that outliers are set onto the boundary.

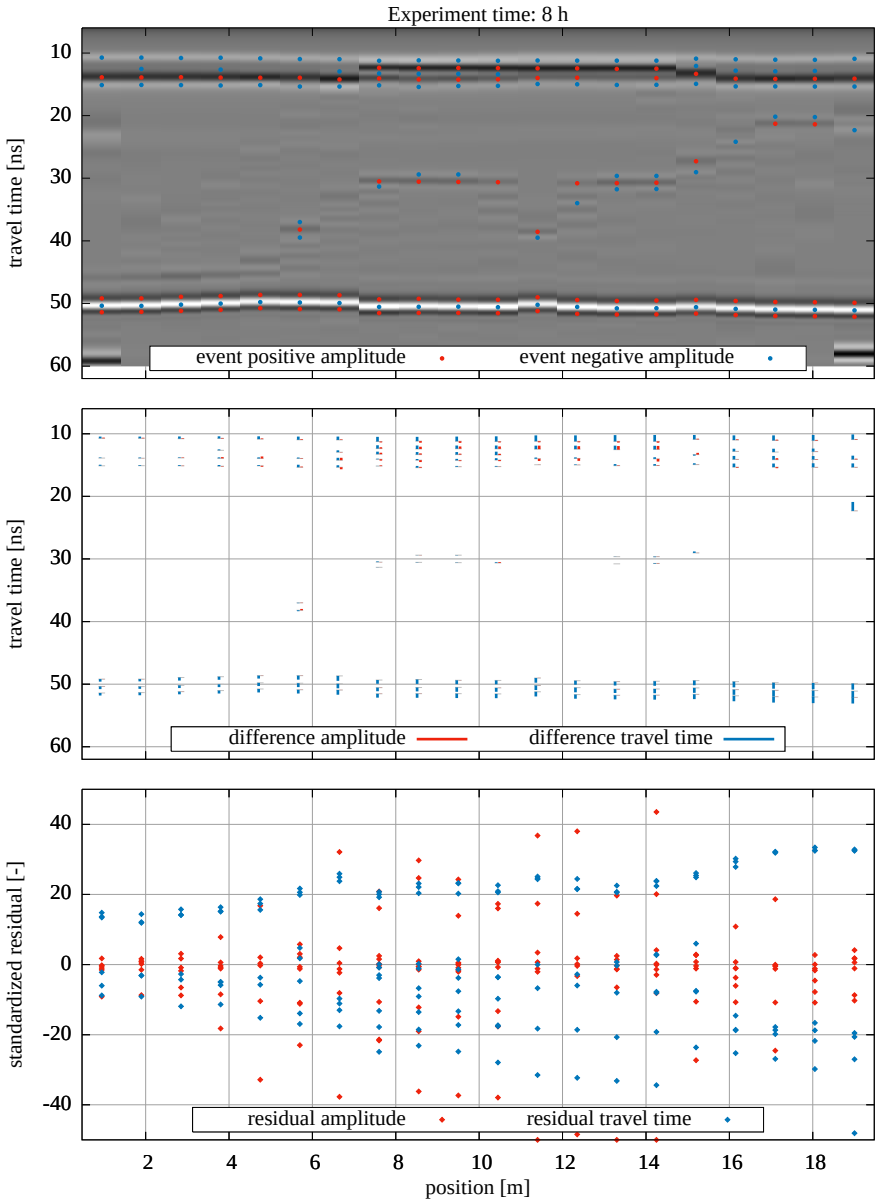

Figure A.18 This evaluation of the synthetic GPR data with the simulated annealing algorithm is separated into three parts: (a) shows the selected (Sect. 6.2.1.3) events which are used as synthetic measurement data. Except for the normalization and the 2D to 3D conversion the data are processed according to Sect. 6.2.1. The radargram is normalized to the maximum absolute amplitude, facilitating visual comparison of the traces. (b) shows resulting differences in travel time and amplitude of the mean parameter set. The differences of the amplitude are given in arbitrary units which are consistently used in this study. (c) shows standardized residuals of the differences, essentially zooming into the small differences given in (b). Note that outliers are set onto the boundary.

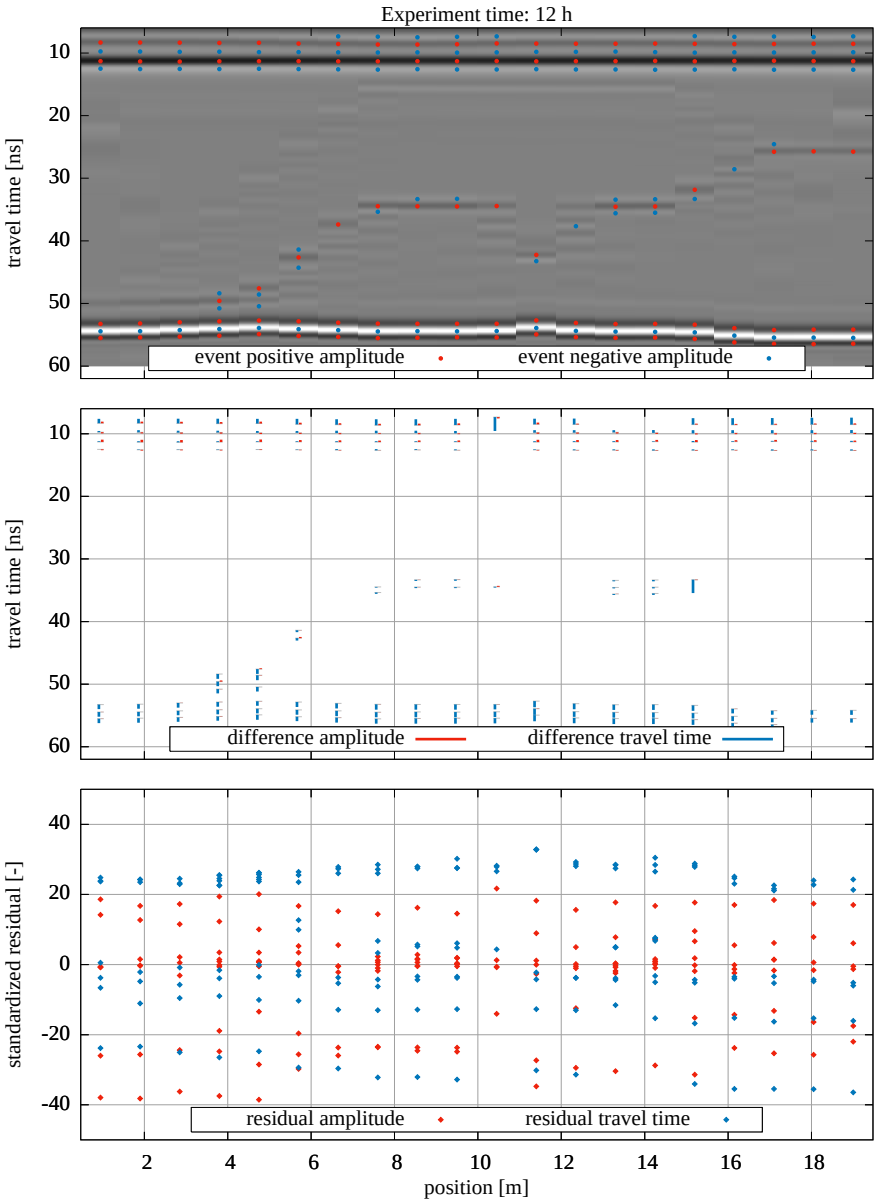

Figure A.19 This evaluation of the synthetic GPR data with the simulated annealing algorithm is separated into three parts: (a) shows the selected (Sect. 6.2.1.3) events which are used as synthetic measurement data. Except for the normalization and the 2D to 3D conversion the data are processed according to Sect. 6.2.1. The radargram is normalized to the maximum absolute amplitude, facilitating visual comparison of the traces. (b) shows resulting differences in travel time and amplitude of the mean parameter set. The differences of the amplitude are given in arbitrary units which are consistently used in this study. (c) shows standardized residuals of the differences, essentially zooming into the small differences given in (b). Note that outliers are set onto the boundary.

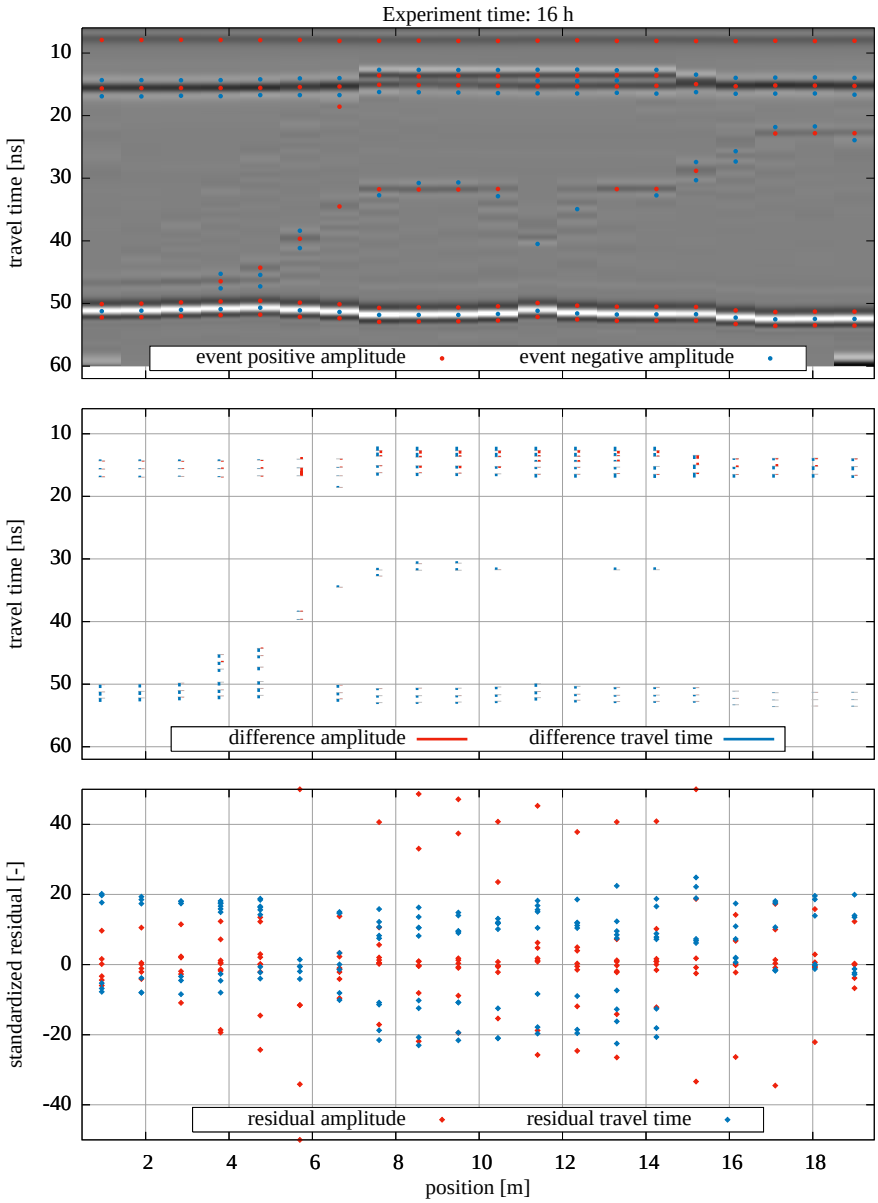

Figure A.20 This evaluation of the synthetic GPR data with the simulated annealing algorithm is separated into three parts: (a) shows the selected (Sect. 6.2.1.3) events which are used as synthetic measurement data. Except for the normalization and the 2D to 3D conversion the data are processed according to Sect. 6.2.1. The radargram is normalized to the maximum absolute amplitude, facilitating visual comparison of the traces. (b) shows resulting differences in travel time and amplitude of the mean parameter set. The differences of the amplitude are given in arbitrary units which are consistently used in this study. (c) shows standardized residuals of the differences, essentially zooming into the small differences given in (b). Note that outliers are set onto the boundary.

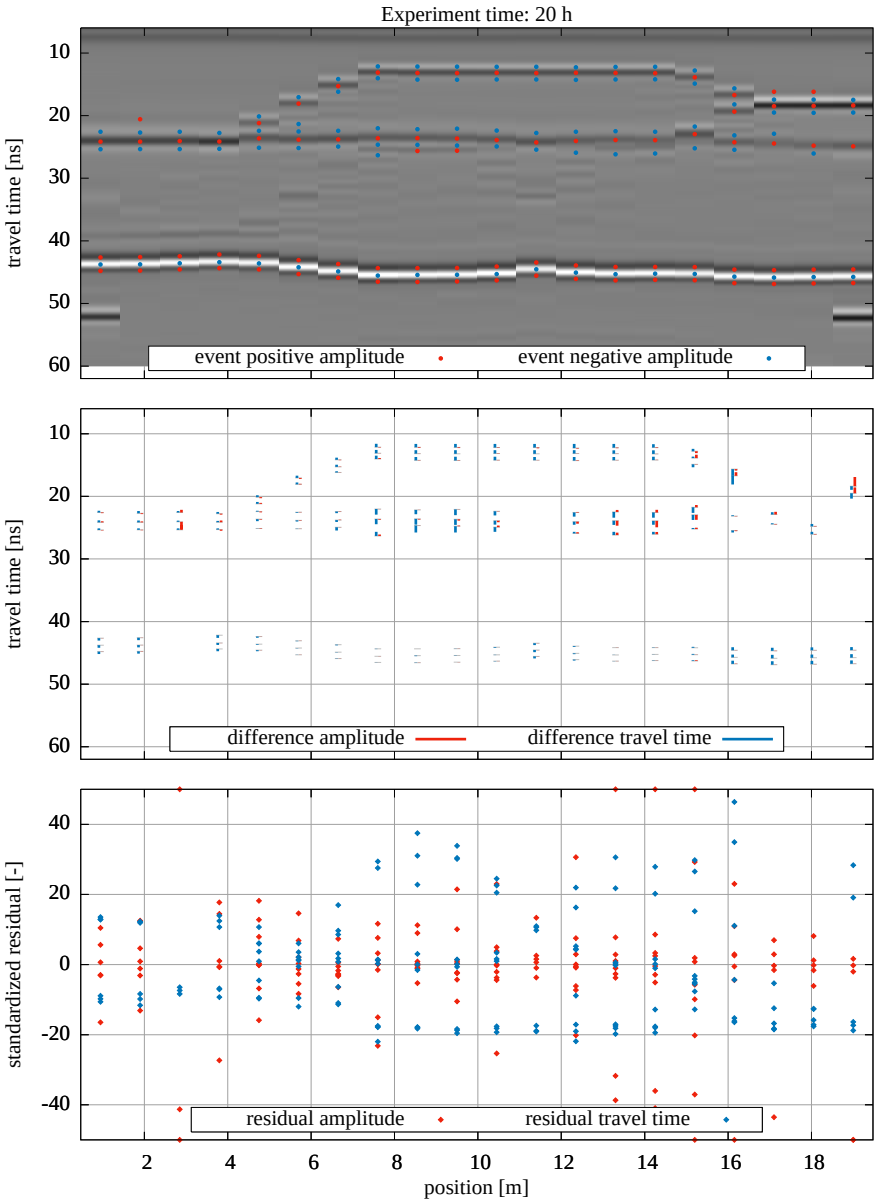

Figure A.21 This evaluation of the synthetic GPR data with the simulated annealing algorithm is separated into three parts: (a) shows the selected (Sect. 6.2.1.3) events which are used as synthetic measurement data. Except for the normalization and the 2D to 3D conversion the data are processed according to Sect. 6.2.1. The radargram is normalized to the maximum absolute amplitude, facilitating visual comparison of the traces. (b) shows resulting differences in travel time and amplitude of the mean parameter set. The differences of the amplitude are given in arbitrary units which are consistently used in this study. (c) shows standardized residuals of the differences, essentially zooming into the small differences given in (b). Note that outliers are set onto the boundary.

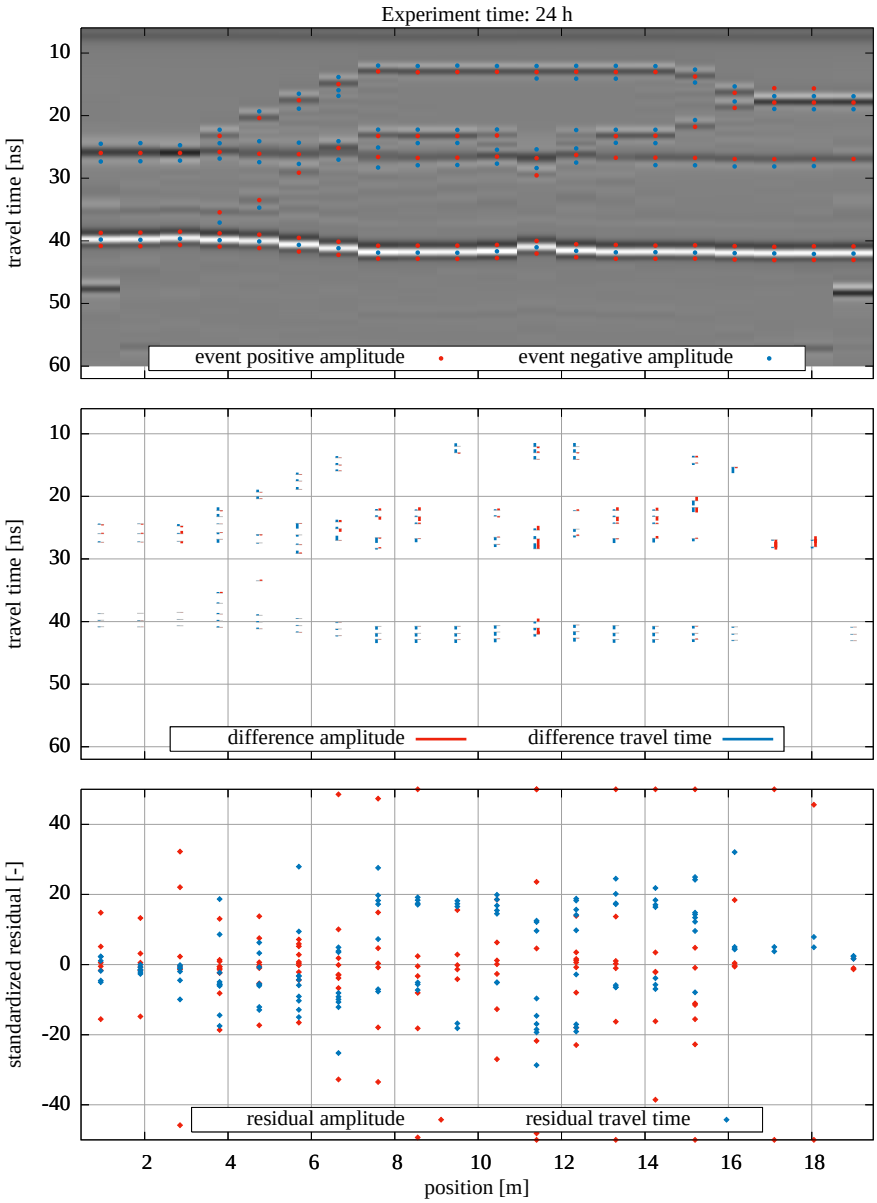

Figure A.22 This evaluation of the synthetic GPR data with the simulated annealing algorithm is separated into three parts: (a) shows the selected (Sect. 6.2.1.3) events which are used as synthetic measurement data. Except for the normalization and the 2D to 3D conversion the data are processed according to Sect. 6.2.1. The radargram is normalized to the maximum absolute amplitude, facilitating visual comparison of the traces. (b) shows resulting differences in travel time and amplitude of the mean parameter set. The differences of the amplitude are given in arbitrary units which are consistently used in this study. (c) shows standardized residuals of the differences, essentially zooming into the small differences given in (b). Note that outliers are set onto the boundary.

Bibliography (associated with the author)

Bauser, H. H., Jaumann, S., Berg, D., and Roth, K.: EnKF with closed-eye period – towards a consistent aggregation of information in soil hydrology, Hydrology and Earth System Sciences, 20, 4999–5014, doi:10.5194/hess-20-4999-2016, 2016.

Jaumann, S. and Roth, K.: Effect of unrepresented model errors on estimated soil hydraulic material properties, Hydrology and Earth System Sciences, 21, 4301–4322, doi:10.5194/hess-21-4301-2017, 2017.

Jaumann, S. and Roth, K.: Soil hydraulic material properties and layered architecture from time-lapse GPR, Hydrology and Earth System Sciences, 22, 2551–2573, doi:10.5194/hess-22-2551-2018, 2018.

Klenk, P., Keicher, V., Jaumann, S., and Roth, K.: Current limits for high precision GPR measurements, in: Proceedings of the 15th International Conference on Ground Penetrating Radar, pp. 734–738, doi:10.1109/ICGPR.2014.6970524, 2014.

Klenk, P., Jaumann, S., and Roth, K.: Quantitative high-resolution observations of soil water dynamics in a complicated architecture using time-lapse ground-penetrating radar, Hydrology and Earth System Sciences, 19, 1125–1139, doi:10.5194/hess-19-1125-2015, 2015a.

Klenk, P., Jaumann, S., and Roth, K.: Monitoring infiltration processes with high-resolution surface-based Ground-Penetrating Radar, Hydrology and Earth System Sciences Discussion, doi:10.5194/hessd-12-12215-2015, 2015b.

Pan, X., Jaumann, S., Zhang, J., and Roth, K.: Brief communication: Estimation of hydraulic properties of active layers using ground-penetrating radar (GPR) and 2D inverse hydrological modeling, The Cryosphere Discussions, 2017, 1–14, doi:10.5194/tc-2017-77, 2017.

Bibliography

Abbasi, F., Feyen, J., and Van Genuchten, M. T.: Two-dimensional simulation of water flow and solute transport below furrows: model calibration and validation, Journal of Hydrology, 290, 63–79, doi:10.1016/j.jhydrol.2003.11.028, 2004.

Abbaspour, K., Kasteel, R., and Schulin, R.: Inverse parameter estimation in a layered unsaturated field soil, Soil Science, 165, 109–123, doi:10.1097/00010694-200002000-00002, 2000.

Annan, A., Waller, W., Strangway, D. W., Rossiter, J. R., Redman, J., and Watts, R.: The electromagnetic response of a low-loss, 2-layer, dielectric earth for horizontal electric dipole excitation, Geophysics, 40, 285–298, doi:10.1190/1.1440525, 1975.

Annan, A. P.: Radio interferometry depth sounding: Part I – Theoretical discussion, Geophysics, 38, 557–580, doi:10.1190/1.1440360, 1973.

Antz, B.: Entwicklung und Modellierung der Hydraulik eines Testfeldes für Geophysikalische Messungen, Master's thesis, Heidelberg University, 2010.

Balanis, C. A.: Antenna Theory, John Wiley Sons, Inc., 2nd edn., 1997.

Bauser, H. H., Jaumann, S., Berg, D., and Roth, K.: EnKF with closed-eye period – towards a consistent aggregation of information in soil hydrology, Hydrology and Earth System Sciences, 20, 4999–5014, doi:10.5194/hess-20-4999-2016, 2016.

Beljaars, A. C. M., Viterbo, P., Miller, M. J., and Betts, A. K.: The anomalous rainfall over the United States during July 1993: Sensitivity to land surface parameterization and soil moisture anomalies, Monthly Weather Review, 124, 362–383, doi:10.1175/1520-0493(1996)124<0362:TAROTU>2.0.CO;2, 1996.

Binley, A., Hubbard, S. S., Huisman, J. A., Revil, A., Robinson, D. A., Singha, K., and Slater, L. D.: The emergence of hydrogeophysics for improved understanding of subsurface processes over multiple scales, Water Resources Research, 51, 3837–3866, doi:10.1002/2015WR017016, 2015.

Birchak, J. R., Gardner, C. G., Hipp, J. E., and Victor, J. M.: High dielectric constant microwave probes for sensing soil moisture, Proceedings of the IEEE, 62, 93–98, doi:10.1109/PROC.1974.9388, 1974.

Bleistein, N.: Two-and-one-half dimensional in-plane wave propagation, Geophysical Prospecting, 34, 686–703, doi:10.1111/j.1365-2478.1986.tb00488.x, 1986.

Box, G. E., Jenkins, G. M., Reinsel, G. C., and Ljung, G. M.: Time Series Analysis: Forecasting and Control, John Wiley & Sons, 2015.

Bradford, J., Thoma, M., and Barrash, W.: Estimating hydrologic parameters from water table dynamics using coupled hydrologic and ground-penetrating radar inversion, in: Proceedings of the 15th International Conference on Ground Penetrating Radar, pp. 232–237, doi:10.1109/ICGPR.2014.6970420, 2014.

Brooks, R. H. and Corey, A. T.: Properties of porous media affecting fluid flow, Journal of the Irrigation and Drainage Division, 92, 61–90, 1966.

Brutsaert, W.: Hydrology: An Introduction, Cambridge University Press, 2005.

Buchner, J. S., Kühne, A., Antz, B., Roth, K., and Wollschläger, U.: Observation of volumetric water content and reflector depth with multichannel ground-penetrating radar in an artificial sand volume, in: 2011 6th International Workshop on Advanced Ground Penetrating Radar (IWAGPR), pp. 1–5, doi:10.1109/IWAGPR.2011.5963910, 2011.

Buchner, J. S., Wollschläger, U., and Roth, K.: Inverting surface GPR data using FDTD simulation and automatic detection of reflections to estimate subsurface water content and geometry, Geophysics, 77, H45–H55, doi:10.1190/geo2011-0467.1, 2012.

Burrus, C. S., Gopinath, R. A., and Guo, H.: Introduction to Wavelets and Wavelet Transforms: A Primer, Prentice-Hall, Inc., 1997.

Busch, S., van der Kruk, J., Bikowski, J., and Vereecken, H.: Quantitative conductivity and permittivity estimation using full-waveform inversion of on-ground GPR data, Geophysics, 77, H79–H91, doi:10.1190/geo2012-0045.1, 2012.

Carmichael, R. S.: Physical Properties of Rocks and Minerals, CRC press, Boca Raton, 1989.

Carsel, R. F. and Parrish, R. S.: Developing joint probability distributions of soil water retention characteristics, Water Resources Research, 24, 755–769, doi:10.1029/WR024i005p00755, 1988.

Christensen, T. R., Johansson, T., Åkerman, H. J., Mastepanov, M., Malmer, N., Friborg, T., Crill, P., and Svensson, B. H.: Thawing sub-arctic permafrost: Effects on vegetation and methane emissions, Geophysical Research Letters, 31, doi:10.1029/2003GL018680, 2004.

Christiansen, J.: Effect of entrapped air upon the permeability of soils, Soil Science, 58, 355–366, 1944.

Clark, M. P., Kavetski, D., and Fenicia, F.: Pursuing the method of multiple working hypotheses for hydrological modeling, Water Resources Research, 47, doi:10.1029/2010WR009827, 2011.

Cousin, I., Levitz, P., and Bruand, A.: Three-dimensional analysis of a loamy-clay soil using pore and solid chord distributions, European Journal of Soil Science, 47, 439–452, doi:10.1111/j.1365-2389.1996.tb01844.x, 1996.

Cushman, J.: An introduction to hierarchical porous media, pp. 1–6, Academic Press, Inc., San Diego, California., 1990.

Dagenbach, A., Buchner, J. S., Klenk, P., and Roth, K.: Identifying a parameterisation of the soil water retention curve from on-ground GPR measurements, Hydrology and Earth System Sciences, 17, 611–618, doi:10.5194/hess-17-611-2013, 2013.

Dai, R. and Young, C. T.: Transient fields of a horizontal electric dipole on a multilayered dielectric medium, IEEE Transactions on Antennas and Propagation, 45, 1023–1031, doi:10.1109/8.585751, 1997.

Daniels, D.: Ground Penetrating Radar, The Institution of Engineering and Technology, 2nd edn., doi:10.1049/PBRA015E, 2004.

de Kool, M., Rawlinson, N., and Sambridge, M.: A practical grid-based method for tracking multiple refraction and reflection phases in three-dimensional heterogeneous media, Geophysical Journal International, 167, 253–270, doi:10.1111/j.1365-246X.2006.03078.x, 2006.

Debye, P.: Polar molecules, Chemical Catalog Company, Incorporated, 1929.

Diamanti, N. and Annan, A. P.: Characterizing the energy distribution around GPR antennas, Journal of Applied Geophysics, 99, 83–90, doi:10.1016/j.jappgeo.2013.08.001, 2013.

Duan, Q., Sorooshian, S., and Gupta, V.: Effective and efficient global optimization for conceptual rainfall-runoff models, Water Resources Research, 28, 1015–1031, doi:10.1029/91WR02985, 1992.

Engheta, N., Papas, C. H., and Elachi, C.: Radiation patterns of interfacial dipole antennas, Radio Science, 17, 1557–1566, doi:10.1029/RS017i006p01557, 1982.

Entekhabi, D., Njoku, E. G., O'Neill, P. E., Kellogg, K. H., Crow, W. T., Edelstein, W. N., Entin, J. K., Goodman, S. D., Jackson, T. J., Johnson, J., Kimball, J., Piepmeier, J. R., Koster, R. D., Martin, N., McDonald, K. C., Moghaddam, M., Moran, S., Reichle, R., Shi, J. C., Spencer, M. W., Thurman, S. W., Tsang, L., and Zyl, J. V.: The soil moisture active passive (SMAP) mission, Proceedings of the IEEE, 98, 704–716, doi:10.1109/JPROC.2010.2043918, 2010.

Erdal, D., Neuweiler, I., and Wollschläger, U.: Using a bias aware EnKF to account for unresolved structure in an unsaturated zone model, Water Resources Research, 50, 132–147, doi:10.1002/2012WR013443, 2014.

Ernst, J. R., Green, A. G., Maurer, H., and Holliger, K.: Application of a new 2D time-domain full-waveform inversion scheme to crosshole radar data, Geophysics, 72, J53–J64, doi:10.1190/1.2761848, 2007.

Farjadpour, A., Roundy, D., Rodriguez, A., Ibanescu, M., Bermel, P., Joannopoulos, J. D., Johnson, S. G., and Burr, G. W.: Improving accuracy by subpixel smoothing in the finite-difference time domain, Opt. Lett., 31, 2972–2974, doi:10.1364/OL.31.002972, 2006.

Faybishenko, B. A.: Hydraulic behavior of quasi-saturated soils in the presence of entrapped air: Laboratory Experiments, Water Resources Research, 31, 2421–2435, doi:10.1029/95WR01654, 1995.

Fezoui, L., Lanteri, S., Lohrengel, S., and Piperno, S.: Convergence and stability of a discontinuous Galerkin time-domain method for the 3D heterogeneous Maxwell equations on unstructured meshes, ESAIM: Mathematical Modelling and Numerical Analysis, 39, 1149–1176, doi:10.1051/m2an:2005049, 2005.

Friedman, S. P.: Soil properties influencing apparent electrical conductivity: A review, Computers and Electronics in Agriculture, 46, 45–70, doi:10.1016/j.compag.2004.11.001, 2005.

Gelhar, L. W.: Stochastic subsurface hydrology from theory to applications, Water Resources Research, 22, doi:10.1029/WR022i09Sp0135S, 1986.

Gerhards, H., Wollschläger, U., Yu, Q., Schiwek, P., Pan, X., and Roth, K.: Continuous and simultaneous measurement of reflector depth and average soil-water content with multichannel ground-penetrating radar, Geophysics, 73, J15–J23, doi:10.1190/1.2943669, 2008.

Giannopoulos, A.: Modelling ground penetrating radar by GprMax, Construction and Building Materials, 19, 755–762, doi:10.1016/j.conbuildmat.2005.06.007, 2005.

Gleeson, T., Wada, Y., Bierkens, M. F., and van Beek, L. P.: Water balance of global aquifers revealed by groundwater footprint, Nature, 488, 197–200, doi:10.1038/nature11295, 2012.

Gleick, P. H.: Water in crisis: Paths to sustainable water use, Ecological Applications, 8, 571–579, doi:10.1890/1051-0761(1998)008[0571:WICPTS]2.0.CO;2, 1998.

Gran, M., Carrera, J., Massana, J., Saaltink, M. W., Olivella, S., Ayora, C., and Lloret, A.: Dynamics of water vapor flux and water separation processes during evaporation from a salty dry soil, Journal of Hydrology, 396, 215–220, doi:10.1016/j.jhydrol.2010.11.011, 2011.

Gupta, H. V., Wagener, T., and Liu, Y.: Reconciling theory with observations: elements of a diagnostic approach to model evaluation, Hydrological Processes, 22, 3802–3813, doi:10.1002/hyp.6989, 2008.

Gupta, H. V., Clark, M. P., Vrugt, J. A., Abramowitz, G., and Ye, M.: Towards a comprehensive assessment of model structural adequacy, Water Resources Research, 48, doi:10.1029/2011WR011044, 2012.

Heimovaara, T. J., Focke, A. G., Bouten, W., and Verstraten, J. M.: Assessing temporal variations in soil water composition with time domain reflectometry, Soil Science Society of America Journal, 59, 689–698, doi:10.2136/sssaj1995.03615995005900030009x, 1995.

Henderson, P., Henderson, G. M., et al.: The Cambridge Handbook of Earth Science Data, Cambridge University Press Cambridge, 2009.

Hopmans, J. W., Šimůnek, J., Nunzio, R., and Wolfgang, D.: Simultaneous determination of water transmission and retention properties. Inverse Methods., in: Methods of Soil Analysis. Part 4. Physical Methods, edited by Dane, J. and Topp, G. C., pp. 963–1008, Soil Science Society of America Book Series, 2002.

Huisman, J., Rings, J., Vrugt, J., Sorg, J., and Vereecken, H.: Hydraulic properties of a model dike from coupled Bayesian and multi-criteria hydrogeophysical inversion, Journal of Hydrology, 380, 62–73, doi:10.1016/j.jhydrol.2009.10.023, 2010.

Huyer, W. and Neumaier, A.: Global Optimization by Multilevel Coordinate Search, Journal of Global Optimization, 14, 331–355, doi:10.1023/A:1008382309369, 1999.

Ippisch, O., Vogel, H.-J., and Bastian, P.: Validity limits for the van Genuchten-Mualem model and implications for parameter estimation and numerical simulation, Advances in Water Resources, 29, 1780–1789, doi:10.1016/j.advwatres.2005.12.011, 2006.

Jackson, J. D.: Classical Electrodynamics, John Wiley & Sons, Inc., New Jersey, USA, 3rd edn., 1999.

Jadoon, K. Z., Slob, E., Vanclooster, M., Vereecken, H., and Lambot, S.: Uniqueness and stability analysis of hydrogeophysical inversion for time-lapse ground-penetrating radar estimates of shallow soil hydraulic properties, Water Resources Research, 44, doi:10.1029/2007WR006639, 2008.

Jadoon, K. Z., Weihermüller, L., Scharnagl, B., Kowalsky, M. B., Bechtold, M., Hubbard, S. S., Vereecken, H., and Lambot, S.: Estimation of soil hydraulic parameters in the field by integrated hydrogeophysical inversion of time-lapse ground-penetrating radar data, Vadose Zone Journal, 11, doi:10.1190/1.3255105, 2012.

Jaumann, S.: Estimation of effective hydraulic parameters and reconstruction of the natural evaporative boundary forcing on the basis of TDR measurements, Diploma Thesis, Heidelberg University, 2012.

Jaumann, S. and Roth, K.: Effect of unrepresented model errors on estimated soil hydraulic material properties, Hydrology and Earth System Sciences, 21, 4301–4322, doi:10.5194/hess-21-4301-2017, 2017.

Jaumann, S. and Roth, K.: Soil hydraulic material properties and layered architecture from time-lapse GPR, Hydrology and Earth System Sciences, 22, 2551–2573, doi:10.5194/hess-22-2551-2018, 2018.

Jin, J.-M.: The Finite Element Method in Electromagnetics, John Wiley & Sons, 2015.

Jonard, F., Weihermüller, L., Schwank, M., Jadoon, K. Z., Vereecken, H., and Lambot, S.: Estimation of hydraulic properties of a sandy soil using ground-based active and passive microwave remote sensing, IEEE Transactions on Geoscience and Remote Sensing, 53, 3095–3109, doi:10.1109/TGRS.2014.2368831, 2015.

Kaatze, U.: Complex permittivity of water as a function of frequency and temperature, Journal of Chemical and Engineering Data, 34, 371–374, doi:10.1021/je00058a001, 1989.

Kavetski, D., Franks, S. W., and Kuczera, G.: Confronting input uncertainty in environmental modelling, Calibration of Watershed Models, pp. 49–68, doi:10.1029/WS006p0049, 2002.

Kavetski, D., Kuczera, G., and Franks, S. W.: Bayesian analysis of input uncertainty in hydrological modeling: 1. Theory, Water Resources Research, 42, doi:10.1029/2005WR004368, 2006.

Keesstra, S., Geissen, V., Mosse, K., Piiranen, S., Scudiero, E., Leistra, M., and van Schaik, L.: Soil as a filter for groundwater quality, Current Opinion in Environmental Sustainability, 4, 507–516, doi:10.1016/j.cosust.2012.10.007, 2012.

Kerr, Y. H., Waldteufel, P., Wigneron, J. P., Martinuzzi, J., Font, J., and Berger, M.: Soil moisture retrieval from space: The soil moisture and ocean salinity (SMOS) mission, IEEE Transactions on Geoscience and Remote Sensing, 39, 1729–1735, doi:10.1109/36.942551, 2001.

Klenk, P., Keicher, V., Jaumann, S., and Roth, K.: Current limits for high precision GPR measurements, in: Proceedings of the 15th International Conference on Ground Penetrating Radar, pp. 734–738, doi:10.1109/ICGPR.2014.6970524, 2014.

Klenk, P., Jaumann, S., and Roth, K.: Quantitative high-resolution observations of soil water dynamics in a complicated architecture using time-lapse ground-penetrating radar, Hydrology and Earth System Sciences, 19, 1125–1139, doi:10.5194/hess-19-1125-2015, 2015a.

Klenk, P., Jaumann, S., and Roth, K.: Monitoring infiltration processes with high-resolution surface-based Ground-Penetrating Radar, Hydrology and Earth System Sciences Discussion, doi:10.5194/hessd-12-12215-2015, 2015b.

Koster, R. D., Dirmeyer, P. A., Guo, Z., Bonan, G., Chan, E., Cox, P., Gordon, C. T., Kanae, S., Kowalczyk, E., Lawrence, D., Liu, P., Lu, C.-H., Malyshev, S., McAvaney,

B., Mitchell, K., Mocko, D., Oki, T., Oleson, K., Pitman, A., Sud, Y. C., Taylor, C. M., Verseghy, D., Vasic, R., Xue, Y., and Yamada, T.: Regions of strong coupling between soil moisture and precipitation, Science, 305, 1138–1140, doi:10.1126/science.1100217, 2004.

Lambot, S., Antoine, M., Van den Bosch, I., Slob, E., and Vanclooster, M.: Electromagnetic inversion of GPR signals and subsequent hydrodynamic inversion to estimate effective vadose zone hydraulic properties, Vadose Zone Journal, 3, 1072–1081, doi:10.2113/3.4.1072, 2004.

Lambot, S., Slob, E. C., Vanclooster, M., and Vereecken, H.: Closed loop GPR data inversion for soil hydraulic and electric property determination, Geophysical Research Letters, 33, doi:10.1029/2006GL027906, 2006.

Lambot, S., Slob, E., Rhebergen, J., Lopera, O., Jadoon, K. Z., and Vereecken, H.: Remote estimation of the hydraulic properties of a sand using full-waveform integrated hydrogeophysical inversion of time-lapse, off-ground GPR data, Vadose Zone Journal, 8, 743–754, doi:10.2136/vzj2008.0058, 2009.

Lampe, B., Holliger, K., and Green, A. G.: A finite-difference time-domain simulation tool for ground-penetrating radar antennas, Geophysics, 68, 971–987, doi:10.1190/1.1581069, 2003.

Legates, D. R. and McCabe, G. J.: Evaluating the use of "goodness-of-fit" measures in hydrologic and hydroclimatic model validation, Water Resources Research, 35, 233–241, doi:10.1029/1998WR900018, 1999.

Léger, E., Saintenoy, A., and Coquet, Y.: Estimating saturated hydraulic conductivity from ground-based GPR monitoring Porchet infiltration in sandy soil, in: Proceedings of the 15th International Conference on Ground Penetrating Radar, pp. 124–130, doi:10.1109/ICGPR.2014.6970399, 2014.

Léger, E., Saintenoy, A., Tucholka, P., and Coquet, Y.: Inverting surface GPR data to estimate wetting and drainage water retention curves in laboratory, in: Advanced Ground Penetrating Radar (IWAGPR), 2015 8th International Workshop on, pp. 1–5, IEEE, doi:10.1109/IWAGPR.2015.7292672, 2015.

Li, C. and Ren, L.: Estimation of unsaturated soil hydraulic parameters using the ensemble Kalman filter, Vadose Zone Journal, 10, 1205–1227, doi:10.2136/vzj2010.0159, 2011.

Light, T. S., Licht, S., Bevilacqua, A. C., and Morash, K. R.: The fundamental conductivity and resistivity of water, Electrochemical and Solid-State Letters, 8, E16–E19, doi:10.1149/1.1836121, 2005.

Looms, M. C., Binley, A., Jensen, K. H., Nielsen, L., and Hansen, T. M.: Identifying unsaturated hydraulic parameters using an integrated data fusion approach on cross-borehole geophysical data, Vadose Zone Journal, 7, 238–248, doi:10.2136/vzj2007.0087, 2008.

Manoli, G., Rossi, M., Pasetto, D., Deiana, R., Ferraris, S., Cassiani, G., and Putti, M.: An iterative particle filter approach for coupled hydro-geophysical inversion of a controlled infiltration experiment, Journal of Computational Physics, 283, 37–51, doi:10.1016/j.jcp.2014.11.035, 2015.

Mertens, J., Stenger, R., and Barkle, G.: Multiobjective inverse modeling for soil parameter estimation and model verification, Vadose Zone Journal, 5, 917–933, doi:10.2136/vzj2005.0117, 2006.

Metropolis, N., Rosenbluth, A. W., Rosenbluth, M. N., Teller, A. H., and Teller, E.: Equation of state calculations by fast computing machines, The Journal of Chemical Physics, 21, 1087–1092, doi:http://dx.doi.org/10.1063/1.1699114, 1953.

Millard, S., Shaari, A., and Bungey, J.: Field pattern characteristics of GPR antennas, Independent Nondestructive Testing and Evaluation International, 35, 473–482, doi:10.1016/S0963-8695(02)00023-3, 2002.

Miller, E. and Miller, R.: Physical theory for capillary flow phenomena, Journal of Applied Physics, 27, 324–332, doi:10.1063/1.1722370, 1956.

Moghadas, D., Jadoon, K. Z., Vanderborght, J., Lambot, S., and Vereecken, H.: Estimation of the near surface soil water content during evaporation using air-launched ground-penetrating radar, Near Surface Geophysics, 12, 623–633, doi:10.3997/1873-0604.2014017, 2014.

Moré, J. J.: The Levenberg-Marquardt algorithm: Implementation and theory, in: Numerical Analysis, pp. 105–116, Springer, doi:10.1007/BFb0067700, 1978.

Mualem, Y.: A new model for predicting the hydraulic conductivity of unsaturated porous media, Water Resources Research, 12, 513–522, doi:10.1029/WR012i003p00513, 1976.

Neal, A.: Ground-penetrating radar and its use in sedimentology: principles, problems and progress, Earth-Science Reviews, 66, 261–330, doi:10.1016/j.earscirev.2004.01.004, 2004.

Nelder, J. A. and Mead, R.: A simplex method for function minimization, The Computer Journal, 7, 308, doi:10.1093/comjnl/7.4.308, 1965.

Nemani, R. R., Keeling, C. D., Hashimoto, H., Jolly, W. M., Piper, S. C., Tucker, C. J., Myneni, R. B., and Running, S. W.: Climate-driven increases in global terrestrial net Primary production from 1982 to 1999, Science, 300, 1560–1563, doi:10.1126/science.1082750, 2003.

Nielsen, D. R., Biggar, J. W., and Erh, K. T.: Spatial variability of field-measured soil-water properties, University of California, Division of Agricultural Sciences, doi:10.3733/hilg.v42n07p215, 1973.

Oki, T. and Kanae, S.: Global hydrological cycles and world water resources, Science, 313, 1068–1072, doi:10.1126/science.1128845, 2006.

Oskooi, A. F., Kottke, C., and Johnson, S. G.: Accurate finite-difference time-domain simulation of anisotropic media by subpixel smoothing, Opt. Lett., 34, 2778–2780, doi:10.1364/OL.34.002778, 2009.

Oskooi, A. F., Roundy, D., Ibanescu, M., Bermel, P., Joannopoulos, J. D., and Johnson, S. G.: MEEP: A flexible free-software package for electromagnetic simulations by the FDTD method, Computer Physics Communications, 181, 687–702, doi:10.1016/j.cpc.2009.11.008, 2010.

Ott, H.: Reflexion und Brechung von Kugelwellen; Effekte 2. Ordnung, Annalen der Physik, 433, 443–466, doi:10.1002/andp.19424330605, 1942.

Over, M. W., Wollschläger, U., Osorio-Murillo, C. A., and Rubin, Y.: Bayesian inversion of Mualem-van Genuchten parameters in a multilayer soil profile: A data-driven, assumption-free likelihood function, Water Resources Research, 51, 861–884, doi:10.1002/2014WR015252, 2015.

Palla, A., Gnecco, I., and Lanza, L.: Unsaturated 2D modelling of subsurface water flow in the coarse-grained porous matrix of a green roof, Journal of Hydrology, 379, 193–204, doi:10.1016/j.jhydrol.2009.10.008, 2009.

Parker, J., Kool, J., and Van Genuchten, M. T.: Determining soil hydraulic properties from one-step outflow experiments by parameter estimation: II. Experimental studies, Soil Science Society of America Journal, 49, 1354–1359, doi:10.2136/sssaj1985.03615995004900060005x, 1985.

Piperno, S., Remaki, M., and Fezoui, L.: A nondiffusive finite volume scheme for the three-dimensional Maxwell's equations on unstructured meshes, SIAM Journal on Numerical Analysis, 39, 2089–2108, doi:10.1137/S0036142901387683, 2002.

Postel, S. L., Daily, G. C., and Ehrlich, P. R.: Human appropriation of renewable fresh water, Science, 271, 785–788, 1996.

Press, W. H.: Numerical Recipes: The Art of Scientific Computing, Cambridge University Press, 3rd edn., 2007.

Radzevicius, S. J., Chen, C.-C., Peters, L., and Daniels, J. J.: Near-field dipole radiation dynamics through FDTD modeling, Journal of Applied Geophysics, 52, 75–91, doi:10.1016/S0926-9851(02)00241-0, 2003.

Rhoades, J. D., Raats, P. A. C., and Prather, R. J.: Effects of liquid-phase electrical conductivity, water content, and surface conductivity on bulk soil electrical conductivity1, Soil Science Society of America Journal, 40, 651–655, doi:10.2136/sssaj1976.03615995004000050017x, 1976.

Richards, L. A.: Capillary conduction of liquids through porous mediums, Physics, 1, 318–333, doi:10.1063/1.1745010, 1931.

Ritter, A. and Muñoz-Carpena, R.: Performance evaluation of hydrological models: Statistical significance for reducing subjectivity in goodness-of-fit assessments, Journal of Hydrology, 480, 33–45, doi:10.1016/j.jhydrol.2012.12.004, 2013.

Ritter, A., Hupet, F., Muñoz-Carpena, R., Lambot, S., and Vanclooster, M.: Using inverse methods for estimating soil hydraulic properties from field data as an alternative to direct methods, Agricultural Water Management, 59, 77–96, doi:10.1016/S0378-3774(02)00160-9, 2003.

Robinson, D., Jones, S. B., Wraith, J., Or, D., and Friedman, S.: A review of advances in dielectric and electrical conductivity measurement in soils using time domain reflectometry, Vadose Zone Journal, 2, 444–475, doi:10.2136/vzj2003.4440, 2003.

Robinson, D. A., Binley, A., Crook, N., Day-Lewis, F. D., Ferré, T. P. A., Grauch, V. J. S., Knight, R., Knoll, M., Lakshmi, V., Miller, R., Nyquist, J., Pellerin, L., Singha, K., and Slater, L.: Advancing process-based watershed hydrological research using near-surface geophysics: A vision for, and review of, electrical and magnetic geophysical methods, Hydrological Processes, 22, 3604–3635, doi:10.1002/hyp.6963, 2008a.

Robinson, D. A., Campbell, C. S., Hopmans, J. W., Hornbuckle, B. K., Jones, S. B., Knight, R., Ogden, F., Selker, J., and Wendroth, O.: Soil moisture measurement for ecological and hydrological watershed-scale observatories: A review, Vadose Zone Journal, 7, 358–389, doi:10.2136/vzj2007.0143, 2008b.

Romanovsky, V. E. and Osterkamp, T. E.: Effects of unfrozen water on heat and mass transport processes in the active layer and permafrost, Permafrost and Periglacial Processes, 11, 219–239, doi:10.1002/1099-1530(200007/09)11:3<219::AID-PPP352>3.0.CO;2-7, 2000.

Rossi, M., Manoli, G., Pasetto, D., Deiana, R., Ferraris, S., Strobbia, C., Putti, M., and Cassiani, G.: Coupled inverse modeling of a controlled irrigation experiment using multiple hydro-geophysical data, Advances in Water Resources, 82, 150–165, doi:10.1016/j.advwatres.2015.03.008, 2015.

Roth, K.: Steady state flow in an unsaturated, two-dimensional, macroscopically homogeneous, Miller-similar medium, Water Resources Research, 31, 2127–2140, doi:10.1029/95WR00946, 1995.

Roth, K.: Soil Physics. Lecture Notes, Institute of Environmental Physics, Heidelberg University, Germany, www.iup.uni-heidelberg.de/institut/forschung/groups/ts/students/sp, 2012.

Roth, K., Schulin, R., Flühler, H., and Attinger, W.: Calibration of Time Domain Reflectometry for water content measurement using a composite dielectric approach, Water Resources Research, 26, 2267–2273, doi:10.1029/WR026i010p02267, 1990.

Rubin, Y. and Hubbard, S. S.: Hydrogeophysics, Springer, 2005.

Rutledge, D. and Muha, M.: Imaging antenna arrays, IEEE Transactions on Antennas and Propagation, 30, 535–540, doi:10.1109/TAP.1982.1142856, 1982.

Scharnagl, B., Vrugt, J., Vereecken, H., and Herbst, M.: Inverse modelling of in situ soil water dynamics: Investigating the effect of different prior distributions of the soil hydraulic parameters, Hydrology and Earth System Sciences, 15, doi:10.5194/hess-15-3043-2011, 2011.

Schellnhuber, H. J., Crutzen, P. J., Clark, W. C., and Hunt, J.: Earth system analysis for sustainability, Environment: Science and Policy for Sustainable Development, 47, 10–25, doi:10.3200/ENVT.47.8.10-25, 2005.

Schneider, K., Ippisch, O., and Roth, K.: Novel evaporation experiment to determine soil hydraulic properties, Hydrology and Earth System Sciences, 10, 817–827, doi:10.5194/hess-10-817-2006, 2006.

Scholer, M., Irving, J., Binley, A., and Holliger, K.: Estimating vadose zone hydraulic properties using ground penetrating radar: The impact of prior information, Water Resources Research, 47, doi:10.1029/2011WR010409, 2011.

Sellers, P. J., Dickinson, R. E., Randall, D. A., Betts, A. K., Hall, F. G., Berry, J. A., Collatz, G. J., Denning, A. S., Mooney, H. A., Nobre, C. A., Sato, N., Field, C. B., and Henderson-Sellers, A.: Modeling the exchanges of energy, water, and carbon between continents and the atmosphere, Science, 275, 502–509, doi:10.1126/science.275.5299.502, 1997.

Sen, P. N.: Grain shape effects on dielectric and electrical properties of rocks, Geophysics, 49, 586–587, doi:10.1190/1.1441695, 1984.

Seneviratne, S. I., Corti, T., Davin, E. L., Hirschi, M., Jaeger, E. B., Lehner, I., Orlowsky, B., and Teuling, A. J.: Investigating soil moisture–climate interactions in a changing climate: A review, Earth-Science Reviews, 99, 125–161, doi:10.1016/j.earscirev.2010.02.004, 2010.

Siebert, S., Burke, J., Faures, J. M., Frenken, K., Hoogeveen, J., Döll, P., and Portmann, F. T.: Groundwater use for irrigation – a global inventory, Hydrology and Earth System Sciences, 14, 1863–1880, doi:10.5194/hess-14-1863-2010, 2010.

Šimůnek, J., van Genuchten, M. T., and Wendroth, O.: Parameter estimation analysis of the evaporation method for determining soil hydraulic properties, Soil Science Society of America Journal, 62, 894–905, doi:10.2136/sssaj1998.03615995006200040007x, 1998.

Smyth, C. P.: Dielectric Behavior and Structure: Dielectric Constant and Loss, Dipole Moment and Molecular Structure, McGraw-Hill, 1955.

Sommerfeld, A.: Über die Ausbreitung der Wellen in der drahtlosen Telegraphie, Annalen der Physik, 333, 665–736, doi:10.1002/andp.19093330402, 1909.

Steelman, C. M. and Endres, A. L.: Comparison of petrophysical relationships for soil moisture estimation using GPR ground waves, Vadose Zone Journal, 10, 270–285, doi:10.2136/vzj2010.0040, 2011.

Taflove, A. and Hagness, S.: Computational Electrodynamics: The Finite-Difference Time-Domain Method, Artech House, 2nd edn., 2000.

Tarantola, A.: Inverse Problem Theory and Methods for Model Parameter Estimation, Society for Industrial and Applied Mathematics, doi:10.1137/1.9780898717921, 2005.

Thoma, M. J., Barrash, W., Cardiff, M., Bradford, J., and Mead, J.: Estimating Unsaturated Hydraulic Functions for Coarse Sediment from a Field-Scale Infiltration Experiment, Vadose Zone Journal, 13, doi:10.2136/vzj2013.05.0096, 2014.

Thompson, R. and Oldfield, F.: Magnetic properties of solids, chap. 2, Springer Netherlands, Dordrecht, doi:10.1007/978-94-011-8036-8_2, 1986.

Topp, G. C. and Miller, E.: Hysteretic moisture characteristics and hydraulic conductivities for glass-bead media, Soil Science Society of America Journal, 30, 156–162, doi:10.2136/sssaj1966.03615995003000020008x, 1966.

Topp, G. C., Davis, J. L., and Annan, A. P.: Electromagnetic determination of soil water content: Measurements in coaxial transmission lines, Water Resources Research, 16, 574–582, doi:10.1029/WR016i003p00574, 1980.

Tran, A. P., Vanclooster, M., Zupanski, M., and Lambot, S.: Joint estimation of soil moisture profile and hydraulic parameters by ground-penetrating radar data assimilation with maximum likelihood ensemble filter, Water Resources Research, 50, 3131–3146, doi:10.1002/2013WR014583, 2014.

Transtrum, M. K. and Sethna, J. P.: Improvements to the Levenberg–Marquardt algorithm for nonlinear least-squares minimization, arXiv:1201.5885 [physics.data-an], https://arxiv.org/abs/1201.5885, 2012.

Trenberth, K. E., Fasullo, J. T., and Kiehl, J.: Earth's global energy budget, Bulletin of the American Meteorological Society, 90, 311–323, doi:10.1175/2008BAMS2634.1, 2009.

Van Dam, J., Stricker, J., and Droogers, P.: Inverse method to determine soil hydraulic functions from multistep outflow experiments, Soil Science Society of America Journal, 58, 647–652, doi:10.2136/sssaj1994.03615995005800030002x, 1994.

van Genuchten, M. T.: A closed-form equation for predicting the hydraulic conductivity of unsaturated soils., Soil Science Society of America Journal, 44, 892–898, doi:10.2136/sssaj1980.03615995004400050002x, 1980.

Vereecken, H., Huisman, J. A., Bogena, H., Vanderborght, J., Vrugt, J. A., and Hopmans, J. W.: On the value of soil moisture measurements in vadose zone hydrology: A review, Water Resources Research, 44, doi:10.1029/2008WR006829, 2008.

Vereecken, H., Huisman, J. A., Hendricks Franssen, H. J., Brüggemann, N., Bogena, H. R., Kollet, S., Javaux, M., van der Kruk, J., and Vanderborght, J.: Soil hydrology: Recent methodological advances, challenges, and perspectives, Water Resources Research, 51, 2616–2633, doi:10.1002/2014WR016852, 2015.

Vogel, H.-J. and Roth, K.: Moving through scales of flow and transport in soil, Journal of Hydrology, 272, 95–106, doi:10.1016/S0022-1694(02)00257-3, 2003.

von Hippel, A. R.: The dielectric relaxation spectra of water, ice, and aqueous solutions, and their interpretation. I. Critical survey of the status-quo for water, IEEE Transactions on Electrical Insulation, 23, 801–816, doi:10.1109/14.8745, 1988.

Vrugt, J. A., Stauffer, P. H., Wöhling, T., Robinson, B. A., and Vesselinov, V. V.: Inverse modeling of subsurface flow and transport properties: A review with new developments, Vadose Zone Journal, 7, 843–864, doi:10.2136/vzj2007.0078, 2008a.

Vrugt, J. A., ter Braak, C. J. F., Clark, M. P., Hyman, J. M., and Robinson, B. A.: Treatment of input uncertainty in hydrologic modeling: Doing hydrology backward with Markov chain Monte Carlo simulation, Water Resources Research, 44, doi:10.1029/2007WR006720, 2008b.

Wada, Y., van Beek, L. P. H., van Kempen, C. M., Reckman, J. W. T. M., Vasak, S., and Bierkens, M. F. P.: Global depletion of groundwater resources, Geophysical Research Letters, 37, doi:10.1029/2010GL044571, 2010.

Warren, C. and Giannopoulos, A.: Investigation of the directivity of a commercial Ground-Penetrating Radar antenna using a finite-difference time-domain antenna model, in: 2012 14th International Conference on Ground Penetrating Radar (GPR), pp. 226–231, doi:10.1109/ICGPR.2012.6254865, 2012.

Wöhling, T., Vrugt, J. A., and Barkle, G. F.: Comparison of three multiobjective optimization algorithms for inverse modeling of vadose zone hydraulic properties, Soil Science Society of America Journal, 72, 305–319, doi:10.2136/sssaj2007.0176, 2008.

Wollschläger, U., Pfaff, T., and Roth, K.: Field-scale apparent hydraulic parameterisation obtained from TDR time series and inverse modelling, Hydrology and Earth System Sciences, 13, 1953–1966, doi:10.5194/hess-13-1953-2009, 2009.

Wu, C.-C. and Margulis, S. A.: Feasibility of real-time soil state and flux characterization for wastewater reuse using an embedded sensor network data assimilation approach, Journal of hydrology, 399, 313–325, doi:10.1016/j.jhydrol.2011.01.011, 2011.

Wöhling, T. and Vrugt, J. A.: Multiresponse multilayer vadose zone model calibration using Markov chain Monte Carlo simulation and field water retention data, Water Resources Research, 47, doi:10.1029/2010WR009265, 2011.

Yee, K.: Numerical solution of initial boundary value problems involving Maxwell's equations in isotropic media, IEEE Transactions on Antennas and Propagation, 14, 302–307, doi:10.1109/TAP.1966.1138693, 1966.

Zangwill, A.: Modern Electrodynamics, Cambridge University Press, 2012.

Danksagung

Die Durchführung der Experimente wurde durch die Deutsche Forschungsgemeinschaft (DFG) über Projekt RO 1080/12-1 unterstützt. Ohne Zugang zum bwforcluster wäre die Arbeit in dieser Form nicht möglich gewesen. Dieser wurde vom Land Baden-Württemberg durch das Projekt bwHPC und durch die DFG durch das Projekt INST 35/1134-1 FUGG finanziell unterstützt.

Ich möchte mich bei meinen Betreuern Kurt Roth und Peter Bastian sowie bei meinen Mentoren Olaf Ippisch und Christoph Garbe herzlich für die Unterstützung während der Promotion bedanken. Herzlichen Dank auch an Norbert Frank für das bereitwillige Erstellen eines Gutachtens zu dieser Arbeit.

Der HGS MathComp möchte ich nicht nur für die Übernahme der (Reise-)Kosten für viele Konferenzen und Workshops, sondern auch für Kaffee, Kekse und Kuchen danken. Das spannende Vorlesungs- und Workshop-Angebot sorgte für Abwechslung im Promotionsalltag. Ich finde es ausgezeichnet, dass es möglich war, Vorlesungen vorzuschlagen und mit zu organisieren. Herzlicher Dank geht dabei an Peter Jan van Leeuwen, der einwilligte, seinen Data Assimilation Kompaktkurs in Heidelberg zu halten und mit uns zu diskutieren. Ebenso schätze ich das Annual Colloquium der HGS MathComp sehr, nicht nur um die Perspektive zu erweitern und um zu Netzwerken, sondern auch um gemeinsam zu feiern.

Bei Stefan Friedel möchte ich mich für raschen und kompetenten Support bezüglich des bwforclusters herzlich bedanken. Besonders bedanken möchte ich mich bei Andreas Dörr für die Idee zum und die Hilfe beim Aufsetzen eines beowulf clusters.

Großer Dank gebührt Jens Buchner und Patrick Klenk, die mir immer Vorbilder geblieben sind. Besonderer Dank geht dabei an Patrick Klenk für die intensiven Jahre, in denen wir nicht nur das Büro, sondern auch den Arbeitsaufwand einer beträchtlichen Anzahl an Experimenten geteilt haben. Die damit verbundenen Anstrengungen, wie reguläres Übernachten neben ASSESS im Frühjahr auch bei Regen und Schnee, motivierten zum Aufbau eines Daches auf ASSESS. Herzlichen Dank an alle, die beim Aufbau dieses Daches geholfen haben. Dies gilt auch für die FP Studenten und allen Mitgliedern der Arbeitsgruppe, die bei teils doch etwas verrückten Experimenten mitgewirkt, mitgeholfen und mitgelitten haben. Besonders bedanken möchte ich mich bei Daniel Berg, Hannes Bauser und Lisa Hantschel für Diskussionen und Zusammenarbeit aller Art. Auch möchte ich mich bei Xicai Pan für die bisherige Zusammenarbeit sehr bedanken.

Herzlich bedanken möchte ich mich natürlich auch bei Angelika Gassama für jegliche Unterstützung bezüglich ASSESS, der Verwaltung und nicht zuletzt für die tollen Feste bei sich zu Hause.

Bei Kurt Roth möchte ich mich im Speziellen bedanken für Inspirationen, Diskussionen, die lockere Arbeitsatmosphäre, die Retreats in Hornberg, Arolla, Oppenau und Egg, sowie für seine Offenheit mich auch an ungewöhnlichen Konferenzen teilnehmen zu lassen. Toll finde ich, dass sich seine Unterstützung nicht nur auf die fachliche Ebene beschränkte.

Nicht bedanken möchte ich mich dafür, dass die meisten Freunde und Verwandte nun endgültig in der Welt verstreut sind. Umso schöner ist es dann, wenn man sich mal wieder sieht.

Nicht genug danken kann man unserer inzwischen zusammengewachsenen Familie – allen (Groß-)Eltern, dem Bruder, den Onkeln, Tanten, Cousinen, Cousins, – für Eure Unterstützung auf unserem gesamten Lebensweg, gute Gespräche, gemeinsame Feiern, Herzlichkeit und Akzeptanz, wenn wir nicht so viel Zeit hatten und wir uns nicht so oft sahen.

Noch mehr möchte ich Elli danken, für ihre Geduld und ihre Unterstützung sogar bei der Durchführung des hier ausgewerteten Experimentes. Dafür, dass Du mich aus dem Alltag entführst und mich nicht nur gegen Ende der Promotion ertragen hast. Ich genieße die gemeinsame Zeit mit Dir außerordentlich und freue mich sehr darauf, jeden Tag mit Dir ein bisschen älter zu werden.

We shall never cease from exploration and the end of all our exploring will be to arrive where we started and know the place for the first time.

—Thomas Stearns Eliot